Seismic Evaluation of Expanded Polystyrene (EPS) Geofoam Bridge Support System for Overpass Structures

Steven F. Bartlett
Associate Professor
Department of Civil and Environmental Engineering
University of Utah
Salt Lake City, Utah, 84112
Phone: (801)587-7726
Email: bartlett@civil.utah.edu

Ramesh Neupane
Graduate Student
Department of Civil and Environmental Engineering
University of Utah
Salt Lake City, Utah, 84112
Phone: (801)587-7726
Email: rameshneupane8@gmail.com

March 2017

ACKNOWLEDGEMENTS

The authors would like to extend their gratitude and thanks to the Mountain Plains Consortium (MPC) under project MPC-422, and the Norwegian Public Roads Administration (NPRA) for their support of this research.

In addition, the authors thank Roald Aaboe, Jan Vaslestad, David Arellano, Evert Lawton Amanda Bordelon, Eunhye Kim, Clifton Farnsworth and Richard Porter for their review and suggestions regarding the execution this study and the suggests for improvements of this report.

The authors also thank ACH Foam Technologies of Murray, Utah for providing the EPS geofoam specimens used in the laboratory testing. The authors also wish to thank Mark Bryant, Trevor Nye and Daniel Seely for their help in setting up the laboratory experiments.

Disclaimer

ABSTRACT

Expanded Polystyrene (EPS) geofoam is a superlight weight material used in various transportation engineering applications. It has been particularly successful as an ultra-light weight alternative to earthen, geosynthetic reinforced soil (GRS), and mechanically-stabilized earth (MSE) embankment systems when deployed as approach embankment for highway bridges located atop soft soil sites.

The goal of this study is to extend the application of EPS geofoam to that of directly supporting relatively light-weight bridge structures without the need of installing intermediate or deep foundation systems or using ground improvement to stabilize the foundation soils. This study evaluates the concept of using EPS blocks to support 2-lane, single-span highway and pedestrian bridge structures under gravity and seismic loads. If the concept is successfully established, an EPS bridge support system might significantly contribute to accelerated bridge construction (ABC) technologies for certain classes and sizes of bridge structures. The deployment of this technology may lead to rapid and more economical deployment of bridge foundations for permanent and temporary bridge structures in areas plagued with soft ground issues that hamper or limit the use of conventional embankment and bridge support construction (e.g., large consolidation and post-construction creep settlement, low bearing capacity, poor construction conditions, relocation of buried utilities, potential settlement damage to adjacent structures and foundations.

TABLE OF CONTENTS

ACKNOWLEDGEMENTS i
ABSTRACT ii
TABLE OF CONTENTS iii
LIST OF TABLES vi
LIST OF FIGURES vii
EXECUTIVE SUMMARY x
1. INTRODUCTION 1
1.1 Background 1
1.2 Problem Statement 3
1.3 Objectives of Study 4
1.4 Research Tasks 4
1.5 Design Methods for Determining Allowable Stress in EPS Blocks 4
1.5.1 U.S. Practice 5
1.5.2 European Practice 6
1.5.3 Comparison of Allowable Stress from U.S. and European Practice 7
1.5.4 Recommendations for Additional Work 8
2 ALLOWABLE STRESS IN EPS FOR EARTHQUAKE LOADINGS 9
2.1 Summary of Previous Cyclic Testing Programs on EPS 9
2.2 Experimental Objectives and Overview 9
2.3 Experimental Device 11
2.4 Experimental Procedure 11
2.4.1 Monotonic Uniaxial Tests 11
2.4.1.1 Sample Preparation 11
2.4.1.2 Monotonic Loading 12
2.4.2 Cyclic Uniaxial Tests 12
2.4.2.1 Consolidation Phase 12
2.4.2.2 Cyclic loading Phase 14
2.4.3 Post-cyclic Creep Tests 15
2.4.3.1 Sample Preparation Phase 17
2.5 Results of Experimental Program 17
2.5.1 Monotonic Uniaxial Tests 17
2.5.2 Cyclic Uniaxial Tests 20
2.5.3 Post-cyclic Creep Tests 36
2.6 Estimation of Total Permeant Strain 43
2.7 Recommendations for Allowable Stress in EPS for Seismic Loadings 43
3 EVALUATION OF EPS BRIDGE SUPPORT SYSTEM 45
3.1 Introduction 45
3.2 General Considerations 45
3.3 Bridge Configurations 47
3.4 Permanent Load Evaluations 47
3.4.1 EPS Compressive Resistance 47
3.4.2 Vertical Stress Distribution Calculation 48

3.4.3 Gravitational Dead Loads 48
3.5 Transient Load Evaluations 49
3.5.1 Design Vehicular Live Loads 49
3.5.2 Evaluation of Bridge Type, Width and Potential Span Length 49
3.5.3 Earthquake Extreme Event Limit State 51
3.5.3.1 Introduction 51
3.5.3.2 General Considerations 51
3.5.3.3 Geometrical Configurations Evaluated 51
3.5.3.4 Limit States and Allowable Stress in the EPS Blocks 52
3.5.3.5 Recommended Design Allowable Stress Limits for EPS Blocks 53
3.5.3.6 Simplified Force-Based Methods Based on Fundamental Period 53
3.5.3.7 Analytical Evaluations of Fundamental Period 54
3.5.3.7.1 Derivation Based on Flexural and Shear Stiffness 55
3.5.3.7.2 Derivation Based on Horvath (1995, 2004) Stark et al. (2000) 57
3.5.3.7.3 Derivation Based on Flexural, Shear and Axial Stiffness 58
3.5.3.7.4 Derivation for Excitation In the Vertical Direction 59
3.5.3.7.5 Numerical Evaluations of Fundamental Period 59
3.5.3.7.5.1 Rectangular Prismatic Embankments 59
3.5.3.7.6 Comparison of Analytical and Numerical Methods for Rectangular Prismatic Embankments 63
3.5.3.7.7 Comparison of Analytical and Numerical Methods for Trapezoidal Rectangular Embankments 67
3.5.3.7.8 Summary of Fundamental Period Evaluations 74
3.5.3.8 Interlayer and Basal Sliding Evaluations 74
3.5.3.8.1.1 General Considerations 74
3.5.3.8.1.2 Methodology 76
3.5.3.8.1.3 Counter Measures for Interlayer Sliding 78
3.5.3.8.1.4 Sliding Evaluation Results 78
3.5.3.8.1.5 Summary and Recommendations for Sliding 79
3.5.3.9 Methods for Evaluating Horizontal Sway and Rocking 80
3.5.3.9.1 Analytical Evaluations of Fundamental Period 80
3.5.3.9.1.1 Sway Fundamental Period Based on Shear Stiffness 80
3.5.3.9.1.2 Rocking Fundamental Period Based on Flexural, Shear and Axial Stiffness 82
3.5.3.9.2 Numerical Evaluation of Fundamental Period for Sway 82
3.5.3.9.2.1 Model Development and Material Properties 85
3.5.3.9.3 Comparison of Methods For Estimating Fundamental Period 87
3.5.3.9.3.1 Sway Mode 87

3.5.3.9.3.2 Rocking Mode 89
3.5.3.9.3.3 Numerical Evaluations of Sway, Rocking and Uplift 91
3.5.3.10 Development of a Seismic Restraint System 110
3.5.3.10.1 Introduction 110
3.5.3.10.2 Evaluation of Countermeasures 111
3.5.3.10.2.1 Sway mode 112
3.5.3.10.2.2 Rocking and Uplift 114
3.5.3.10.2.3 Recommendations for Cabling System 116
4 Summary and Conclusions 117
5 References 119

LIST OF TABLES

Table 2.1. Summary of monotonic uniaxial test results..... 20
Table 2.2. Summary of pre-cyclic creep tests..... 21
Table 2.3. Summary of cyclic uniaxial test results..... 2-31
Table 2.4. Young's modulus for repeated cyclic loads..... 35
Table 2.5. Summary of pre and post-cyclic creep and estimated total strain permanent strain for 50-year design period..... 2-38
Table 3.1. Compressive resistance of EPS geofoam at various levels of strain..... 47
Table 3.2. Material properties for modeling of EPS geofoam support system..... 61
Table 3.3. Percentage error of FLAC with Method I and Method II for single lane and double lane with various length of footing for rectangular prismatic shape embankment..... 66
Table 3.4. Percentage error of FLAC with Method I and Method II for single lane and double lane with various length of footing for trapezoidal prismatic shape embankment..... 68
Table 3.5. Summary of critical acceleration for rectangular and trapezoidal prismatic shape embankments..... 79
Table 3.6. Material properties of EPS geofoam embankment system for sway mode..... 83
Table 3.7. EPS geofoam embankment system material properties for rocking mode..... 86
Table 3.8. Percentage error of analytical method with FLAC for single and double lane with various length of footing for rectangular prism..... 89
Table 3.9. Percentage error of analytical and FLAC for single and double lane with various length of footing for rectangular prism..... 91

LIST OF FIGURES

Figure 1-1 Single-lane, single-span, steel bridge structure supported on EPS block at Lokkeberg, Norway (Aabøe and Frydenlund, 2011). 2
Figure 1-2 Single-lane, single-span, concrete bridge structure supported on EPS block abutment at Hjelmungen, Norway (Aabøe and Frydenlund, 2011) 2
Figure 1-3 Axial stress- axial strain curve for EPS 19 (i.e., density = 19 kg/m^3) normalized to compressive resistance at 10 percent strain. 6
Figure 2-1. Cyclic triaxial equipment at the University of Utah , after Geocomp (2006) 11
Figure 2-2 A completed set-up EPS specimen for monotonic and cyclic uniaxial testing 12
Figure 2-3 Density distribution of tested EPS geofoam specimens 13
Figure 2-4 Vertical strain versus time for pre-cyclic test 14
Figure 2-5 Vertical strain versus logarithmic of time for pre-cyclic test 14
Figure 2-6 Cyclic deviatoric stress versus cyclic axial strain 15
Figure 2-7 Vertical strain versus time for post-cyclic test 16
Figure 2-8 Vertical strain versus logarithm of time for post-cyclic test 17
Figure 2-9 Combined plots of deviatoric stress versus axial strain 18
Figure 2-10 Combined plots of normalized vertical stress versus axial strain 18
Figure 2-11 Correlation of Young's modulus and EPS density 19
Figure 2-12 Results of cyclic uniaxial test at same level of cyclic deviatoric stresses but at different number of cycles (5, 15 and 30 number of cycles) on EPS 25 22
Figure 2-13 Results of cyclic uniaxial tests on three samples at three different cyclic deviatoric stresses with same number of cycles on EPS 25 23
Figure 2-14 Results of cyclic uniaxial tests on three samples at same cyclic deviatoric stresses with three different number of cycles on EPS 25 23
Figure 2-15 Results of cyclic uniaxial tests on four samples at 15 number of cycles with three different cyclic deviatoric stresses on EPS 25 24
Figure 2-16 Results of cyclic uniaxial tests on three samples at same level of cyclic deviatoric stresses with three different number of cycles on EPS 25 24
Figure 2-17 Results of cyclic uniaxial tests on three samples at three different level of cyclic deviatoric stresses with 30 number of cycles on EPS 25 26
Figure 2-18 Results of cyclic uniaxial tests on three samples at three different level of cyclic deviatoric stresses under peak load with 15 number of cycles on EPS 25 26
Figure 2-19 Results of cyclic uniaxial tests on four samples at two different level of cyclic deviatoric stresses with three different number of cycles on EPS 29 27
Figure 2-20 Results of cyclic uniaxial tests on three samples at same level of cyclic deviatoric stresses with three different number of cycles on EPS 39 27
Figure 2-21 Cyclic stress-strain hysteresis loop and corresponding Young's modulus (E_c) (a) EPS 25 (b) EPS 29 and (c) EPS 39 29
Figure 2-22 Correlation of mean degraded shear modulus and nominal EPS density 30
Figure 2-23 Repeated cyclic uniaxial tests at two differing cyclic deviatoric stresses (a) Stress corresponds to 1 % strain, (b) Stress corresponds to 0.5 % strain, as measured from monotonic tests. 33
Figure 2-24 Repeated cyclic uniaxial tests at two different cyclic deviatoric stresses (a) Stress corresponds to 4 % strain (b) Stress corresponds to 0.5 % strain, as measured in the monotonic tests. 34
Figure 2-25 Cyclic plastic axial strain with number of cycles at different cyclic deviatoric stresses (a) 15 number of cycles (b) 30 number of cycles 36
Figure 2-26 Results of post-cyclic uniaxial test at same level of cyclic deviatoric stresses and at different number of cycles on EPS 25 39
Figure 2-27 Results of post-cyclic uniaxial tests on three samples at three different cyclic deviatoric stresses with same number of cycles on EPS 25 39
Figure 2-28 Results of post-cyclic uniaxial tests on three samples at same cyclic deviatoric stresses with three different number of cycles on EPS 25 40
Figure 2-29 Results of post-cyclic uniaxial tests on four samples at 15 number of cycles with four different cyclic deviatoric stresses on EPS 25 40

Figure 2-30 Results of post-cyclic uniaxial tests on three samples at same cyclic deviatoric stresses (corresponds to 1% strain) with three different number of cycles on EPS 25 41
Figure 2-31 Results of post-cyclic uniaxial tests on three samples at 30 number of cycles with three different cyclic deviatoric stresses on EPS 25 41
Figure 2-32 Results of post-cyclic uniaxial tests on four samples at two different level of cyclic deviatoric stresses with three different number of cycles on EPS 29 42
Figure 2-33 Results of post-cyclic uniaxial tests on three samples at same level of cyclic deviatoric stresses with three different number of cycles on EPS 39 42
Figure 2-34 Post cyclic axial strain with time for EPS 25 under the peak load (stress same as the total stress during cyclic phase)..... 43
Figure 2-35. Recommended allowable stresses for dead load and dead load + earthquake loading combinations for EPS bridge support systems. 44
Figure 3-1 Conceptual bridge support with a rectangular prismatic shaped EPS embankment 46
Figure 3-2 Conceptual bridge support with a trapezoidal prismatic shaped EPS embankment..... 46
Figure 3-3 Approximate stress distribution by the 2V to 1H method (NCHRP 529). 48
Figure 3-4 Characteristic of the HL-93 design truck (AASHTO, 2012) 49
Figure 3-5 Relationship of length of bridge with length of footing for single and double-lane bridges supported on EPS 22 (red) and EPS 29 (black)..... 50
Figure 3-6 Longitudinal and cross section of rectangular prismatic shape EPS Embankment..... 52
Figure 3-7 Longitudinal and cross section of trapezoidal prismatic shape EPS embankment..... 52
Figure 3-8 Idealization of an EPS free-standing embankment to a single degree of freedom (SDOF) system (after Riad and Horvath, 2004). 54
Figure 3-9 EPS geofoam embankment system 60
Figure 3-10 Displacement at top versus dynamic time under forced vibration 62
Figure 3-11 Sine wave pulse used for free vibration simulation 62
Figure 3-12 Displacement at top node versus time at fundamental period for free vibration simulation 63
Figure 3-13. Fundamental period of rectangular prismatic shape embankment from numerical (red) and analytical methods at various length of footing for single lane bridge 64
Figure 3-14. Fundamental period of rectangular prismatic shape embankment from numerical (red) and analytical methods at various length of footing for double lane bridge..... 64
Figure 3-15 Simplified method for converting trapezoidal shape to rectangular shape (after Horvath, 1995). 67
Figure 3-16 Fundamental period of trapezoidal prismatic shape embankment for double lane obtained from numerical and analytical methods for various length of footing 69
Figure 3-17 Percentage of error with length of footing for single lane between FLAC and Method I..... 70
Figure 3-18. Percentage of error with length of footing for double lane between FLAC and Method I 71
Figure 3-19. Percentage of error with length of footing for single lane between FLAC and Method II 72
Figure 3-20. Percentage of error with length of footing for double lane between FLAC and Method II 73
Figure 3-21 Comparison of maximum sliding extents in two cases of only horizontal and both horizontal and vertical harmonic input motion at varying acceleration amplitudes. 76
Figure 3-22. EPS geofoam embankment system 83
Figure 3-23. Displacement versus dynamic time at top node under free vibration for excitation in the longitudinal direction..... 84
Figure 3-24. Displacement versus time at top node under force vibration for excitation in the longitudinal direction..... 84
Figure 3-25. EPS embankment with soil and foundation of bridge..... 86
Figure 3-26. Fundamental period of analytical and FLAC for single lane rectangular prismatic embankment 88
Figure 3-27. Fundamental period of analytical and FLAC for double lane rectangular prismatic embankment 88
Figure 3-28. Fundamental period of rectangular prism embankment for single lane from analytical and FLAC..... 90
Figure 3-29. Fundamental period of rectangular prism embankment for double lane from analytical and FLAC..... 90
Figure 3-30. EPS geofoam embankment model under sway mode during excitation in the longitudinal direction..... 92

Figure 3-31. Zone numbers of EPS embankment model for sway condition 93
Figure 3-32. Relationship of shear stresses with dynamic time at different level of excitations during fundamental period for sway in the longitudinal direction 94
Figure 3-33. Relationship of normal stresses with dynamic time at different level of excitations during fundamental period for sway in longitudinal direction 94
Figure 3-34. Relationship of shear stresses with dynamic time at different level of excitations during fundamental period for sway in the transverse direction 95
Figure 3-35. Relationship of normal stresses with dynamic time at different level of excitations during fundamental period for sway in the transverse-direction 96
Figure 3-36. Relationship of acceleration and maximum shear stress for sway in the longitudinal direction 96
Figure 3-37. Relationship of acceleration and maximum normal stress for sway in the longitudinal direction 97
Figure 3-38. Relationship of acceleration and maximum shear stress for sway in the transverse direction. 97
Figure 3-39. Relationship of acceleration and maximum normal stress for sway in the transverse-direction 98
Figure 3-40. EPS geofoam embankment model under rocking along transverse direction due to excitation along longitudinal-direction 99
Figure 3-41. Number of zones on EPS embankment model under rocking condition..... 99
Figure 3-42. Relationship of normal stress with dynamic time at left and right corner zones under rocking in the transverse direction due to the excitation in the longitudinal-direction at 0.2 g acceleration 100
Figure 3-43. Relationship of shear stress with dynamic time at left and right corner zones under rocking in the transverse direction due to the excitation in the longitudinal direction at 0.2 g acceleration 100
Figure 3-44. Relationship of acceleration with maximum normal stress for rocking in the transverse direction due to the excitation in the longitudinal direction 102
Figure 3-45. Relationship of acceleration with maximum shear stress for rocking in the transverse direction due to excitation in the longitudinal direction 102
Figure 3-46. Relationship of acceleration with maximum normal stress for rocking in the transverse direction due to excitation in the longitudinal direction and transverse directions simultaneously.....103
Figure 3-47. Relationship of acceleration with maximum shear stress for rocking in the transverse direction due to excitation in the longitudinal and transverse directions simultaneously.....103
Figure 3-48. Relationship of acceleration with maximum normal stress for rocking in the transverse direction for the excitation in the longitudinal, transverse and vertical-directions simultaneously.....104
Figure 3-49. Relationship of acceleration with max shear stress for rocking in the transverse-direction due to excitation in the longitudinal, transverse and vertical-directions simultaneously 104
Figure 3-50. Uplift at right side of the model due to excitation of 0.5 g acceleration in the longitudinal direction for rocking in the transverse direction.....105
Figure 3-51. Relationship of normal stress and dynamic time at two level of acceleration shows the initiation of uplift for the excitation in the longitudinal direction 106
Figure 3-52. Cross-section of EPS embankment with forces acting on it 107
Figure 3-53. Relative displacement with dynamic time at level of acceleration of 0.2 g for the excitation along longitudinal-direction 109
Figure 3-54. Relationship of acceleration and uplift for the excitation in the longitudinal direction 109
Figure 3-55. Relationship of acceleration and uplift for the excitation in the longitudinal and transverse directions 110
Figure 3-56. Relationship of acceleration and uplift for the excitation in the longitudinal, transverse and vertical directions 110
Figure 3-57. Force versus displacement relationship of EPS and cable 112
Figure 3-58. Force versus horizontal displacement relationship for combined EPS block and cable system. 114
Figure 3-59 Relationship of horizontal acceleration and uplift of basal layer of EPS embankment for case without cabling 115
Figure 3-60. Relationship of horizontal acceleration and uplift of basal concrete foundation slab for case with cabling 115

EXECUTIVE SUMMARY

This study improves on the EPS bridge support technology recently developed by the Norwegian Public Roads Administration (NPRA) (Aaboe and Frydenlund, 2011) in that additional evaluations were carried out to evaluate the seismic and post-seismic performance of a conceptual EPS bridge support system. From a material property standpoint, monotonic and cyclic uniaxial compression tests were performed on EPS specimens to define the allowable static and dynamic stresses that might develop within the EPS block without incurring unacceptable cyclic and long-term creep deformation of the embankment. These laboratory test results were used in conjunction with analytical and numerical methods to evaluate the potential behavior(s) of the EPS embankment support system subjected to three components of harmonic motion (i.e., two horizontal and one vertical). In these evaluations, various external and internal failure modes were explored (e.g., interlayer and basal sliding, EPS block overstressing due to horizontal sway and rocking/uplift) using dynamic analyses based on the explicit finite difference method. In the end, the acceleration required to initiate these potential failure modes (i.e., critical acceleration) was determined for two EPS bridge support embankment configurations: (1) free-standing, and (2) sloped. The critical accelerations for interlayer and basal sliding, sway and rocking/uplift were estimated to be 0.6, 0.2 and 0.3 g, respectively. Lastly, a cable restraint system is proposed and evaluated to improve the dynamic performance of the bridge support system so as to limit the development and deformation associated with these potential failure modes.

1. INTRODUCTION

1.1 Background

Expanded polystyrene (EPS) geofoam is a super-lightweight, closed-cell, rigid plastic foam-like material used in many civil engineering applications. The predominant shape of EPS product used in most cases is prismatic block, which can vary in size based on the size of the mold. Block molders, or manufactures of EPS block, use a process where beads of EPS are expanded to form relatively rigid block. EPS beads consist of closed-cell polystyrene plastic containing pentane gas. The EPS blocks are created from these beads in a two-stage process namely: (1) pre-expansion and (2) molding. In the pre-expansion stage, beads are placed within a container and heated with steam to temperatures between 80 and 110^0C. During pre-expansion heating, the pentane vaporizes within the closed cell softening the polystyrene and causing an expansion of the bead to around 50 times its original volume. The expanded beads (called pre-puffs) are then allowed to cool for several hours. Following this, the pre-puff beads are placed in an enclosed, fixed-wall, stainless steel mold where the spherical beads are continuously re-softened and further expanded using injected, pressurized steam. In this molding stage, further expansion of the beads forms a closed-cell relatively rigid block with no significant void space between the spheres. The blocks are then released from the mold and allowed to cure for several days in an environmentally-controlled space (Horvath, 1994).

The funding for this research is associated with "Highway Structures Supported on EPS Embankment without Deep Foundations" funded by the Mountain Plains Consortium (MPC) with funding coming from its affiliate at the Utah Transportation Center (UTC) at the University of Utah. Other research participation for this topic has been also provided by the Norwegian Public Roads Administration (NPRA). The use of block-molded EPS geofoam in roadway embankment applications was pioneered by the Norwegians in 1972 (Refsdal, 1985; Aaboe, 1987), and subsequent work and development has been reported by many researchers and practitioners. It has been used as light-weight embankment (Elragi, 2000; Zou et al., 2000; Newman et al., 2009), as a compressible inclusion within earth retaining structures (Elragi, 2000; Trandafir et al., 2010), for pavement support (Beinbrech and Hillmann, 1997; Duškov, 1997), for protection of buried pipeline systems (Elragi, 2000; Lingwall, 2011) and as light-weight backfill for bridge abutments (Elragi, 2000; Snow and Nickerson, 2004; Stuedlein and Negussey, 2013).

In the past, embankments with conventional fill materials have been used for bridge approach and bridge support systems, and depending on ground conditions intermediate or deep foundation systems have usually been required. However, similar to a geosynthetic reinforced soil (GRS) bridge abutment, EPS geofoam blocks could be used for bridge support without the installation of other foundation systems, or the use of significant ground improvement. Unlike GRS bridge abutments, and EPS bridge support system can be built rapidly on soft ground due to its extreme light-weight characteristics. For example, the Norwegian Public Roads Administration (NPRA) has pioneered EPS bridge support technology for applications at quick clay sites where EPS blocks were used to support relatively light-weight, steel, concrete and wooden bridge structures having relatively short spans (e.g., about 30 to 40 m) (Figures 1-1 and 1-2). These EPS bridge support systems have demonstrated relatively good long-term performance in terms of bearing capacity and creep settlement within the EPS blocks and the underlying foundation soils (Aaboe and Frydenlund, 2011).

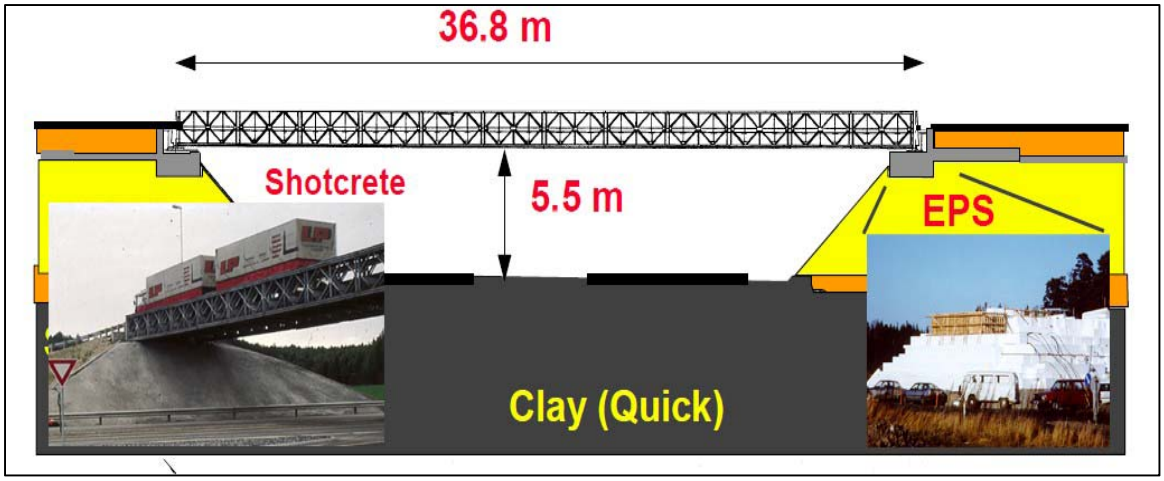

Figure 1-1 Single-lane, single-span, steel bridge structure supported on EPS block at Lokkeberg, Norway (Aabøe and Frydenlund, 2011).

Figure 1-2 Single-lane, single-span, concrete bridge structure supported on EPS block abutment at Hjelmungen, Norway (Aabøe and Frydenlund, 2011).

However, Norway is relatively aseismic when compared with the U.S., and the NPRA has not made allowances for significant earthquake forces in the design and construction of their systems. In addition, there are no documented cases worldwide of using EPS blocks for direct bridge support at locations with significant seismicity where relatively large horizontal and vertical seismic loadings are possible.

The extension of EPS bridge support technology originally developed by NPRA into accelerated bridge construction (ABC) for potential U.S. application, and the evaluations, testing and development required for the deployment of this technology in earthquake-prone areas, is the primary focus of this research. It is the goal of this research to demonstrate proof of concept of an EPS bridge support system that can be constructed rapidly and does not require installation of

intermediate or deep foundations systems or significant ground improvement to support the bridge structure and resist the required seismic loadings.

A light-weight EPS bridge support system would have several distinct advantages over conventional earthen embankment, MSE walls, and GRS abutments constructed on soft ground: (1) extremely rapid construction could occur using pre-fabricated bridge and bridge support components, (2) EPS support and light-weight bridge systems could be design to be re-useable in that they could be modular and constructed and deconstructed and the components transported and reused, as might be useful for temporary bridge structures, or for pedestrian bridges. (3) significant consolidation settlement and bearing capacity issues can be avoided at soft ground sites, thus eliminating the construction delay associated with waiting for the completion of primary consolidation, or the concerns with potential failure of the foundation soils, (4) light-weight bridge support systems can be constructed in urban areas atop or near buried utilities and adjacent to nearby structures without undergoing costly relocation of these utilities, or causing settlement damage to adjacent facilities and structures, and (5) inertial loadings from the EPS embankment system to the bridge system can be significantly reduced due to the light-weight nature of the EPS blocks.

1.2 Problem Statement

The NPRA has pioneered an EPS bridge support system where the bridge structure rests solely on EPS blocks without the aid of deep foundations. This has been done for a limited number of relatively small bridge overpass structures founded on quick clays in Norway. However, the design and construction of the NPRA system considered only the vertical static (i.e.., dead) load from the weight of the structure and the live vehicular loads.
However in the United States, where bridge systems may be exposed to extreme loading events, like earthquakes, the bridge and EPS support system will undergo additional dynamic loadings that include significant horizontal and vertical components of strong motion. For 3D earthquake shaking, the possible modes of excitation and limit states for prismatic embankments are: (1) interlayer sliding occurring between adjacent layers of EPS blocks, (2) basal sliding occurring between the lowest layer of EPS blocks and the foundation soil, and (3) potential overstressing and damage to the EPS blocks resulting from excessive shear and compression of the blocks due to horizontal sway and (4) excessive rocking and uplift of the embankment.

Overturning of an EPS embankment is not a likely extreme event limit state for the width to height aspect ratios typically used in roadway construction. Previous dynamic modeling of rocking and sway suggests that internal deformation caused by these mechanisms can cause localized tensile yielding of some blocks within the core of the embankment, usually near the base (Bartlett and Lawton, 2008). In the extreme case, at high levels of strong ground motion, tensile yielding within the EPS mass may propagate upward and cause the embankment to begin to decouple dynamically. This decoupling of the embankment between the blocks within the embankment precludes the potential for overturning of the embankment. However, such rocking may lead to excessive deformation of the EPS blocks.

In order to assess the potential dynamic behavior and performance of an EPS bridge support system, evaluations are required that estimate the critical acceleration associated with the potential failure modes mentioned above. The critical acceleration is defined as the acceleration level at which the factor of safety becomes 1.0 for each of the respective modes of failure. In addition to these evaluations, a seismic lateral restraint system(s) will be conceptually developed and evaluated

herein with the goal of improving the seismic performance of the EPS support system without overstressing the system members, including the EPS block components.

1.3 Objectives of Study

The primary objectives associated with this evaluation are: (1) conceptualize an EPS support system for one to two-lane, single-span bridge structures and pedestrian overpasses using experience gained from cases implemented by the Norwegian Public Roads Administration (NPRA) and from information obtained from additional laboratory tests and calculations performed herein, (2) develop design criteria for the allowable stress in EPS blocks under static and dynamic loadings, (3) evaluate the stability and potential performance of such system(s) under static, vehicular and seismic loadings, and (4) make recommendations for future research, testing and development required for the implementation of this technology in the U.S. and elsewhere.

1.4 Research Tasks

The primary tasks required to complete these objectives are: (1) develop prototype geometry and configurations of EPS support embankments and the size and length of the associated bridge systems, (2) perform laboratory-scale experiments to estimate the potential amount of cyclic and post-cyclic creep strain that develops in EPS blocks undergoing various levels and number of cycles of excitation, (3) use the information from the laboratory test program to define the allowable stress level in the EPS for seismic design purposes, (4) conduct numerical evaluations of the prototype system(s) considering the gravity and vehicular loads and the internal and external seismic stability of EPS support geofoam embankments specifically considering the potential for interlayer and basal sliding, rocking and sway modes of failure, and (5) develop and evaluate a seismic restraint system(s) that might be employed to resist the dynamic forces associated with these potential failure modes, thus potentially increasing the internal and external dynamic stability of the system(s).

This report directly addresses the above objectives and tasks with the ultimate goal of making recommendations for the future design and construction of bridge structures at soft soil sites where the bridge is supported directly by EPS geofoam blocks without the need of intermediate or deep foundation systems, or the use of significant soil improvement. If this system is not conceptualized, designed and properly constructed, it could be subjected to large and unacceptable amount of pre- and post-earthquake movement, deformation and settlement resulting from the shifting and overstressing of blocks and/or failure or yielding within the foundation soils.

1.5 Design Methods for Determining Allowable Stress in EPS Blocks

The topic of potential deformation of EPS blocks becomes especially germane for EPS bridge support systems where the anticipated dead and live loads will be significantly higher than for EPS bridge approach embankments that have only modest loading requirements. The stress-strain behavior of EPS geofoam under monotonic and cyclic loadings is time and rate dependent for both short-term and long-term loading conditions. The short-term loadings for the EPS support system may originate from impact, earthquake, large trucks, construction activities, etc., and the long-term loading is produced by gravity (i.e., self-weight of the materials and components of the system). These long-term, sustained loadings can produce deformation of the EPS block under a constant applied stress condition. Such deformation is commonly referred to as creep. One of the primary goals of EPS design for civil engineering applications is to limit the combination of short-term and

long-term stresses imposed within the EPS blocks in order to limit the permanent deformation to acceptable levels. Excessive deformation in EPS bridge support systems may lead to reaching a serviceability limit state in terms of unacceptable settlement of the bridge and its support components. This in turn may reduce the performance of the bridge system or shorten its operational lifespan. A commonly selected project performance goal for EPS systems is to limit the total deformation (elastic + creep deformation) to 2 percent, or less, in a 50-year post-construction period (Bartlett et al., 2000; EPS White Book, 2011).

Both the potential for reaching an ultimate limit state (ULS) and a serviceability limit state (SLS) from excessive creep and cyclic deformation within the EPS blocks are addressed by this study. For seismic events, the EPS support system and any additional seismic restraint system employed must be sufficient to resist the gravity and seismic forces associated with the following potential modes of failure: (1) ULS - basal and interlayer sliding, (2) SLS – component overstressing from horizontal sway and embankment rocking, (3) ULS – uplift and overturning of the embankment. The forces associated with these modes must be resisted without overstressing the system members, including the EPS block components. Overstressing of the EPS blocks may result from several sources, most important of which are: (1) gravity loads from the weight of the structure and other bridge support components, (2) gravity loads from other live load sources (e.g., trucks and vehicles present on the structure during the earthquake) and (3) internal cyclic axial and shear loadings caused by the design seismic event.

The following sections describe current design practice for evaluating the allowable stress for EPS blocks used in embankment systems. Following this summary, recommendations will be made regarding implementation or improvement of these methods for evaluating EPS bridge support systems undergoing seismic loadings.

1.5.1 U.S. Practice

In the U.S., the National Cooperative Highway Research Program guidelines for EPS design (NCHRP 529) recommends limiting the vertical stress in the EPS block resulting from the combination of the dead and live loads to a factored value that is equal to or less than the “elastic limit stress”. The “elastic limit stress,” as defined by this document corresponds to the uniaxial compressive resistance of the EPS specimen measured at 1 percent axial strain. In calculating the allowable stress, a load factor of 1.3 is applied to the stress resulting from the traffic loads to account for potential impact loading. Lastly, a safety factor of 1.2 is applied to the combined stresses resulting from all dead and live loads. The factored combined stress is then compared with the “elastic limit stress” to verify that the latter stress exceeds the former.

At first glance, it may seem reasonable to adopt the “elastic limit stress” and load factors of NCHRP 529 as design criteria for determining the allowable stress for future U.S. projects. However, the primary focus of this work is to develop design criteria for EPS bridge support systems and not for EPS embankment systems. There are significant differences in the applied loads and performance requirements for these two systems. The latter system has relatively modest requirements in terms of vertical support of dead loads, whereas the former system must directly support the weight of the bridge, bridge vehicular loads, and be able to resist rather large temporary inertial loads induced by earthquake events. Because of these relatively large stresses, it is possible that the total stress induced in the EPS blocks may temporarily exceed the NCHRP “elastic limit stress,” especially for peak stress cycles occurring during earthquake events. The consequences of any temporary exceedance may result in inelastic cyclic and additional post-cyclic creep deformation of the EPS bridge support system. The amount of potential deformation originating from these sources needs to be estimated and explicitly accounted for in the design procedure.

1.5.2 European Practice

EPS laboratory testing and research from the Netherlands has shown that if the stress from the permanent dead load is limited to a value of 30 percent of the compressive resistance at 10 percent strain, σ_{10}, for the selected type and density of EPS, then the compressive creep deformation will be 2 percent, or less, in 50 years (Duškov, 1997; EPS White Book, 2011). Subsequent research by Srirajan et al. (2001) on 300-mm cube samples found that EPS geofoam would experience a total strain of less than 2 percent in 50 years when subjected to 50 percent of the compressive resistance at 5 percent strain, σ_5. Note that σ_5, as used in Norwegian practice, is approximately 93 percent of σ_{10} for typical specimens of EPS 19, Figure 1-3). Therefore, the Srirajan et al. (2001) recommendation, written in terms of $\sigma_{10,}$ would state that EPS subjected to working loads (i.e., permanent dead loads) less than or equal to about 46.5 percent of σ_{10} would experience a total strain of less than 2 percent in 50 years. Note that the axial strain corresponding to 50 percent of σ_5 is just slightly less than the "elastic limit stress of NCHRP 529 (Figure 1-3). However, 50 percent of σ_5 is applied only to the dead loads as used by Srirajan et al. (2001) and is not applied to the factored combination of dead and live load, as required by NCHRP 529. Nonetheless, the recommendation of Srirajan et al. (2001) has not been widely adopted by European or U.S. practice.

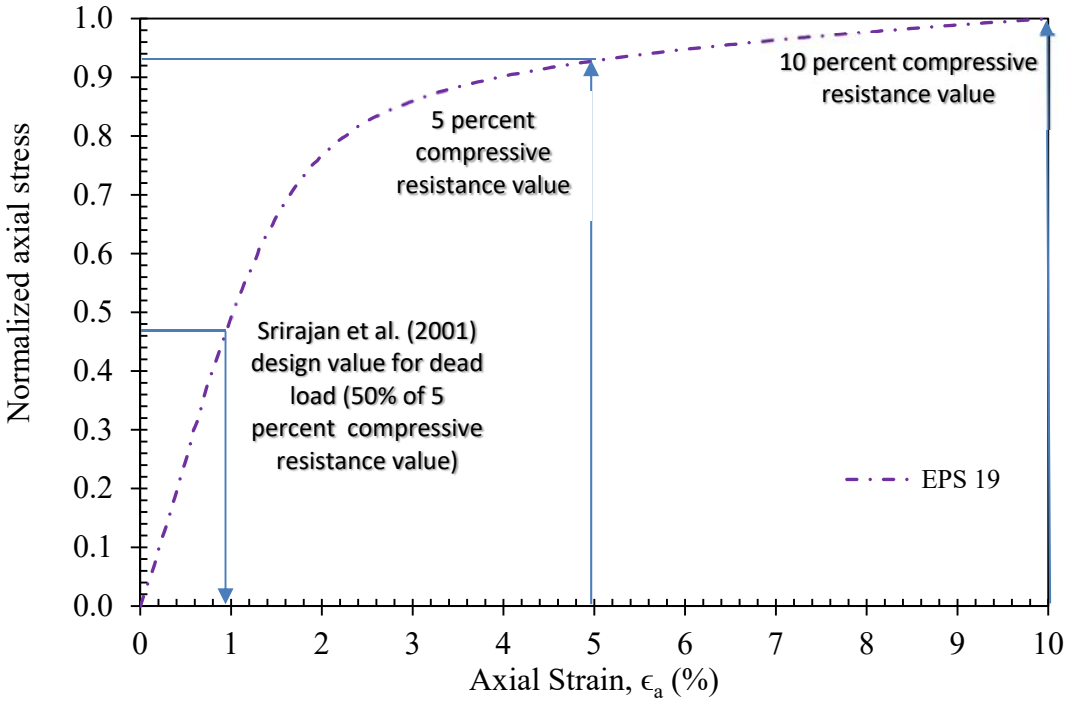

Figure 1-3 Axial stress- axial strain curve for EPS 19 (i.e., density = 19 kg/m^3) normalized to compressive resistance at 10 percent strain.

Although not specifically developed for seismic loadings, European design practice has developed a design evaluation case that addresses short-term loadings, presumably associated with construction activities. This case allows for the development of higher stress levels in the EPS block for temporary conditions (EPS White Book, 2011). For an Ultimate Limit State for short term loading, ULS-STR short-term, the guidance states: "Multiply the dead and imposed load with their respective loading factors and combine both loads. Calculate the acting design compressive stress

$\sigma_{10;d}$ and compare it with the short term design compressive strength (e.g. 80 kPa for EPS 100). The short term acting stress should be less than or equal to the short term strength."

EPS 100 in the above paragraph signifies EPS specimens having a compressive resistance of 100 kPa at 10 percent axial strain. This value is the so called "declared short-term value of compressive strength, σ_{10}." Importantly, European design guidance starts the design calculations for various load combinations using σ_{10}, instead of the "elastic limit stress" (i.e. 1 percent resistance value) used by NCHRP 529, and the σ_5 value used in Norwegian practice. However the declared value is factored to a design value, $\sigma_{10,d}$, by dividing σ_{10} by a material resistance factor, γ_m, of 1.25, which is equivalent to using 80 percent of the σ_{10} value. Ultimately, the design value is compared with and must exceed the factored load combination for the ULS-STR short term case. This load combination considers the permanent dead loads, construction-related dead and live loads, and traffic loads.

1.5.3 Comparison of Allowable Stress from U.S. and European Practice

It is possible to make a comparison of the allowable stress obtained from NCHRP 529 with that of the EPS White Book (2011) for the ULS-STR short term case using a typical stress-strain curve for EPS 19 (Figure 1-3). For this comparison, it will be assumed that the compressive resistance at 10 percent strain is 100 kPa, a typical value for EPS 19. Therefore in this case, the elastic limit stress from NCHRP 529 is 48 kPa which also corresponds to 48 percent of the compressive resistance at 10 percent strain. In contrast, based on the ULS-STR short term (EPS White Book 2011), the declared short-term value of compressive strength, σ_{10}, is 100 kPa, which is subsequently divided by a material resistance factor of 1.25. Hence, the allowable stress in the EPS for this case is 80 kPa, which corresponds to an axial strain of about 2.2 percent.

Based on the comparison it is clear that the allowable stress for temporary or short-term conditions in the EPS blocks, $\sigma_{10,d}$, found in EPS White Book (2011) is considerably higher than the "elastic limit stress" of NCHRP 529 (Figure 1-4). However for final design evaluations, it is also important to consider the recommended safety factors or load factors used by each method. NCHRP 529 applies a safety factor of 1.2 to the combined dead and live loads; whereas the EPS White Book (2011) for the short term load case applies a load factor of 1.35 to permanent and temporary dead loads and a factor of 1.5 to traffic loads. Although the load factors from the EPS White Book (2011) applied to $\sigma_{10,d}$ are somewhat larger than the safety factor applied by NCHRP 529 to the "elastic limit" stress, it is clear that for all cases, the design allowable stress in the EPS block obtained by the EPS White Book (2011) will be somewhat higher than that of NCHRP 529.

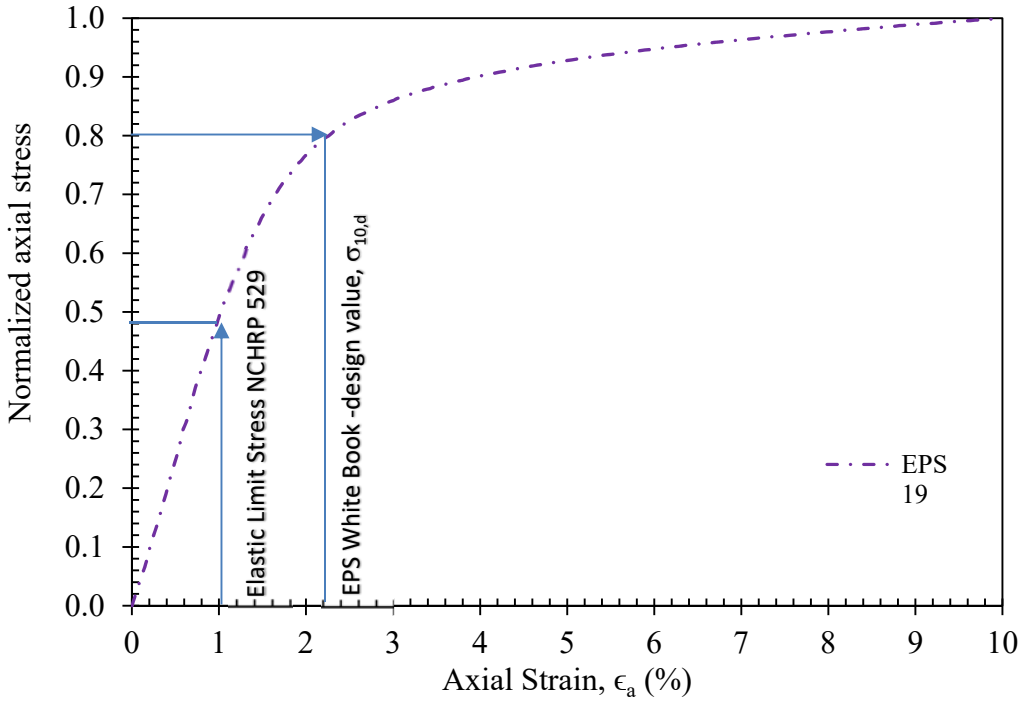

Figure 1-4. Typical axial stress versus axial strain curve for EPS 19 (i.e., density = 19 kg/m^3) normalized to compressive resistance at 10 percent strain.

1.5.4 Recommendations for Additional Work

This research seeks to define the allowable stress for EPS blocks used in bridge support systems considering the potential for permanent deformation arising from significant earthquake loadings and from creep under long-term dead loads. The performance goal adopted herein is to limit the total permanent deformation originating from earthquake cycling and from creep to 1 percent, or less, in a 50-year post-construction period and to limit the total deformation (elastic + creep + cyclic) to 2 percent, or less, in a 50-year post-construction period. In addition, based on the approach given in the EPS White Book (2011), the allowance for higher temporary stresses in the EPS during a seismic event may be a more rational way of approaching EPS design, because earthquake loadings are short-lived (lasting a few tens of seconds) and occur very infrequently. However, in terms of allowable stress design (ASD), if the combined stresses from dead, live, vehicular and transient seismic loads are too high, then significant inelastic behavior may occur. The resulting deformation might result in the bridge support system reaching a serviceability limit state (SLS), which would be manifested by unacceptably large creep deformation within the EPS support system with the passing of time.

2 ALLOWABLE STRESS IN EPS FOR EARTHQUAKE LOADINGS

2.1 Summary of Previous Cyclic Testing Programs on EPS

There has been previous work focusing on the behavior of EPS under cyclic loading (e.g., Duškov, 1997; Athanasopoulos et al., 1999; Trandafir et al., 2010); however, these studies varied considerably regarding study objectives, methods and the conditions for cyclic loading (i.e., amplitude, rate, method of application, etc.). Most importantly, none of these studies explored the effects of cycling on the post-cyclic creep behavior of EPS at the strain levels expected for seismic loadings.

European design guidance (EPS White Book, 2011) is based on work performed by Duškov (1997). Duškov conducted uniaxial strain-controlled, cyclic loading tests on EPS geofoam to study the impact of traffic loading on pavement/geofoam systems. Permanent vertical deformations ranging from 0.4 to 0.7 percent were observed for the applied range of cyclic axial stresses. Later, Athanasopoulos et al. (1999) conducted resonant column and cyclic uniaxial tests under strain-controlled conditions on EPS specimens with average densities of 12.4 and 17.1 kg/m^3. These test results were used to develop the material properties needed for dynamic response modeling of EPS embankments (i.e., shear modulus degradation and damping curves); however, no post-cyclic creep deformation was measured by these researchers, so the potential for post-cyclic creep remained unquantified. The test results of Athanasopoulos et al. (1999) indicated the geofoam density significantly affects the dynamic shear modulus, whereas no substantial effect on the damping ratio was observed. More recently, Trandafir et al. (2010) conducted stress-controlled cyclic uniaxial tests on EPS geofoam specimens with densities of 15, 25 and 32 kg/m^3 in both the elastic and plastic strain ranges. From these test results, cyclic strain amplitudes of up to 0.87 to 1.0 percent were considered as threshold amplitudes for viscoelastic and visco-elasto-plastic behavior, respectively. No post-cyclic creep deformation was measured as part of this study

2.2 Experimental Objectives and Overview

From an experimental design perspective, it is important to consider the nature and duration of the permanent and temporary loads and their relationship in affecting the long term creep behavior of the EPS specimens. From a field performance standpoint, it is important that the total permanent deformation from these two sources remain within tolerable limits so that the serviceability of the bridge support system is not compromised. Ultimately, it is hoped that the results of the laboratory test program can be generalized and used in determining the allowable or acceptable stress level for EPS bridge support systems undergoing seismic excitation.

The main objectives of the laboratory investigations described herein are to: (1) quantify the total permanent strain considering both cyclic and post-cyclic creep strain induced in the laboratory specimens, (2) quantify these strains for the following experimental factors: (a) density of EPS specimens, (b) number of uniform stress cycles, (c) magnitude of uniform stress cycles, and (d) magnitude of applied post-cyclic axial stress.

To address the pre- and post-earthquake deformation performance of EPS blocks under dead and cyclic loadings, a laboratory test program was executed in the Soil Mechanics Laboratory at the University of Utah. The laboratory test program included monotonic, cyclic and post-cyclic loadings performed in a cyclic triaxial test apparatus. Initially, routine monotonic uniaxial

compression tests were done to obtain the stress-strain properties of the EPS specimens of densities ranging from 15 to 39 kg/m^3.

Because relatively high densities of EPS may be required for bridge support systems, specimens of EPS 25, EPS 29 and EPS 39 were used in the cyclic part of the test program. In addition, because EPS support embankments are primarily above ground systems (i.e., no significant burial), which produces little to no horizontal confinement of the EPS blocks, all laboratory tests conducted herein were done in unconfined compression. The cyclic uniaxial stress-controlled tests were performed using 5, 15 and 30 uniform stress cycles.

Subsequently, a representative stress representing the dead load was reapplied to the specimens after the cyclic loading, and the post-cyclic creep strain was measured. This strain is associated with the long-term deformation under a constant dead load that persists and must be resisted by the system following seismic excitation. In this phase of the test program, the EPS specimens were immediately re-subjected to a constant vertical stress corresponding to the pre-cycling vertical stress level. The post-cyclic creep strain for a 50-year design period was then estimated from these test results using the slope of a creep strain versus logarithm of time plot. The total strain (i.e., cyclic and creep) was then calculated as the sum of the permanent cyclic plastic axial strain and the 50-year post-cyclic creep strain, as described in Section 2.6.

2.3 Experimental Device

The cyclic test equipment is shown in Figure 2-1, which was manufactured by GeoComp Corporation of Foxborough, Massachusetts. It consists of the LoadTrac™, FlowTrac™, and a hydraulic power unit. The LoadTrac™ consists of a load frame, load cell, displacement transducer and a plexiglass cell. Two FlowTrac™ pumps, one for the sample pressure and the other for the cell pressure were available, but were not used due to the uniaxial (unconfined) conditions of the test. The hydraulic power unit was connected with the servo controller. The power unit in conjunction with the servo provides the cyclic loading on the specimen.

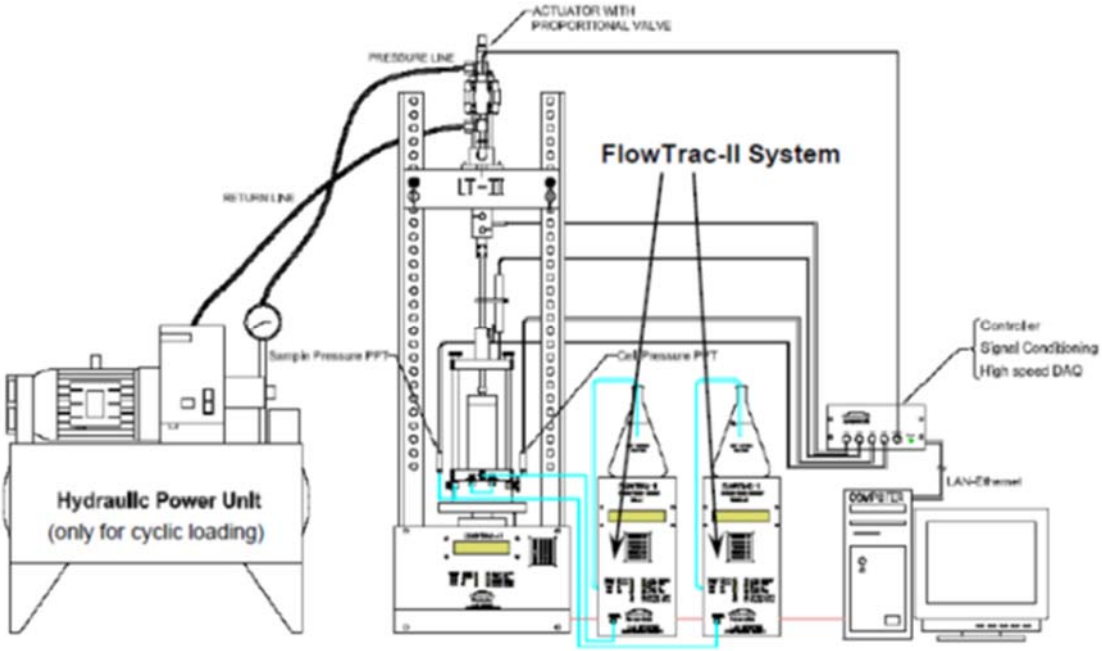

Figure 2-1. Cyclic triaxial equipment at the University of Utah , after Geocomp (2006)

The data acquisition system utilized a state of the art microprocessor with controlled and fully-automated test equipment. The system is a complete, self-contained unit with all of the capabilities required to perform fully-automated cyclic tests and to automatically record and store experimental data. The system had the capability for applying both monotonic and cyclic loadings. The cylindrical specimen selected for this study were of sizes: 50 mm, 71 mm and 100 mm diameter, all of which can be accommodated in the plexiglass cell.

2.4 Experimental Procedure

The laboratory test program was organized into three series of tests: monotonic uniaxial testing, cyclic uniaxial testing and post-cyclic uniaxial testing with creep measurements.

2.4.1 Monotonic Uniaxial Tests

In the monotonic uniaxial load tests, specimens of EPS 15, EPS 19, EPS 25, EPS 29 and EPS 39 were used. These tests were done in two steps: sample preparation and monotonic loading.

2.4.1.1 Sample Preparation

Cylindrical EPS specimens of 100-mm diameter by 100-mm high were used for the testing. These specimens were hot-wire cut by ACH Foam in Murray, Utah and given to the University of Utah for this research effort. An example specimen is shown in Figure 2-2. The dimension and weight of the sample were measured and recorded in order to calculate the actual bulk density of each specimen. The specimens were then placed in the load cell. A porous stone was placed on the lower platen of the cell to ensure a flat, uniform surface. The specimen was then placed above the porous stone and an identical stone was placed on the top of the specimen. The completed set up of the specimen prepared for testing is shown in Figure 2-2.

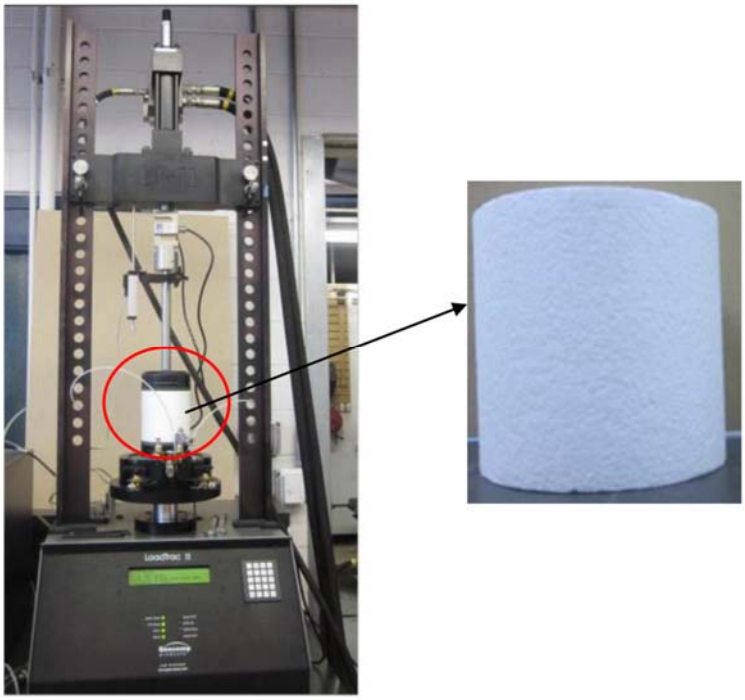

Figure 2-2 A completed set-up EPS specimen for monotonic and cyclic uniaxial testing

2.4.1.2 Monotonic Loading

The specimen was subsequently monotonically loaded under strain-controlled conditions at a vertical strain rate of 10 percent per minute, which is the industry standardized rate for QC/QA testing of EPS specimens (ASTM D6817/D6817M). Once the loading had been completed, the data were collected and plotted to produce the relation between applied deviatoric stress versus axial strain. From plots of this type, the compressive resistance of the EPS corresponding to uniaxial strain values of 1, 1.5, 1.75, 2, 5 and 10 percent were determined and used in the subsequent cyclic test program, as described below.

2.4.2 Cyclic Uniaxial Tests

The cyclic uniaxial stress-controlled tests were done in three steps: sample preparation, consolidation and cyclic loading. For these tests, specimens of EPS 25, EPS 29 and EPS 39 were used. The distribution of measured densities used in this program is shown in Figure 2-3

2.4.2.1 Consolidation Phase

In this step, a constant static deviatoric stress (σ_{ds}) was applied to the specimen until the elastic strain was essentially completed and creep strain was well developed. In this phase, the applied deviatoric stress level generally corresponded to that obtained at 1 percent axial strain based from the results of the monotonic uniaxial tests; however a few exploratory tests were consolidated at higher stress levels.

To ensure that all specimens had experienced a relatively uniform amount of secondary (i.e., creep) compression before initiating the cycling, the creep behavior duration of the consolidation phase was evaluated using plots of percent of vertical strain versus elapsed time (for example see, Figures 2-4 and 2-5). From the data plotted in these figures, it is clear that creep strain dominated the strain behavior after about one minute following the application of the deviatoric stress (Figure 2-4). After this, strain was occurring more or less at a constant rate in regards to the logarithm of elapsed time (Figure 2-5). Similar behavior was observed for all EPS specimens of varying density. Therefore, the duration of the consolidation phase was set to 30 minutes for all EPS specimens tested by this research. This standardized consolidation duration ensured that the creep behavior and duration was uniform amongst all of the specimens and that at least one-log cycle of creep had been completed before starting the cycling phase.
Nonetheless, in field applications, where EPS blocks are used for bridge support systems, the amount of creep strain occurring under static dead loads will be variable and dependent upon the elapsed time between bridge/embankment construction and the earthquake event. The amount of pre-earthquake creep strain incurred in the field by full-size blocks may somewhat affect their cyclic behavior, but generally in a beneficial way. For example, it is well-documented that "pre-loaded" or consolidated specimens of EPS have a higher Young's modulus, as long as the specimens have not been loaded to a state of stress that causes significant yielding of the EPS.

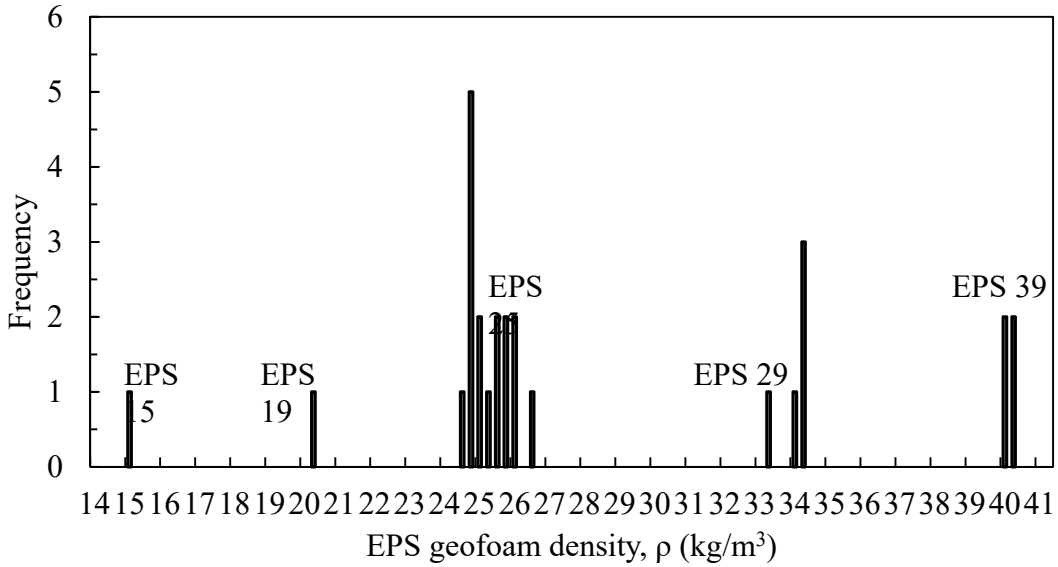

Figure 2-3 Density distribution of tested EPS geofoam specimens

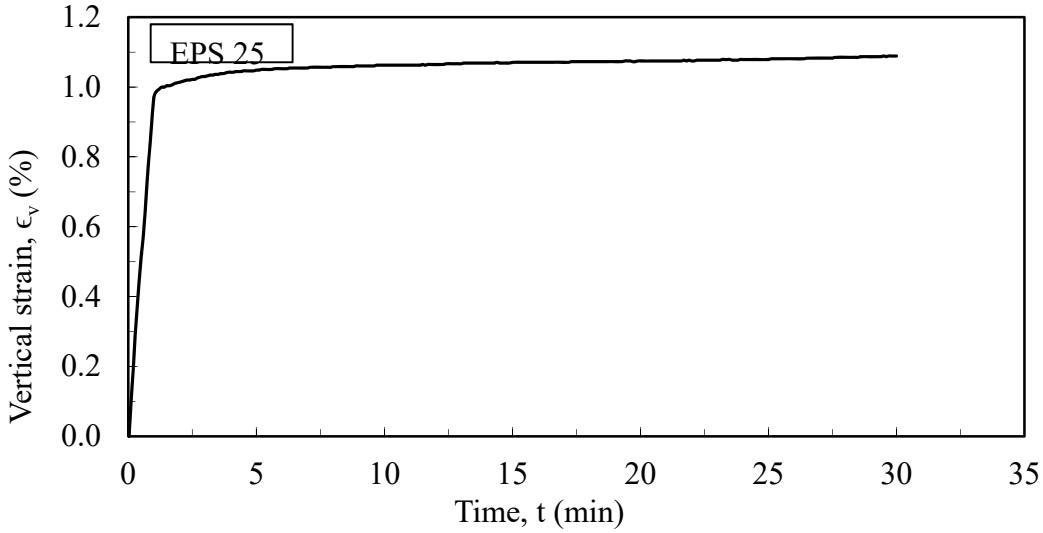

Figure 2-4 Vertical strain versus time for pre-cyclic test

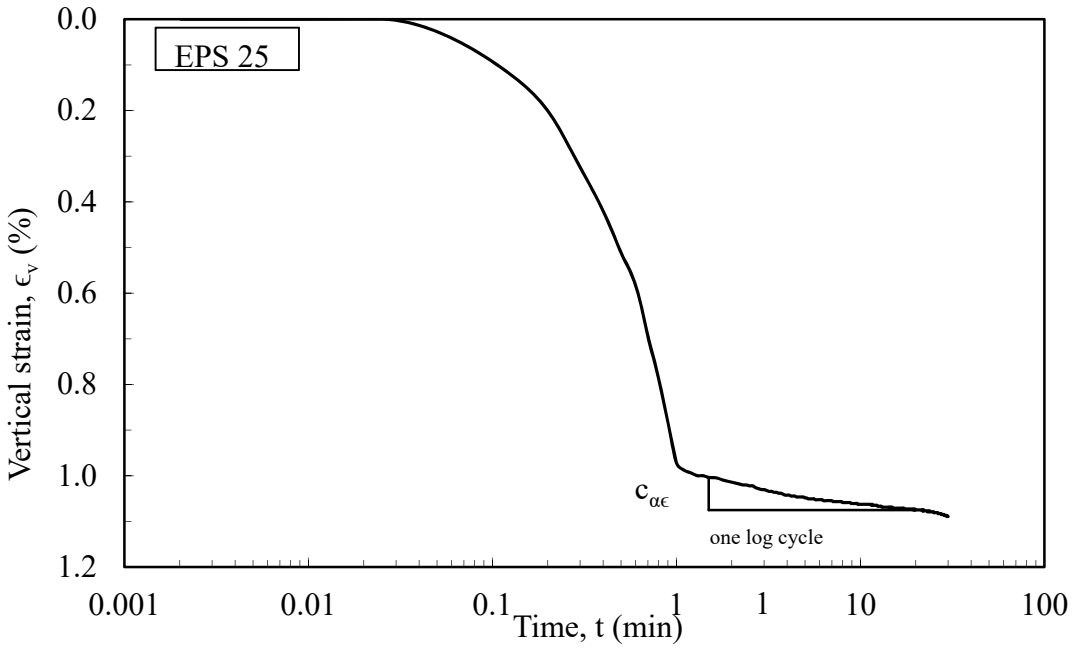

Figure 2-5 Vertical strain versus logarithmic of time for pre-cyclic test

2.4.2.2 Cyclic loading Phase

A relationship between the number of equivalent stress cycles and earthquake magnitude was developed by Seed and Idriss (1982). On the basis of this study, with minor adjustments, 5, 15 and 30 stress cycles were selected to represent small (M=6), moderate (M=7.5), and large (M>8.5) magnitude earthquakes with their short, moderate, and long durations of seismic excitation, respectively. The frequency (*f*) of cycling was set to 1 Hz and the sampling rate for the data acquisition system was set to 20 Hz.

Upon completion of the consolidation phase, the static deviatoric stress was maintained and an additional cyclic deviatoric stress ($\Delta\sigma_{dc}$) was applied to the specimens. For example, in the cyclic part of the test program, if the testing goal was to reach a stress level associated with 1.5 percent total axial strain, as obtained from the monotonic tests for the respective density of EPS, then the specimens were consolidated to a stress level corresponding to 1 percent axial strain. After completion of 30 minutes, an additional cyclic deviatoric stress, $\Delta\sigma_{dc}$, was applied which corresponded obtained from the monotonic test results for the respective density of EPS.
Figure 2-6 shows a representative test of the additional stress required to achieve 1.5 percent total strain in the specimens, as a cyclic test result for EPS 25 consolidated to 72 kPa for 30 minutes and cycled at 1 Hz at $\Delta\sigma_{dc}$ value of 27 kPa for 15 cycles. The 72 kPa value corresponds to the 1 percent strain value from the monotonic test, and the 27 kPa value corresponds to the increase stress required to produce 1.5 percent strain in the monotonic test (see Table 2.1). It is important to note that the realized cyclic axial strain, ϵ_{ac}, of about 0.3 percent in the specimen from Figure 2-6 is somewhat less than the 0. 5 axial strain produced for the same axial stress increase in the monotonic tests (Table 2.1). The smaller cyclic strain is a result of an apparent increase in the modulus of the specimen resulting from the creep deformation realized during the consolidation phase of the cyclic testing.

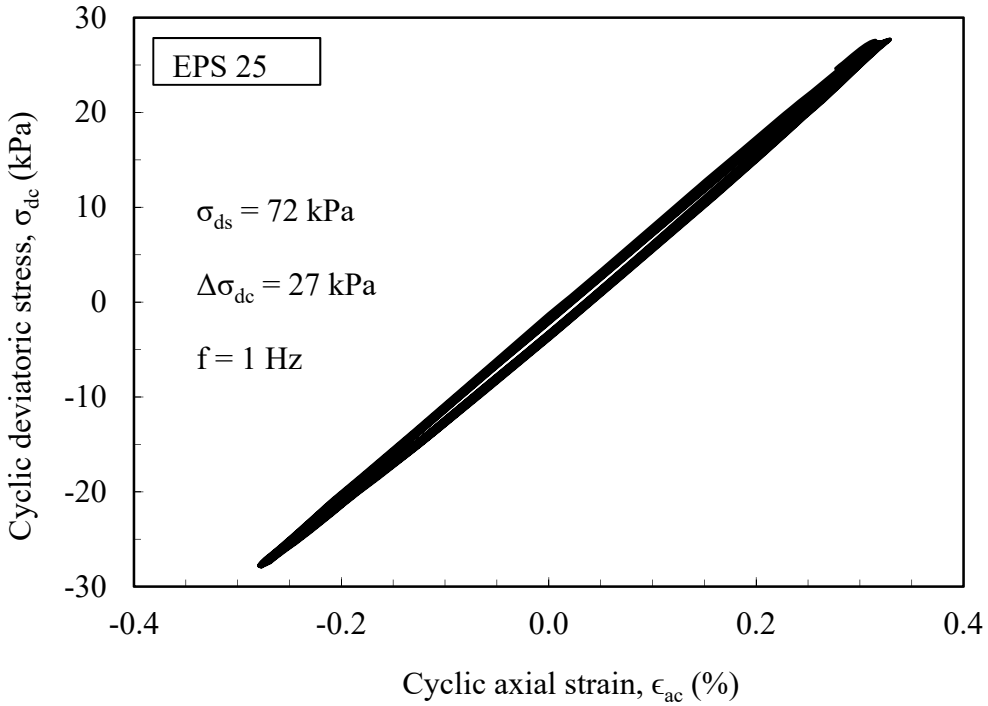

Figure 2-6 Cyclic deviatoric stress versus cyclic axial strain

2.4.3 Post-cyclic Creep Tests

The post-cyclic creep tests were conducted immediately following the cyclic tests using the same test device. The post-cyclic creep strain is the vertical strain associated with the vertical stress applied immediately after cycling. This stress is meant to represent the post-earthquake long-term dead load of the EPS bridge support system. In these tests, the samples were subjected to a post-cyclic constant uniaxial vertical stress corresponding to the stress level at 1 percent axial strain obtained from the monotonic tests. In the cyclic testing equipment, there was no provision of reapplying the vertical load on the specimen immediately after the cyclic loading without unloading

the sample. (The system is programed to automatically unload after cycling.) Therefore, the sample was immediately reloaded back to the appropriate stress level and allowed to undergo post-cyclic creep strain. Most samples were reloaded back to a vertical stress level equivalent to 1 percent axial strain obtained from the monotonic tests. However, a few specimens were loaded at higher post-cyclic stress levels to explore the influence of this factor on the post-cyclic creep behavior.

The duration of application of the load for the post-cyclic creep measurements was determined from several trials. In order to establish the duration of the post-cyclic phase, plots were made of the percentage of total axial vertical strain versus elapsed time and logarithm of elapsed time. The plot of vertical total strain against time and logarithm of time for EPS 25 at a stress level corresponding to 1.5 percent total strain (i.e., 1 percent consolidation and 0.5 percent cyclic) and for 15 stress cycles is shown in Figures 2-7 and 2.8.

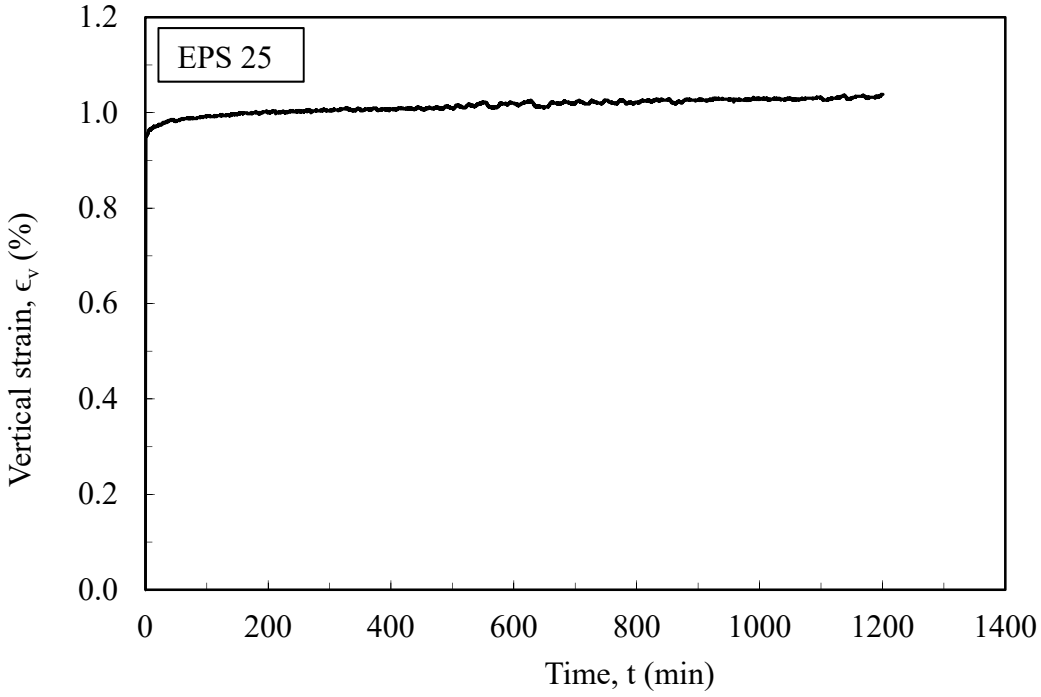

Figure 2-7 Vertical strain versus time for post-cyclic test

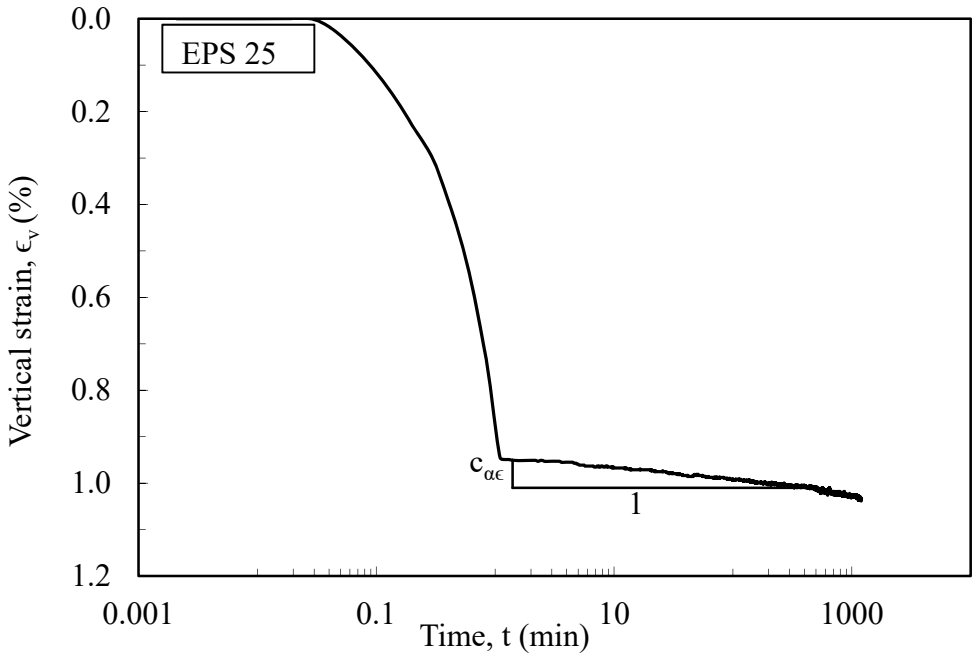

Figure 2-8 Vertical strain versus logarithm of time for post-cyclic test

Based on Figure 2-8, it is clear that creep strain was well developed at about one minute after applying the post-cyclic stress. The rate of creep behavior occurred at a constant value of $C_{\alpha\epsilon}$ thereafter.

2.4.3.1 Sample Preparation Phase

The same specimen dimensions used for the monotonic tests were used in the cyclic tests. The density of each specimen was calculated and recorded. The distribution of specimen density for the monotonic and cyclic uniaxial tests is shown in Figure 2-3.

2.5 Results of Experimental Program

2.5.1 Monotonic Uniaxial Tests

The data from the monotonic tests were analyzed to find the relation of the deviatoric stress versus axial strain. The deviatoric stress was calculated as the ratio of the applied load per cross-sectional unit area for the specimen, and the vertical strain was calculated as the ratio of vertical displacement to the original height of the specimen. For these tests, a seating correction was made on the results to account for small non-linear deformation associated with initially loading (i.e., seating) the specimens. Subsequently, data plots were made of the adjusted values of deviatoric stress and vertical strain. Combined plots for EPS 15, EPS 19, EPS 25, EPS 29 and EPS 39 are shown in Figure 2-9, and combined plots of normalized vertical stress against vertical strain are given in Figure 2-10. (The normalized vertical stress values were calculated as the measured deviatoric stress divided by the deviatoric stress measured at 10 percent axial strain.)

The stress levels corresponding to the linear range and the yield point can be determined from these normalized plots. It is clear that the upper bound value of the linear range varies for different densities of EPS with a higher linear range corresponding to higher density of EPS. The nonlinearity of EPS 25 begins at a vertical strain of about 1.5 percent, and the yield point occurs at

a vertical strain value slightly less than 2 percent. These points occur at slightly higher axial strain values for higher densities of EPS (Figure 2-10). (Note that the use of "linear range" does not imply the range elastic behavior. It is likely that small inelastic (i.e., irrecoverable) strain occurs near the upper limit of the linear range.)

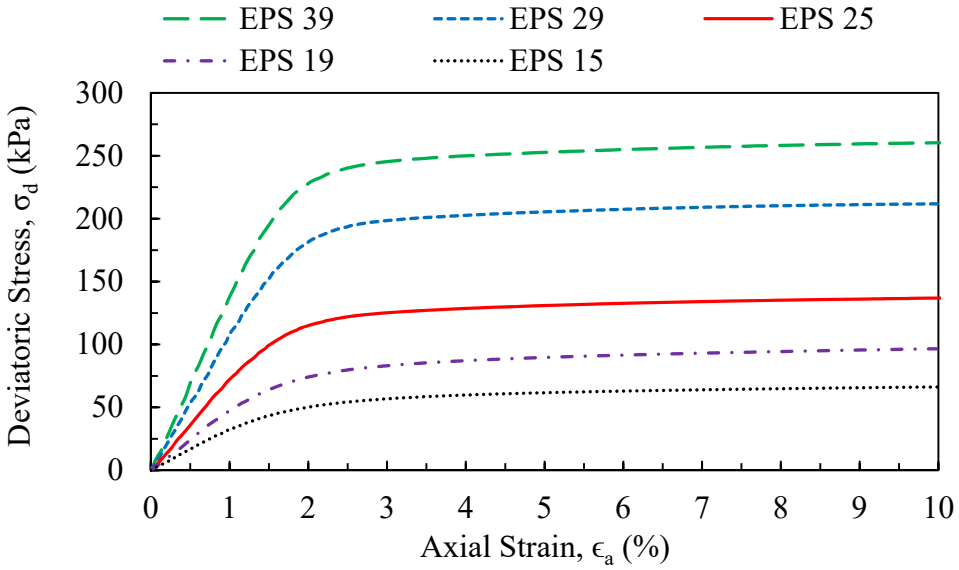

Figure 2-9 Combined plots of deviatoric stress versus axial strain

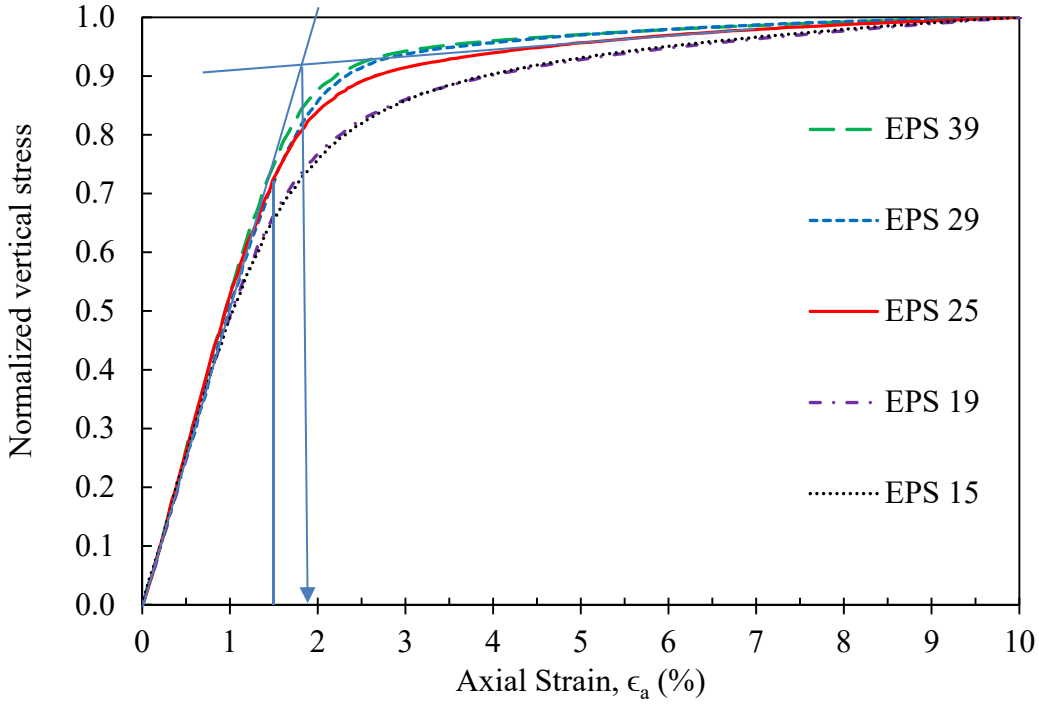

Figure 2-10 Combined plots of normalized vertical stress versus axial strain

The data from the plots of deviatoric stress versus axial strain (Figure 2-9) were also used to determine the axial stresses corresponding to 1, 1.5, 1.75, 2, 5 and 10 percent axial strain, respectively. The Young's modulus (E) is the slope of the elastic portion of the stress-strain curves, which is usually calculated at 1 percent strain (ASTM D6817/D6817M). The moduli for the various densities of EPS was determined from Figure 2-9 and tabulated in Table 2.1 as per ASTM recommendations. To calculate E, this axial stress was divided by the 1 percent axial strain value expressed in decimal fraction (i.e., the measured axial stress at 1 percent strain was divided by 0.01).

A relationship between E and EPS density is shown in Figure 2-11 for the test data obtained from the monotonic tests. The relationship given in Eq. (2.1) is a second order polynomial, which is the same functional relationship used by Horvath (1995).

$$E = 4.8719\rho^2 + 150.69\rho \quad \textbf{(2.1)}$$

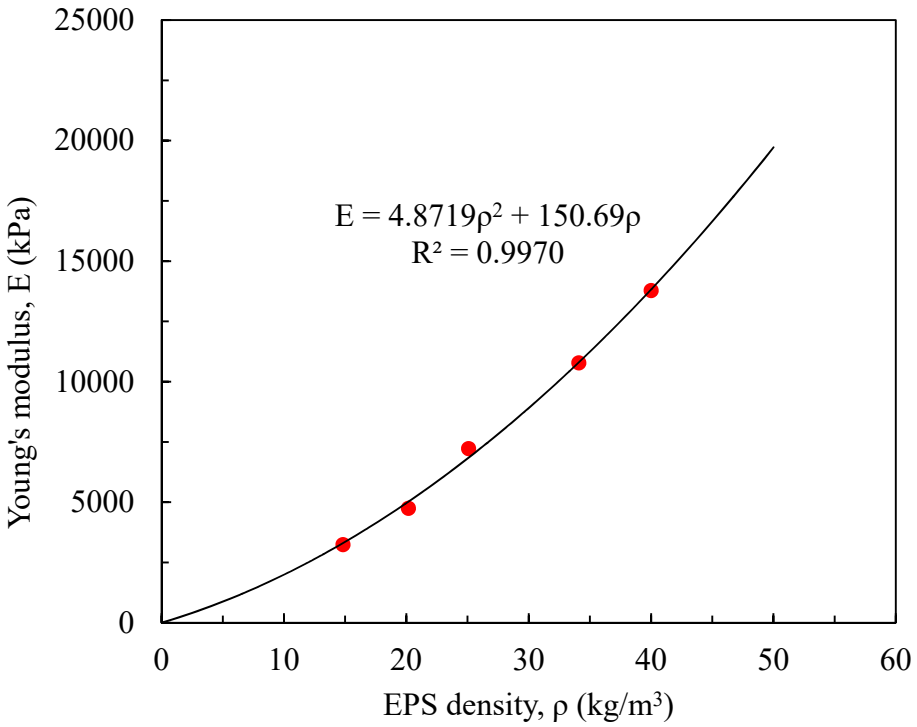

Figure 2-11 Correlation of Young's modulus and EPS density

Table 2.1. Summary of monotonic uniaxial test results

EPS type	Density	Monotonic	Young's modulus	Static deviatoric stress
		Axial strain		
----------	(kg/m^3)	(%)	(kPa)	(kPa)
EPS 15	14.8	1	3242	32
		1.5		43
		1.75		47
		2		50
		5		62
		10		66
EPS 19	20.2	1	4747	47
		1.5		64
		1.75		70
		2		74
		5		90
		10		97
EPS 25	25.1	1	7223	72
		1.5		99
		1.75		109
		2		115
		5		131
		10		137
EPS 29	34.1	1	10778	108
		1.5		152
		1.75		169
		2		182
		5		205
		10		212
EPS 39	40.1	1	13779	138
		1.5		196
		1.75		215
		2		228
		5		253
		10		260

2.5.2 Cyclic Uniaxial Tests

During the consolidation phase of the cyclic tests, measurements of the vertical displacement and elapsed time were collected for each specimen. From this information, the axial strain versus elapsed time was calculated and plotted similar to that shown in Figures 2-4 and 2-5. Subsequently, the rate of pre-cyclic creep strain was determined as a function of elapsed time. This deformation was evaluated in a manner similar to that used for secondary settlement of soils, as described in Holtz et al. (2010). The equation for secondary settlement (S_s) is:

$$S_s = C_{\alpha\epsilon} H_0 log \frac{t}{t_p} \quad \textbf{(2.2)}$$

where: $C_{\alpha\epsilon}$ is the secondary compression strain index, H_0 is the original height of the specimen, t is the design time and t_p is the time required to complete primary consolidation. In these tests, the vertical stress corresponding to a compressive resistance at 1 percent strain was applied for 30 minutes, and the rate of creep strain was measured under this constant load. The creep strain was calculated as the vertical compression occurring after about 1 minute of elapsed time (i.e., once creep was well-established) divided by the original height of the specimen. These data were plotted and the slope of the creep measurements versus log of elapsed time, $C_{\alpha\epsilon}$, was used to estimate the amount of pre-cyclic creep strain for a 50-year service life period for a hypothetical bridge support system using Equation 2.2. The density of EPS, static deviatoric stress at 1 percent strain and the estimated 50-year pre-cyclic creep strain for various specimens are tabulated in Table 2.2.

Following this, the cyclic part of the test was performed on each specimen. These test provided plots of cyclic uniaxial deviatoric stress versus cyclic axial strain. The cyclic uniaxial deviatoric stress was determined from the shear stresses recorded by the GeoComp^{TM} system. It was calculated as two times the shear stress minus the average static deviatoric stress. Subsequently, plots were made of the cyclic uniaxial deviatoric stress and cyclic axial strain. These plots were later used to estimate the potential amount of inelastic, permanent deformation resulting from cycling. An example plot for EPS 25 is shown in Figure 2-12. For this case, the consolidation stress of 72 kPa corresponds to the vertical stress associated with 1.0 percent vertical strain, as obtained from the monotonic test (Table 2.2). The cyclic axial stress of 27 kPa corresponds to an increase in stress, $\Delta\sigma_{dc}$, required to produce an additional 0.5 percent axial strain, as measured in the monotonic test. The cyclic and permanent deformation for 5, 15 and 30 applied cycles is also shown in this figure.

Table 2.2. Summary of pre-cyclic creep tests

EPS type	Density	Monotonic Axial strain	Static deviator stress	Pre-cyclic creep strain in 50 years
	(kg/m^3)	(%)	(kPa)	(%)
EPS 25	25.0	1	72	0.311
	25.4	1	72	0.356
	25.5	1	72	0.351
	24.7	1	72	0.226
	25.6	1	72	0.267
	24.6	1	72	0.372
	24.9	1	72	0.389
	24.5	1	72	0.393
	25.8	1	72	0.250
	26.3	1	72	0.364
	24.5	1	72	0.436
	24.6	1	72	0.267
	24.8	1	72	0.286
EPS 29	33.8	1	108	0.441
	34.0	1	108	0.541
	33.2	1	108	0.352
	34.2	1	108	0.205
EPS 39	40.0	1	138	0.697
	41.1	1	138	0.243
	39.8	1	138	0.391

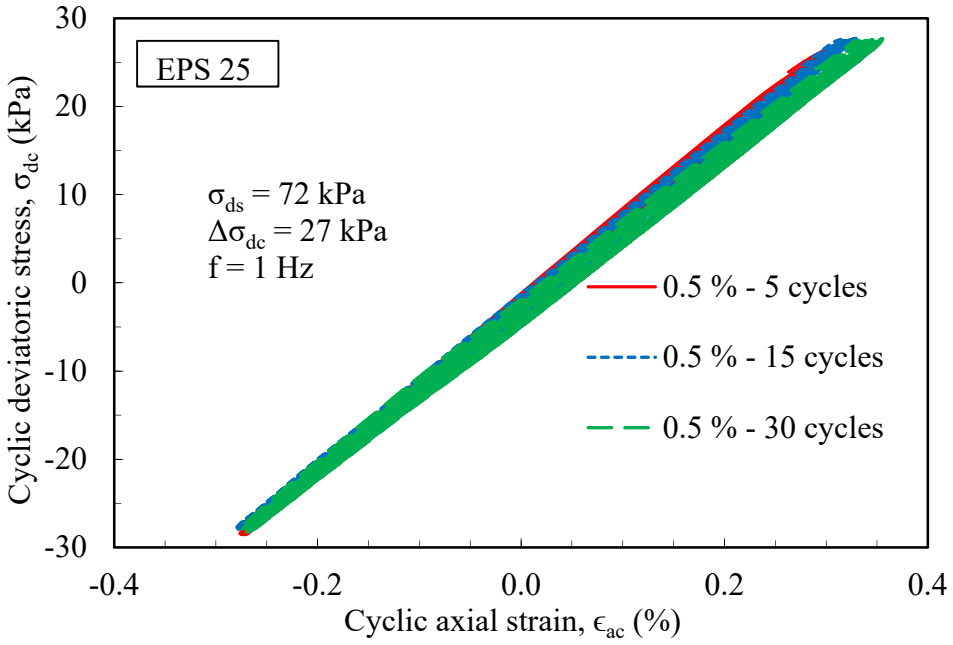

Figure 2-12 Results of cyclic uniaxial test at same level of cyclic deviatoric stresses but at different number of cycles (5, 15 and 30 number of cycles) on EPS 25

Figure 2-13 shows the results for cyclic uniaxial tests performed on EPS 25 with three different levels of cyclic deviatoric stress and 5 applied cycles. Figure 2-14 shows the results of the same deviatoric stress but with a differing number of applied cycles (5, 15 and 30 cycles). Figures 2-15 shows the results of cyclic uniaxial tests for three different levels of cyclic deviatoric stresses (27, 35 and 43 kPa) at 15 cycles. Figure 2-16 shows the results for cyclic tests performed at the same cyclic deviatoric stress of 43 kPa for three different number of cycles on EPS 25. The values of 27, 35 and 43 kPa shown in these plots are the $\Delta\sigma_{dc}$ values corresponding to the change in axial stress required to produce an additional 0.5, 0.75 and 1.0 percent axial strain in the monotonic specimens beyond the 1 percent stress level of 72 kPa.

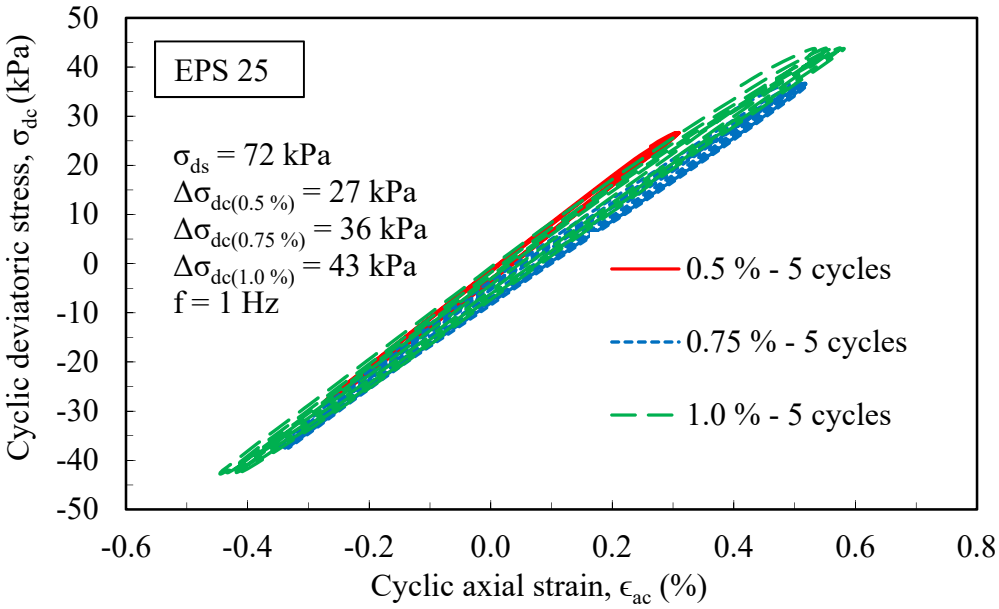

Figure 2-13 Results of cyclic uniaxial tests on three samples at three different cyclic deviatoric stresses with same number of cycles on EPS 25

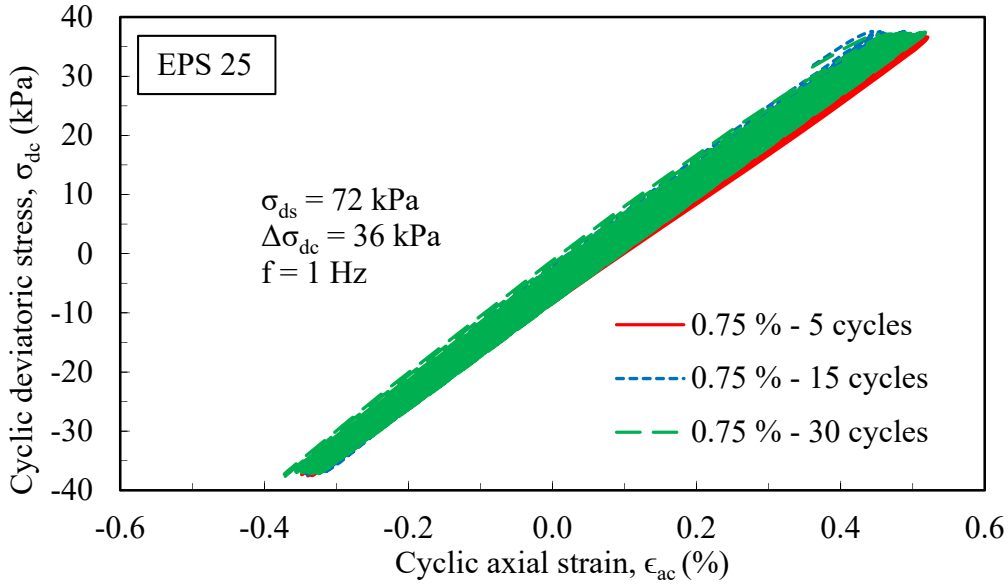

Figure 2-14 Results of cyclic uniaxial tests on three samples at same cyclic deviatoric stresses with three different number of cycles on EPS 25

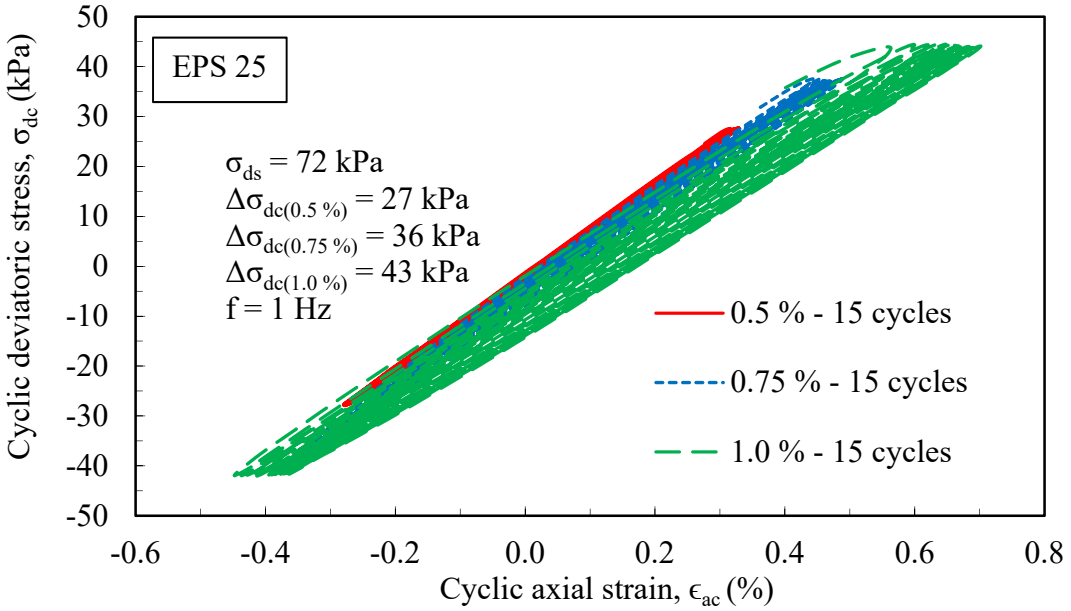

Figure 2-15 Results of cyclic uniaxial tests on four samples at 15 number of cycles with three different cyclic deviatoric stresses on EPS 25

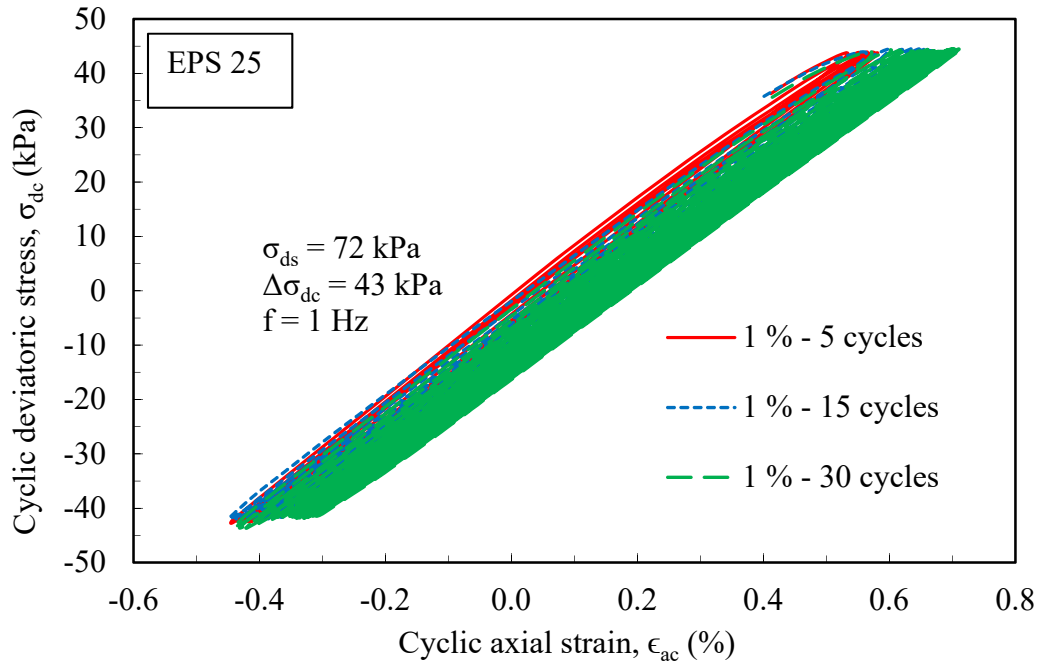

Figure 2-16 Results of cyclic uniaxial tests on three samples at same level of cyclic deviatoric stresses with three different number of cycles on EPS 25

Figure 2-17 shows the test results of cyclic uniaxial tests for EPS25 performed at three different levels of cyclic deviatoric stress and for 30 cycles. Figure 2-18 shows the test results for three different levels of cyclic deviatoric stresses at 15 cycles for EPS 25. In the series of tests shown in Figure 2-18, the post-cyclic deviatoric stress was set equal to the cyclic + consolidation deviatoric stresses which produced a post cyclic loading equal to the peak loading obtained during cycling. Figure 2-19 shows the cyclic uniaxial test results for two different levels of cyclic deviatoric stresses (74 and 98 kPa) for three differing number of cycles (5, 15, 30) performed on EPS 29. Figure 2-20 shows the results for the same level of cyclic deviatoric stress (90 kPa) performed at three differing number of cycles (5, 15, 30) performed EPS 39, respectively.

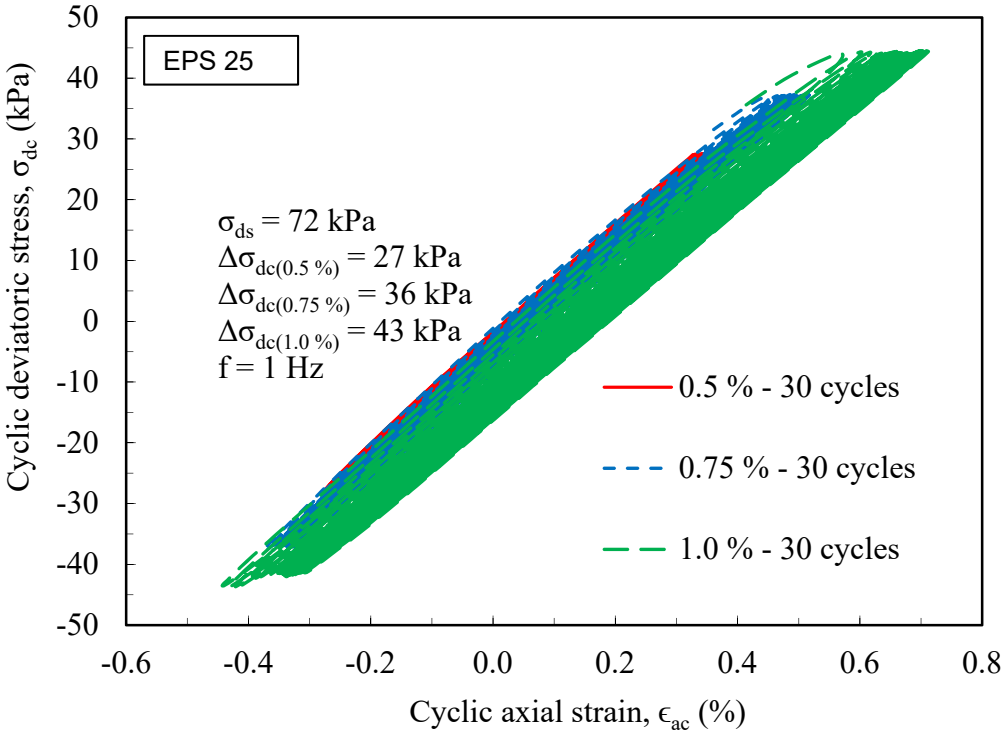

Figure 2-17 Results of cyclic uniaxial tests on three samples at three different level of cyclic deviatoric stresses with 30 number of cycles on EPS 25

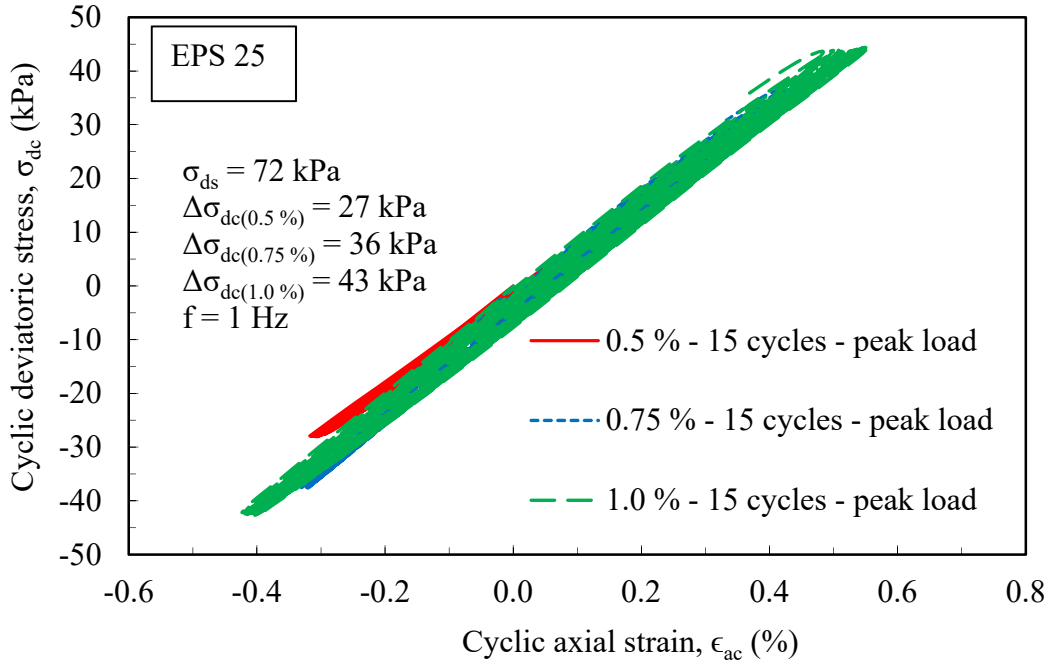

Figure 2-18 Results of cyclic uniaxial tests on three samples at three different level of cyclic deviatoric stresses under peak load with 15 number of cycles on EPS 25

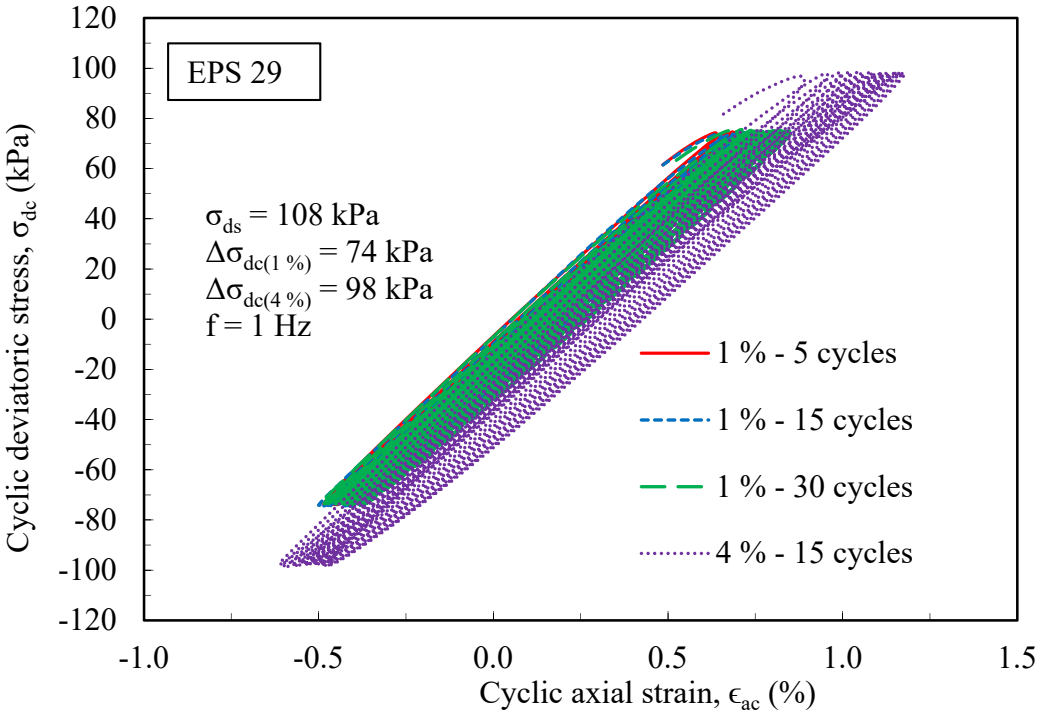

Figure 2-19 Results of cyclic uniaxial tests on four samples at two different level of cyclic deviatoric stresses with three different number of cycles on EPS 29

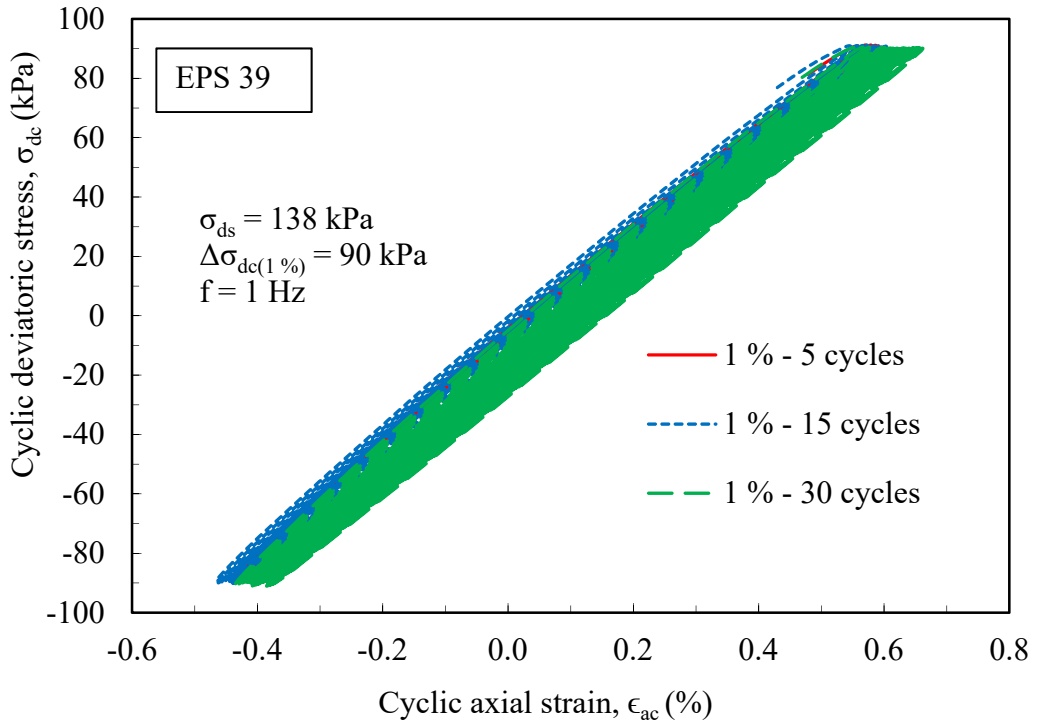

Figure 2-20 Results of cyclic uniaxial tests on three samples at same level of cyclic deviatoric stresses with three different number of cycles on EPS 39

Based on the results of the cyclic uniaxial tests, it is clear and obvious that EPS specimens showed a larger amount of permanent plastic strain at higher levels of applied cyclic deviatoric stress. This was also true for the tests where the deviatoric stress was kept constant, but the number of cycles increased, as would be expected. Therefore, the amount of permanent cyclic strain increased with increased applied cyclic deviatoric stress and with increased number of applied stress cycles. These results are expected and consistent with the known cyclic behavior of EPS undergoing cyclic permanent deformation.

The degraded Young's modulus (E_c) for the cyclic testing was calculated as the secant modulus that represents the slope of the line drawn through the middle of the hysteresis loop (Figure 2-21). The load reversal point is the highest point of stress-strain loop and the origin is the center of hysteresis loop. The mean value of the modulus was calculated by taking the average value of E_c using the average of E for the first and last cycles of test (Table 2.3).

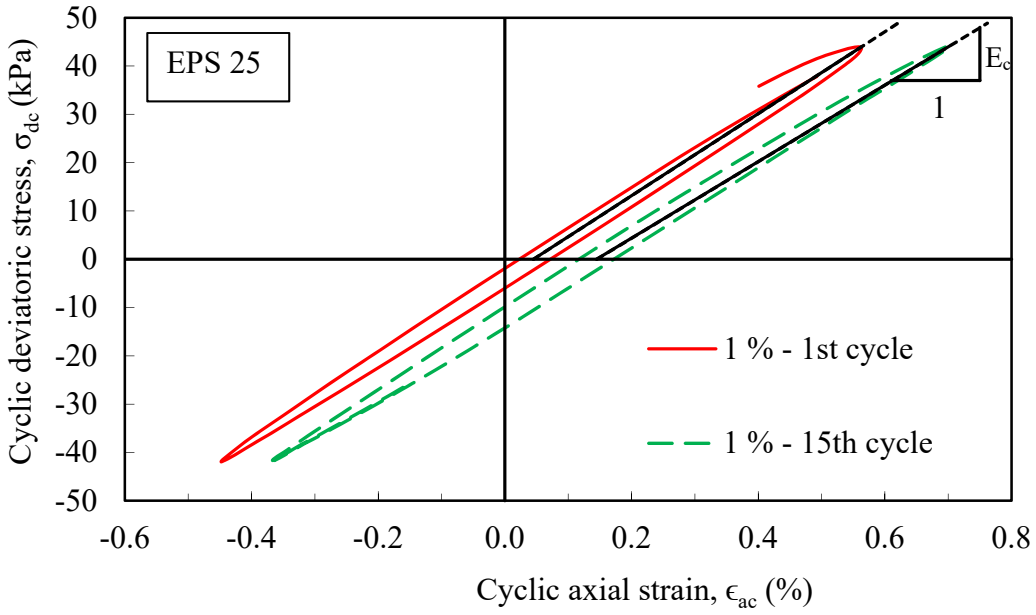

(a)

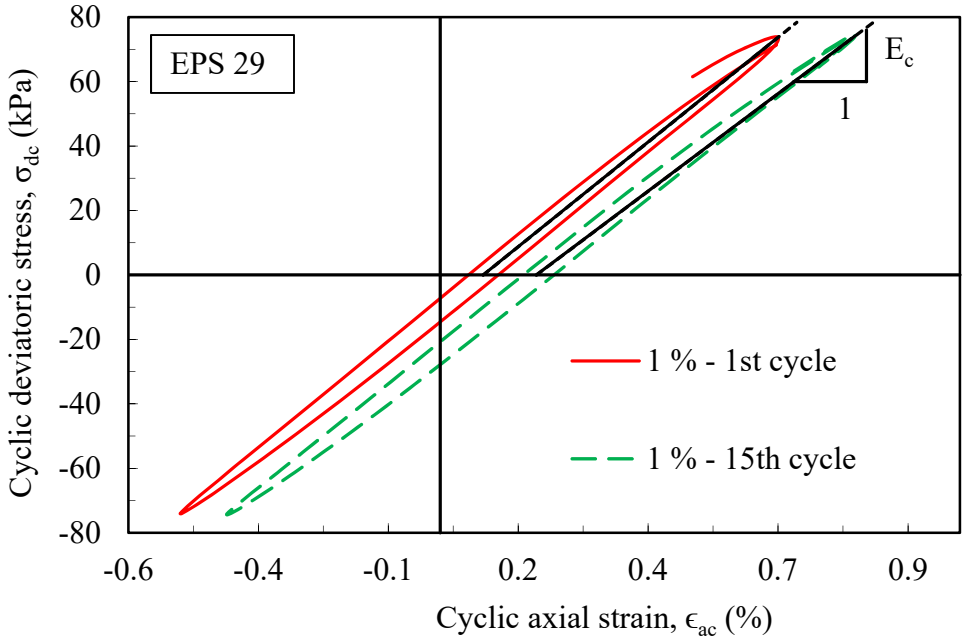

(b)

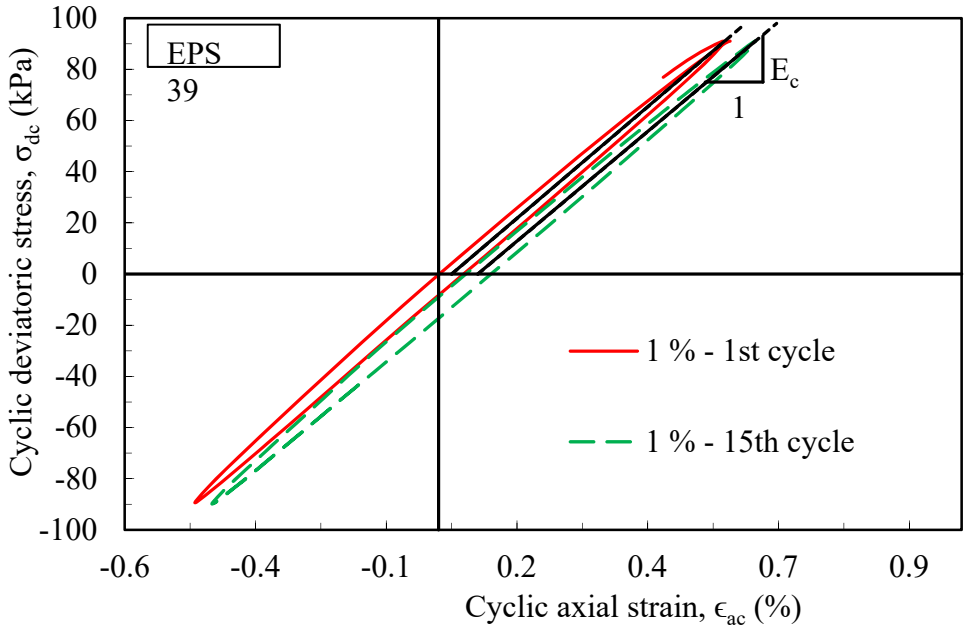

(c)

Figure 2-21 Cyclic stress-strain hysteresis loop and corresponding Young's modulus (E_c) (a) EPS 25 (b) EPS 29 and (c) EPS 39

The plots of cyclic deviatoric stress versus cyclic axial strain to determine E_c for EPS 25, EPS 29 and EPS 39 at stress levels corresponding to 2 percent at 15 cycles are shown in Figure 2-21.

Because the specimens were below the yield point in a quasi linear range, the mean shear modulus (G) was approximated from elastic theory using Eq. (2.2).

$$G = \frac{E}{2(1+\nu)} \quad \textbf{(2.3)}$$

In Eq. (2.3), ν is the Poisson's ratio. The relation of ν as a function of EPS density was given in Horvath (1995) is presented in Eq.(2.4).

$$\nu = 0.0056\rho + 0.0024 \quad \textbf{(2.4)}$$

The calculated values of ν and mean G_c are given in Table 2.3. The plots of mean G_c and ρ are also shown in Figure 2-22, which provides the relationship of mean G_c and ρ. The shear modulus versus ρ relation was fitted with a second order polynomial equation, Eq. (2.5).

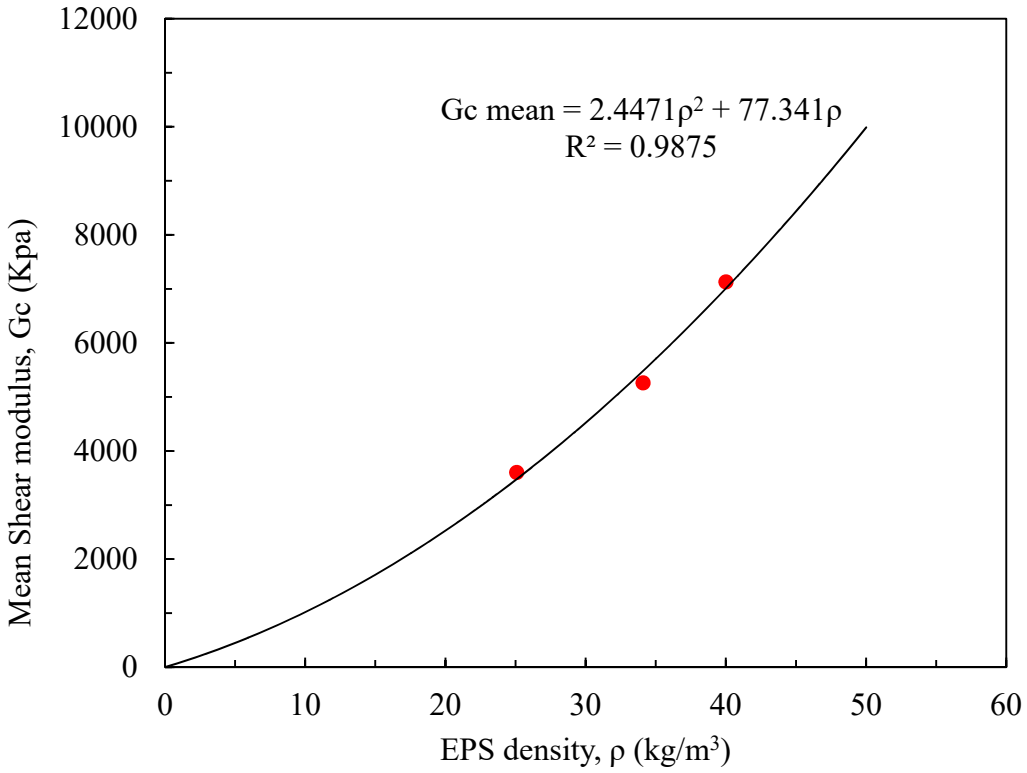

Figure 2-22 Correlation of mean degraded shear modulus and nominal EPS density

Table 2.3. Summary of cyclic uniaxial test results

EPS type	ρ	$\epsilon_{a\ monotonic}$	N	σ_{ds}	$\Delta\sigma_{dc}$	σ_t	$E_{c\ (mean)}$	ν	$G_{c\ (mean)}$	ϵ_{ap}
----------	(kg/m^3)	(%)	----------	(kPa)	(kPa)	(kPa)	(kPa)	----------	(kPa)	(%)
EPS 25	25.0	1.5	5	72	27	99	9796	0.142	4288	0.008
	25.4	1.5	15	72	27	99	9544	0.145	4168	0.014
	25.5	1.5	30	72	27	99	9234	0.145	4033	0.028
	24.7	1.75	5	72	36	109	8499	0.141	3725	0.030
	25.6	1.75	15	72	36	109	9284	0.146	4051	0.045
	24.6	1.75	30	72	36	109	8739	0.140	3833	0.065
	24.9	2	5	72	43	115	8678	0.142	3800	0.048
	24.5	2	15	72	43	115	8209	0.140	3602	0.139
	25.8	2	30	72	43	115	8548	0.147	3727	0.140
	26.3	5	15	72	59	131	8455	0.150	3677	0.239
	24.5	1.5	5	72	27	99	8823	0.139	3872	0.029
	24.6	1.75	15	72	36	109	9428	0.140	4134	0.036
	24.8	2	30	72	43	115	9466	0.141	4148	0.067
EPS 29	33.8	2	5	108	74	182	13457	0.192	5646	0.070
	34.0	2	15	108	74	182	12547	0.193	5259	0.147
	33.2	2	30	108	74	182	12409	0.188	5222	0.179
	34.2	5	15	108	98	205	12606	0.194	5278	0.288
EPS 39	40.0	2	5	138	90	228	17482	0.226	7127	0.032
	41.1	2	15	138	90	228	17298	0.232	7018	0.060
	39.8	2	30	138	90	228	17548	0.225	7161	0.110

$$Gc\ mean = 1.1126\rho^2 + 127.31\rho \quad \textbf{(2.5)}$$

The axial strain under cyclic loading was calculated for all densities and is depicted in Table 2.3. Figure 2-23 shows the repeated cyclic tests at which a cyclic deviatoric stress corresponding to 2 percent strain was applied in the first phase and a cyclic deviatoric stress corresponding to 1.5 percent strain was applied in the second phase. Similarly, Figure 2-24 reveals the repeated cyclic tests in which cyclic deviatoric stresses corresponded to 5 percent and 1.5 percent were applied in the first and second phases, respectively. In the repeated cyclic tests, the change in Young's modulus between the two cyclic loads were measured. The values of E_c were determined from Figures 2-23 and 2-24 are shown in Table 2.4.

From these data, it is apparent that low applied cyclic stress levels (e.g., Figure 2-23b), the E_c and E are relatively similar. However, at higher applied cyclic stress levels, the value of E_c decreases as a result of cycling (Figure 2-23a). The decrease in E_c becomes larger notable when the applied cyclic stress level is increased significantly (Figure 2-24). This means that EPS may become slightly to somewhat softened in terms of modulus after the seismic excitation depending on the magnitude of the applied stress and the number of significant earthquake stress cycles.

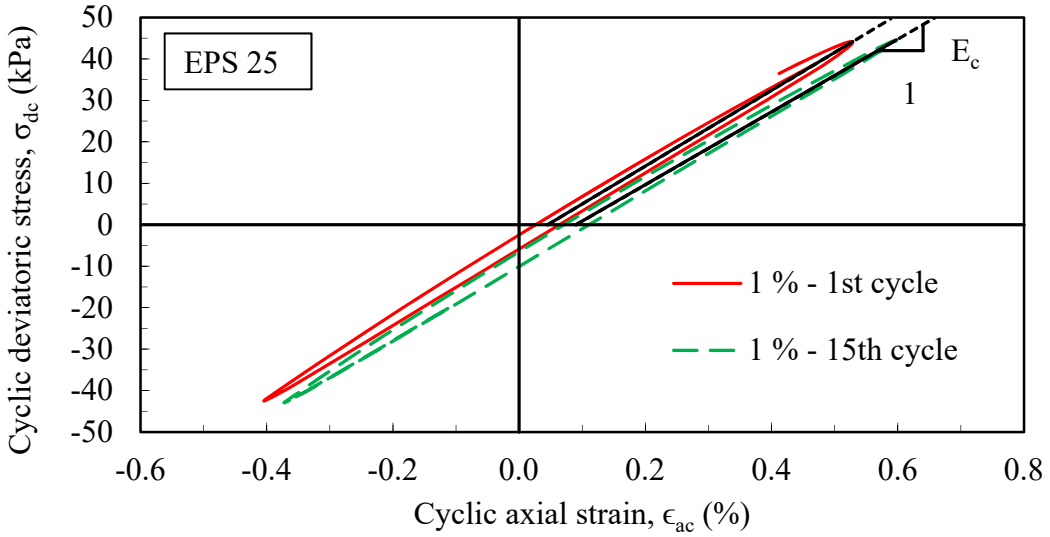

(a)

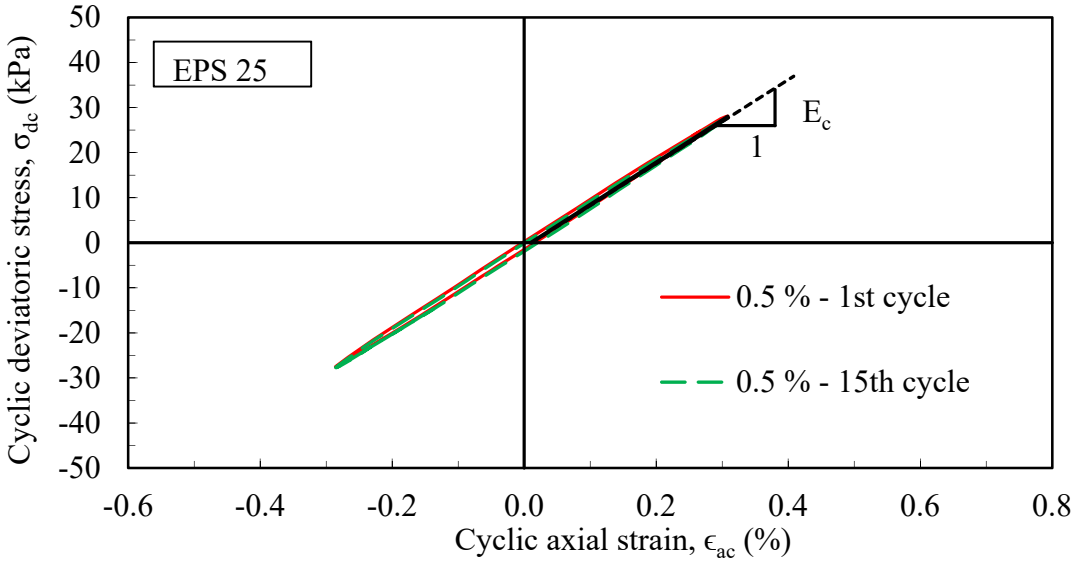

(b)

Figure 2-23 Repeated cyclic uniaxial tests at two differing cyclic deviatoric stresses (a) Stress corresponds to 1 % strain, (b) Stress corresponds to 0.5 % strain, as measured from monotonic tests.

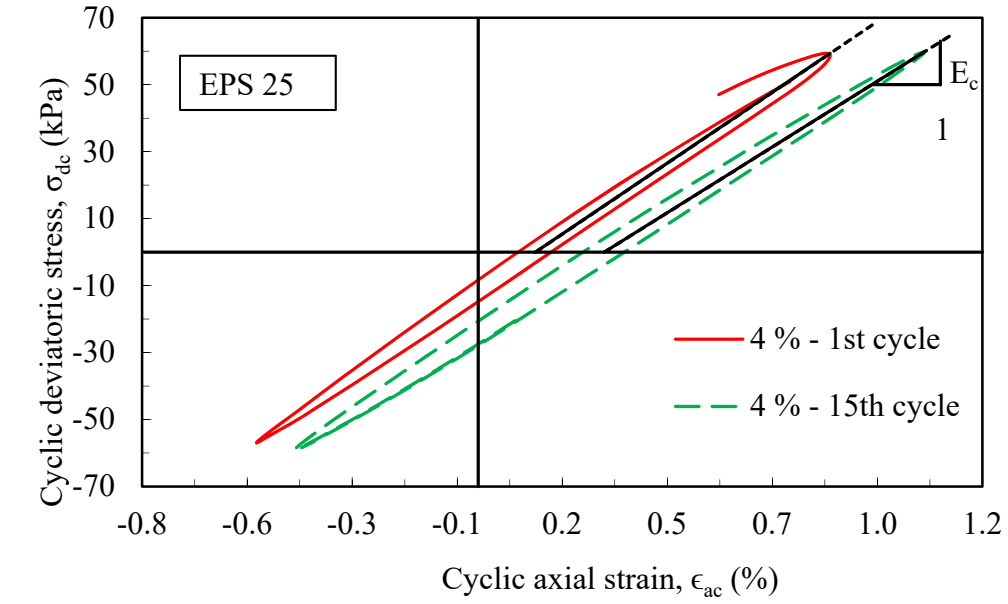

(a)

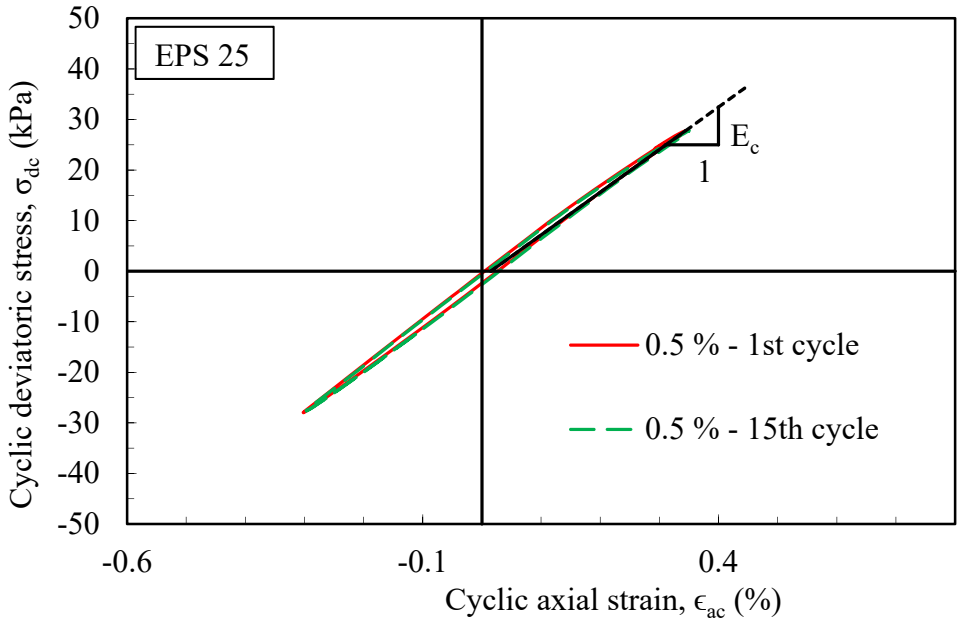

(b)

Figure 2-24 Repeated cyclic uniaxial tests at two different cyclic deviatoric stresses (a) Stress corresponds to 4 % strain (b) Stress corresponds to 0.5 % strain, as measured in the monotonic tests.

Table 2.4. Young's modulus for repeated cyclic loads

EPS type	ρ	N	ϵ_a	$E_{c\ (mean)}$
----------	(kg/m^3)	----------	(%)	(kPa)
EPS 25	25.8	15	2	8959
			1.5	9350
	25.8		5	8159
			1.5	8419

The amount of permanent axial strain due to cycling, ϵ_{ap}, was also calculated for the cyclic tests and is reported in Table 2.3. This type of strain is a non-recoverable plastic strain, which was calculated by subtracting the peak cyclic strain from the last cycle with that obtained from obtained from the first cycle. Plots of cyclic plastic axial strain versus number of cycles for various cyclic deviatoric stresses are shown in Figure 2-25 for EPS 25. The plastic axial strain increased with increasing cyclic deviatoric stresses, as expected. The total permanent strain for 30 cycles was about 0.14 percent.

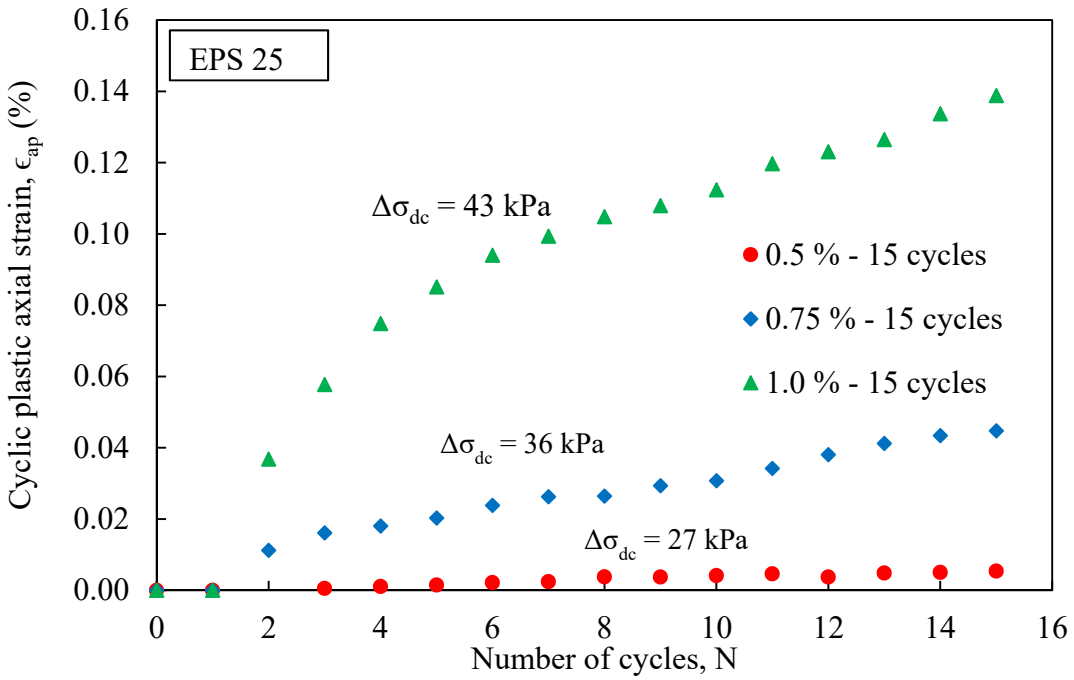

(a)

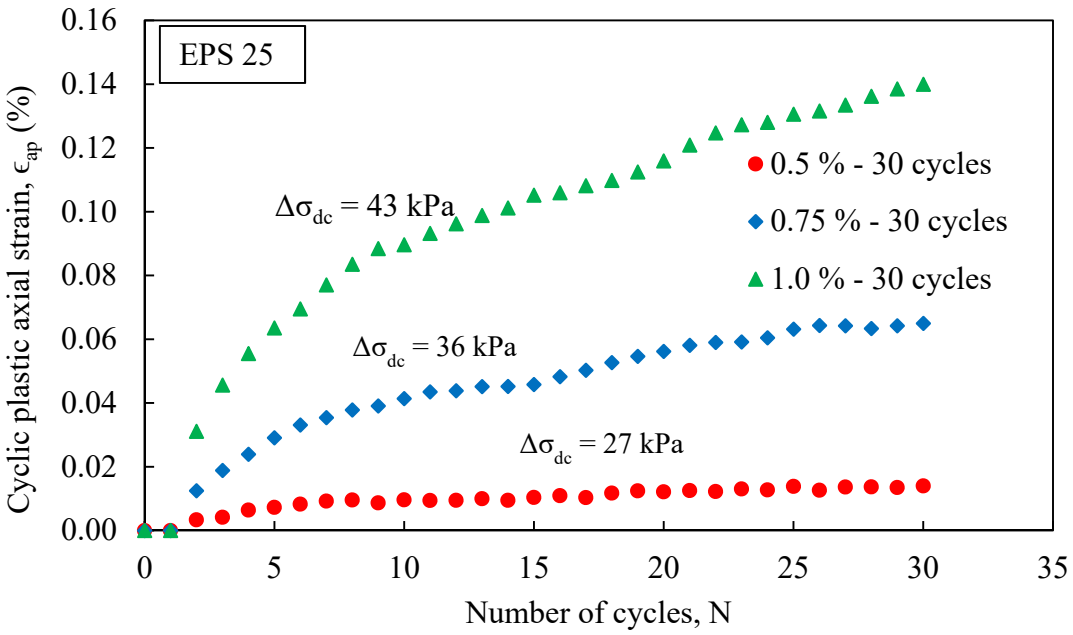

(b)

Figure 2-25 Cyclic plastic axial strain with number of cycles at different cyclic deviatoric stresses (a) 15 number of cycles (b) 30 number of cycles

2.5.3 Post-cyclic Creep Tests

The post-cyclic creep tests provided information related to rate of creep displacement for specimens subjected to cyclic loading. This is useful in estimating the potential rate of post-earthquake creep in an EPS embankment. The post-cyclic creep strain for a 50 year design period was calculated in similar manner to the pre-cyclic creep strain using the results of the post-cyclic creep tests. The results given in Table 2.5 depict the amount of post-cyclic creep strain obtained after a constant dead load (i.e., stress corresponding to 1 per cent strain from the monotonic tests) was applied for 20 hours to the specimens which had been subjected to differing number of cycles at different levels of cyclic stress. The post-cyclic creep strain for a 50-year post-construction period was then estimated using a linear extrapolation of the rate of creep strain obtained from the 20-hour post-cyclic creep strain tests.

Figures 2-26 through 2-33 show the results for post-cyclic uniaxial creep tests conducted for various levels of cyclic deviatoric stress and number of applied stress cycles. From the results tabulated in Table 2.5, it can be concluded that when subjected to the same level of cyclic deviatoric stress, the post-cyclic creep strain increases as more stress cycles are applied. The post-cyclic creep strain also increases with the magnitude of the cyclic deviatoric stress when subjected to an equal number of stress cycles. The former is due to the progressive softening of EPS geofoam as its exposure to cycling increases. The latter is also a softening phenomenon resulting from inelastic behavior of the EPS at higher levels of strain.

Most importantly, Table 2.5 shows that the amount of post-cyclic creep strain is generally acceptable (0.43 percent, or less), for cases where the post-cyclic stress level was returned to the stress associated with 1 percent axial strain, as measured from the monotonic tests. This implies

that the post-earthquake creep strain will generally be acceptable for cases where the combination of dead and live loads does not exceed the stress associated with 2 percent axial strain, as measured from the monotonic test results; and the post-earthquake dead load returns to a state of stress associated with 1 percent axial strain, as measured from the monotonic tests.

However for one experimental test case, where the post-cyclic stress was returned to the value associated with 1.5 percent axial strain (i.e., “peak load” case), unacceptable post-cyclic creep deformation was realized (Figure 2-34). However, from a field application standpoint, this case represents an unrealistic situation because the post-earthquake vertical stress should be expected to return to its pre-earthquake value, which from a design standpoint, should not be greater than the stress associated with 1 percent axial strain.

Table 2.5. Summary of pre and post-cyclic creep and estimated total strain permanent strain for 50-year design period

EPS nominal type	Density	Pre-cyclic Static deviatoric stress	Cyclic deviatoric stress	Total deviatoric stress	Axial strain from monotonic test	Number of cycles	Cyclic plastic axial strain	Estimated pre-cyclic creep strain in 50 years	Estimated post-cyclic creep strain in 50 years	Estimated permanent strain in 50 years
---------	(kg/m3)	(kPa)	(kPa)	(kPa)	(%)	(N)	(%)	(%)	(%)	(%)
EPS 25	25.0	72	27	99	1.5	5	0.008	0.311	0.298	0.319
	25.4	72	27	99	1.5	15	0.014	0.356	0.252	0.370
	25.5	72	27	99	1.5	30	0.028	0.351	0.283	0.379
	24.7	72	36	108	1.75	5	0.03	0.226	0.207	0.256
	25.6	72	36	108	1.75	15	0.045	0.267	0.262	0.312
	24.6	72	36	108	1.75	30	0.065	0.372	0.33	0.437
	24.9	72	43	115	2	5	0.048	0.389	0.286	0.437
	24.5	72	43	115	2	15	0.139	0.393	0.333	0.532
	25.8	72	43	115	2	30	0.14	0.25	0.351	0.491
	26.3	72	59	131	5	15	0.239	0.364	0.368	0.607
	24.5	72	27	99	1.5	5	0.029	0.436	14.834	14.863
	24.6	72	36	108	1.75	15	0.036	0.267	25.67	25.706
	24.8	72	43	115	2	30	0.067	0.286	41.26	41.327
EPS 29	33.8	108	74	182	2	5	0.07	0.411	0.353	0.481
	34.0	108	74	182	2	15	0.147	0.541	0.381	0.688
	33.2	108	74	182	2	30	0.179	0.352	0.43	0.609
	34.2	108	98	206	5	15	0.288	0.205	0.419	0.707
EPS 39	40.0	138	90	228	2	5	0.032	0.697	0.393	0.729
	41.1	138	90	228	2	15	0.06	0.243	0.425	0.485
	39.8	138	90	228	2	30	0.11	0.391	0.397	0.507

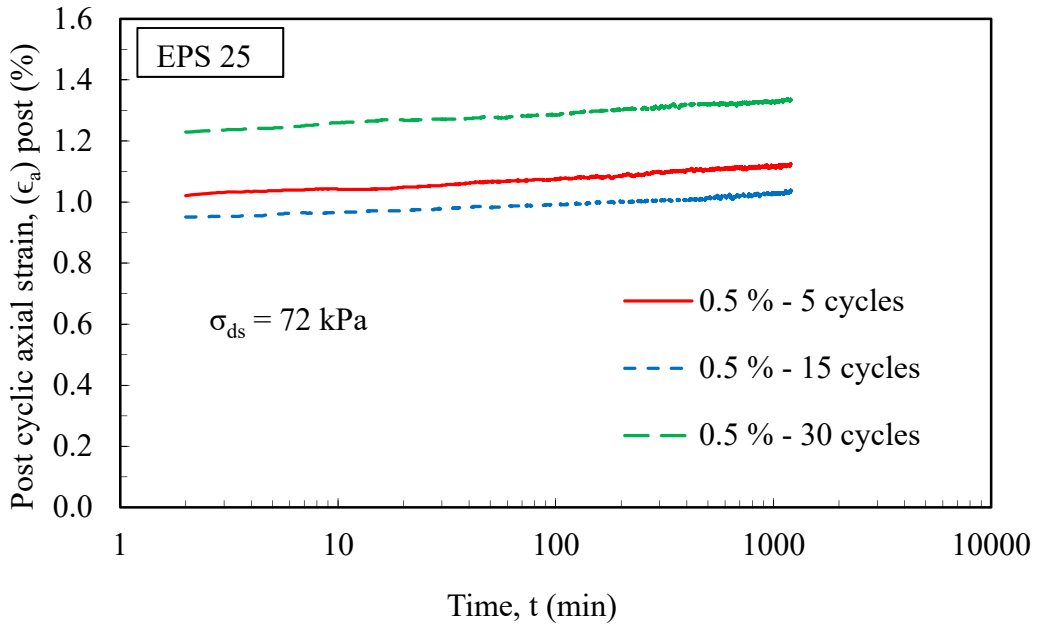

Figure 2-26 Results of post-cyclic uniaxial test at same level of cyclic deviatoric stresses and at different number of cycles on EPS 25

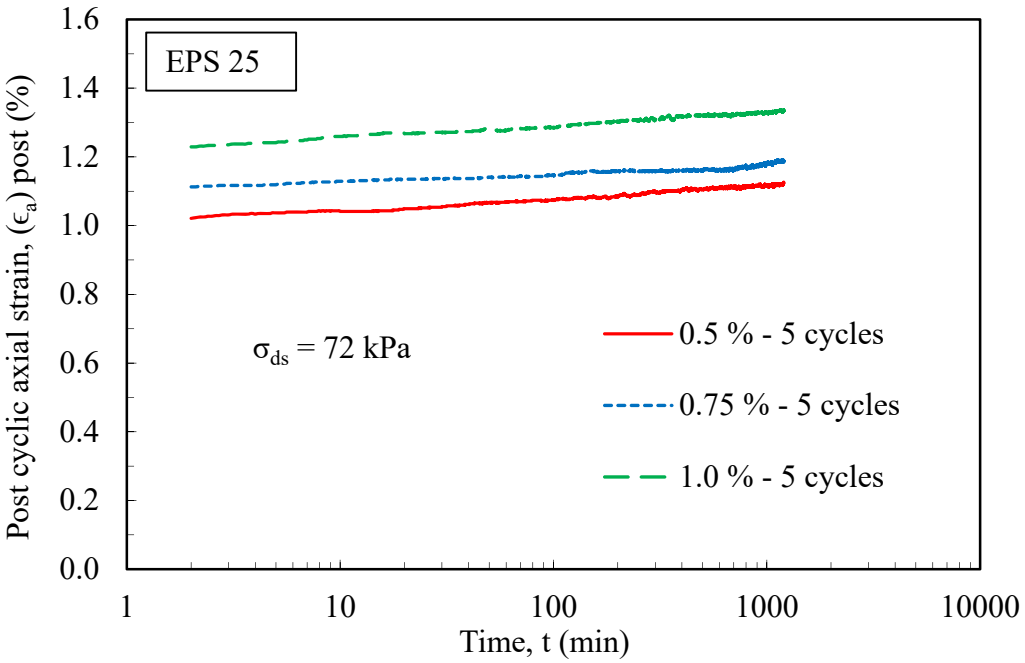

Figure 2-27 Results of post-cyclic uniaxial tests on three samples at three different cyclic deviatoric stresses with same number of cycles on EPS 25

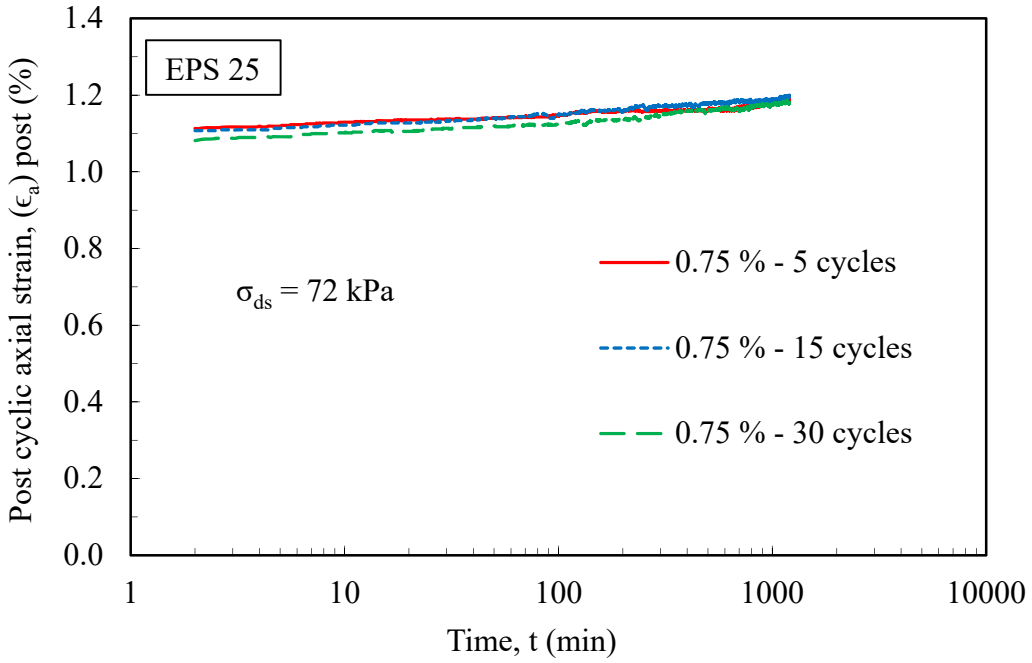

Figure 2-28 Results of post-cyclic uniaxial tests on three samples at same cyclic deviatoric stresses with three different number of cycles on EPS 25

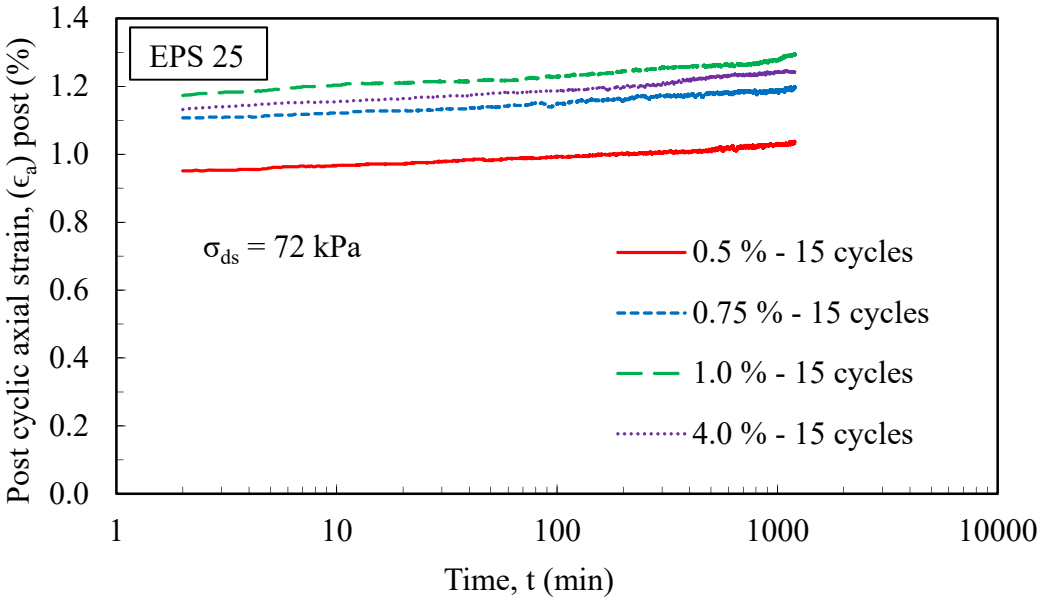

Figure 2-29 Results of post-cyclic uniaxial tests on four samples at 15 number of cycles with four different cyclic deviatoric stresses on EPS 25

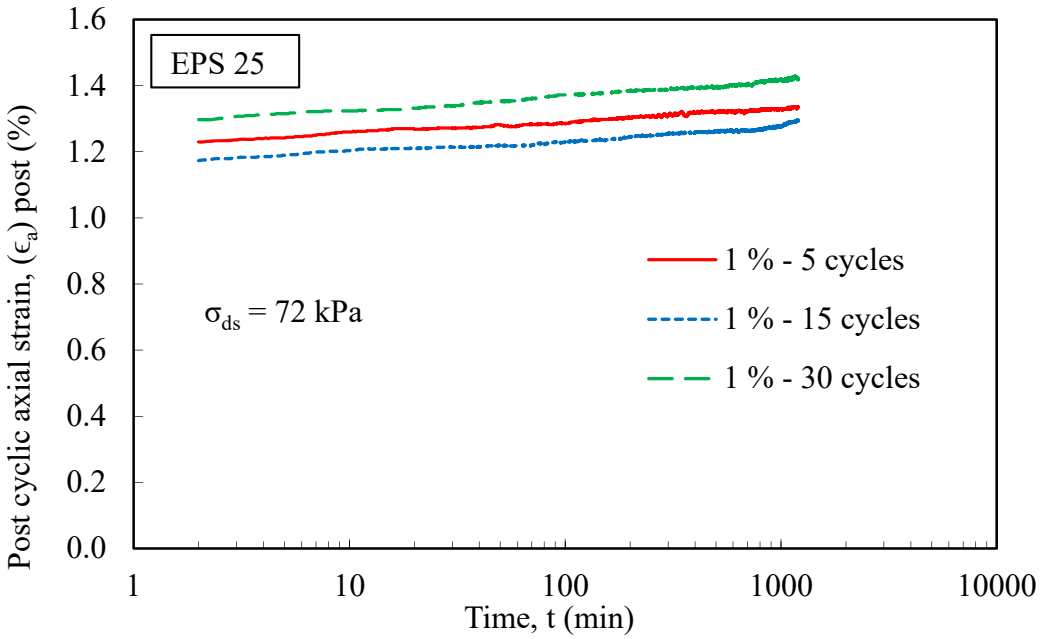

Figure 2-30 Results of post-cyclic uniaxial tests on three samples at same cyclic deviatoric stresses (corresponds to 1% strain) with three different number of cycles on EPS 25

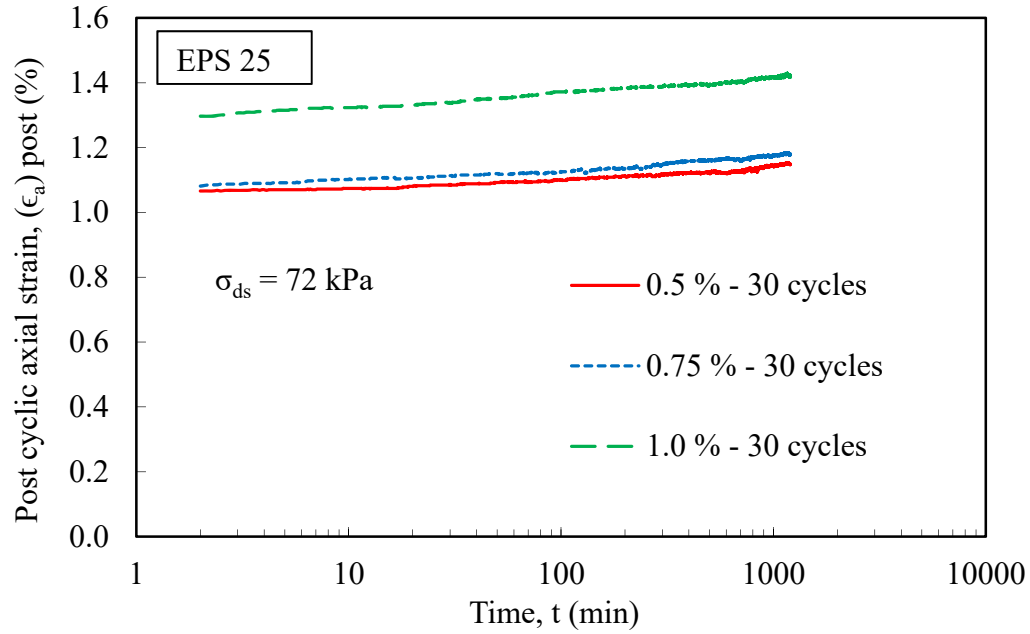

Figure 2-31 Results of post-cyclic uniaxial tests on three samples at 30 number of cycles with three different cyclic deviatoric stresses on EPS 25

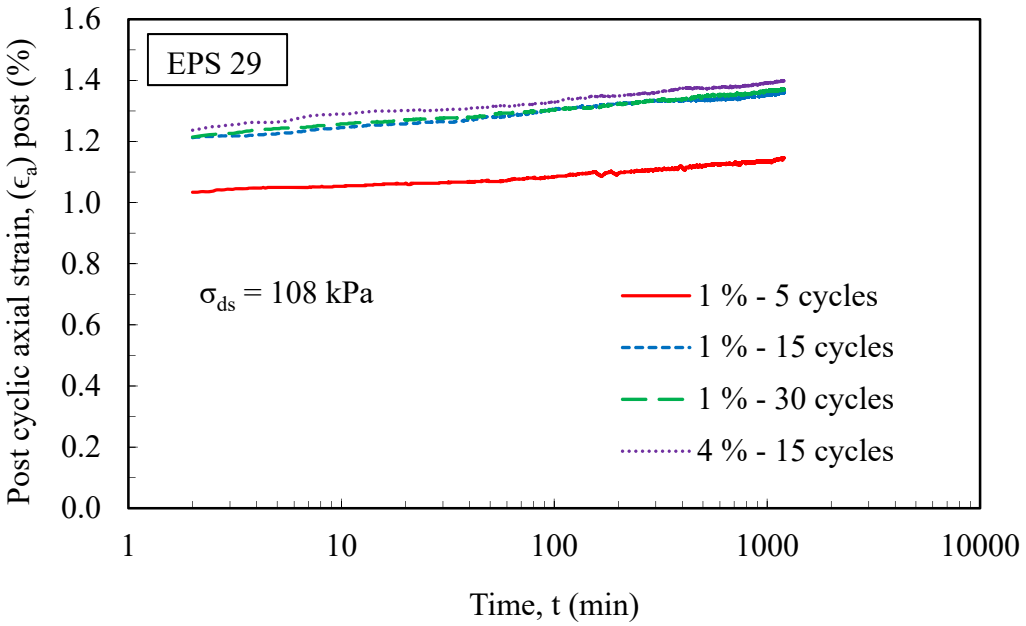

Figure 2-32 Results of post-cyclic uniaxial tests on four samples at two different level of cyclic deviatoric stresses with three different number of cycles on EPS 29

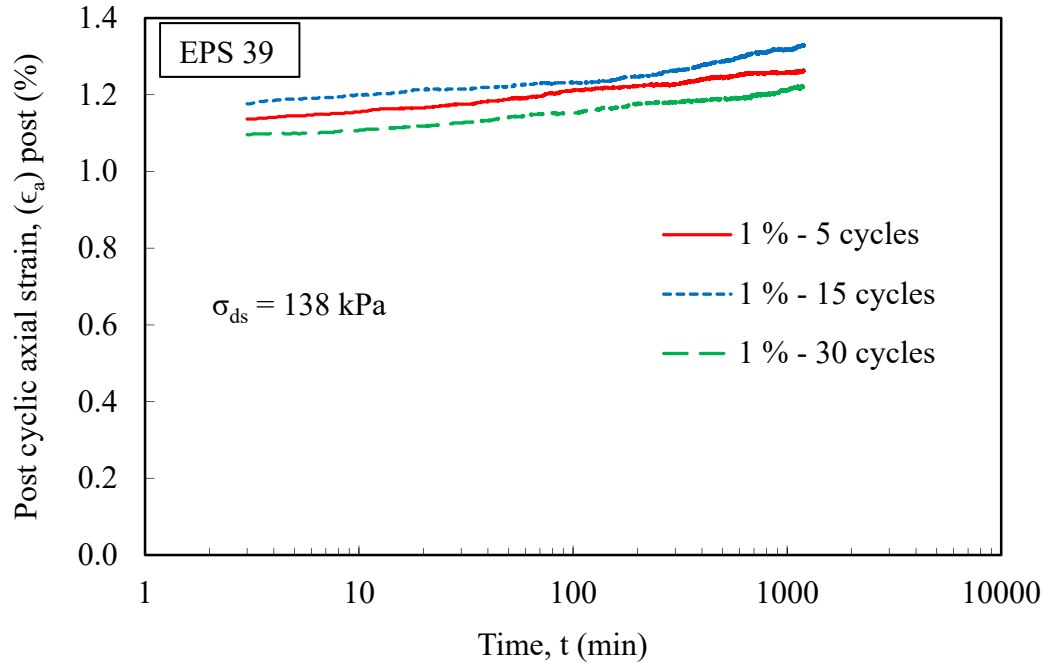

Figure 2-33 Results of post-cyclic uniaxial tests on three samples at same level of cyclic deviatoric stresses with three different number of cycles on EPS 39

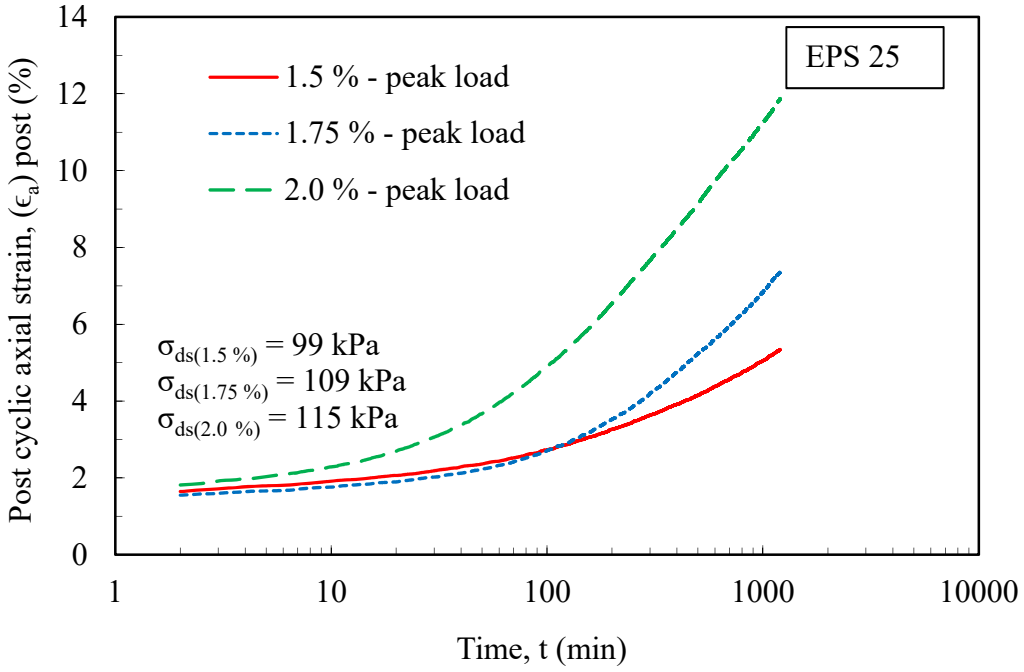

Figure 2-34 Post cyclic axial strain with time for EPS 25 under the peak load (stress same as the total stress during cyclic phase)

2.6 Estimation of Total Permeant Strain

The total permanent axial strain resulting from cyclic plastic deformation and post-cyclic creep deformation was calculated for a 50-year post construction period (Table 2.5). From these results, the highest estimated total permanent strain is 0.7 percent, or less, for a 50-year post-construction period for cases where the post cyclic axial stress was returned to the stress level of 1 percent, as measured from the monotonic test results. From these series of cyclic tests performed, it is clear that applying a monotonic loading corresponding to 1 percent axial strain followed by cycling the EPS to a peak cyclic deviatoric stress levels corresponding to 2 percent total axial strain (i.e., an additional 1 percent cyclic strain beyond the initial monotonic loading), did not significantly increase the post-cyclic creep behavior when compared with uncycled specimens. In fact, the cycling and its associated axial strain appears to have slightly conditioned (i.e., stiffened) the EPS, so that the rate of post-cyclic creep strain was somewhat diminished when compared with the pre-cyclic creep rate for uncycled EPS (Table 2.5).

2.7 Recommendations for Allowable Stress in EPS for Seismic Loadings

Based on the results of the monotonic, cyclic and pre and post-cyclic creep test results, it is recommended that the stress level associated with the applied gravitational dead load in the EPS blocks be limited to the stress level corresponding to 1 percent axial strain as measured from a monotonic uniaxial load test (Figure 2-35). This recommendation is similar to that of Srirajan et al. (2001) (Figure 1-3), but is different from that of NCHRP 529 in that the live loads are not considered in this recommended loading combination.

Based on the cyclic loading and post-cyclic loading creep tests, it is also recommended that the applied dead, live and earthquake loads in the EPS block be limited to a combined stress level that does not exceed the compressive resistance associated with 2 percent axial strain, as measured in a monotonic uniaxial lad test for the selected density of EPS (Figure 2-35). This recommendation is similar to that of the EPS White Book (2011) for the factored allowable stress for short term loading conditions which is taken to be 80 percent of the compressive resistance at 10 percent axial strain. This document recommends the use of the compressive resistance measured at 2 percent axial strain, which is approximately equivalent to 85 percent of the compressive resistance at 10 percent strain (Figure 2-35)

The above recommendations are made assuming the EPS blocks used for bridge support systems will have moduli and stress-strain behavior similar to or higher than that of EPS 25 (Figure 2-35). If designed and constructed in manner recommended above, the results of the laboratory testing suggest the permanent cyclic and creep strain is expected to be less than 1 percent vertical strain in 50 years. In addition, the combined strain originating from all sources: elastic + creep + cyclic is expected to be less than 2 percent in 50 years, which is deemed an acceptable value from a performance standpoint. These above recommendations provide the recommended basis of design for evaluations of an EPS bridge system support system undergoing seismic loadings. The additional evaluations required to assess internal and external seismic stability of the bridge support system are further discussed in the subsequent chapters.

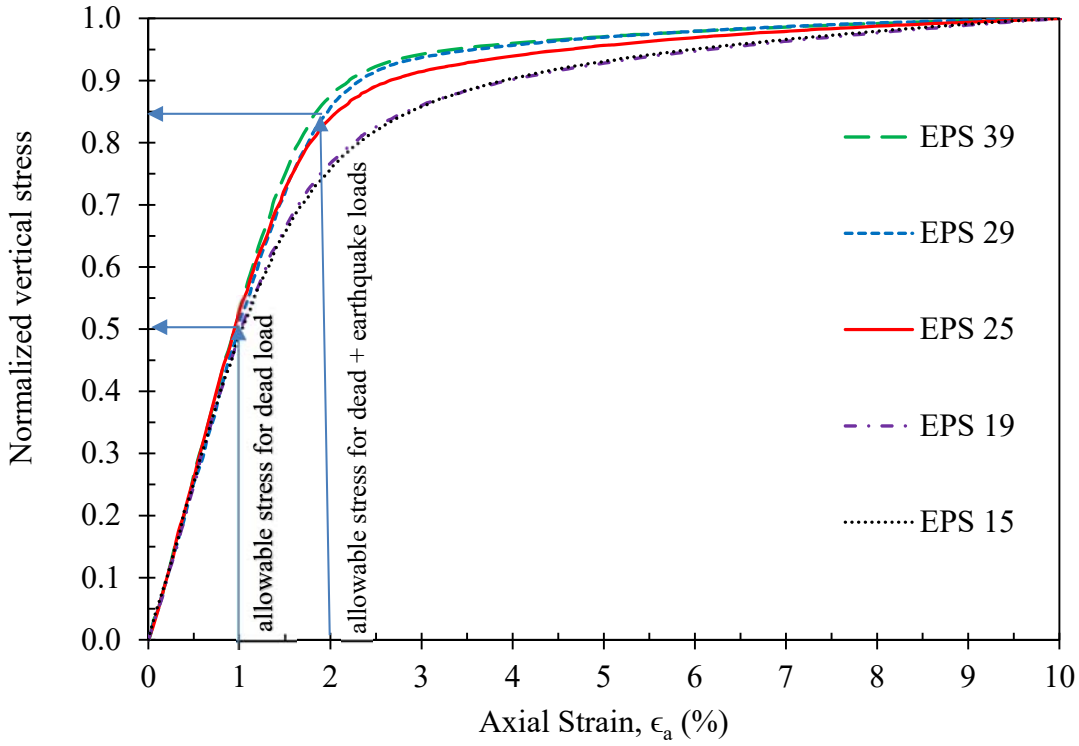

Figure 2-35. Recommended allowable stresses for dead load and dead load + earthquake loading combinations for EPS bridge support systems.

3 EVALUATION OF EPS BRIDGE SUPPORT SYSTEM

3.1 Introduction

This study focuses on the evaluation of bridge structures supported directly by EPS geofoam blocks placed atop soft ground conditions without the support of deep foundations or soil improvement. The capacity of EPS geofoam to support the associated structural dead loads and live loads without being overstressed is central to this new application.

The proposed criterion for determining the allowable stress in EPS blocks in terms of dead and live loads was discussed in Section 2. In short, the installed blocks must be capable of resisting dead loads (e.g., weight of bridge system, foundation footings and the EPS support system itself), live loads (e.g., routine cyclic traffic and vehicular impact loads) and other cyclic loadings originating from extreme events (e.g., earthquake loadings). The main objectives of this section are to: (1) determine the types and sizes of bridge structures that can be potentially supported on EPS blocks, (2) explore the fundamental period of simple EPS support systems under harmonic excitation, (3) evaluate the potential for excessive translation due to basal and inter-layer sliding during large horizontal accelerations, (4) evaluate the potential for internal overstressing of the blocks resulting from excessive horizontal sway, rocking and uplift during seismic excitation, and (5) explore possible seismic restraint mechanisms to prevent any significant damage to the bridge support system resulting from items (3) and (4).

3.2 General Considerations

Construction of embankment approach and support systems for highway bridges on soft soil sites offers unique challenges. Understandably, bearing capacity and consolidation settlement of the foundation soils are major design and construction considerations. Traditionally in geotechnical practice, excessive deformation and settlement has been minimized by: (1) decreasing the embankment loading to the foundation soils, (2) using bridge foundation types that minimize settlement and improve bearing capacity (e.g., deep foundations), or (3) using ground improvement to change the soil conditions. However, options (2) and (3) require specialized construction techniques and may introduce considerable construction time in the project schedule depending on the nature and thickness of the compressible sediments. In regards to option 1, the extremely light-weight nature of EPS blocks offers an attractive means for significant load reduction; hence eliminating consolidation settlement and reducing construction time.

In addition, the use of EPS embankments has significantly reduced the amount of post-construction settlement experienced by bridge structures and approach embankments for the I-15 Reconstruction Project in Salt Lake City, Utah (Farnsworth et al., 2008). In general, field monitoring of I-15 embankment settlement performance has shown that the amount of differential settlement between the embankment and bridge abutment has been greatly reduced by using EPS geofoam in the bridge approach areas when compared with other conventional embankment and soil improvement technologies (Farnsworth et al., 2008). Contemporaneously to this important project and subsequently, the use of EPS geofoam as light-weight embankment for bridge approaches situated atop soft ground has been applied by many highway projects nationwide; hence it is considered a proven technology by the Federal Highways Administration (FHWA) and many State DOTs (https://www.fhwa.dot.gov/research/deployment/geofoam.cfm).

Typically EPS embankments are constructed as rectangular or trapezoidal in shape. However, when specifically used for bridge support systems, the trapezoidal-shaped embankment has been used for bridges constructed in Norway (i.e., Lokkeberg, Hjelmungen and Grimsoyvegen Bridges) as reported in Aaboe and Frydenlund (2011). The reason for the trapezoidal-shape was to help reduce the bearing pressure on quick clays that are pervasively found in Norway. Nonetheless, Stuedlein and Negussey (2013) have explored the use of EPS geofoam as a prismatic compensating foundation system to support a single span bridge at the "Buffalo Road Bridge" crossing of Oatka Creek, New York, USA.

This study will evaluate the use of both prismatic rectangular and trapezoidal EPS bridge support systems as conceptually shown in Figures 3-1 and 3-2. Because EPS bridge support systems may be susceptible to instability and overstressing resulting from dead and live loads experienced during extreme events (e.g., earthquakes), the EPS bridge support system must be evaluated for ultimate limit states associated with: (1) basal sliding at the foundation soil / block interface, (2) inter-layer sliding between the various EPS layers, (3) horizontal sway of the entire EPS mass, and (4) potential rocking and uplift of the base of the EPS mass.

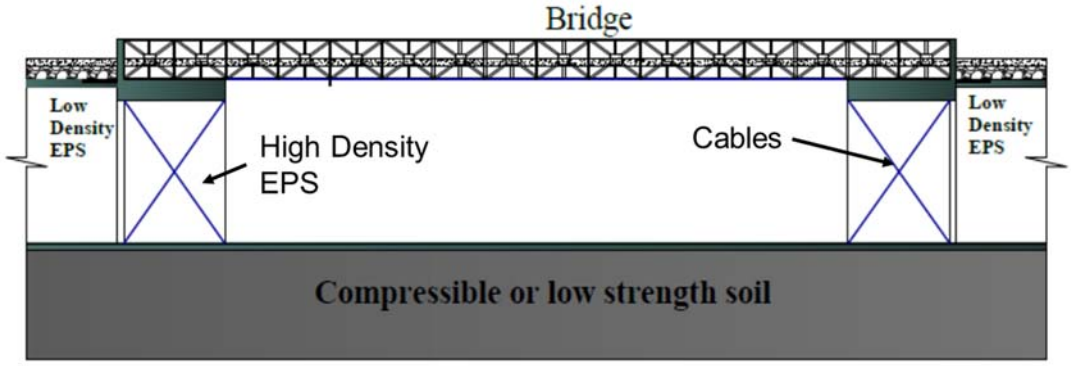

Figure 3-1 Conceptual bridge support with a rectangular prismatic shaped EPS embankment

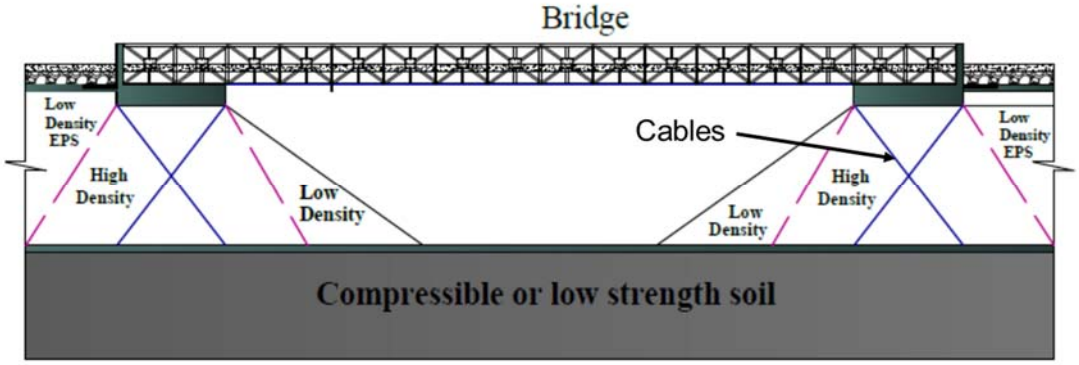

Figure 3-2 Conceptual bridge support with a trapezoidal prismatic shaped EPS embankment

It is important to note that this study focuses on evaluating the portion of the EPS embankment used for direct bridge support. The support zone of the embankment is shown as "high density EPS" in Figures 3-1 and 3-2. Due to the weight and inertial forces imposed on the EPS blocks by the bridge system in this portion of the embankment, it is expected that relatively high modulus EPS blocks will be required in these areas. For trapezoidal embankment geometries (Figure 3-2), a high modulus EPS will be evaluated in the trapezoidal zone directly under the bridge (i.e., zone found inside the sloping pink dashed lines). A lower modulus EPS will be evaluated for use in the

remaining part of embankment outside of the support zone. In addition, a 1V:2H toe and back slope will be evaluated, as was used in the Norway systems (Aaboe and Frydenlund, 2011), but in contrast to the Norwegian systems, the side slopes of the embankment will be prismatic (i.e., vertical) instead of sloped. Lastly, the potential use of cabling (see blue lines in Figures 3-1 and 3-2) to connect the bridge foundation to an embedded concrete slab placed at the base of the EPS embankment to form a seismic horizontal restraint system will be evaluated in the final parts of this report

3.3 Bridge Configurations

This study evaluated two general bridge types to be supported by EPS blocks: steel truss and concrete girder bridges. The steel truss bridges evaluated consisted of one and two-lane, single-span steel truss bridges, and the concrete girder bridges consisted of one and two-lane, single-span concrete girder bridges. The potential size and span of these bridge types were determined based on the allowable compressive resistance of the EPS blocks as discussed in Chapter 2, and the required size and weight of the bridge and supporting concrete spread footing placed atop the EPS. These footings have the function to distribute the vertical loading of the bridge structure into the EPS embankment without causing localized overstressing in the zone immediately under the bridge (Figures 3-1 and 3-2).

3.4 Permanent Load Evaluations

3.4.1 EPS Compressive Resistance

Based on the laboratory test results from Chapter 2, it is recommended that the stress level associated resulting from the applied gravitational dead load in the EPS blocks should not be higher than the stress level corresponding to 1 percent axial strain as measured from a monotonic load tests.

For the initial sizing of the bridge and support systems, published values of compressive resistances for EPS 22 and EPS 29 were selected for these preliminary evaluations. The design values for EPS 22 and EPS 29 at the 1 percent axial strain level were selected from ASTM D6817 (2007) (Table 3.1) as initial design values for resisting the gravitational dead loads. In addition, the height of the prototype support embankment was assumed to be 6 m, and the sizing of bridge was done using the geometry of a rectangular prismatic embankment, which is the most conservative case in terms of surface area and volume available to resist the applied loadings. The thickness of the bridge spread footing and unit weight of concrete were assumed to be 0.5 m and 23.56 kN/m^3, respectively, for the dead load calculations.

Table 3.1. Compressive resistance of EPS geofoam at various levels of strain (ASTM D6817, 2007)

Type	EPS12	EPS15	EPS19	EPS22	EPS29	EPS39	EPS46
Density, min., kg/m^3(lb/ft^3)	11.2 (0.70)	14.4 (0.90)	18.4 (1.15)	21.6 (1.35)	28.8 (1.80)	38.4 (2.40)	45.7 (2.85)
Compressive Resistance, min., kPa (psi) at 1 %	15 (2.2)	25 (3.6)	40 (5.8)	50 (7.3)	75 (10.9)	103 (15.0)	128 (18.6)
Compressive Resistance, min., kPa (psi) at 5 %	35 (5.1)	55 (8.0)	90 (13.1)	115 (16.7)	170 (24.7)	241 (35.0)	300 (43.5)
Compressive Resistance, min., kPa (psi) at 10 %[4]	40 (5.8)	70 (10.2)	110 (16.0)	135 (19.6)	200 (29.0)	276(40.0)	345 (50)
Flexural Strength, min., kPa (psi)	69 (10.0)	172 (25.0)	207 (30.0)	276 (40.0)	345 (50.0)	414 (60.0)	517 (75.0)
Oxygen index, min., volume %	24.0	24.0	24.0	24.0	24.0	24.0	24.0

3.4.2 Vertical Stress Distribution Calculation

One important design consideration in sizing the concrete footings of the bridge system, is the nature of the vertical stress redistribution that develops within the EPS embankment underneath the bridge footings. This topic has been evaluated by relatively few researchers, but some guidelines are studies are available. Tefera et al. (2011) provide Finite Element Method (FEM) simulation results for the vertical stress distribution in a bridge support system based on PLAXIS™ modeling. In addition, confirmatory laboratory and field tests were conducted by these researches to measure the vertical stress distribution within the EPS blocks. Their FEM modeling results showed a vertical stress distribution bulb within the EPS embankment of about 60 degrees, as measured from the horizontal. This result compared well with the experimentally obtained values. Similarly, the work of Tsukamoto (2011) found that the vertical stress distribution blub inside an EPS embankment was 70 degrees, as measured from the horizontal. Thus for this study, a simple vertical stress redistribution of 2V:1H (i.e., 63.4 degrees) was used as recommended by NCHRP 529 (Figure 3-3). This recommendation falls between the results reported by Tsukamoto (2011) and Tefera et al. (2011) and is considered sufficiently accurate for preliminary evaluations.

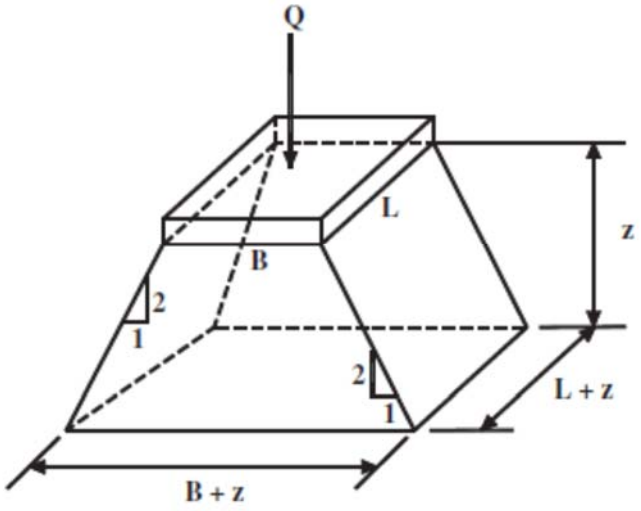

Figure 3-3 Approximate stress distribution by the 2V to 1H method (NCHRP 529).

3.4.3 Gravitational Dead Loads

The dead loads consist of the components of the superstructure, substructure and bridge foundations considering both structural and non-structural features. The weights of these items were used to determine the gravitational loads on the EPS bridge support system. The detailed calculations for sizing of the bridge types and foundations are found in Appendix A. For the steel bridge evaluations, Acrow™ and Mabey™ bridges were chosen as typical examples. The weight per meter length of Acrow bridges was based on (Needham, Randy, personal communication, Jan. 14, 2014) and for Mabey bridge, the value was calculated from the data given on their website (Maybehire, 2012). The weight per meter of Acrow bridges was higher than Mabey bridges, therefore the value obtained from Acrow bridges were used in the evaluations. For the concrete bridges, the bridge weight per unit length calculation was based on Modjeski-Masters-Inc (2003). The total width of bridges for single and double lanes with one sided side walk was chosen to be 5.25 and 9 m, respectively. The spread footing foundation placed atop the EPS embankment was evaluated as a

rectangular-shaped element. The transverse dimension was set equal to the width of the bridge (i.e., 5.25 and 9 m, respectively) and the longitudinal dimension was set equal to 4 m, but this parameter was also varied, as discussed later.

3.5 Transient Load Evaluations

3.5.1 Design Vehicular Live Loads

The AASHTO HL93 design truck load generally consists of a design truck plus design lane load. The design truck is identical to the HS20 truck load configuration. The lane load applies to the design of above grade bridge decks, but is not applied to below ground structures. Because the EPS embankment is part of the support system for the bridge and is not part of the bridge per se, a lane load was not considered in the live load in terms of sizing the bridge.

The live truck load was calculated based on the design truck given in AASHTO (2012) as shown in Figure 3-4. For a consideration of the maximum load, the spacing of the middle and rear axle was taken as 4.27 m (14 feet). The spacing between the two consecutive vehicles on the bridge was assumed to be 1.52 m (5 feet). Live load per meter was calculated for the single lane and double lane configurations by dividing the axle load by the length of loading.

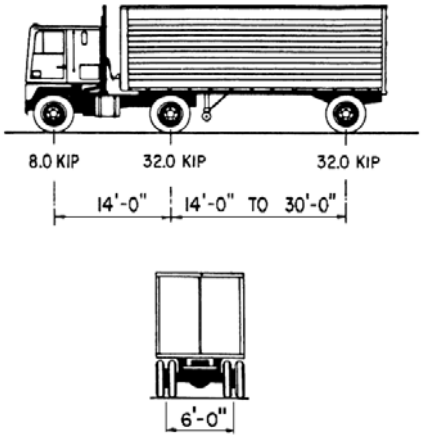

Figure 3-4 Characteristic of the HL-93 design truck (AASHTO, 2012)

3.5.2 Evaluation of Bridge Type, Width and Potential Span Length

The potential span length of the bridge system was calculated considering the dead load (i.e., gravitational weight of superstructure, substructure and bridge foundation components) and the live vehicular load. A factor of safety of 1.2 was applied to the combination of the dead and live loads, as suggested by NCHRP 529. The results for steel and concrete structures supported by EPS 22 and 29 blocks for a 4-m wide spread footing are summarized in Table 3.2. In this particular case, if a steel bridge is deployed, the maximum span length is approximately 34 m and 31 m for single-lane and double lane bridges, respectively, founded on EPS 29 blocks.

Table 3.2. Potential Span length of concrete and steel bridge for EPS 22 and 29 with 4-m wide footing

Material	Lane	Transverse length of bridge footing	Type of EPS	Span length of bridge
---	---	m	---	m
Steel	Single	5.25	22	20
Steel	Double	9	22	18
Steel	Single	5.25	29	34
Steel	Double	9	29	31
Concrete	Single	5.25	22	12
Concrete	Double	9	22	11
Concrete	Single	5.25	29	21
Concrete	Double	9	29	18

In addition, the length of steel and concrete bridges for single and double lane by using EPS 22 and 29 were parametrically calculated for footing widths varying from 2 m to 6 m (Figure 3-5). The analyses shown in this figure suggest that a 47-m span length is possible for a double lane steel bridge supported on EPS 29. Similarly a 27-m span length is possible for a double lane concrete girder bridge supported on EPS 29. If longer span lengths are required than these examples, the density or modulus of the EPS would need to be increased to EPS 39 or EPS 45. However, for typical overpass structures, it appears that EPS 29 is sufficient, in many cases, to use as a bridge support system.

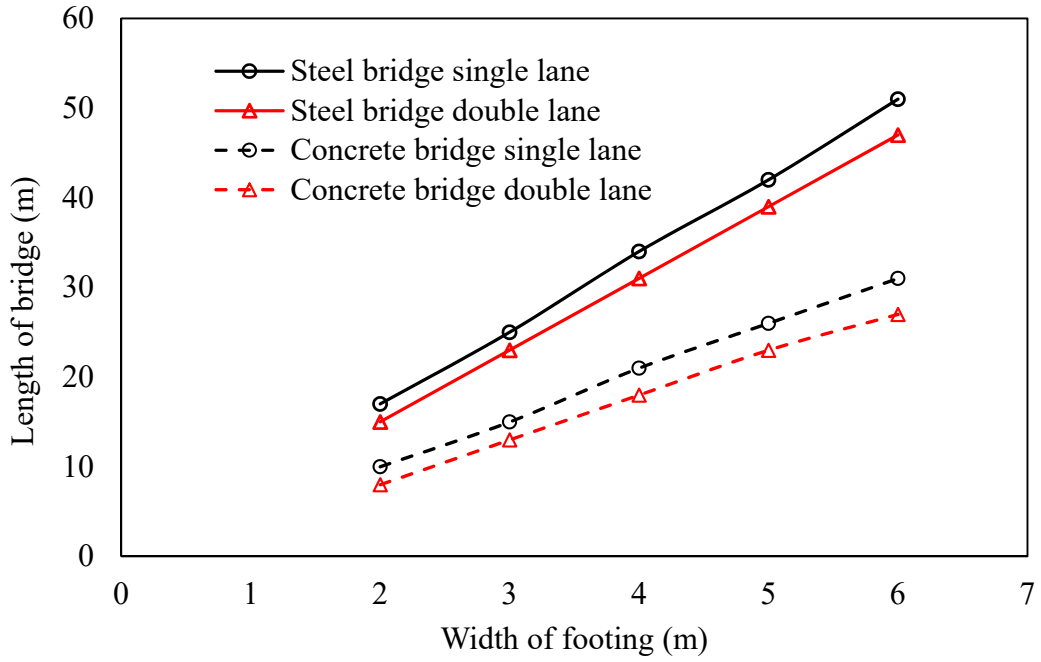

Figure 3-5 Relationship of length of bridge with length of footing for single and double-lane bridges supported on EPS 22 (red) and EPS 29 (black)

3.5.3 Earthquake Extreme Event Limit State

3.5.3.1 Introduction

A few researchers (McDonald and Brown, 1993; Snow and Nickerson, 2004; Aaboe and Frydenlund, 2011; Stuedlein and Negussey, 2013) have studied the use of EPS geofoam for bridge support systems. These studies mainly focused on static loading conditions and did not consider extreme loadings, such as earthquakes.

The dynamic response of an EPS embankment is very complex at high levels of seismic excitation. The potential modes of excitation listed by Riad and Horvath (2004) are: (1) rigid-body translation (i.e., sliding), (2) horizontal flexibility and deformation (i.e., lateral sway), and (3) rigid-body rotation (i.e., seismic rocking).

Sliding may occur between the blocks or at other horizontal interfaces in the bridge support system. Horizontal sway occurs due to the flexibility of EPS mass in the horizontal direction and rocking results from two dimensional (2D) rigid body rotation (Riad and Horvath, 2004). When an EPS embankment attempts horizontal sway, it produces alternating internal shear, tensile and compressional stresses during earthquake cycling. In the rocking mode, alternating tensile and compressive stresses are produced primarily along with their associated strains. In addition, uplift at the edges of the embankment may occur during extreme rocking.

The EPS embankment may have unsuitable movement or become overstressed from internal forces associated with these excitation modes. Only a handful of U.S. researchers have done analytical and numerical studies on EPS embankment undergoing seismic excitation. The majority of these studies have focused on EPS embankment used to support roadway pavement systems (Riad and Horvath, 2004; Stark et al., 2004; Bartlett and Lawton, 2008; Amini 2014). No studies or evaluations have been completed on the seismic performance of EPS bridge support system.

3.5.3.2 General Considerations

Therefore, the remainder of this report focuses on the evaluations, conceptual design and considerations for EPS bridge support systems undergoing earthquake loadings. Other types of extreme loading events (e.g., wind, flood, impact, etc.) are not considered herein.

AASHTO (2012) describes the load combinations and load factors for various evaluation cases. Previous editions of the AASHTO Standard Specifications have used an earthquake live load factor of $\gamma EQ = 0.0$. However, the issue surrounding the selection of an appropriate live load factor for earthquakes has not been completely resolved. The possibility of a partial live load factor, i.e., $\gamma EQ < 1.0$, should be considered in conceptual or preliminary analyses, such as those presented herein. Application of Turkstra's rule for combining uncorrelated loads indicates that $\gamma EQ = 0.50$ is reasonable for a wide range of values of average daily truck traffic (ADTT). This is the approach taken by this study. Therefore, W, as used in this study is the combination of dead load and 50 percent of live truck load for the seismic evaluations.

3.5.3.3 Geometrical Configurations Evaluated

The geometry of the EPS support embankment and the magnitude of the supported mass (i.e., bridge structure) play vital roles in influencing the dynamic behavior of the support system. These general embankment configurations evaluated herein are: (1) free-standing vertical embankment

and (2) sloped embankment (Figure 3-6 and 3-7, respectively). The mass density of EPS geofoam is almost 100 times lighter than other conventional geotechnical materials like soil and rock. Therefore, the majority of the mass in a bridge support application is located at the top of the EPS embankment due to the large gravitational loads of the bridge structure and its components and any vehicles present.

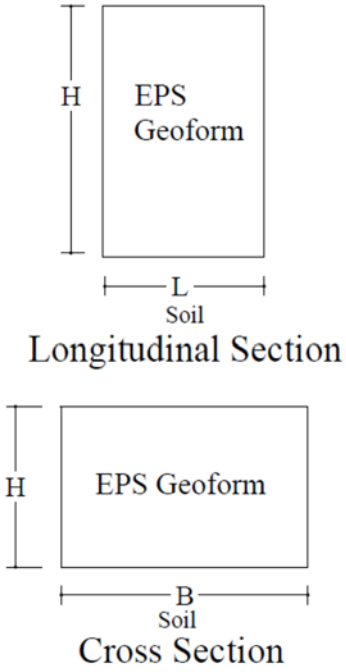

Figure 3-6 Longitudinal and cross section of rectangular prismatic shape EPS Embankment

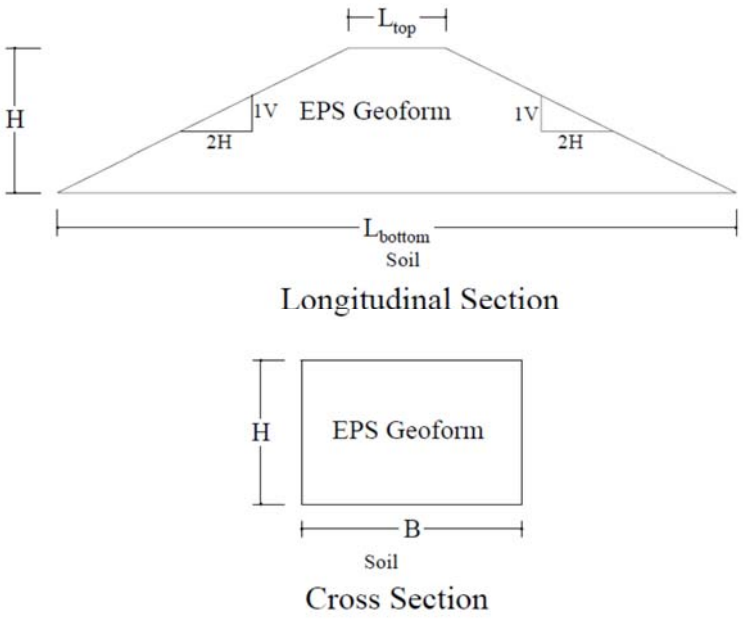

Figure 3-7 Longitudinal and cross section of trapezoidal prismatic shape EPS embankment

3.5.3.4 Limit States and Allowable Stress in the EPS Blocks

A simple way to evaluate the seismic performance of an EPS bridge support system is to calculate the critical acceleration for each excitation mode or limit state listed above. The critical horizontal acceleration (g) is that value which produces a factor of safety equal to unity for the respective mode of excitation or limit state. The limit states considered in the following sections are: (1) interlayer sliding between the EPS blocks, (2) basal sliding between the foundation soil and the first layer of EPS blocks, (3) sliding between the uppermost EPS block layer and the bridge foundation, (4) internal overstressing of the EPS blocks resulting from excessive horizontal sway, and (5) internal overstressing of the EPS blocks due to excessive seismic rocking. Modes 1, 2 and 3 are ultimate limit states which could cause severe and immediate damage to the bridge support system. Modes 4 and 5 are serviceability limit states associated with excessive post-event creep deformation of the support embankment due to overstressing of the EPS blocks during the seismic event. It should be noted that overturning of an EPS embankment is not considered as a likely extreme event limit state for the width to height aspect ratios typically used in construction of EPS embankments, as previously discussed in Section 1.2.

3.5.3.5 Recommended Design Allowable Stress Limits for EPS Blocks

In regards to the potential for overstressing of the EPS block resulting from gravity and live loads and from excitation modes 4 and 5, the following evaluation criteria is offered for determining the allowable stress in the EPS blocks. It is recommended that the applied gravitational dead load and 50 percent of the live truck load does not exceed the compressive resistance associated with 1 percent axial strain, as measured in a monotonic uniaxial compression test for the selected density of EPS. Furthermore, it is recommended that the combined applied gravitational dead, 50 percent of the live truck load and peak earthquake loads in the EPS block be limited to a stress level that does not exceed the compressive resistance associated with 2 percent axial strain, as measured in a monotonic uniaxial compression test for the selected density of EPS. These recommendations are based on the testing and evaluations previously presented in Chapter 2.

The potential for failure or excessive deformation of the foundation soils is not considered by this study, but such evaluations would be required based on site-specific investigations and analyses.

3.5.3.6 Simplified Force-Based Methods Based on Fundamental Period

It is recommended that live loads be determined on a project specific basis for extreme events like earthquakes by developing a design acceleration response spectrum. This design spectrum becomes the basis of determining the inertial forces in the system for many of the excitation modes. In simplified, force-based seismic evaluations, the calculation of the fundamental period of the bridge support system is important because it affects dynamic behavior and accelerations experienced within the EPS system.

Simplified analytical methods have been proposed to estimate the fundamental period of EPS embankments by EDO (1993), Horvath (1995, 2004), Stark et al. (2000) and Amini (2014). In the approach taken by these researchers, the EPS embankment is treated as a plane-strain case (i.e., assumed that the longitudinal dimension is infinitely large). In addition, it is assumed that the embankment is fixed at the base and the lumped mass is rigid and concentrated at the top of an elastic, weightless EPS embankment. (This approach is similar to a weightless cantilevered beam with the cyclic load placed at the free end.) Thus, the system is idealized as a single degree of freedom (SDOF) system undergoing dynamic excitation (i.e., horizontal sway) (Figure 3-8). The peak inertial force at the top of the SDOF system is calculated using Newton's second law. For the case of this report, the peak inertial force was estimated by multiplying the lumped mass of the bridge support system by the design horizontal earthquake acceleration. The lumped mass includes

the combined dead load of the bridge system, foundations, roadway and 50 percent of the live truck load. This lumped mass is multiplied by the design spectral acceleration at the frequency corresponding to the fundamental (i.e., first) mode of vibration of the embankment. For project specific evaluations, the design horizontal spectral acceleration value is obtained from the design acceleration response spectrum, as required by AASHTO (2012).

In this simplified method, the internal forces and stresses within an EPS embankment are determined using a linear interpolation between the peak inertial force due to the lump mass acting at the top of the EPS embankment and peak ground acceleration acting at the base of the embankment (NCHRP Web document 65). In this approach, the potential for geofoam-soil interaction (i.e., kinematic and inertial interaction) is neglected due to the relatively shallow embedment of the embankment and the relatively low mass (light-weight nature) of typical EPS embankment systems, respectively (Amini, 2014).

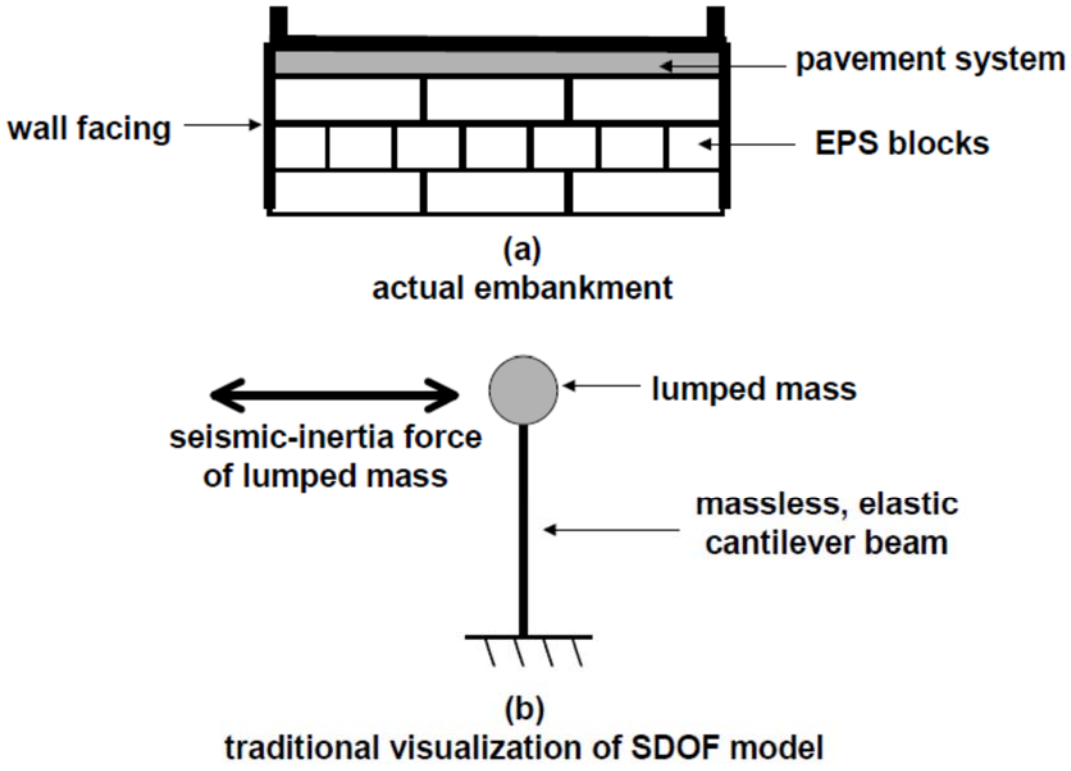

Figure 3-8 Idealization of an EPS free-standing embankment to a single degree of freedom (SDOF) system (after Riad and Horvath, 2004).

3.5.3.7 Analytical Evaluations of Fundamental Period

In calculating the fundamental period of an EPS support embankment, the concepts of flexural, shear and axial stiffness based on the work of Timoshenko and Gere (1972) were used. The flexural stiffness, shear stiffness and axial stiffness were calculated based on the direction of seismic excitation. For this part of the study, equations developed in the Japanese manual of practice (EDO, 1993) and summarized by Stark et al. (2000) and Horvath (1995, 2004) was used to estimate the fundamental period. The usefulness and limitations of this and other equations presented by Stark et al. (2000) were further investigated by Amini (2014) who found that the embankment aspect

ratio (i.e., embankment width to height ratio) plays a role in controlling the fundamental period of rectangular-shaped embankments. Amini (2014) concluded that numerically obtained results reasonably matched the Japanese equation for embankment aspect ratio higher than 2, and reasonably matched the Stark et al. (2000) equation for aspect ratios less than 1.5.
The following sections present the development of these equations from beam theory.

3.5.3.7.1 Derivation Based on Flexural and Shear Stiffness

The method of derivation of the fundamental period with consideration of flexural and shear stiffness is denoted as "Method I" hereafter.

The fundamental period of any SDOF system is:

$$T_0 = 2\pi \left[m \left(\frac{1}{k} \right) \right]^{0.5} \quad \textbf{(3.1)}$$

where: m and k represents the mass and spring stiffness of the SDOF system. Equation (3.1) written in terms of weight is:

$$T_0 = 2\pi \left[\left(\frac{W}{g} \right) \left(\frac{1}{k} \right) \right]^{0.5} \quad \textbf{(3.2)}$$

For a fixed-end cantilever beam with transverse concentrated force (P) at the free end and the maximum transverse displacement (Δ), the stiffness is defined by:

$$k = \frac{P}{\Delta} \quad \textbf{(3.3)}$$

Timoshinko's beam theory considered two components of spring stiffness which are: flexural stiffness (k_F) and shear stiffness (k_S). In this case, two springs are in series with the applied force P. The equivalent spring constant for two stiffness in series is:

$$k = \frac{1}{\frac{1}{k_F} + \frac{1}{k_S}} \quad \textbf{(3.4)}$$

$$\frac{1}{k} = \frac{1}{\frac{1}{\frac{1}{k_F} + \frac{1}{k_F}}} = \frac{1}{k_F} + \frac{1}{k_S} \quad \textbf{(3.5)}$$

Substituting the value of k in Eq. (3.2),

$$T_0 = 2\pi \left[\left(\frac{W}{g} \right) \left(\frac{1}{k_F} + \frac{1}{k_S} \right) \right]^{0.5} \quad \textbf{(3.6)}$$

the maximum flexural transverse displacement Δ_F is:

$$\Delta_F = \frac{PL^3}{3EI} \quad \textbf{(3.7)}$$

where: E is the Young's modulus of the beam material, I is the moment of inertia of the beam, L is the beam length. For the EPS geofoam embankment, E equals to E_{ti} which is the initial tangent (i.e., Young's) modulus of EPS. The values of L equals to H and I depend upon the direction of seismic excitation.

For excitation in transverse direction, the equation is:

$$I = \frac{BL^3}{12} \tag{3.8}$$

where: B is the width of embankment. Equation (3.7) becomes:

$$\Delta_F = \frac{12PH^3}{3E_{ti}BL^3} = \frac{4PH^3}{E_{ti}BL^3} \tag{3.9}$$

Combining Eqs (3.3) and (3.9),

$$k_F = \frac{P}{\Delta_F} = \frac{PE_{ti}BL^3}{4PH^3} = \frac{E_{ti}BL^3}{4H^3} \tag{3.10}$$

$$\frac{1}{k_F} = \frac{4H^3}{E_{ti}BL^3} \tag{3.11}$$

The shear deflection at free end is:

$$\Delta_S = \alpha_S \frac{PL}{GA} \tag{3.12}$$

where: α_s is the shear coefficient used to calculate the shear stress at centroid, G is the shear modulus of the beam material and A is the beam cross-sectional area. According to Cowper (1966), the shear coefficient for a solid rectangular section is:

$$\alpha_S = \frac{12 + 11\nu}{10(1+\nu)} \tag{3.13}$$

$$k_S = \frac{P}{\Delta_S} = \frac{GA}{\alpha_S L} = \frac{10(1+\nu)GA}{(12+11\nu)L} \tag{3.14}$$

$$\frac{1}{k_S} = \frac{(12+11\nu)L}{10(1+\nu)GA} \tag{3.15}$$

For the linear elastic material, the equation is:

$$G = \frac{E}{2(1+\nu)} \tag{3.16}$$

where: E is the Young's modulus of the material and v is the Poisson's ratio of the material. Replacing L by H, E by E_{ti} and G by relation with E in Eq. (3.15),

$$\frac{1}{k_S} = \frac{(12+11v)2H(1+v)}{10(1+v)E_{ti}A} = \frac{H(12+11v)}{5E_{ti}LB} \quad \textbf{(3.17)}$$

Combining Eqs (5.6), (5.11) and (5.17) produces the following for the transverse direction,

$$T_0 = 2\pi\left[\left(\frac{W}{g}\right)\left(\frac{4H^3}{E_{ti}BL^3} + \frac{H(12+11v)}{5E_{ti}LB}\right)\right]^{0.5} \quad \textbf{(3.18)}$$

$$T_0 = 2\pi\left\{\left[\frac{WH}{gE_{ti}LB}\right]\left[4\left(\frac{H}{B}\right)^2 + \frac{(12+11v)}{5E_{ti}LB}\right]\right\}^{0.5} \quad \textbf{(3.19)}$$

$$T_0 = 2\pi\left\{\left[\frac{\sigma'_{v0}H}{E_{ti}g}\right]\left[4\left(\frac{H}{B}\right)^2 + \frac{(12+11v)}{5}\right]\right\}^{0.5} \quad \textbf{(3.20)}$$

where: σ'_{v0} is vertical effective stress at the top acting on the top of the EPS.

Similarly, the equation for excitation in the longitudinal direction,

$$I = \frac{LB^3}{12} \quad \textbf{(3.21)}$$

and similar to derivation of excitation in the transverse direction, the fundamental period for the longitudinal direction is:

$$T_0 = 2\pi\left\{\left[\frac{\sigma'_{v0}H}{E_{ti}g}\right]\left[4\left(\frac{H}{L}\right)^2 + \frac{(12+11v)}{5}\right]\right\}^{0.5} \quad \textbf{(3.22)}$$

3.5.3.7.2 Derivation Based on Horvath (1995, 2004) Stark et al. (2000)

The shear coefficient used in Stark et al. (2000) is:

$$\alpha_S = \frac{5}{6} \quad \textbf{(3.23)}$$

By substituting α_S in Eq. (3.14), the final result for excitation in the transverse and longitudinal directions are for excitation in the transverse direction:

$$T_0 = 2\pi\left\{\left[\frac{\sigma'_{v0}H}{E_{ti}g}\right]\left[4\left(\frac{H}{B}\right)^2 + \frac{(12+12v)}{5}\right]\right\}^{0.5} \quad \textbf{(3.24)}$$

and for excitation in the longitudinal direction:

$$T_0 = 2\pi \left\{ \left[\frac{\sigma'_{v0} H}{E_{ti} g} \right] \left[4 \left(\frac{H}{L} \right)^2 + \frac{(12 + 12\nu)}{5} \right] \right\}^{0.5} \quad \textbf{(3.25)}$$

3.5.3.7.3 Derivation Based on Flexural, Shear and Axial Stiffness

The derivation with consideration of all three stiffness (flexural, shear and axial) is denoted as "Method II" hereafter. As mentioned in Horvath (2004), EDO (1993) also developed an equation that considers flexural, shear and axial stiffness. This equation is obtained by adding one additional spring representing the axial stiffness to the flexural and shear springs (Amini, 2014). The axial displacement of beam is:

$$\Delta_A = \frac{PL}{AE} \quad \textbf{(3.26)}$$

Replacing L and E by H and E_{ti},

$$\Delta_A = \frac{PH}{AE_{ti}} \quad \textbf{(3.27)}$$

$$k_A = \frac{P}{\Delta_A} = \frac{H}{AE_{ti}} \quad \textbf{(3.28)}$$

$$\frac{1}{k_A} = \frac{AE_{ti}}{H} \quad \textbf{(3.29)}$$

Eq. (3.5) can be written as:

$$\frac{1}{k} = \frac{1}{k_F} + \frac{1}{k_S} + \frac{1}{k_A} \quad \textbf{(3.30)}$$

Eq. (3.6) can be rewritten as:

$$T_0 = 2\pi \left[\left(\frac{W}{g} \right) \left(\frac{1}{k_F} + \frac{1}{k_S} + \frac{1}{k_A} \right) \right]^{0.5} \quad \textbf{(3.31)}$$

For excitation in the transverse direction and by substituting the values from Eq. (3.11), Eq. (3.17) and Eq. (3.29) in Eq. (3.31):

$$T_0 = 2\pi \left\{ \left[\frac{\sigma'_{v0} H}{E_{ti} g} \right] \left[4 \left(\frac{H}{B} \right)^2 + \frac{(12 + 11\nu)}{5} + 1 \right] \right\}^{0.5} \quad \textbf{(3.32)}$$

For excitation in the longitudinal direction,

$$T_0 = 2\pi \left\{ \left[\frac{\sigma'_{v0} H}{E_{ti} g} \right] \left[4 \left(\frac{H}{L} \right)^2 + \frac{(12 + 11\nu)}{5} + 1 \right] \right\}^{0.5} \quad \textbf{(3.33)}$$

3.5.3.7.4 Derivation for Excitation In the Vertical Direction

This is the case where the force acts perpendicular to the cross section of cantilever beam. The beam is in compression in this case. The stiffness is equivalent to the axial stiffness only.

$$k = \frac{AE}{L} \quad \textbf{(3.34)}$$

Replacing *L* by *H* and *E* by E_{ti} in Eq. (3.34) and substituting the value of *k* in Eq. (3.2),

$$T_0 = 2\pi \left[\left(\frac{W}{g} \right) \left(\frac{H}{AE_{ti}} \right) \right]^{0.5} = 2\pi \left[\left(\frac{W}{g} \right) \left(\frac{H}{LBE_{ti}} \right) \right]^{0.5} \quad \textbf{(3.35)}$$

$$T_0 = 2\pi \left[\frac{\sigma'_{v0} H}{E_{ti} g} \right]^{0.5} \quad \textbf{(3.36)}$$

The excitation in the vertical-direction from analytical method is denoted as "Analytical" here after. In the above equations, *W* is the total weight at the top of an embankment which includes the dead load and any live truck loads, as applicable.

The trapezoidal prismatic embankment is complex shape and therefore calculation its stiffness is difficult. Therefore, the trapezoidal shape was converted into equivalent rectangular shape by calculating the equivalent length without altering the height and width as shown by Horvath (1995) for 2D embankments.

The fundamental period were calculated for single and double lane with footing length 2 m, 3 m, 4 m, 5 m and 6 m. The detailed calculation for two different types of embankments using 4 m length of embankment employing analytical method is shown in Appendix C.

3.5.3.7.5 Numerical Evaluations of Fundamental Period

3.5.3.7.5.1 Rectangular Prismatic Embankments

In addition to simplified solutions based on beam theory, the fundamental period and dynamic response of EPS embankments can be evaluated using numerical methods. Amini (2014) used Fast Lagrangian Analysis of Continua (FLAC) (Itasca, 2005) simulations, which is based on the finite difference method (FDM), to numerically determine the fundamental period of prototype free-standing EPS embankments. Amini (2014) compared numerical results with analytical results, where the latter results were based on equations summarized in Section 3.5.3.6 of this report. A similar approach is taken by this study.

Rectangular and trapezoidal prismatic shaped EPS geofoam embankments were modeled in FLAC 3D to estimate the fundamental period of the prototype embankments and compared with the analytical methods. In this modeling, 2-m to 6-m long footings were used and oriented in the longitudinal direction of the bridge support system (i.e., in the direction parallel to the bridge). A typical FLAC model for 4-m long, 9-m wide (i.e., where width is taken in the transverse direction of the embankment) and 6-m high is shown in Figure 3-9. In this figure, the blue and red colors represent the lump mass of the system (i.e., mass of bridge and concrete bridge foundation and live truck loads) and the mass of the EPS embankment, respectively.

For each prototype model, dynamic excitation was made in the longitudinal, transverse and vertical directions using typical material properties for the respective materials. For example, the calculation for a 4-m long footing placed on the EPS support system is found in Appendix D. The compressive strength of concrete was assumed to be 5000 psi (34474 kPa) (Concrete-Properties, 2014). MacGregor and Wight (2005) mentioned that Poisson's ratio for typical concrete falls in the range of 0.15 to 0.20. In this study, a Poisson's ratio of 0.18 was selected.

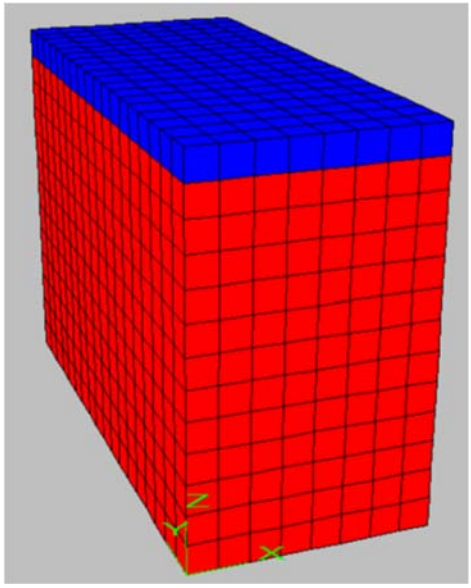

Figure 3-9 EPS geofoam embankment system

The modulus of elasticity of concrete was calculated from the Eq.(3.37) as given in MacGregor and Wight (2005):

$$E_C = 33(w^{1.5})\sqrt{f'_c}\, psi \qquad \textbf{(3.37)}$$

where: w is the weight of the concrete in lb/ft^3 and f'_c is the compressive strength of concrete (psi). The shear modulus and bulk modulus were calculated from the Eqs (3.16) and (3.38) respectively.

$$K = \frac{E_C}{3(1-2\nu)} \qquad \textbf{(3.38)}$$

The density of EPS 29 used in the evaluations was obtained from the laboratory test results summarized in Chapter 2. The density and modulus of elasticity of EPS 29 geofoam were 34.02 kg/ m^3 and 12547 kPa, respectively. Poisson's ratio of EPS was calculated from the relation of Poisson's ratio and density as given in Eq. (3.39) by Horvath (1995).

$$\nu = 0.0056\rho + 0.0024 \quad \textbf{(3.39)}$$

The shear and bulk modulus of EPS were calculated from the Eqs (3.16) and (3.38), respectively. The density of concrete used for the lumped mass in the numerical modeling was adjusted to incorporate the total mass of the bridge support system (i.e., weights of the bridge and its foundation) and 50 percent of the live truck load. This adjusted mass density was incorporated by first calculating the volume of footing based on the recommended footing size, and then calculating the adjusted material density based on the total mass of the system divided by the footing volume. The material properties used in the FLAC model are shown in Table 3.2.

Table 3.2. Material properties for modeling of EPS geofoam support system

Material	ρ	E	□	G	K
----------	kg/m^3	MPa	----------	MPa	MPa
EPS	34.02	12.55	0.19	5.26	6.81
Concrete	2400[1]	29557	0.18	12523	15394

[1]The mass density of concrete used in the model is different from the usual density of concrete. The mass density used here includes the lumped mass of the bridge structure, foundation and 50 percent live loads.

For determining the fundamental period, the EPS support system was modeled as a single-body, elastic mass with no vertical or horizontal interfaces between the blocks. The sides of embankment were set free in all coordinate directions. The fixity of the base varied depending on the direction of excitation. For example, the transverse and vertical directions were fixed at the base of the model in order to excite the model in the longitudinal direction. In addition, no material damping was provided to the model; hence the fundamental period evaluated herein is the undamped value. A velocity forcing function was assigned at the base of the model in the direction of excitation. In order to explore the harmonic response of the embankment, both free vibration and forced vibration simulations were carried out. The results of both simulations were compared.

For the force vibration simulations, a trial and error method was used. In this method, the period was changed for a velocity sinusoidal forcing function wave equation and the displacement was monitored at the uppermost node of the lumped mass. Because damping was not present in the model, the displacement increased until it reached the resonance condition. The displacement at the top node versus dynamic time for an EPS embankment of 4-m length, 6-m height and 9-m width due to excitation along the longitudinal-direction with a period of 1.095 s is shown in Figure 3-10. This trial and error method for finding the fundamental period at resonance proved to be too time consuming and a better method was sought using free vibration simulations, as described below.
The free vibration simulation was employed to the same FLAC model and properties. In this method, a single cycle of a *sine* wave was used as a "pulse" input to the model causing free vibration of the system (Figure 3-11).

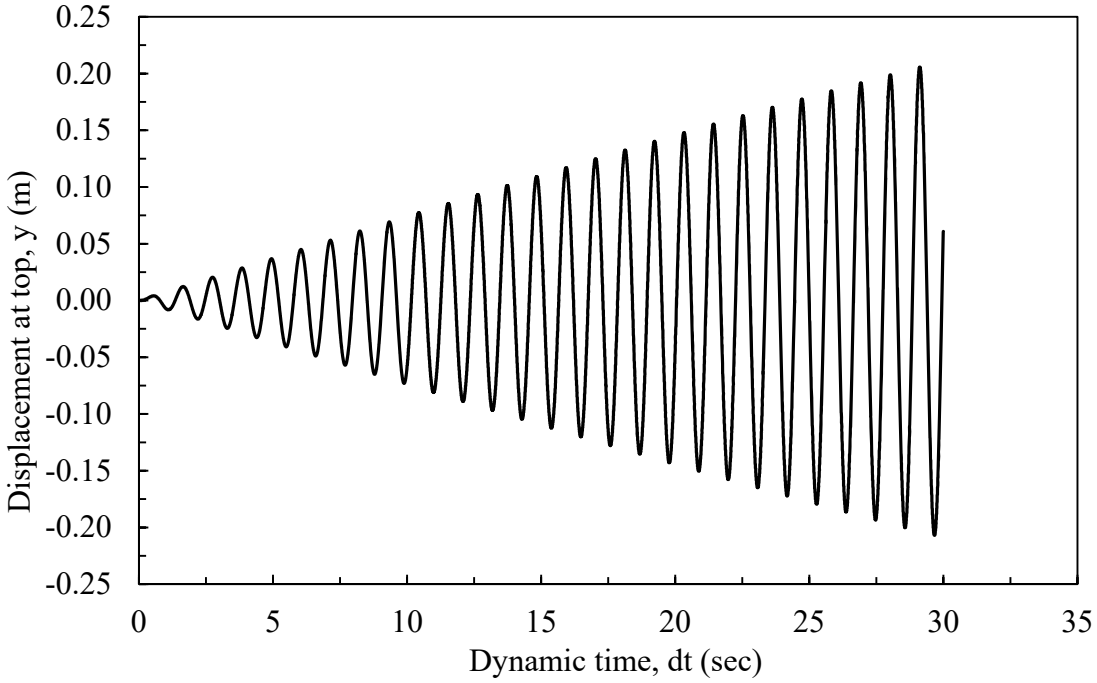

Figure 3-10 Displacement at top versus dynamic time under forced vibration

Figure 3-12 shows undamped, free vibration response of the model to the pulse loading. The time increment required to complete 1 cycle represents the fundamental period of the system (i.e., 1.095 s for this case). The FLAC code for the calculation of the fundamental period by using free vibration for the longitudinal-direction for a 4-m length footing is given in Appendix E.

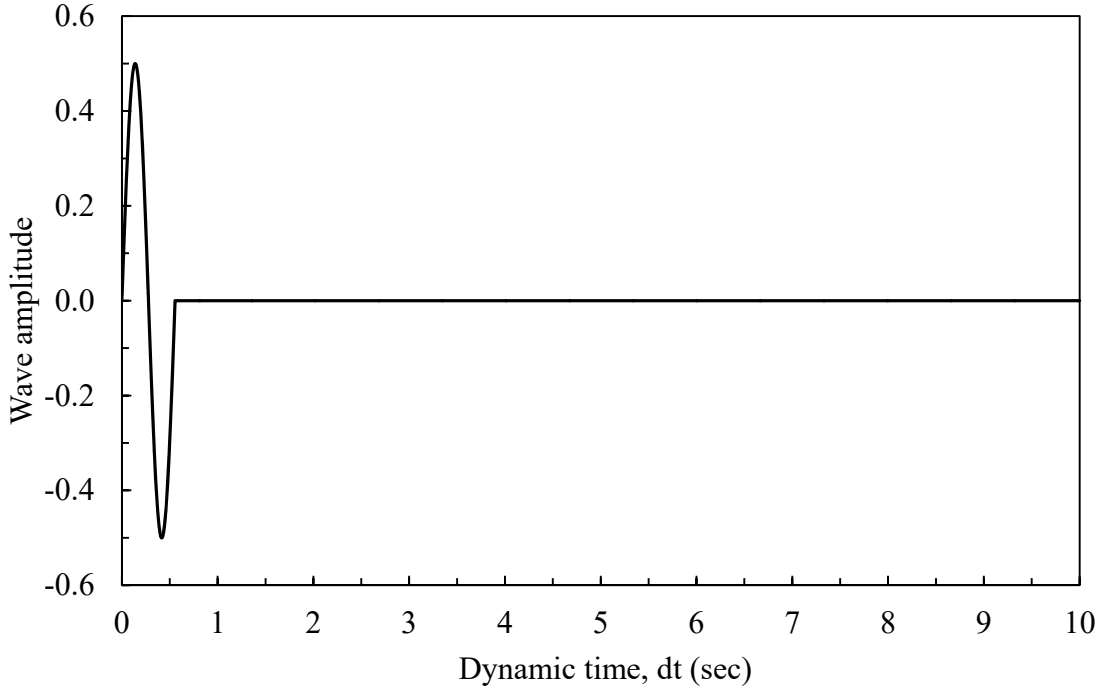

Figure 3-11 Sine wave pulse used for free vibration simulation

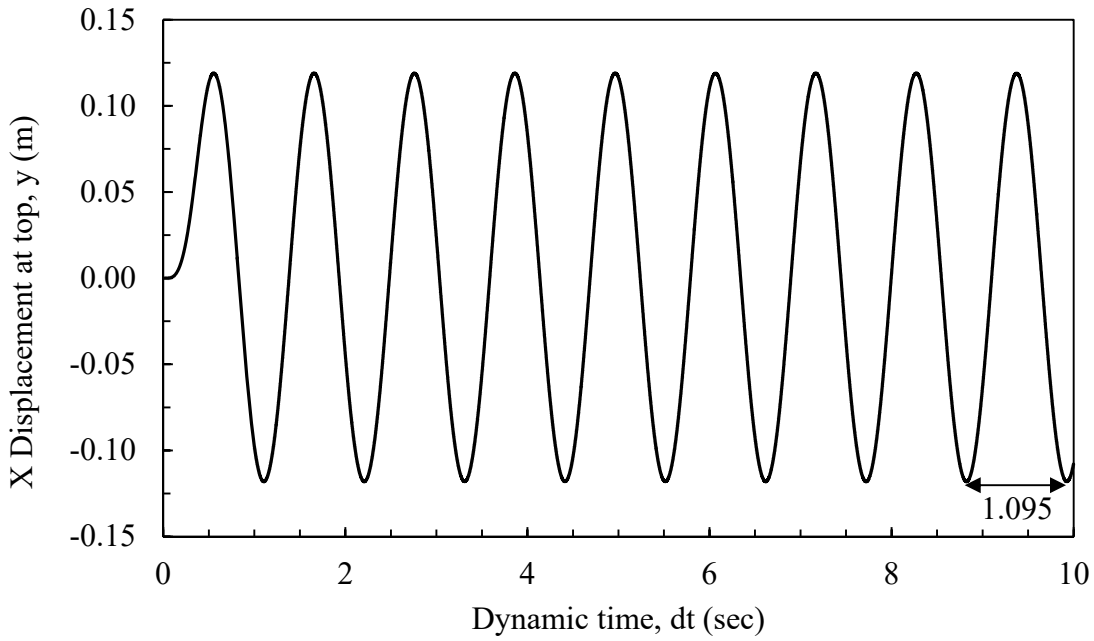

Figure 3-12 Displacement at top node versus time at fundamental period for free vibration simulation

3.5.3.7.6 Comparison of Analytical and Numerical Methods for Rectangular Prismatic Embankments

The fundamental period versus footing length for rectangular prismatic embankments when excited in three directions for the single and double lane cases is shown Figures 3-13 and 3-14, respectively. These figures reveal that the fundamental period decreased with increasing length of footing when the seismic excitation was introduced in the longitudinal direction. This is due to the change in the aspect ratio of the embankment in the longitudinal direction as represented by the footing length. Because the width and height remained constant for all cases analyzed, the stiffness increased with increases in length, and the fundamental period decreased. However, the fundamental period in the transverse and vertical directions was essentially constant because of the constant width and height ratio for these simulations. For the single lane, the fundamental period in the longitudinal direction was higher than the transverse direction for cases where the length was less than width. However, once the length exceeded the width, the fundamental period in the longitudinal direction decreased and was less than the transverse direction.

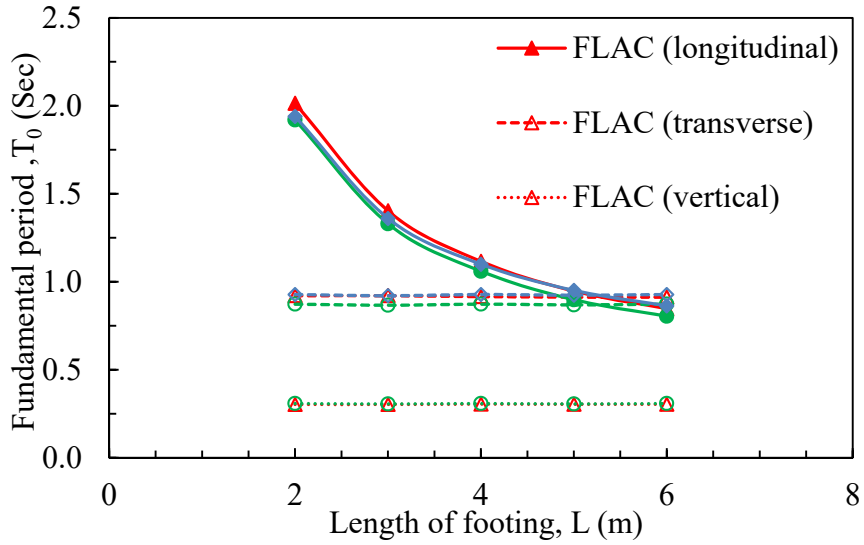

Figure 3-13. Fundamental period of rectangular prismatic shape embankment from numerical (red) and analytical methods at various length of footing for single lane bridge

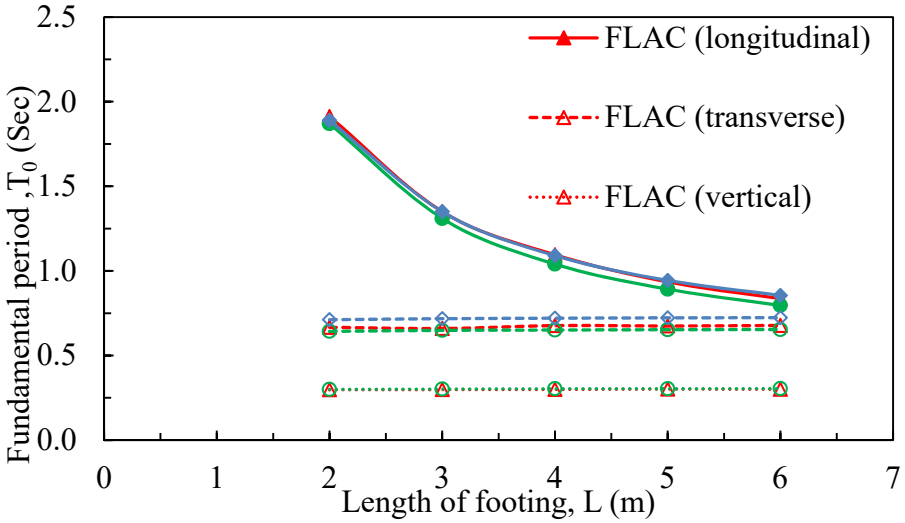

Figure 3-14. Fundamental period of rectangular prismatic shape embankment from numerical (red) and analytical methods at various length of footing for double lane bridge

Similar trends were obtained for the FLAC model for the support embankment with double lanes. In this case, the width exceeded the length in all cases, and the fundamental period was higher in the longitudinal direction for all cases. The fundamental period for the excitation along the longitudinal direction was in the range of 0.8 to 2.0 sec. The fundamental period was between 0.9 sec and 0.3 sec for excitation in the transverse and vertical directions, respectively.

The percentage of error for the different geometries modeled is presented in Table 5.4, as calculated by Eq. 3.40. The FLAC results were used as the baseline to find the percentage of error because the FLAC 3D analysis included all three stiffness (i.e., flexural, shear and axial) in the numerical formulation, which is considered to be more rigorous than some analytical formulations (see Section 3.5.3.6)

$$Percentage\ error = \frac{T_{0(Analytical)} - T_{0(FLAC)}}{T_{0(FLAC)}} 100 \qquad \textbf{(3.40)}$$

A comparison of the results suggests that in most cases, the percentage of error was smaller for larger lengths of embankment. In addition, Method II (Section 3.5.3.7.3) results were very close to the FLAC results for single lane configurations, whereas Method I (Section 3.5.3.7.1) results were close to FLAC results for double lane configurations with excitation in the transverse direction. In all cases, the percentage of error was usually less than 5 percent and always less than 10 percent.

This relatively good agreement suggests that the modeling technique is sound and either the analytical or numerical methods are generally sufficient for determining the fundamental period for rectangular prismatic embankments. However, it is recommended that Method II be used for most cases, because it includes flexural, shear and axial stiffness in its formulation. Lastly, numerical techniques are required for more complex geometrical configurations, as illustrated in the case for trapezoidal prismatic embankments, as dis.

Table 3.3. Percentage error of FLAC with Method I and Method II for single lane and double lane with various length of footing for rectangular prismatic shape embankment

	Percentage Error									
	Single Lane					Double Lane				
	Method I and FLAC			Method II and FLAC		Method I and FLAC			Method II and FLAC	
Length of Footing	Longitudinal	Transverse	Vertical	Longitudinal	Transverse	Longitudinal	Transverse	Vertical	Longitudinal	Transverse
m	*%*	*%*	*%*	*%*	*%*	*%*	*%*	*%*	*%*	*%*
2	-4.667	-5.212	1.650	-3.674	0.760	-2.197	-3.598	-1.151	-1.151	6.747
3	-5.203	-5.863	0.990	-3.065	0.000	-2.963	-1.667	1.003	0.000	8.788
4	-5.018	-4.694	0.984	-1.434	1.310	-5.023	-3.840	1.333	-0.457	6.499
5	-5.174	-4.819	0.658	0.422	1.205	-4.599	-3.259	0.662	0.963	7.111
6	-5.077	-4.381	1.316	1.889	1.643	-4.785	-3.540	1.329	2.273	6.785

3.5.3.7.7 Comparison of Analytical and Numerical Methods for Trapezoidal Rectangular Embankments

A simplified method has been proposed for evaluating the fundamental period of non-rectangular shaped prismatic embankments (Figure 3-15) (Horvath 1995). In this approach, a non-rectangular cross-section view of the embankment is converted to an equivalent rectangular prismatic embankment of equal cross-sectional area and with an equivalent top width of embankment B. This is achieved by adjusting the actual height of the embankment, H, to an adjusted H' that produces an equivalent cross sectional area.

The estimated fundamental period of trapezoidal prismatic shaped embankments for single and double lane bridge cases and for various bridge lengths and directions of excitation are shown in Figure 3-16. When the results from the analytical solution are compared with the numerical methods from FLAC using Methods I and II (Section 3.5.3.7.1 and 3.5.3.7.3, respectively), it is clear that significant differences exist between analytical and numerical methods. Because the FLAC 3D models were developed using actual cross sectional and longitudinal geometries, and because the FLAC numerical method has proven reliable for estimating the fundamental period of rectangular prismatic embankments (Section 3.5.3.7.5.1.1), it is assumed that the numerical results are more representative of the fundamental period for trapezoidal prismatic shaped embankments. Hence the results from the simplified analytical method were compared with the FLAC results in terms of differences or percentage of error using the FLAC modeling results for Methods I and II as the basis of the comparison (Table 3-4 and Figures 3-17 to 3-20).

Based on these comparisons in terms of differences or percentage of error, it is clear that the simplified analytical solution is not very reliable for estimating the fundamental period of trapezoidal prismatic shaped embankments; however the amount of error does reduce as the length of the footing increases. Lastly, from an evaluation of the two different FLAC methods (Methods I and II), it also appears to be more reasonable to consider the flexural, shear and axial stiffness (i.e., use Method II) for the numerical evaluation of the fundamental period of such embankments.

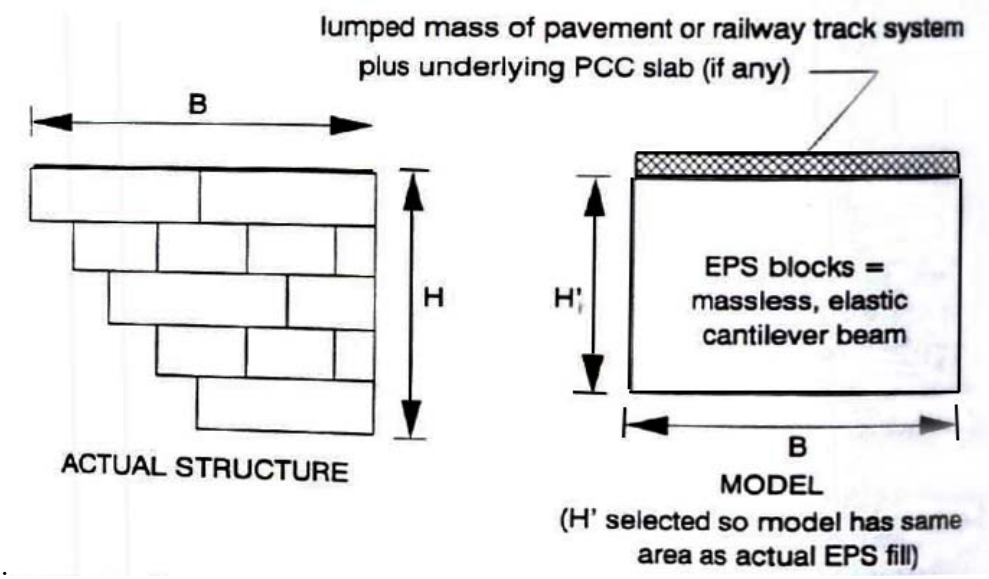

Figure 3-15 Simplified method for converting trapezoidal shape to rectangular shape (after Horvath, 1995).

Table 3.4. Percentage error of FLAC with Method I and Method II for single lane and double lane with various length of footing for trapezoidal prismatic shape embankment

	Percentage Error									
	Single Lane					Double Lane				
	Method I and FLAC			Method II and FLAC		Method I and FLAC			Method II and FLAC	
Length of Footing	Longitudinal	Tranverse	Vertical	Longitudinal	Transverse	Longitudinal	Transverse	Vertical	Longitudinal	Transverse
m	%	%	%	%	%	%	%	%	%	%
2	-23.9	-29.5	-40.2	-13.8	-25.0	-25.17	-31.9	-33.7	-15.03	-24.6
3	-19.9	-27.1	-37.7	-8.5	-22.6	-20.75	-31.0	-33.8	-9.75	-23.6
4	-17.5	-26.6	-34.7	-5.5	-20.8	-17.46	-26.7	-33.9	-5.62	-18.9
5	-14.4	-23.4	-32.1	-2.0	-18.7	-13.26	-25.0	-31.1	-0.58	-16.9
6	-12.8	-20.9	-29.1	0.3	-15.9	-12.15	-23.9	-28.2	0.83	-15.9

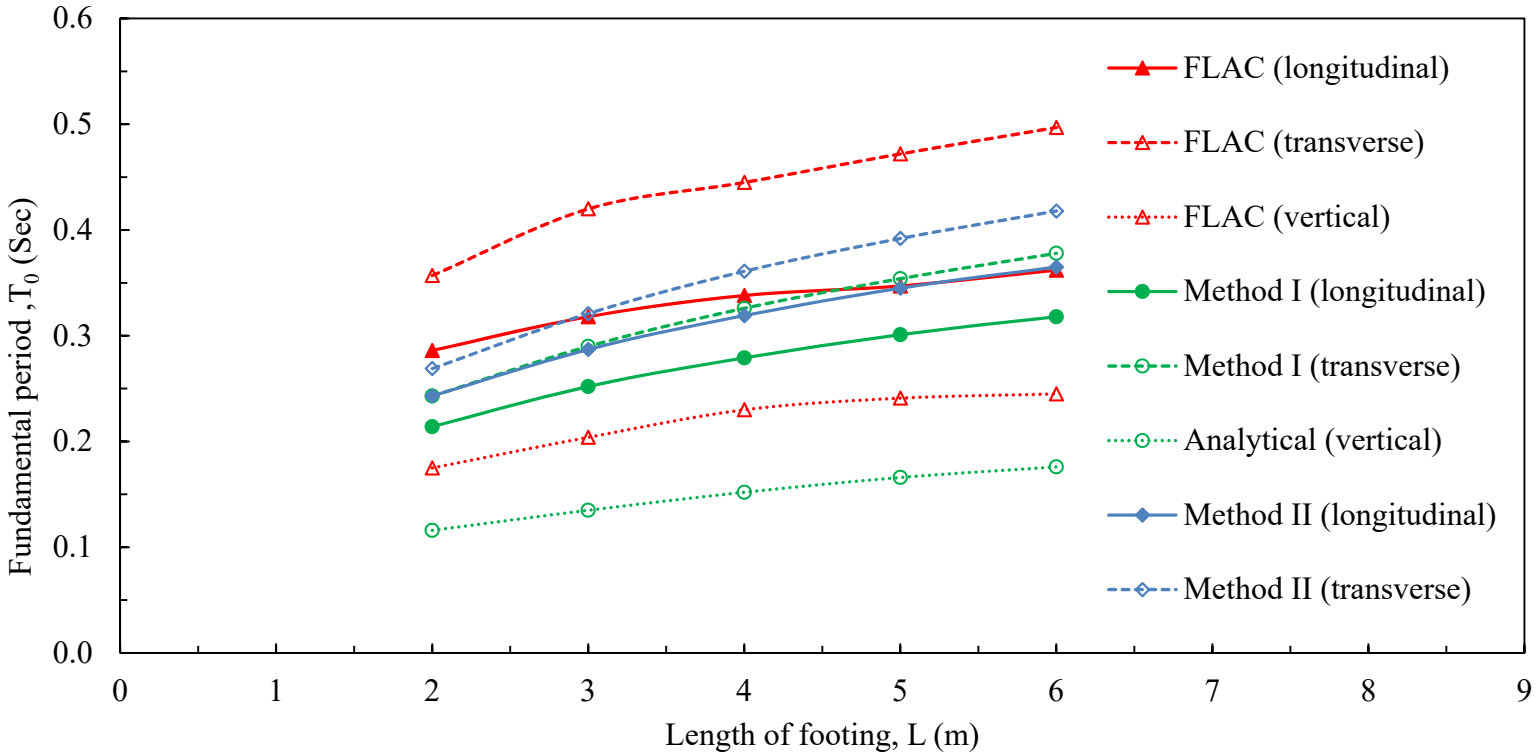

Figure 3-16 Fundamental period of trapezoidal prismatic shape embankment for double lane obtained from numerical and analytical methods for various length of footing

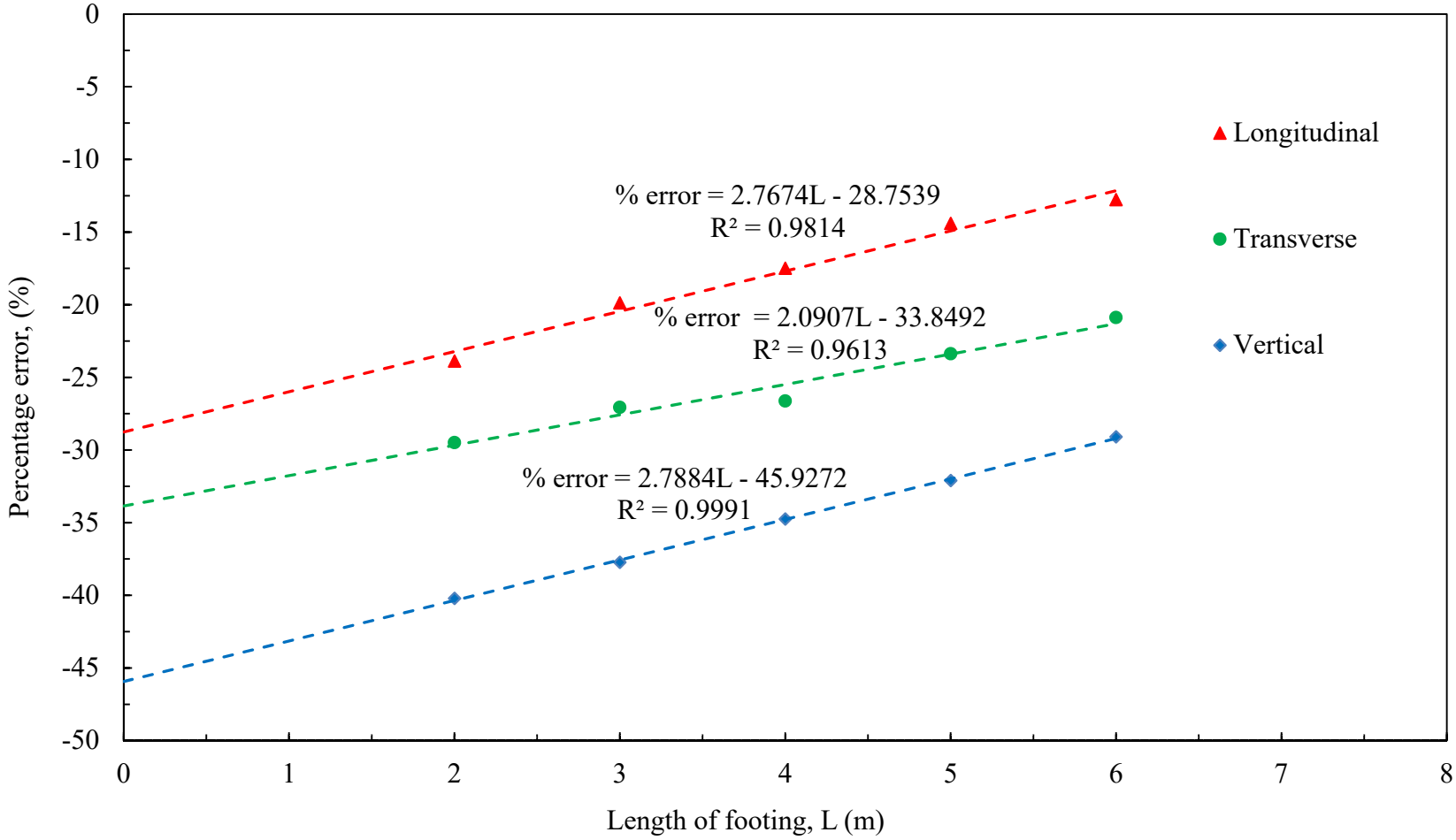

Figure 3-17 Percentage of error with length of footing for single lane between FLAC and Method I

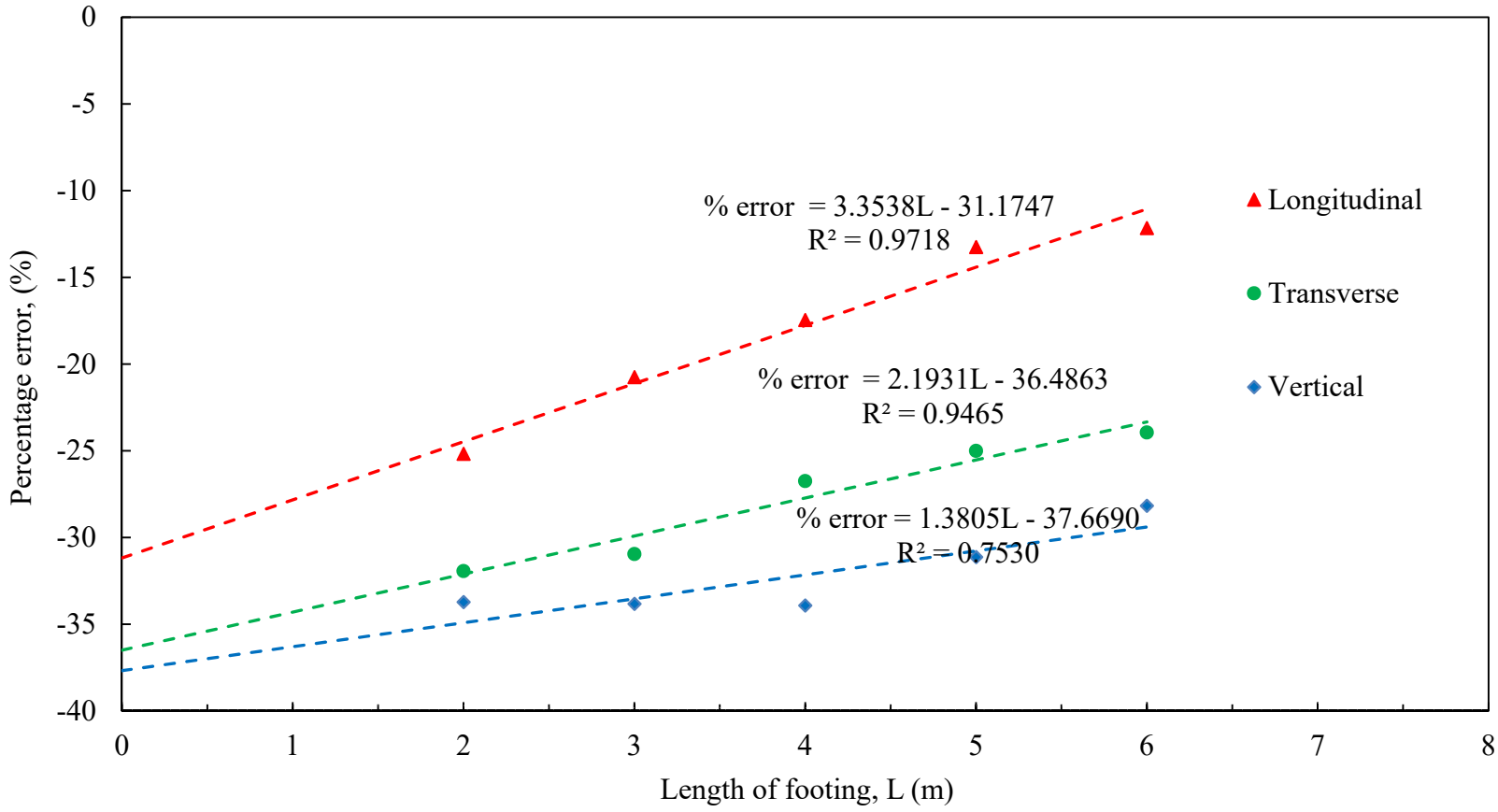

Figure 3-18. Percentage of error with length of footing for double lane between FLAC and Method I

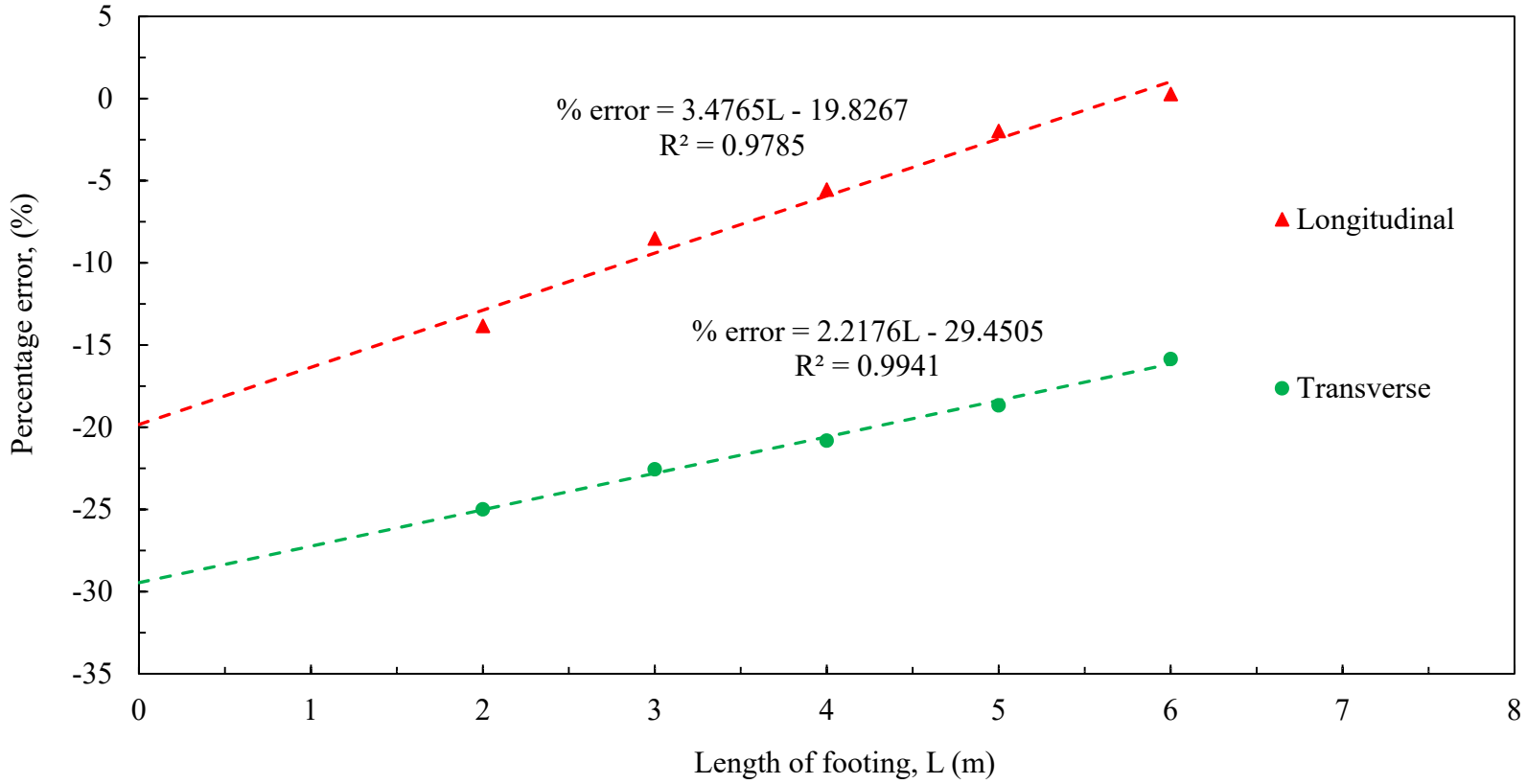

Figure 3-19. Percentage of error with length of footing for single lane between FLAC and Method II

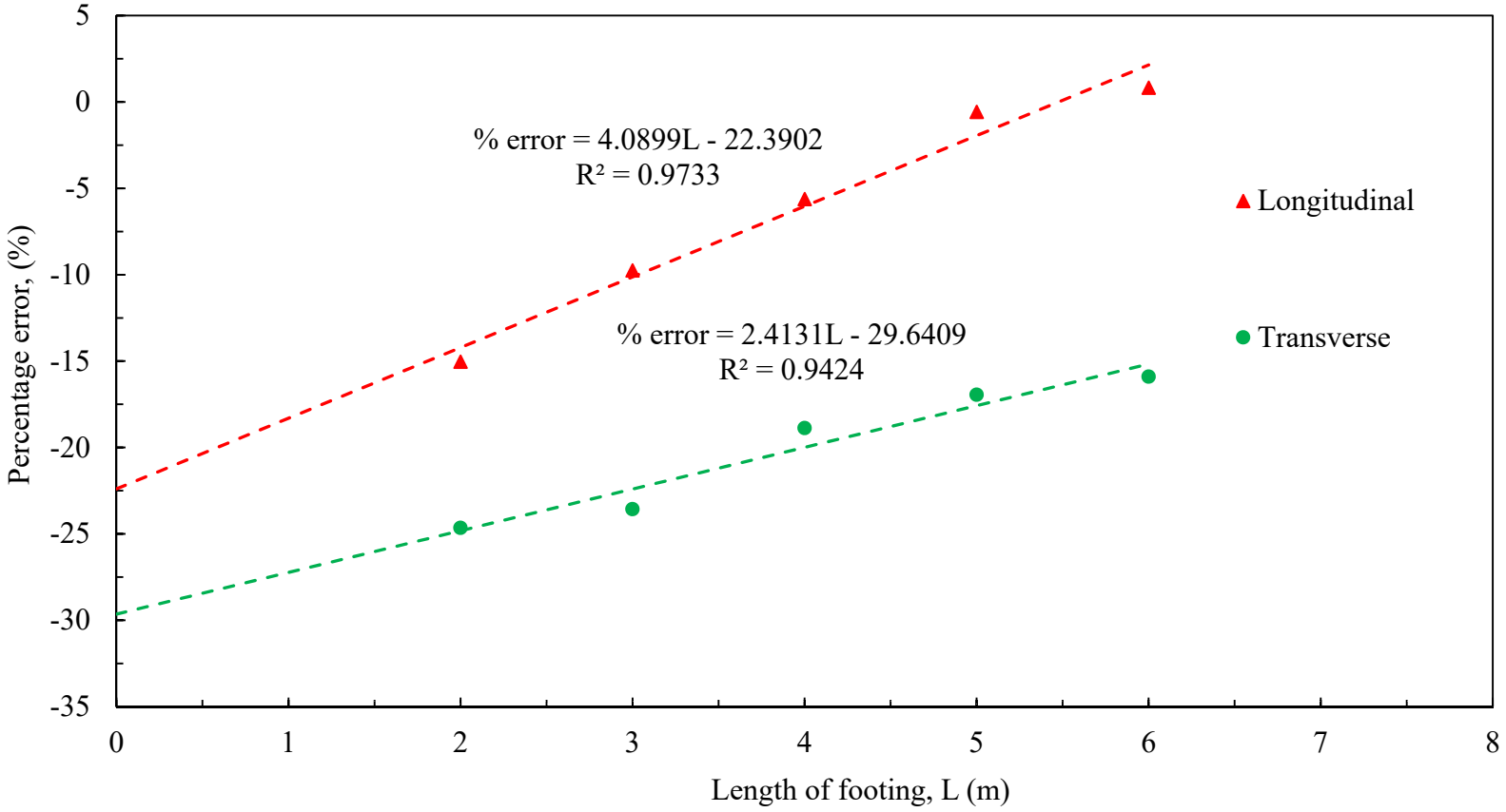

Figure 3-20. Percentage of error with length of footing for double lane between FLAC and Method II

3.5.3.7.8 Summary of Fundamental Period Evaluations

The size of the bridge and fundamental period of the EPS support embankment were evaluated for EPS densities of 22 and 29 kg/m^3. These representative densities were evaluated, but higher densities (i.e., higher modulus) EPS blocks could be used in actual bridge support system, as required. The length and width of the potential bridge was determined for various lengths of footing, and for steel and concrete bridges. The length of bridge increased with increasing EPS density and with the length of footing. A typical length for a steel bridge was about 30 m using EPS 29 combined with a 4-m long spread footing.

The fundamental period of the bridge support systems was evaluated for seismic design purposes by considering rectangular and trapezoidal prismatic shapes and by using analytical and numerical methods. For the analytical methods, the concept of Timoshenko and Gere (1972) was used for the calculation of flexural, shear and axial stiffness. The stiffness calculation of a trapezoidal prismatic shape was difficult; therefore it was converted into an equivalent-area rectangular prismatic shape to apply the analytical methods to this type of embankment. The results of analytical method were compared with numerical results. The results from analytical methods for rectangular prismatic shapes were very close to the numerical results. The differences for the estimated values were within 10 percent for the analytical and numerical methods. For these cases, the fundamental period in the longitudinal direction varied from about 0.8 - 2.0 sec, depending on the length of the bridge support system. The fundamental period for excitation in the transverse and vertical directions was about 0.9 sec and 0.3 s, respectively for the typical width and height ratio that was evaluated.

The percentage difference between the two methods was much greater for trapezoidal prismatic shaped embankments because an adjusted "equivalent" rectangular prism was used instead of the actual geometry. The fundamental periods were in the range of 0.2-0.4 sec, 0.2-0.5 sec and 0.1-0.3 sec for excitation along the longitudinal, transverse and vertical directions, respectively. However, it is concluded that numerical methods are required to evaluate the fundamental period of the support system for this more complex geometry.

3.5.3.8 Interlayer and Basal Sliding Evaluations

3.5.3.8.1.1 General Considerations

Because EPS geofoam is an extremely light weight material, its weight is often neglected when calculating inertial forces for seismic evaluations. In addition, AASHTO (2012) describes the requirements for determining the horizontal and vertical acceleration coefficients, kh and kv, respectively, for retaining wall design.
"In most situations, vertical and horizontal acceleration are at least partially out of phase. Therefore, kv is usually rather small when kh is near its maximum value. The typical assumption is to assume that kv is zero for wall design (AASHTO, 2012)."

Similarly, NCHRP 529 and Web Document 65 do not include the vertical component of acceleration in the evaluation methodology for interlayer and basal sliding for seismic events. Nonetheless, more rigorous dynamic numerical analyses regarding the potential for interlayer sliding between EPS block for rectangular prismatic embankments (i.e., free-standing vertical embankments) have been carried out by Bartlett and Lawton (2008) and by Amini (2014). These evaluation used preselected earthquake time histories and simple sinusoidal motion that included both horizontal and vertical components of the strong ground motion.

The work of Bartlett and Lawton (2008) suggests that the amount of interlayer sliding can, in some cases, increase when the vertical component of strong motion is included in the numerical analysis. They found that for cases where interlayer sliding was just initiating in the model, the sliding displacement increased by a factor of 2 to 5 times when the vertical component of strong motion was added to the analyses. However, when the interlayer sliding displacements were larger, the presence of the vertical component in the model was less important and the displacements remained about the same or only slightly increased. These authors concludes that it is generally unconservative to ignore the vertical component of strong motion when estimating the amount of sliding displacement, but its inclusion is less important when the interlayer sliding displacement is well developed. All models used by Bartlett and Lawton (2008) showed the interlayer sliding was generally concentrated in the basal layers of the EPS embankment and diminishes greatly in the upper layers.

The results of interlayer sliding numerical analyses conducted by Amini (2014) on rectangular prismatic EPS embankment showed that relative horizontal movement between EPS block layers occurred relatively early in the analysis along horizontal interfaces when the model was executed in the elastic mode. This relative horizontal movement was generally initiated at the lowermost interlayer and propagated upwards to the top of the embankment. However, relative movement at the interfaces appeared to be a very efficient energy dissipating mechanism. Not only did it decrease the extent of sliding with time, but also once initiated, it isolated the higher levels from large accelerations and displacements associated with these accelerations. This effect was mostly observed when the model was excited with only horizontal seismic forces.

Amini (2014) found that the addition of the vertical component of input motion produced larger values of interlayer sliding when compared to those obtained with only the horizontal acceleration present for the majority of cases. Only at very high amplitudes (i.e., 1 g), did the vertical component of seismic motion appear not to have altered the maximum amount of sliding (Figure 3-21). Therefore, it was concluded that disregarding the vertical component of the input motion did not appear to be conservative in predicting both the maximum amount of sliding displacement and its location in the embankment for high levels of input acceleration.

Hence, for site-specific evaluations and/or more detailed studies, the displacement-based modeling and evaluations discussed in Bartlett and Lawton (2008) and Amini (2014) could be useful for evaluating the sliding performance of free-standing EPS embankment systems. However for simplicity sake, and because of the preliminary, exploratory nature of this research, this report focuses on simple and routine force-based evaluation methods instead of displacement-based methods to evaluate sliding. This is done because force-based methods are more widely applied in engineering practice and because the validation and experience with displacement-based methods for evaluating EPS systems is still in development. Hence, this approach is consistent with method of determining an appropriate kh value for design and neglecting the kv value as done in routine design practice of retaining wall systems (AASHTO (2012).

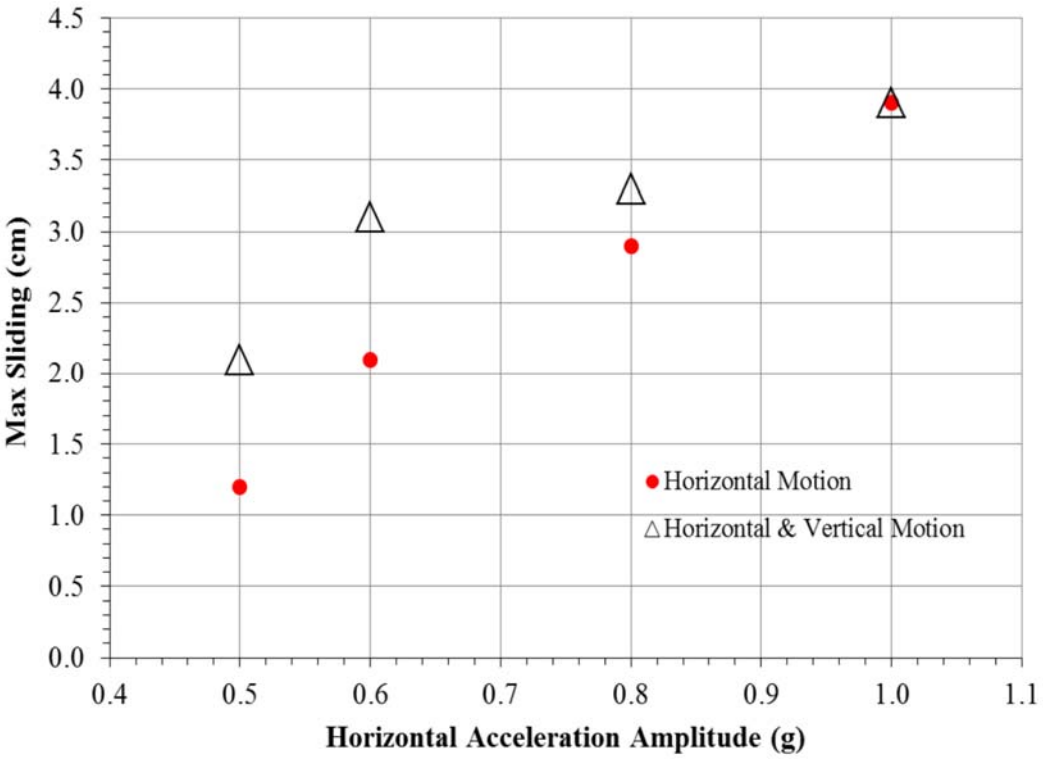

Figure 3-21 Comparison of maximum sliding extents in two cases of only horizontal and both horizontal and vertical harmonic input motion at varying acceleration amplitudes.

3.5.3.8.1.2 Methodology

For implementation of force-based methods, the initial input is the peak horizontal acceleration at the fundamental frequency of the EPS support embankment. This input is usually obtained from a design horizontal acceleration response spectrum developed for the project site and soil conditions. The sliding evaluations discussed subsequently are based on evaluating the harmonic response of the EPS bridge support system at its fundamental period. This information is used to determine the critical acceleration associated with that response (Section 3.5.3.4). The critical horizontal acceleration (g) is the value which produces a factor of safety against sliding equal to unity for the horizontal mode of excitation.

The dynamic response of rectangular and trapezoidal prismatic shape embankments will be analyzed in a similar manner. The potential sliding surfaces were assumed to be horizontal and continuous throughout the EPS mass, as is commonly the case for typical EPS embankment construction. No vertical joints or interfaces were included in the evaluation, nor were mechanical fasteners (i.e., gripper plates) or other mechanisms included as resistance to sliding. The frictional resisting force at the geofoam-geofoam and geofoam-soil interfaces was calculated from the normal (i.e., vertical) stress and the respective coefficients of friction for these interfaces. The geofoam-geofoam and geofoam-soil internal friction was calculated from of the work Sheeley and Negussey (2001).

For rectangular prismatic shaped embankments, the vertical stress was considered constant with depth within the EPS embankment part of the system. For trapezoidal prismatic shaped embankments, the vertical stress redistribution was considered to be 2V:1H. So, the vertical stress

concentration was different on each layer and diminishing with depth below the bridge foundation. This stress distribution was calculated from the following relationship:

$$\sigma_z = \frac{\sigma_v L_{top} B}{\left[L_{top} + (n-1)\Delta z\right] B} \tag{3.41}$$

where: σ_z is stress at any depth, σ_v is stress at the top of embankment, n is the number of layers measured from top, L_{top} is the length of trapezoidal footing at the top of embankment, Δz is the thickness of each layer and B is the width of embankment.

In this study, the EPS embedment depth below the ground surface was assumed to be 1.5 m, or less, and surrounded by well-compacted, free-draining, granular soil. According to AASHTO (2012) for such depth, the passive pressure that develops on the leading edge of the buried embankment should be calculated using the static methods. For the trailing side, the active earth pressure was also calculated from static methods using Coulomb's Theory. The active earth pressure coefficient (K_{AE}) was calculated from Eq. (3.42).

$$K_{AE} = \frac{cos^2(\varphi - \beta)}{cos^2\beta\cos(\delta + \beta)\left[1 + \sqrt{\frac{\sin(\varphi + \delta)\sin(\varphi - i)}{\cos(\delta + \beta)\cos(i - \beta)}}\right]^2} \tag{3.42}$$

where: φ is the soil backfill friction angle, i is the backfill slope angle, K_{AE} is the seismic active earth pressure coefficient, δ is the soil-EPS interface friction angle and β is the slope of EPS embankment relative to the vertical.

The seismic passive earth pressure coefficient was calculated using the static method mentioned in AASHTO (2012). The coefficient of passive pressure (K_P) was determined from the plot reported in AASHTO. In this plot, K_P was the relation between φ and the angle of back face of wall to the horizontal (θ). The reduction factor (R) was calculated according to the ratio of δ to φ and φ. The corrected value was the simple product of K_P and R. The active and passive force was then calculated by using Eqs (3.43) and (3.44) respectively.

$$P_{AE} = \frac{1}{2} K_{AE} \gamma D^2 B \tag{3.43}$$

where: γ is the unit weight of soil, D is depth of embedment, B is the width of embankment.

$$P_{PE} = \frac{1}{2} K_{PE} \gamma D^2 B \tag{3.44}$$

where: K_{PE} is the seismic passive earth pressure coefficient.

Once the seismic active and passive earth pressure were calculated, the resisting and driving forces were obtained. The resisting force was calculated as the combination of the horizontal component of the passive force developed along the leading edge of the embedded EPS mass and the basal frictional force. The frictional force was calculated as the product of the normal force and the tangent of the friction angle of the foundation soil. The driving force was calculated as the sum of the inertial force and the horizontal component of the active force developed along the trailing edge of the embedded EPS mass. The factor of safety against sliding was calculated as the ratio of the resisting forces to the driving forces. The factor safety against sliding due to excitation in both the transverse and longitudinal embankment directions was subsequently determined.

3.5.3.8.1.3 Counter Measures for Interlayer Sliding

One simple method to prevent interlayer sliding is the use of shear keys that are made during placement of the EPS block during the time of construction (Amini, 2014). Shear keys are half-height EPS blocks placed within the EPS mass which interrupt the formation of continuous horizontal slide planes that may develop between the layers during high levels of seismic excitation. The shear key resistance is calculated in terms of percentage of coverage within each layer and provides an additional cohesive resisting force in addition to sliding. The cohesive resisting force per unit area is the product of the peak geofoam shear strength and the area of shear key coverage within each layer (Amini, 2014).

The peak geofoam shear strength used to evaluate the shear key resistance should be obtained from laboratory tests on the specific density of EPS planned for the project. The direct shear test is a commonly used test for shear strength determinations, but it is more suitable for the evaluation of frictional interface shear resistance of relatively rigid bodies. However, because EPS is a flexible material and develops non-uniform stress concentrations during direct shear, a more appropriate method for determining the shear resistance is the direct simple shear (DSS) apparatus. However, values of shear strength from the DSS test were unavailable at the time of this evaluation, hence the shear strength of EPS used was based on ASTM (2010) as mentioned in BenchmarkFoam (2009). In this method, a punch type shear tool is used for determining the shear strength. The specimen is clamped during the test and the punching tool is pushed through the specimen. The shear strength is then calculated by dividing the load required to shear the specimen by the area of sheared edge.

3.5.3.8.1.4 Sliding Evaluation Results

The critical acceleration for single lane and double lane bridges with various lengths of footing for rectangular and trapezoidal prismatic shape EPS embankment was calculated (Table 3.5). In this evaluation, simplified analytical techniques like shear keys and 1.0 to 1.4 m embedment at the base of the EPS embankment were evaluated to reduce the sliding potential. The shear keys were evaluated as a preventative means between the EPS interlayers where the factor of safety against sliding was less than 1.1 as obtained from initial analyses. Subsequently, interlayer sliding was inhibited by using an adequate percentage of shear key coverage in the layer(s) where the calculated factor of safety was less than the minimum 1.1. Similarly, the embankment was embedded where the factor of safety was less than 1.1. In these cases, the passive earth pressure on the leading edge of the embedded EPS blocks was used to provide additional sliding resistance.

Table 3.5. Summary of critical acceleration for rectangular and trapezoidal prismatic shape embankments

	Critical acceleration for single lane		Critical acceleration for double lane	
Footing length	Rectangular	Trapezoidal	Rectangular	Trapezoidal
M	g	g	G	g
2	0.6	0.6	0.6	0.6
4	0.6	0.6	0.6	0.6
6	0.6	0.6	0.6	0.6

The depth of embedment and shear key coverage varied according to the embankment size. Shear key and embedment requirements for double lane bridges with 4-m long footings for EPS 22 and 29 is given in Appendix F for the longitudinal and transverse directions. In these calculations, it was shown that shear keys were not required to prevent interlayer sliding for horizontal accelerations of less than or equal to 0.8 g. For horizontal accelerations higher than 0.8 g, some shear key coverage was required within the EPS mass. The calculation for shear key coverage and factor of safety against sliding for 1.0 g is shown in Appendix F. A shear key coverage of 8 percent of the layer area is recommended for a horizontal acceleration of 1.0 g.

For non-embedded embankments, basal sliding begins at about 0.6 g for rectangular and trapezoidal prismatic embankments. The required depths of embedment for trapezoidal and rectangular prismatic shape embankments for a horizontal acceleration of 1.0 g were found to be about 1.0 m and 1.4 m, respectively (Appendix F). In the case of the trapezoidal prismatic shape, the factor of safety was higher when the system was excited along the transverse-direction. As the dimension of embankment became larger, the factor of safety became higher. For the rectangular prismatic shape case, the factor of safety against basal sliding was higher when it was excited along the longitudinal-direction because the dimension of resisting side was larger in this direction.
Lastly, because a 1.0 g horizontal acceleration is extreme value of excitation in most cases, and is not likely to be exceeded, the recommended depth of embedment of about 1.5 m should be sufficient for seismic stability of EPS bridge support systems.

3.5.3.8.1.5 Summary and Recommendations for Sliding

In many cases, the critical acceleration corresponding to sliding and potential countermeasures against sliding can be evaluated by using analytical methods; however more detailed numerical evaluations may be required for unusual conditions or case where the EPS embankment geometries differ significantly than those presented in this report.

Two densities of EPS were evaluated (i.e., EPS22 and EPS29) for the bridge support system and for potential sliding under seismic excitation. These, or even higher densities of EPS may be required, because the dead and live loads for bridge support system are much greater than those experienced by routine EPS embankments used solely for pavement support.
The critical acceleration for sliding for rectangular prismatic and trapezoidal prismatic embankments was found to be about 0.6 g for both cases. The interlayer sliding did not occur for

the acceleration of less than or equal to 0.8 g; whereas basal sliding occurred for values that exceeded 0.6 g.

The inclusion of shear keys and basal embedment were evaluated as mechanisms to prevent interlayer and basal sliding. For a horizontal excitation level of 1.0 g, the required shear key coverage was 8 percent and an embedment depth of 1.4 m was required to achieve sliding stability. Due to the differences in the dead and live loadings, it is also recommended that a floating reinforced concrete approach slab be constructed between the footing of bridge footings and the pavement section to overcome the effects of possible differential settlement at this location.

3.5.3.9 Methods for Evaluating Horizontal Sway and Rocking

3.5.3.9.1 Analytical Evaluations of Fundamental Period

The fundamental period for sway mainly depends on the mass and stiffness of the EPS system. The fundamental period of sway is related to shear stiffness whereas rocking is related to shear, flexural and axial stiffness. The fundamental period for horizontal sway was calculated using both numerical and analytical approaches. Timoshinko's beam theory and FLAC 3D were used for these approaches, respectively.

3.5.3.9.1.1 Sway Fundamental Period Based on Shear Stiffness

For the sway mode, the fundamental period was calculated by considering only shear from the basic equation of a SDOF system. The fundamental period of any SDOF system is:

$$T_0 = 2\pi \left[m \left(\frac{1}{k} \right) \right]^{0.5} \tag{3.45}$$

where: k is the spring stiffness of the SDOF system and m is the mass of the SDOF system. Eq. (6.1) in terms of weight W is:

$$T_0 = 2\pi \left[\left(\frac{W}{g} \right) \left(\frac{1}{k} \right) \right]^{0.5} \tag{3.46}$$

where: W is the weight of the SDOF system. For a fixed-end cantilever beam with transverse concentrated force (P) at the free end and the maximum transverse displacement (Δ), the stiffness is defined by:

$$k = \frac{P}{\Delta} \tag{3.47}$$

According to Timoshenko and Gere (1972), shear deflection at the free end is:

$$\Delta_S = \alpha_S \frac{PL}{GA} \tag{3.48}$$

where: α_s is the shear coefficient used to get shear stress at centroid, G is the shear modulus of the beam material, A is the beam cross-sectional area and L is the length of beam. According to Cowper (1966), the shear coefficient for solid rectangular section is:

$$\alpha_S = \frac{12 + 11\nu}{10(1 + \nu)} \tag{3.49}$$

$$k_S = \frac{P}{\Delta_S} = \frac{GA}{\alpha_S L} = \frac{10(1 + \nu)GA}{(12 + 11\nu)L} \tag{3.50}$$

$$\frac{1}{k_S} = \frac{(12 + 11\nu)L}{10(1 + \nu)GA} \tag{3.51}$$

For a linear elastic material:

$$G = \frac{E}{2(1 + \nu)} \tag{3.52}$$

where: E is the Young's modulus of the material, ν is Poisson's ratio of the material. Replacing L by H, E by E_{ti} and G by relation with E in Eq. (3.51),

$$\frac{1}{k_S} = \frac{(12 + 11\nu)2H(1 + \nu)}{10(1 + \nu)E_{ti}A} = \frac{H(12 + 11\nu)}{5E_{ti}LB} \tag{3.53}$$

For the EPS geofoam embankment, E equals to E_{ti} is initial tangent Young's modulus of EPS and L equal to H is the height of embankment. Substituting the reciprocal of k_s in Eq. (3.46) by replacing k with k_s,

$$T_0 = 2\pi \left[\left(\frac{W}{g} \right) \left(\frac{H(12 + 11\nu)}{5E_{ti}LB} \right) \right]^{0.5} \tag{3.54}$$

$$T_0 = 2\pi \left\{ \left[\frac{\sigma'_{v0}H}{E_{ti}g} \right] \left[\frac{(12 + 11\nu)}{5} \right] \right\}^{0.5} \tag{3.55}$$

where: σ'_{v0} is vertical effective stress at the top acting on the top of the EPS. Eq. (3.55) reveals that the fundamental period depends on σ'_{v0}, H, ν, E_{ti} and these parameters are independent with

direction of excitation. It means that fundamental period remains same for excitation along longitudinal and transverse directions.

3.5.3.9.1.2 Rocking Fundamental Period Based on Flexural, Shear and Axial Stiffness

For the rocking mode, the fundamental period was calculated considering flexural, shear and axial stiffness. This was done because the results obtained with these stiffness included provided the best match when compared with numerical results obtained from FLAC modeling. The value obtained for the fundamental period depends on the direction of excitation because the moment of inertia is different in each direction.
For excitation in the longitudinal-direction, the following applies:

$$T_0 = 2\pi \left\{ \left[\frac{\sigma'_{v0} H}{E_{ti} g} \right] \left[4 \left(\frac{H}{B} \right)^2 + \frac{(12 + 11\nu)}{5} + 1 \right] \right\}^{0.5} \quad \textbf{(3.56)}$$

For excitation along the transverse-direction, the following applies:

$$\mathrm{T_0} = 2\pi \left\{ \left[\frac{\sigma'_{v0} \mathrm{H}}{\mathrm{E_{ti} g}} \right] \left[4 \left(\frac{\mathrm{H}}{\mathrm{L}} \right)^2 + \frac{(12 + 11\nu)}{5} + 1 \right] \right\}^{0.5} \quad \textbf{(3.57)}$$

where: L is the length of embankment, B is the width of embankment.

For excitation in the vertical-direction, the following applies:

$$T_0 = 2\pi \left[\frac{\sigma'_{v0} H}{E_{ti} g} \right]^{0.5} \quad \textbf{(3.58)}$$

3.5.3.9.2 Numerical Evaluation of Fundamental Period for Sway

For the numerical evaluation of the sway mode, a FLAC model with lengths of footing varying between 2 m to 6 m and for single and double lane bridges with a height of 6 m were chosen. A typical model for 4-m long and 6-m high embankment is shown in Figure 3-22. In this figure, the dark red color represents the foundation for bridge and the light red color is the EPS embankment. The material properties used in this model for the EPS embankment is shown in Table 3-6.

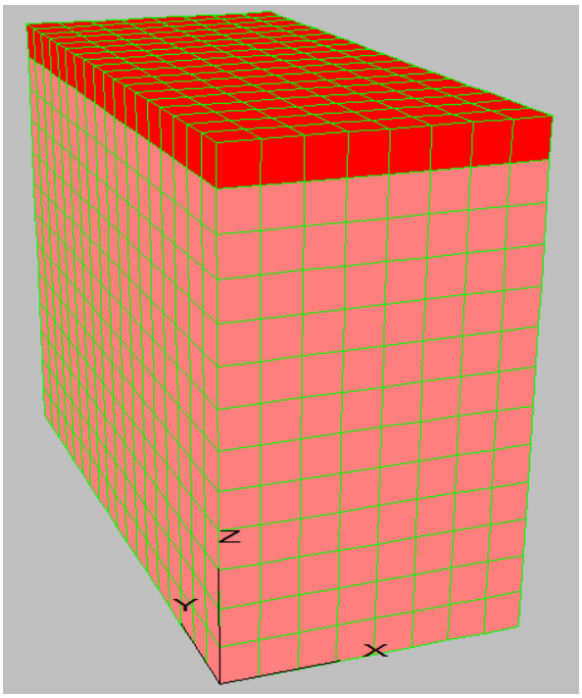

Figure 3-22. EPS geofoam embankment system

Table 3.6. Material properties of EPS geofoam embankment system for sway mode

Material	ρ	E	□	G	K
----------	kg/m^3	MPa	----------	MPa	MPa
EPS	34.02	12.55	0.19	5.26	6.81
Concrete	2400.00	29557.00	0.18	12523.00	15394.00

The EPS embankment was modeled as a coherent mass that included no interface nodes between the EPS layers. The basal boundary was fixed in the direction perpendicular to the applied excitation. For example, the transverse direction was fixed when the model was excited in the longitudinal direction, and a free-field boundary was used on the side of the model. In this case, the free field motion was enforced in such a way that the side boundaries retained their non-reflecting properties so that the outward waves originating from the EPS were absorbed. The side boundaries of the main grid were coupled with a free-field grid by using dashpots as described in Itasca (2006). The dynamic input was applied as a velocity time history at the base. The resulting waves were assigned in two ways to cause either a free vibration or a forced vibration of the EPS mass.

A trial and error method was used to determine the fundamental period in the case of forced vibration. For free vibration, a pulse load was applied at the base and the displacement versus time was plotted for the top node. The elapsed time required to complete one cycle was taken to be the fundamental period using that part of the response where the initial pulse vibration had muted. The free vibration method for determining the fundamental period was found to be less time consuming, so this method was applied for the remainder of the evaluations. The fundamental period of

embankment using both free and force vibration are shown in Figures 3-23 and 3-24. The fundamental period of the embankment was found to be 0.472 sec for this case.

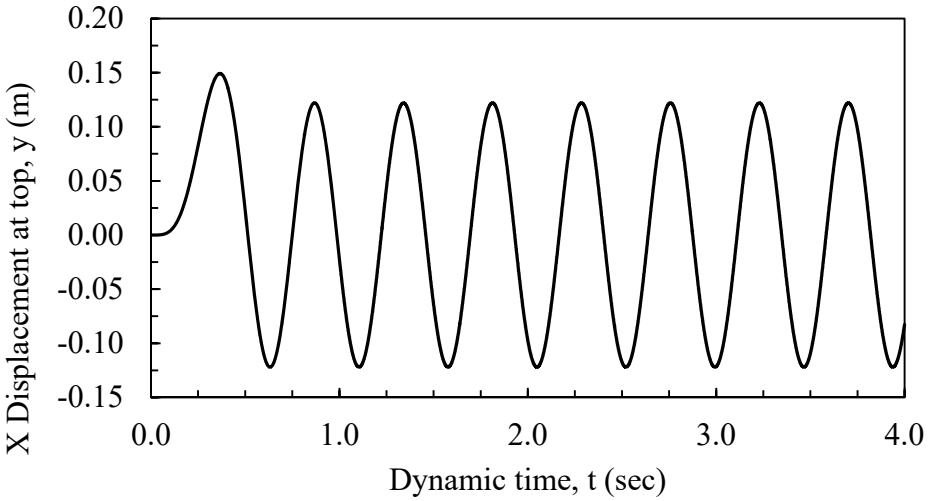

Figure 3-23. Displacement versus dynamic time at top node under free vibration for excitation in the longitudinal direction

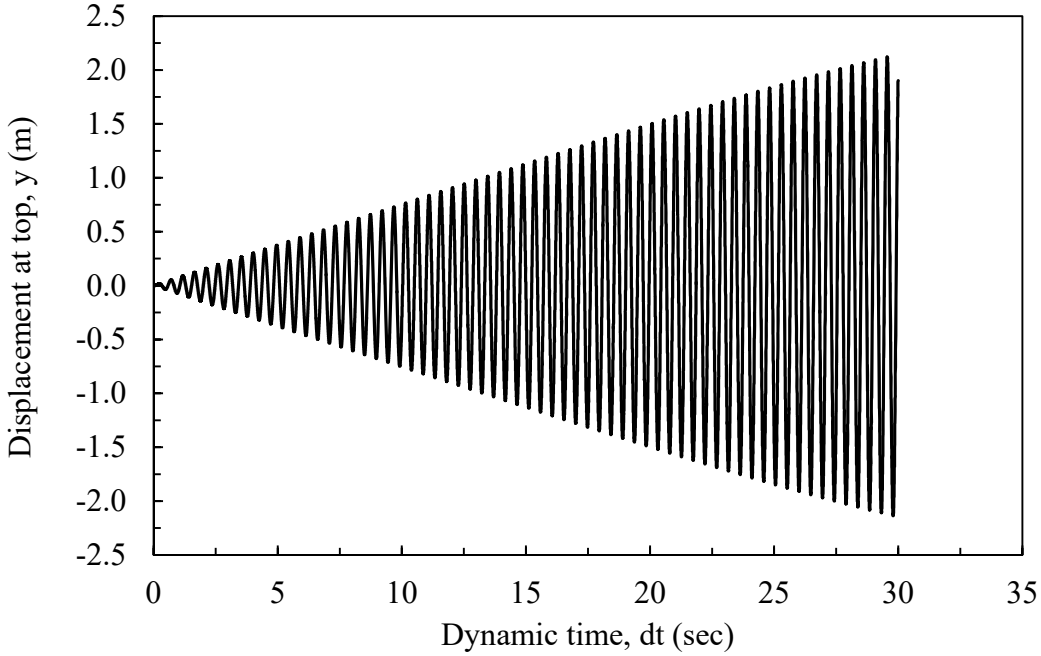

Figure 3-24. Displacement versus time at top node under force vibration for excitation in the longitudinal direction

For the rocking mode, the same FLAC model with free vibration was used for determining the fundamental period. However, the vertical sides of the EPS embankment system had no boundary condition applied along the sides. The velocity history was applied at the base of the model as a vertical velocity input, and the excitation was also applied in the longitudinal and transverse directions.

3.5.3.9.2.1 Model Development and Material Properties

3.5.3.9.2.1.1 Sway Mode Model Development

For the numerical evaluation of the sway mode, the FLAC model shown in Figure 3.22 was also used. The material properties used in this model were the same as the properties shown in Table 3.6. The base was fixed in all directions to establish the static condition. Gravity was turned on in the model, and static equilibrium was achieved. Following this, the boundary conditions of the model were changed for the dynamic simulation. The basal nodes of the model were changed to the fixed condition in all directions other than the direction where the dynamic input motion was applied. Free-field boundaries were applied on the vertical sides of the model. The horizontal harmonic motion at various amplitudes such as: 0.2 g, 0.3 g, 0.4 g, 0.5 g, and 0.6 g were introduced at the fundamental period along the longitudinal and transverse-direction in separate simulations. The shear and vertical stresses were calculated at various zones of the model to check for potential overstressing of the EPS due to excitation.

For these simulations, two percent Rayleigh damping was applied at the fundamental period of the embankment for the sway mode. This amount of damping was selected based on the work Athanasopoulos et al. (1999). These authors conducted laboratory tests on EPS geofoam specimens under zero confining pressure in torsional resonant column tests and cyclic uniaxial tests. The test results showed the upper bound value of damping in the resonant column and lower bound value of damping in the cyclic uniaxial test to be about 2 percent at 2 percent cyclic shear strain.

3.5.3.9.2.1.2 Rocking Mode Model Development

For the rocking and uplift evaluations, an interface was introduced between the basal EPS layer and the underlying soil (Figure 3.25). In this figureFigure 3-25, the red, green and blue colors represent the foundation for the bridge, EPS embankment and foundation soil, respectively in the FLAC model. The elastic material properties for this model are shown in Table 3.7.
Previous modeling experience has shown that exciting the rocking mode of the embankment is difficult when basal sliding is also allowed (Bartlett and Lawton, 2008; Housner, 1963). Hence to induce the rocking mode, the coefficient of friction at the interface between the foundation soil and basal layer of EPS was assigned a very high value (i.e., 89 degrees) such that sliding would be inhibited.

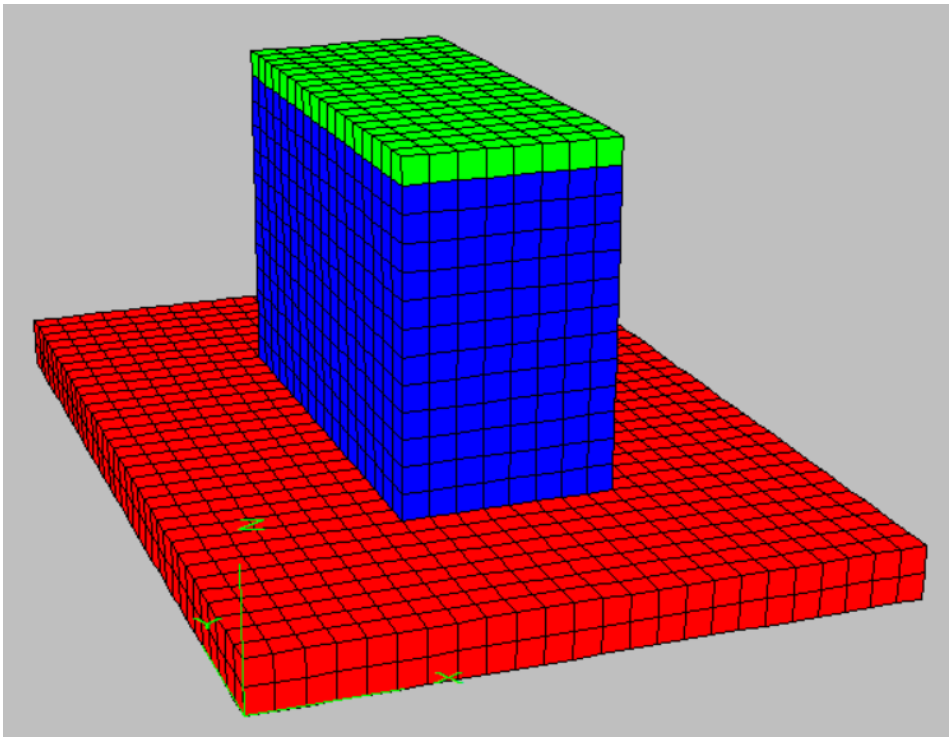

Figure 3-25. EPS embankment with soil and foundation of bridge

Table 3.7. EPS geofoam embankment system material properties for rocking mode

Material	ρ	E	□	G	K
----------	kg/m^3	MPa	----------	MPa	MPa
EPS	34.2	12.55	0.19	5.26	6.81
Concrete	2400.00	29557.00	0.18	12523.00	15394.00
Soil	1900.00	20.00	0.40	7.14	33.33

The FLAC 3D manual (Itasca, 2006) recommends that the normal spring stiffness k_n and shear stiffness k_s values for the interface be set to ten times the stiffness of the neighboring zone.

$$k_n = k_s = 10\left[\left(\frac{K + \frac{4}{3}G}{\Delta z_{min}}\right)\right] \quad \textbf{(3.59)}$$

where: K is the bulk modulus, G is the shear modulus, Δz_{min} is the smallest width of the adjoining zone in the normal direction.

However, Amini (2014) compared the acceleration response of embankment with no interface and interfaces. Amini (2014) recommended that the shear and normal stiffness values be set to at least fifty times the stiffness of the neighboring zone so as not to affect the dynamic response of the system when compared with a similar model having no interface nodes. Thus, the recommendation

provided by Amini (2014) was used in this study. The final equation for k_n and k_s is given in Eq. (3.60).

$$k_n = k_s = 50\left[\left(\frac{K + \frac{4}{3}G}{\Delta z_{min}}\right)\right] \quad \textbf{(3.60)}$$

However, if the material on one side of the interface is much stiffer than the other, then Eq. (3.60) is applied using the material properties of the softer side (Itasca, 2006). In this case, the deformability of the interface was dominated by the soft side, which is the geofoam. Hence, the geofoam properties were used to calculate the normal and shear stiffness at the interface. The detail calculation is shown in Appendix D.

A fixed boundary was applied at the base of the model for all directions. The vertical sides of the model were kept free while solving for the static condition. Once static equilibrium was reached, the bottom boundary was the same as the dynamic condition. Two percent Rayleigh damping was applied for EPS material at the fundamental period of embankment. The horizontal harmonic motion for various amplitudes namely: 0.2, 0.3, 0.4, 0.5 and 0.6 g were introduced at the fundamental periods for the following cases: (1) longitudinal-direction, (2) longitudinal and transverse-directions, and (3) longitudinal, transverse and vertical-directions at the top of the model. The shear and normal stresses were queried for the basal corner zones of the EPS embankment. Also, the relative vertical displacements were calculated at the corner grid points at the base of the embankment. A 0.15-g harmonic vertical motion was also applied in conjunction with the longitudinal-direction to check for rocking/uplift behavior in the initial analyses.

For the final rocking analyses, the inputted horizontal amplitudes along the longitudinal and transverse-directions were the same; whereas the vertical harmonic motion amplitude was assumed as 70 percent of the horizontal motion amplitude according to ASCE (2005). According to this guidance, the ratio of vertical to horizontal spectral ordinates can be taken as at least unity for frequencies higher than 5 Hz, 2/3 for frequencies below 3 Hz, and a transition from 2/3 to 1 for frequencies between 3 Hz and 5 Hz. In this study, the frequency was chosen in between 3 Hz and 5 Hz and the vertical motion amplitude was taken as 70 percent of the horizontal value.

3.5.3.9.3 Comparison of Methods For Estimating Fundamental Period

3.5.3.9.3.1 Sway Mode

The fundamental period results for the sway mode obtained from analytical and FLAC modeling for the single and double lane case of rectangular prismatic embankments for various bridge footing lengths are shown in Figures 3.26 and 3.27, respectively.

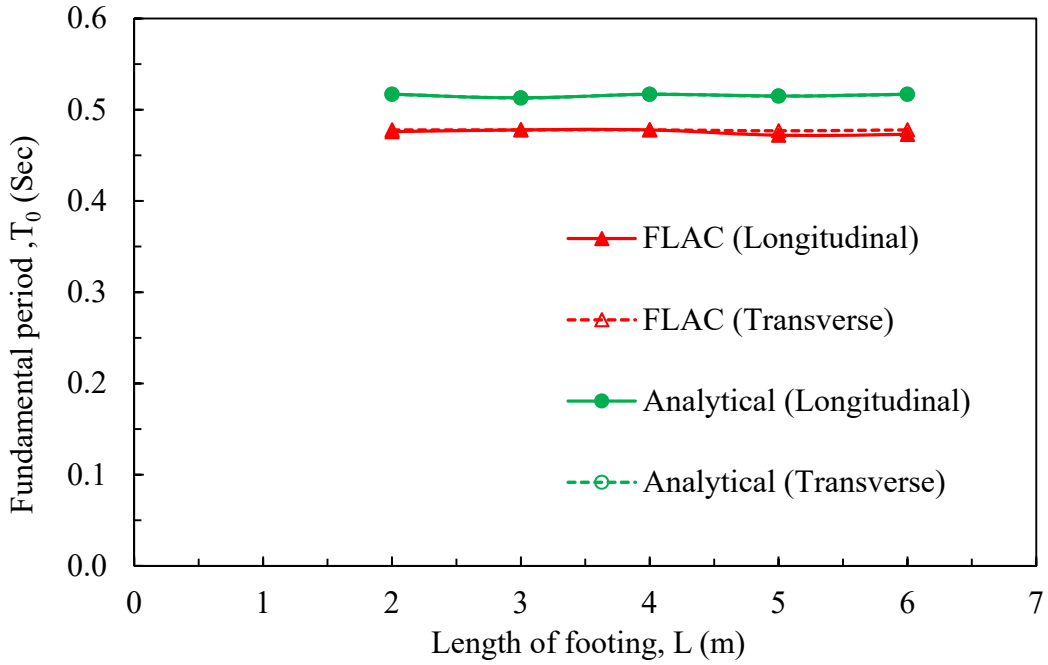

Figure 3-26. Fundamental period of analytical and FLAC for single lane rectangular prismatic embankment

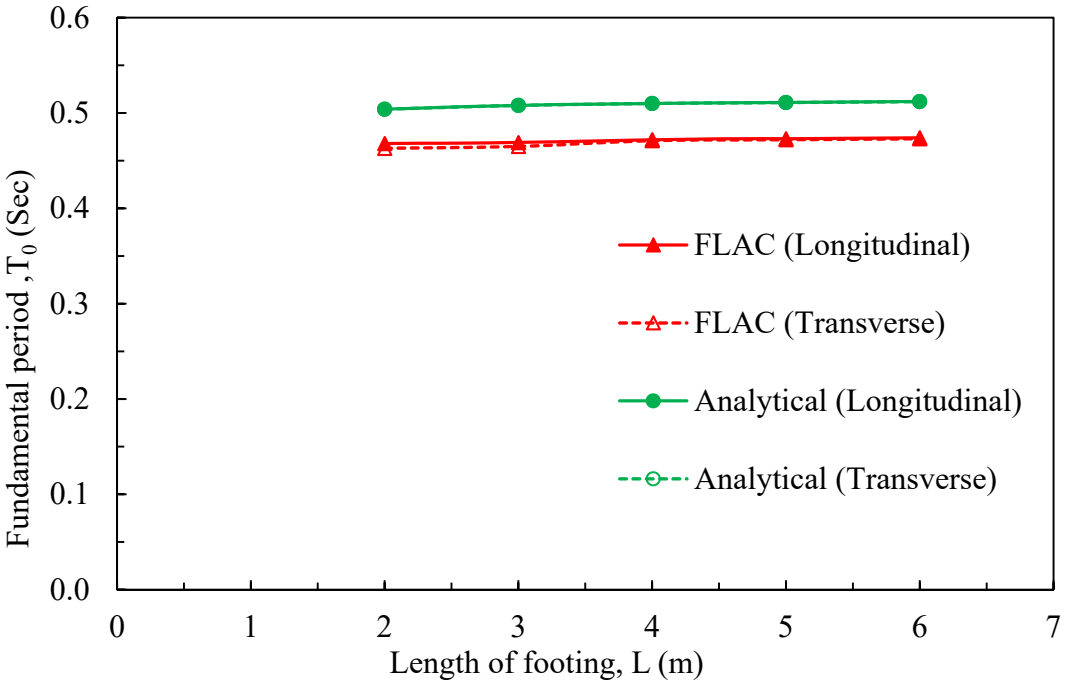

Figure 3-27. Fundamental period of analytical and FLAC for double lane rectangular prismatic embankment

The calculated values were very similar for the analytical and numerical methods. The percentage error of different geometries is shown in Table 3.8. The percentage error was calculated using Eq. 3.61.

$$Percentage\ error = \frac{T_{0(Analytical)} - T_{0(FLAC)}}{T_{0(FLAC)}} 100 \qquad \textbf{(3.61)}$$

Because the percentage of error between the methods was less than 10 percent, it was concluded that numerical methods can reasonably match the results obtained from analytical methods, and that analytical methods are the simplest way to evaluate the fundamental period for embankments with rectangular prismatic shapes. However, numerical methods are recommended for embankments with more complex geometry (see Section 3.5.3.7.7)

Table 3.8. Percentage error of analytical method with FLAC for single and double lane with various length of footing for rectangular prism

Percentage Error				
	Single Lane Analytical and FLAC		Double Lane Analytical and FLAC	
Length of Footing m	Longitudinal %	Transverse %	Longitudinal %	Transverse %
2	8.61	8.16	7.69	8.86
3	7.32	7.32	8.32	9.25
4	8.16	8.16	8.05	8.28
5	9.11	7.97	8.03	8.26
6	9.30	8.16	8.02	8.25

3.5.3.9.3.2 Rocking Mode

The fundamental period obtained from analytical and numerical methods for rectangular prismatic geofoam embankments with consideration of flexural, shear and axial stiffness are shown in Figures 3.28 and 3.29. Because the results from analytical "Method II" are closest to those of FLAC, Method II was chosen for these evaluations. More detailed explanation of Method II is given in Section 3.5.3.7.3.

The evaluations revealed that the fundamental period decreases with increasing length of the footing for both single and double lane bridges when excitation occurs along the longitudinal-direction. The values of fundamental period were almost constant for excitations along the transverse-direction and vertical-directions. This is because the geometry remains constant in these directions; therefore the fundamental period for these directions remained constant. The percentage error (Eq. 3.61) from the comparison of the analytical and numerical methods is given in Table 3.9 as a function of footing length. The percentage error was less than 10 percent for all cases, which suggests that analytical methods are sufficiently accurate for evaluation purposes.

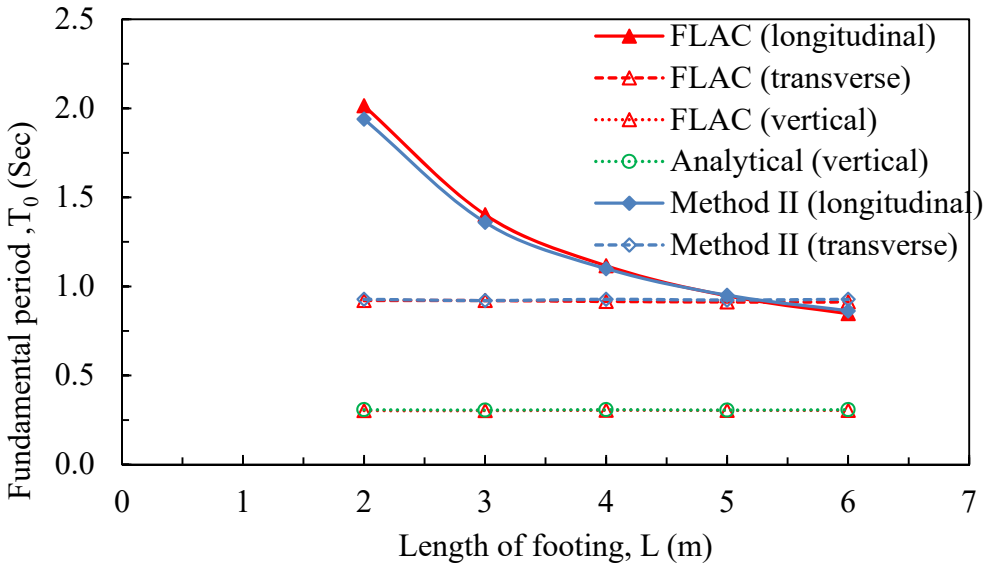

Figure 3-28. Fundamental period of rectangular prism embankment for single lane from analytical and FLAC

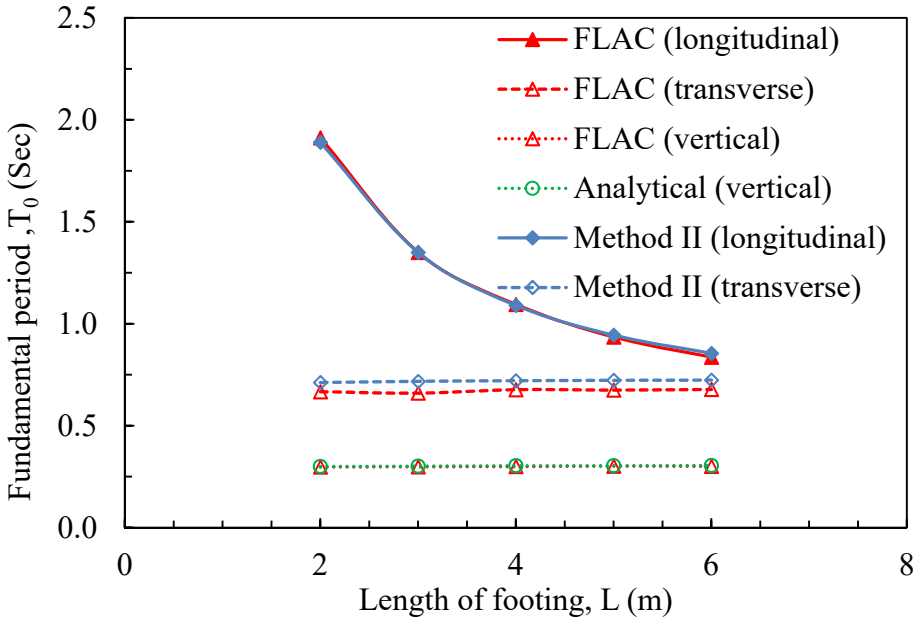

Figure 3-29. Fundamental period of rectangular prism embankment for double lane from analytical and FLAC

Table 3.9. Percentage error of analytical and FLAC for single and double lane with various length of footing for rectangular prism

Percentage Error				
	Single Lane		Double Lane	
	Analytical and FLAC		Analytical and FLAC	
Length of Footing	Longitudinal	Transverse	Longitudinal	Transverse
m	%	%	%	%
2	8.61	8.16	7.69	8.86
3	7.32	7.32	8.32	9.25
4	8.16	8.16	8.05	8.28
5	9.11	7.97	8.03	8.26
6	9.30	8.16	8.02	8.25

3.5.3.9.3.3 Numerical Evaluations of Sway, Rocking and Uplift

3.5.3.9.3.3.1 Sway Mode

The relationship between normal and shear stress within the elastic limit is shown in Equation 3.62 (Athanasopoulos et al., 1999):

$$\tau = \frac{1}{2}\sigma \qquad \textbf{(3.62)}$$

where: τ and σ represent the shear and normal stresses, respectively. The cyclic triaxial test results on specimens of EPS 29 described in Chapter 2 revealed that EPS remains in the quasi-elastic range for cyclic axial strain values up to about 2 percent. Hence for evaluation of the allowable stress under cyclic loading, the allowable normal stress for EPS 29 is about 182 kPa and a corresponding shear stress is 91 kPa, which are the values obtained at 2 percent axial strain. In order to check for potential overstressing of the EPS during cyclic loading, the stresses obtained from the FLAC model at the basal corner zones of the embankment model were compared with the allowable normal and shear stresses described in the previous paragraph for both the sway and rocking modes. The maximum shear and normal stresses at the basal corner locations were monitored for 0.2, 0.3, 0.4, 0.5 and 0.6 g accelerations which were inputted into the model at the fundamental period. A snap shot of the nodal displacement vectors for the embankment excited in the longitudinal direction for the sway mode is shown in Figure 3.30. The zone number assigned to each zone is shown in Figure 3.31, for which zone numbers of 1 and 8 represent the left and right corner zones, respectively, of the FLAC model.

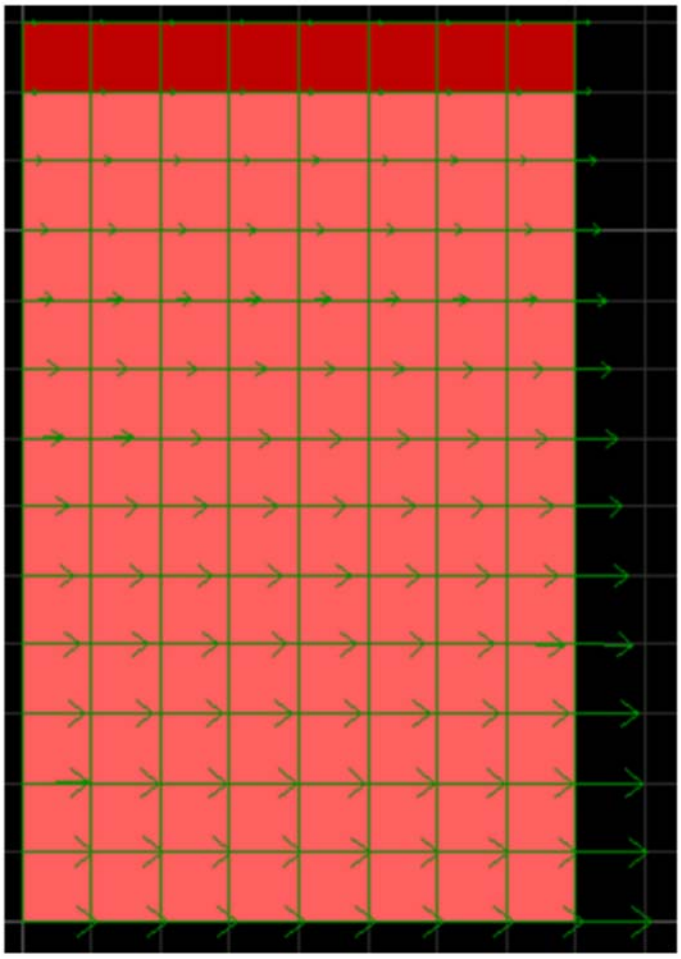

Figure 3-30. EPS geofoam embankment model under sway mode during excitation in the longitudinal direction

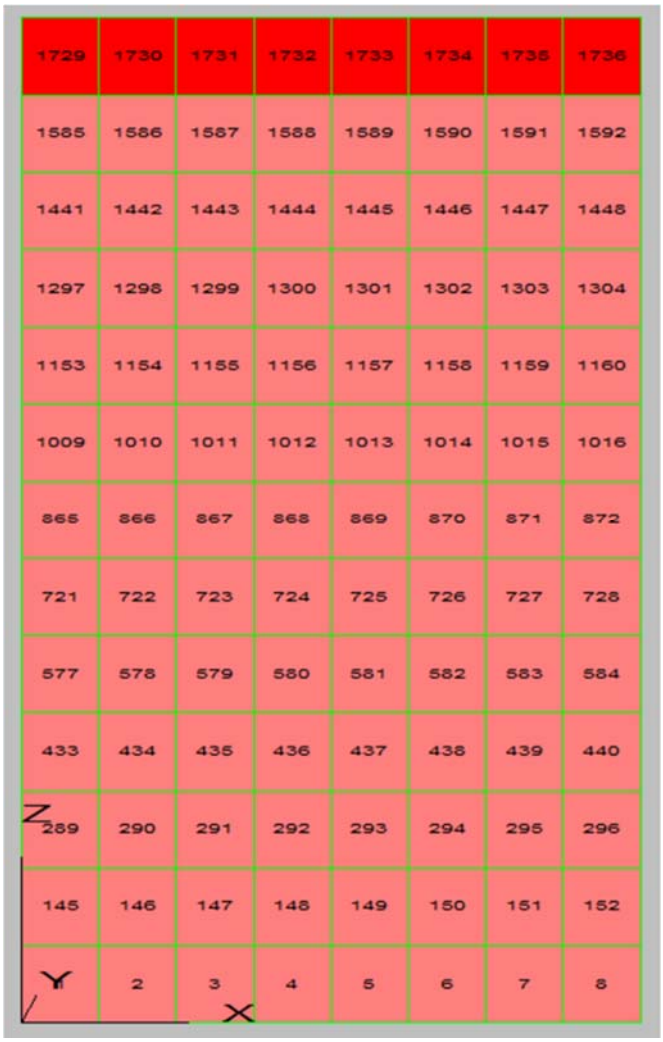

Figure 3-31. Zone numbers of EPS embankment model for sway condition

The resulting shear stresses were found to be largest in the direction of the applied excitation; whereas the normal stresses were found to be largest in the vertical direction, as expected. For excitation in the longitudinal direction, the maximum shear and normal stresses were τ_{xz} and σ_{zz}. Similarly, τ_{yz} and σ_{zz} were the maximum shear and normal stresses for the excitation in the transverse direction. Figures 3.32 and 3.33 show the relationship of shear and normal stresses with dynamic time for excitation in the longitudinal direction.

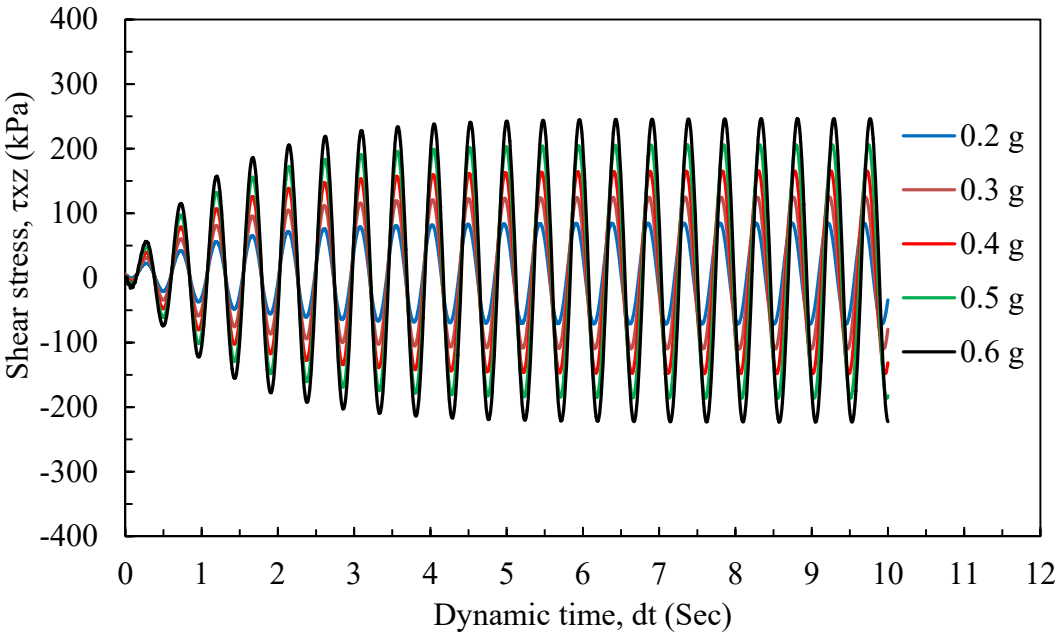

Figure 3-32. Relationship of shear stresses with dynamic time at different level of excitations during fundamental period for sway in the longitudinal direction

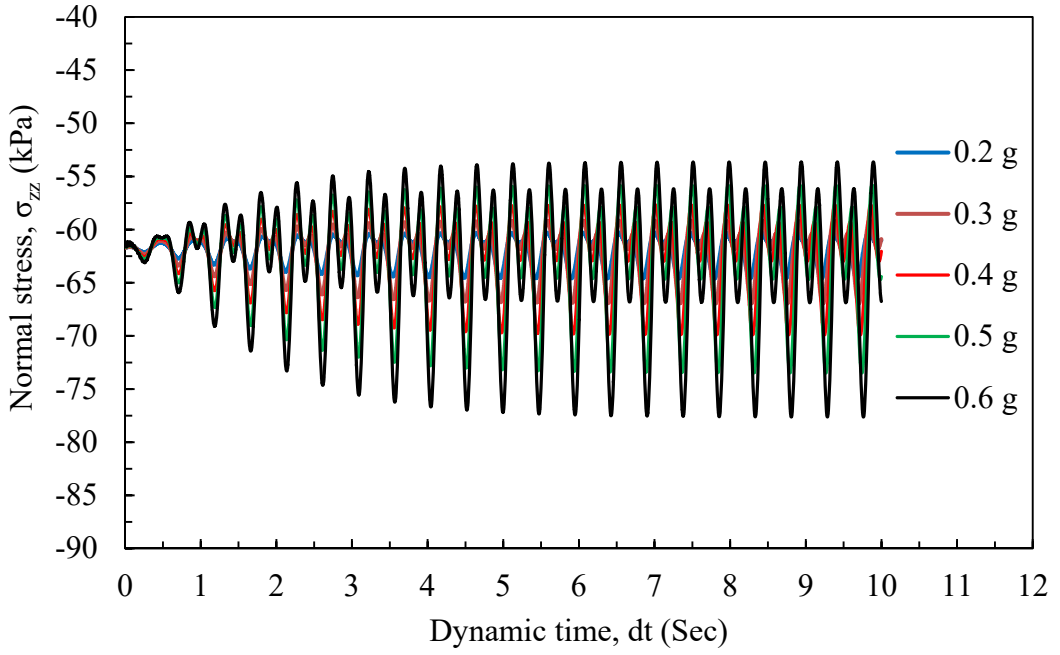

Figure 3-33. Relationship of normal stresses with dynamic time at different level of excitations during fundamental period for sway in longitudinal direction

Similarly, Figures 3.34 and 3.35 show the relationship between shear and normal stresses with dynamic time for excitation in the transverse direction. These figures show how the value of shear stresses and normal stresses increase with increasing level of excitation.

A relationship that describes the maximum shear and normal stresses was developed from these figures (Figures 3.36 - 3.39). The critical acceleration found in these figures is defined as the acceleration value that corresponds to the allowable values of shear and vertical stresses, as previously discussed. Figure 3.36 shows that critical acceleration with respect to allowable shear stress for excitation in the longitudinal direction is 0.215 g. Figure 3.37 shows the critical acceleration with respect to allowable vertical stress is 3.78 g for excitation in the longitudinal direction.

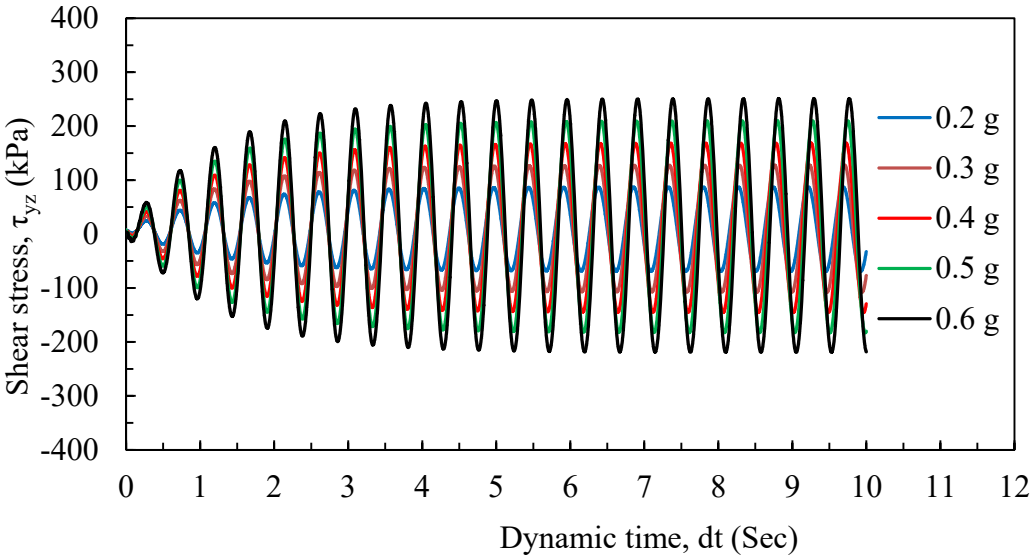

Figure 3-34. Relationship of shear stresses with dynamic time at different level of excitations during fundamental period for sway in the transverse direction

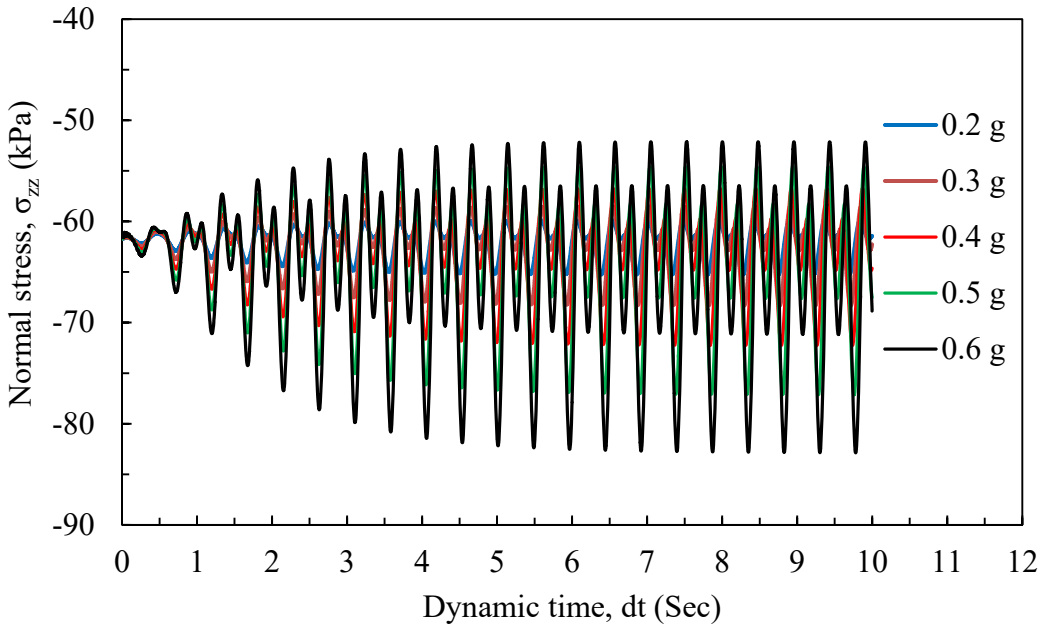

Figure 3-35. Relationship of normal stresses with dynamic time at different level of excitations during fundamental period for sway in the transverse-direction

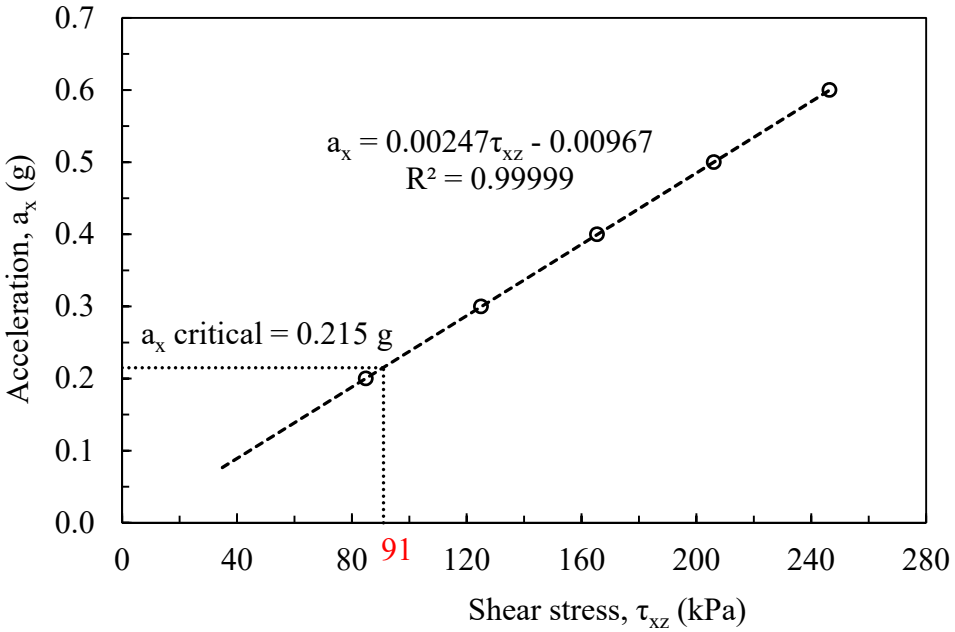

Figure 3-36. Relationship of acceleration and maximum shear stress for sway in the longitudinal direction

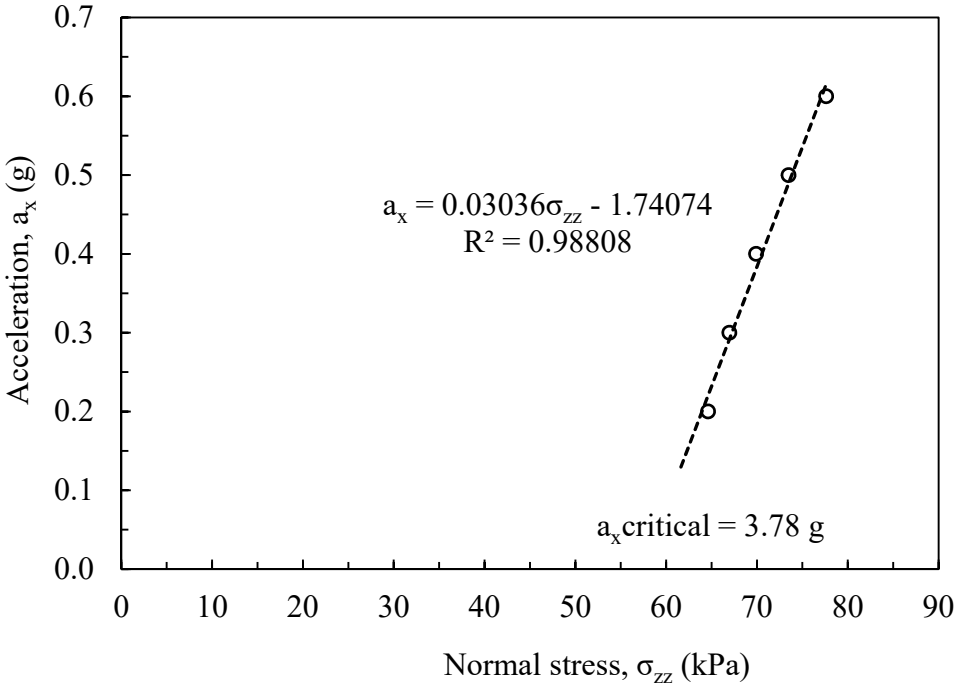

Figure 3-37. Relationship of acceleration and maximum normal stress for sway in the longitudinal direction

Similarly, Figures 3.38 and 3.39 show the relation of acceleration with shear and normal stresses for the excitation in the transverse-direction. These figures reveal that the peak cyclic shear stress started to exceed the allowable shear stress in the EPS 29 at excitation values of about 0.21 g; whereas the exceedance did not occur in compression until the excitation reached about 2.84 g. From the results of excitation in the longitudinal and transverse directions, it can be concluded that EPS geofoam as used in bridge support systems does not exceed the allowable stress proposed in Chapter 2 until the horizontal acceleration value exceeds about 0.2 g.

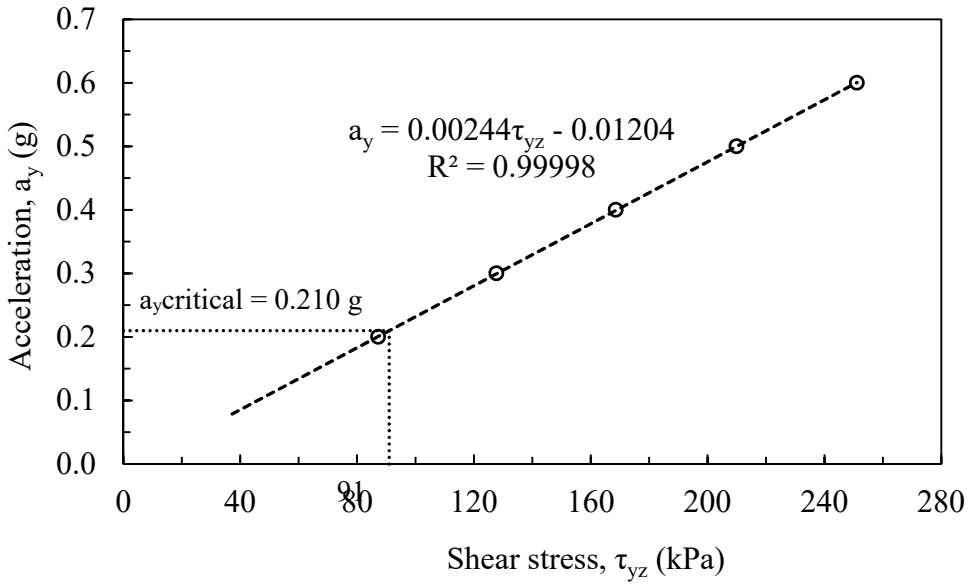

Figure 3-38. Relationship of acceleration and maximum shear stress for sway in the transverse direction

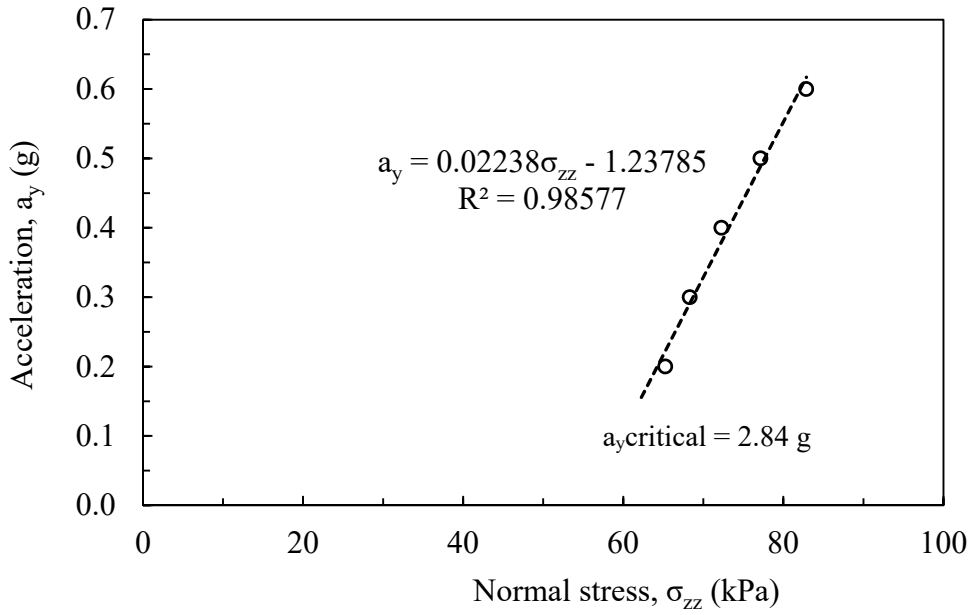

Figure 3-39. Relationship of acceleration and maximum normal stress for sway in the transverse-direction

These critical acceleration values might be increased by using a higher density (i.e., modulus) of EPS geofoam, especially at the corner (i.e., edge) locations, or by using a seismic restraint system, as described in the next chapter.

3.5.3.9.3.3.2 Rocking Mode

For the rocking mode of excitation, the maximum normal and shear stresses were observed at basal corners (i.e., edges) of the EPS embankment. The maximum stresses were determined from normal stresses and shear stresses plots with dynamic time for different level of excitations ranging from 0.2 to 0.6 g applied at the fundamental period for excitation in the: (1) longitudinal, (2) longitudinal and transverse and (3) longitudinal, transverse, and vertical directions. The numerical model predicts significant rocking in the transverse direction, as expected; however significant rocking in the longitudinal direction is not likely to occur due to the resistance provided by the bridge deck. Further, it is not likely that maximum excitation occur in all three direction at the same time. However in this study, the excitation(s) were applied in a harmonic fashion for the above cases to understand the behavior at most critical condition.

A snapshot of the embankment in rocking mode with the corresponding displacement vectors is shown in Figure 3.40. The zone numbers are shown in Figure 3.41. For example, 1633 and 1640 correspond to the left and right corner zones. The normal and shear stress plots with dynamic time for rocking in the transverse direction due to 0.2g excitation in the longitudinal direction are shown in Figures 3.42 and 3.43.

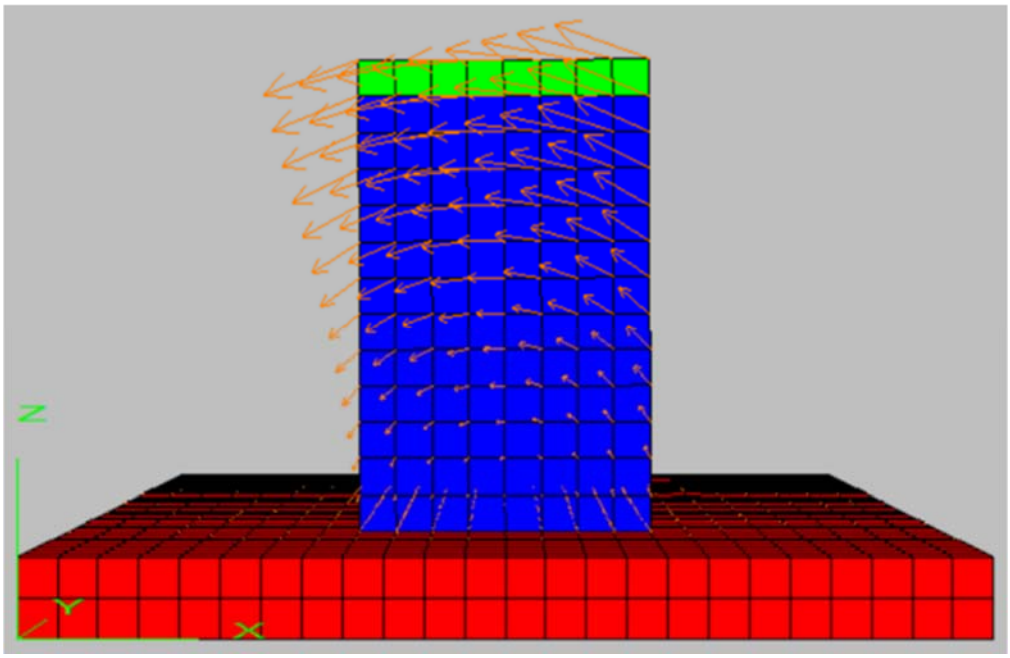

Figure 3-40. EPS geofoam embankment model under rocking along transverse direction due to excitation along longitudinal-direction

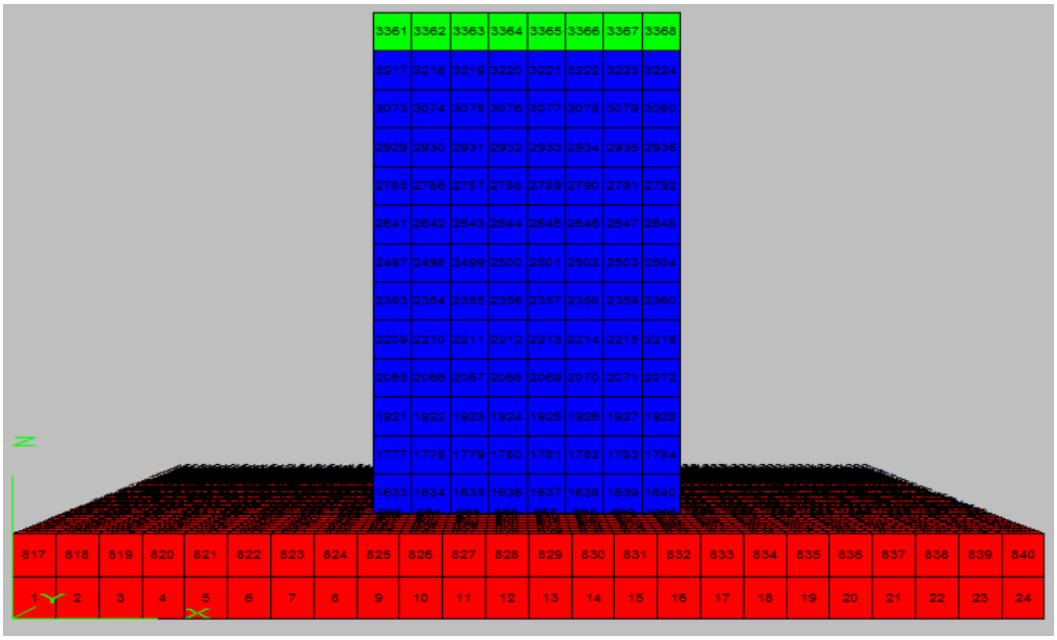

Figure 3-41. Number of zones on EPS embankment model under rocking condition

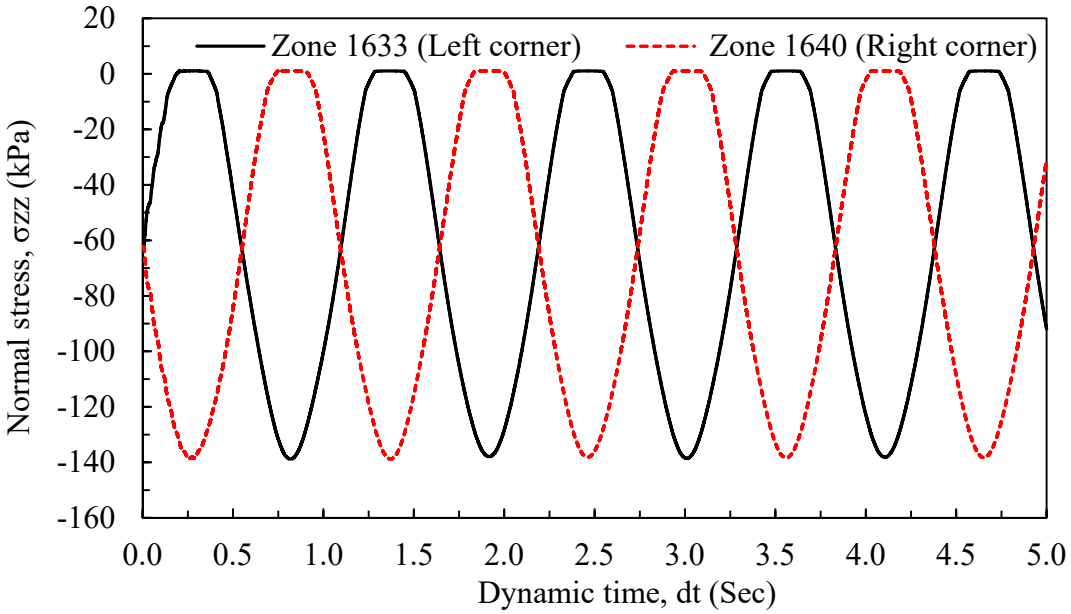

Figure 3-42. Relationship of normal stress with dynamic time at left and right corner zones under rocking in the transverse direction due to the excitation in the longitudinal-direction at 0.2 g acceleration

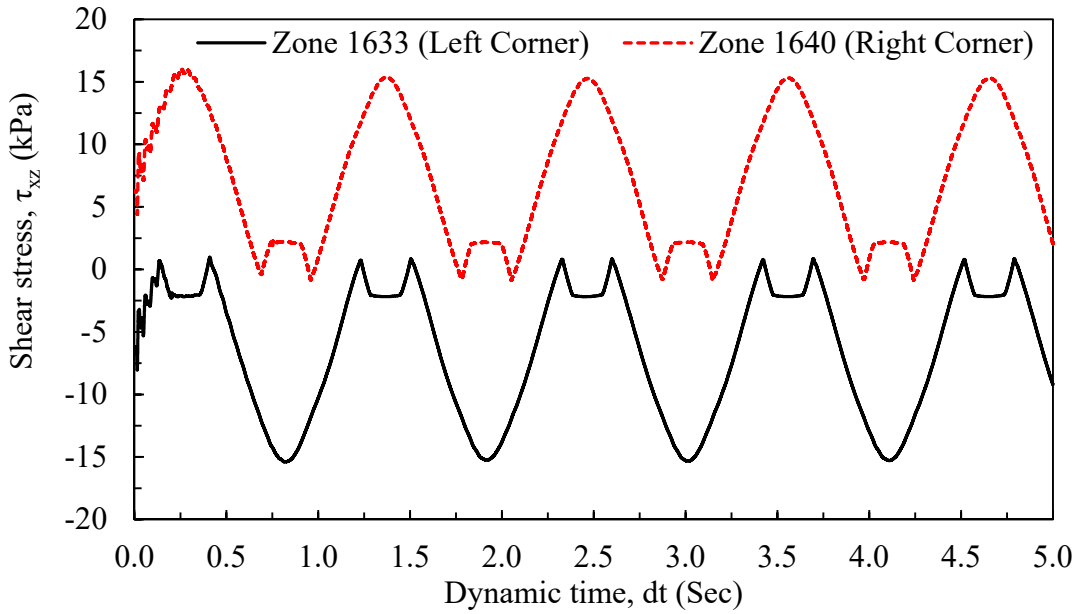

Figure 3-43. Relationship of shear stress with dynamic time at left and right corner zones under rocking in the transverse direction due to the excitation in the longitudinal direction at 0.2 g acceleration

Figure 3.42 shows the relationship of normal stress with dynamic time at the level of excitation of 0.2 g in the longitudinal direction for zones located at the left and right corners. It is clear that alternative compression and tension occurs throughout the embankment due to rocking. The figure

also shows that normal stress remains relatively constant for small interval of time even if the dynamic time is increased. The reason for this constant stress is due to the separation of nodes at the interface during rocking. Similarly, Figure 3.43 shows the relationship of shear stress with dynamic time for 0.2 g acceleration input. In this figure, the shear stress also remained constant for a small interval of time due to separation that occurs at interface during rocking.

The relationship of acceleration with maximum normal stresses for excitation in the longitudinal direction is shown in Figure 3.44. For this case, the critical acceleration for rocking in the transverse direction is 0.332 g. The corresponding maximum shear stress for this mode of excitation and rocking is 1.32 g (Figure 3.45).

The relationships for the maximum normal and shear stresses for excitation in both the longitudinal and transverse directions are shown in Figures 3.46 and 3.47, respectively. The critical accelerations are 0.189 and 0.868 g, respectively, for rocking in the transverse direction.
Similarly, the relationships for the maximum normal and shear stresses for the excitation in the longitudinal, transverse and vertical-directions simultaneously are shown in Figures 3.48 and 3.49, respectively. The critical accelerations are 0.161 and 0.373 g, respectively, for rocking in the transverse direction.

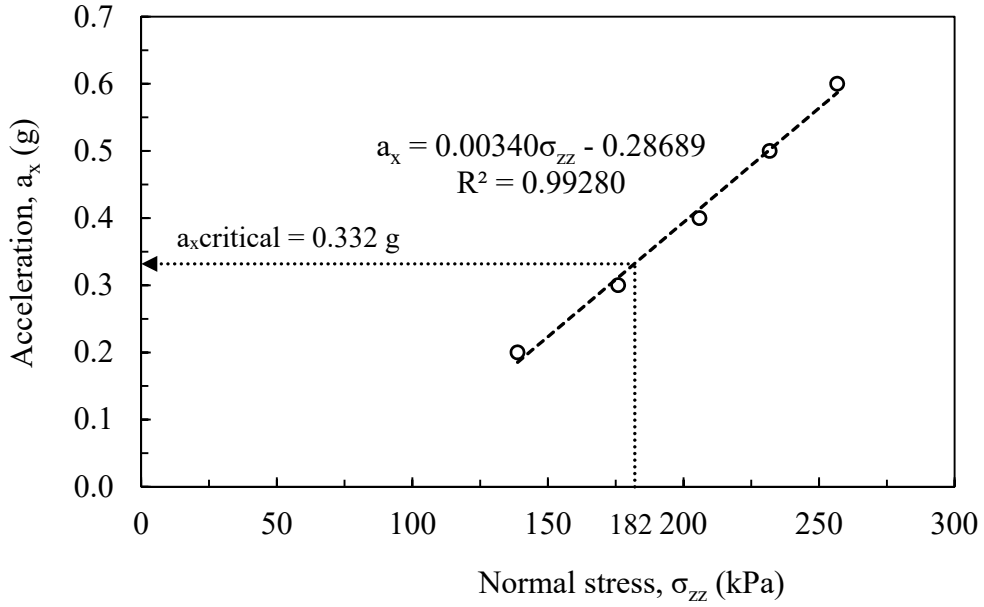

Figure 3-44. Relationship of acceleration with maximum normal stress for rocking in the transverse direction due to the excitation in the longitudinal direction

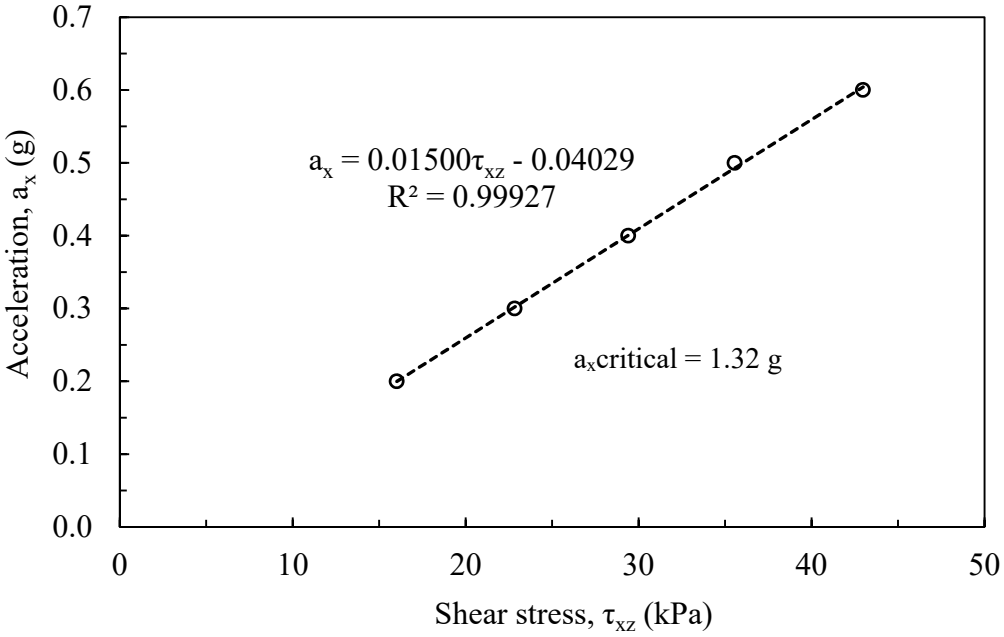

Figure 3-45. Relationship of acceleration with maximum shear stress for rocking in the transverse direction due to excitation in the longitudinal direction

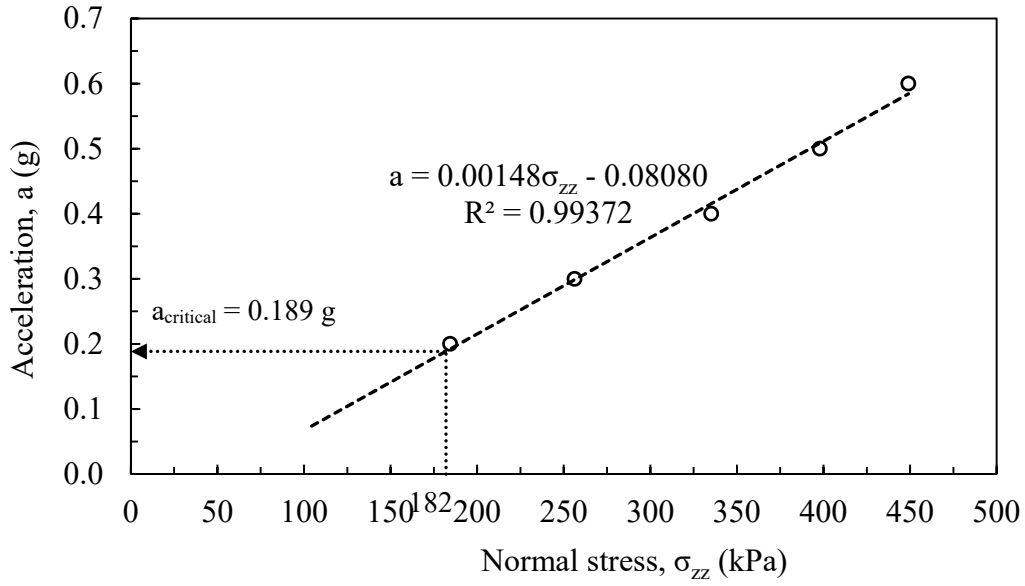

Figure 3-46. Relationship of acceleration with maximum normal stress for rocking in the transverse direction due to excitation in the longitudinal direction and transverse directions simultaneously

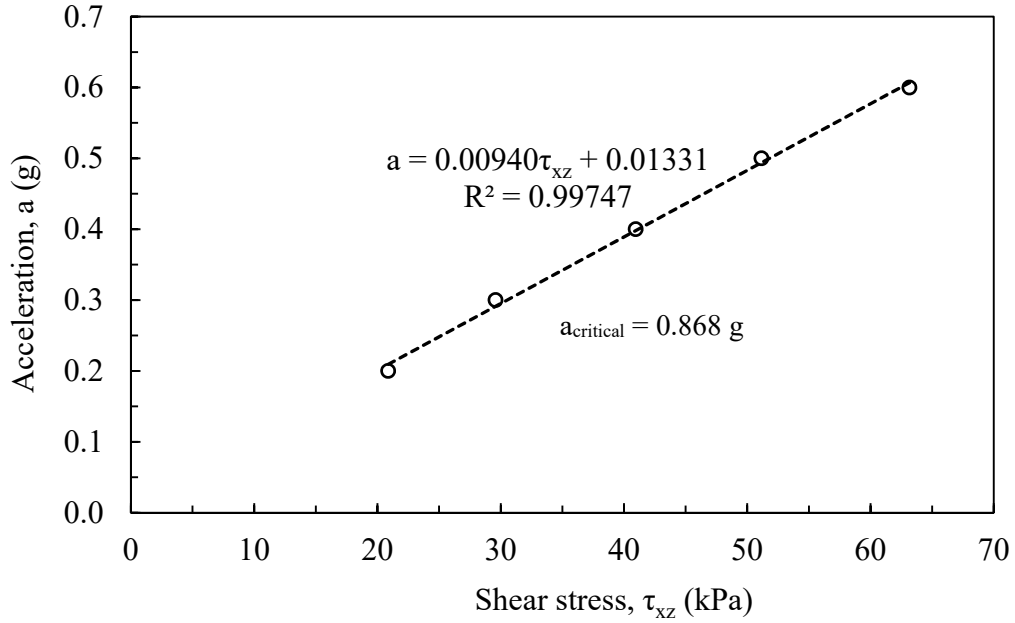

Figure 3-47. Relationship of acceleration with maximum shear stress for rocking in the transverse direction due to excitation in the longitudinal and transverse directions simultaneously

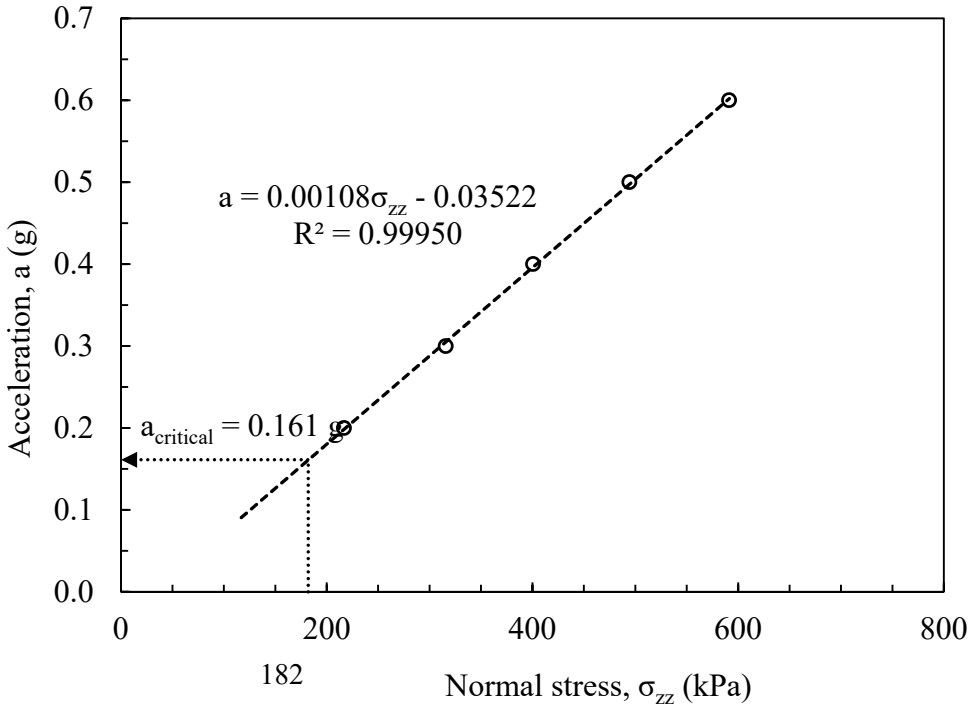

Figure 3-48. Relationship of acceleration with maximum normal stress for rocking in the transverse direction for the excitation in the longitudinal, transverse and vertical-directions simultaneously

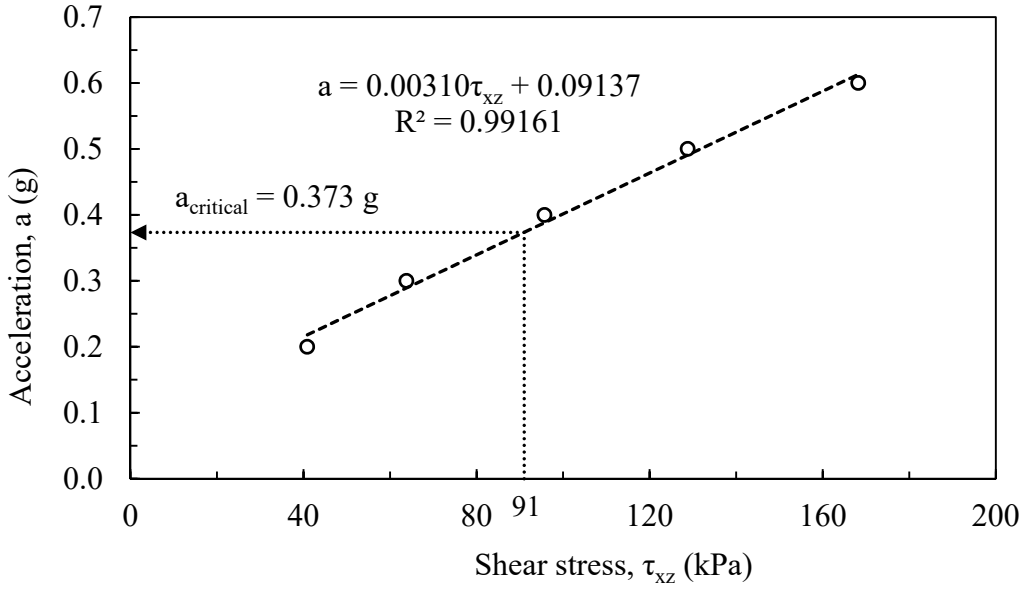

Figure 3-49. Relationship of acceleration with max shear stress for rocking in the transverse-direction due to excitation in the longitudinal, transverse and vertical-directions simultaneously

3.5.3.9.3.3.3 Uplift

Uplift may occur during excitation as part of the rocking mode. In concept, a small amount of uplift is advantageous because it dissipates energy in the bridge support system. Uplift is manifest in the numerical model by separation between two adjacent interface nodes during rocking. For example, the uplift at the right side of model due to a 0.5 g acceleration in the longitudinal direction is shown in Figure 3-500. The amount of uplift was calculated from the relative displacement of the nodes at this interface.

Figure 3.51 shows the relationship of normal stresses as a function of dynamic time for the excitation in the longitudinal direction due to accelerations of 0.15 and 0.2 g. In the figure, for the 0.2 g cases, it is seen that the normal stress remained constant (i.e., zero) for a short period of time, which represent the time when separation occurred at the interface. In the same figure, it is seen that there was no separation for the excitation at acceleration 0.15 g. Thus, uplift initiated in the model at horizontal acceleration between 0.15 g and 0.2 g.

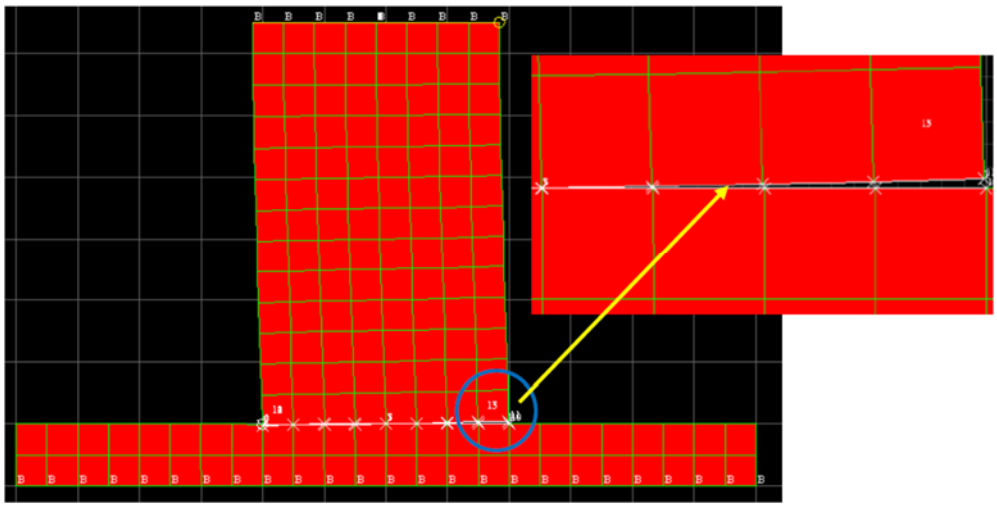

Figure 3-50. Uplift at right side of the model due to excitation of 0.5 g acceleration in the longitudinal direction for rocking in the transverse direction

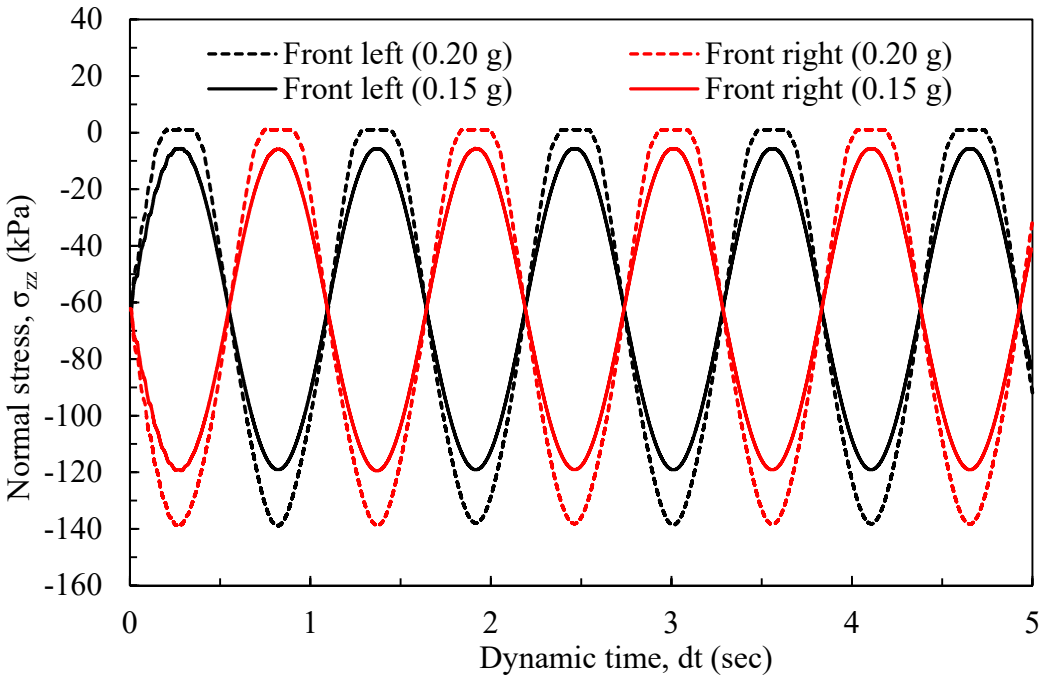

Figure 3-51. Relationship of normal stress and dynamic time at two level of acceleration shows the initiation of uplift for the excitation in the longitudinal direction

According to Brinch (1953), the allowable eccentricity for a swallow foundation for the case of dynamic load where uplift initiated is initiated is *B*/4, where *B* represents the width of footing. The forces acting on EPS embankment during rocking are depicted in Figure 3.52. At the upper bound of equilibrium, the resisting moment is equal to overturning moment as expressed in Equation 3.63.

$$F_i H = R_v e \tag{3.63}$$

where: F_i is the inertial force acting at the top of embankment, H is the height of embankment, e is the eccentricity and R_v is the resultant of vertical forces. In Figure 3.52, q_{max} and q_{min} are the maximum and minimum bearing pressures on soil. W is the total weight at the top of the embankment. The back calculation of the critical acceleration for the rocking case was made by considering the eccentricity equal to *B*/4.

$$F_i H = W \frac{B}{4} \tag{3.64}$$

$$F_i = \frac{Wa}{4g} = \frac{WB}{4H} \tag{3.65}$$

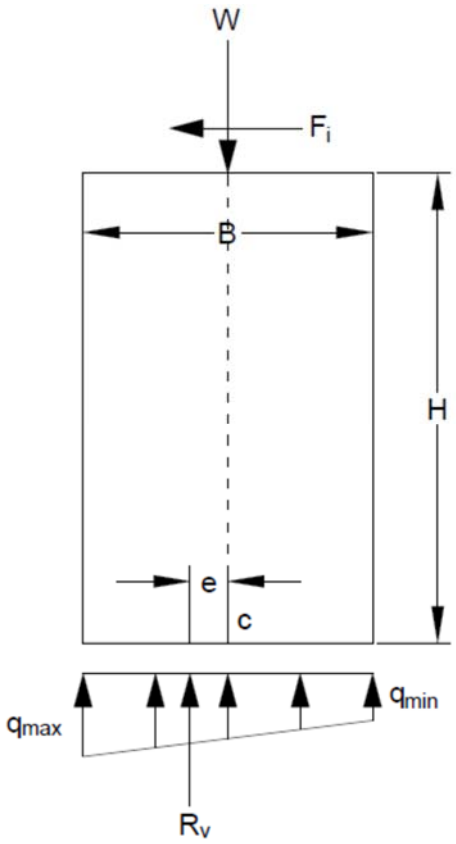

Figure 3-52. Cross-section of EPS embankment with forces acting on it

$$a = \frac{gB}{4H} \tag{3.66}$$

By substituting *B* equals to 4 and *H* equal to 6, the acceleration is given in Eq. (3.67).

$$a = \frac{1}{6}g \tag{3.67}$$

The range of acceleration value for the initiation of uplift from numerical method is in reasonable agreement with the acceleration results obtained from Equation 3.67. The uplift was calculated from the relationship of relative displacement with dynamic time.

The plot of relative displacement with time at an acceleration level of 0.2 g for the excitation in the longitudinal direction is shown in Figure 3.53. The peak value on the plot was taken as the point where uplift initiated for this level of excitation (Figure 3.54).

To explore the magnitude of uplift versus the amount of horizontal acceleration, the relationship of acceleration with uplift at different level of excitations are shown Figures 3.54, 3.55 and 3.56 for the following cases, respectively: (1) excitation in the longitudinal direction, (2) excitation in the

longitudinal and transverse directions, and (3) excitation in the longitudinal, transverse and vertical directions.

In summary, there is no known design guidelines regarding an “acceptable” amount value of uplift for EPS embankment during seismic rocking. However, this study found that the EPS blocks of the bridge support was not significantly overstressed even as rocking was initiated at the levels of excitation ranging between 0. 15 g to 0.2 g.

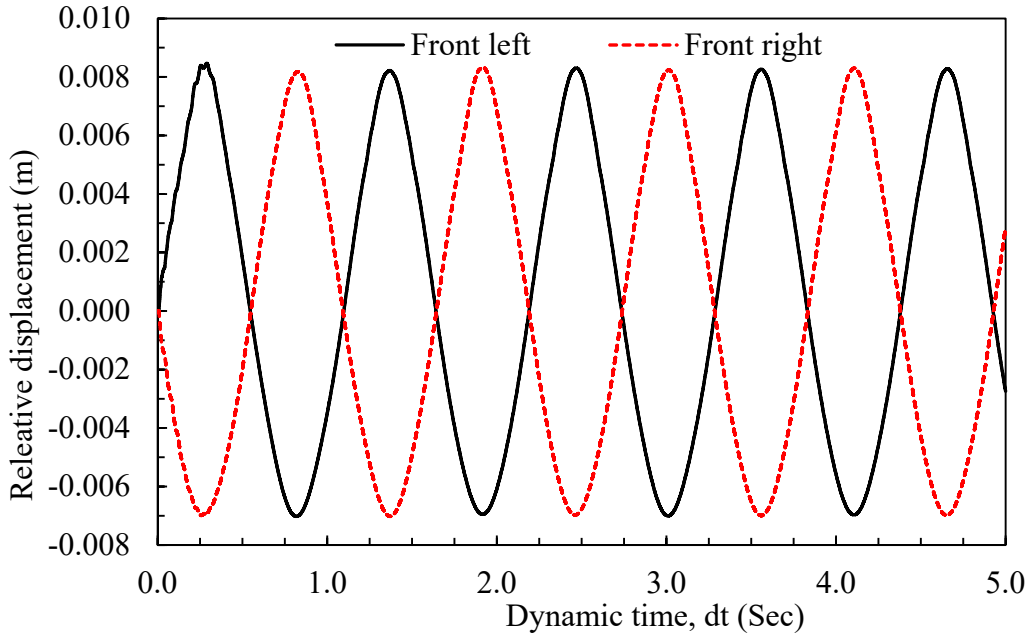

Figure 3-53. Relative displacement with dynamic time at level of acceleration of 0.2 g for the excitation along longitudinal-direction

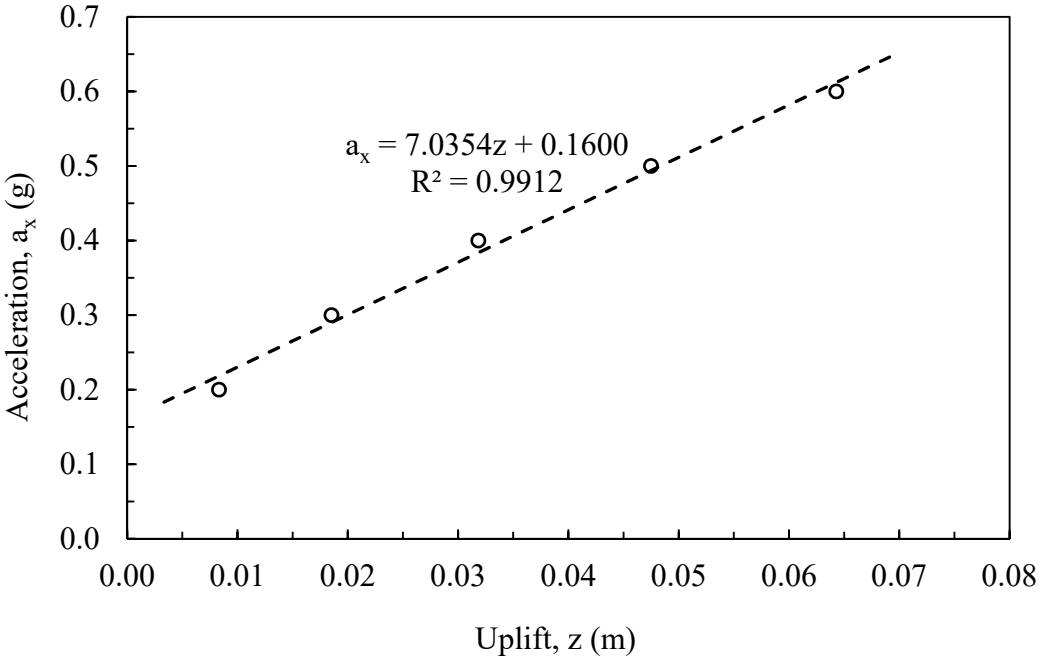

Figure 3-54. Relationship of acceleration and uplift for the excitation in the longitudinal direction

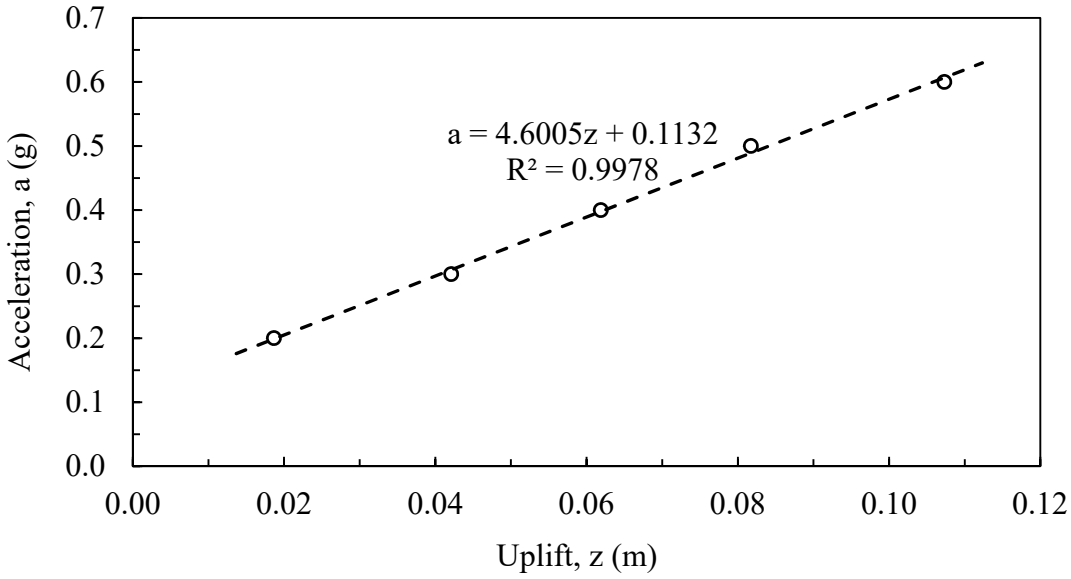

Figure 3-55. Relationship of acceleration and uplift for the excitation in the longitudinal and transverse directions

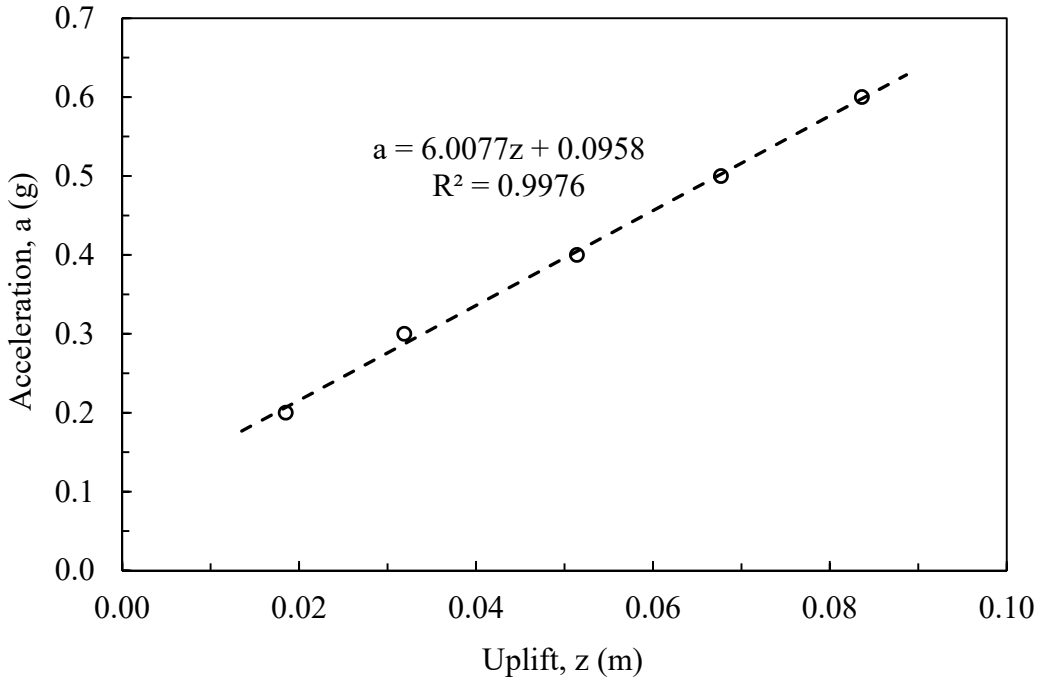

Figure 3-56. Relationship of acceleration and uplift for the excitation in the longitudinal, transverse and vertical directions

3.5.3.10 Development of a Seismic Restraint System

3.5.3.10.1 Introduction

To improve the seismic and post-seismic performance of the proposed EPS bridge support system, strategies can be included in the design and construction to improve the seismic resistance, redundancy and robustness of the system. These may consist of material, physical, mechanical devices or countermeasures deployed within or external to the geofoam support system. For example, Bartlett and Lawton (2008) and Amini (2014) explored the deployment of the following mechanisms to reduce the potential for interlayer or basal sliding of the EPS blocks: (1) shear keys constructed of high density geofoam blocks placed in strategic locations within the embankment, (2) adhesion (glue) placed between the geofoam blocks and (3) embedment of the support system. Based on the evaluations of this study, it is recommended that consideration be given to increasing the density (i.e., modulus) of geofoam blocks in zones that are susceptible to overstressing (e.g., basal edges of the embankment).

As an additional feature to these countermeasures, a cable restraint system is evaluated in this chapter. The overall objective of the cabling system is to reduce the amount of interlayer sliding, sway and rocking so that the bridge support system is not compromised due to excessive translation or internal overstressing of the EPS blocks. The primary mechanism used to achieve this goal is to introduce high-strength steel cabling as a mechanical restraint system that connects the bridge foundations with the basal foundation slab or grade beam placed below the EPS blocks (Figures 3.1 and 3.2). It is recommended that this connection be made using a diagonal or crisscross cabling pattern. The cables are high-strength tensile members positioned in the longitudinal and transverse directions of the embankment which connect the reinforced concrete bridge footings to the basal reinforced concrete slab. Hence, the cabling provides a load path for tensile and shear forces to be transferred from the bridge system to the embedded basal slab. It also performs the function of a lateral restrain system that can be used to limit the amount of interlayer sliding.

The cabling restraint system should be designed to accomplish the following: (1) limit the amount of tensile stress that develops in the cables to the allowable elastic limit for the selected size of cable, (2) limit the amount of cyclic shear strain that develops in the EPS blocks due to horizontal sway to about 1 percent, (3) prevent vertical separation between EPS blocks at horizontal interfaces with the support system including bridge footings, within the EPS mass itself, and with the basal concrete slab, and (4) prevent horizontal sliding along these same interfaces. In addition, embedment of the basal concrete slab or foundation and part of the EPS blocks is recommended to limit the amount of sliding or uplift due to rocking.

3.5.3.10.2 Evaluation of Countermeasures

The potential performance of the proposed EPS bridge support system will be evaluated using analytical and numerical methods based on the criteria discussed in the following sections. The proposed EPS bridge support system consists of (from top to bottom) bridge structure, bridge footings, layers of EPS block, basal reinforced concrete foundation slab and diagonal cabling connecting the bridge footing with the basal slab. The general shape of the EPS bridge support system may consist of rectangular prismatic, trapezoidal prismatic, or a 3D trapezoidal shape. Because of its relatively slender nature, the rectangular prismatic embankment was selected as the critical or controlling case for evaluation of the system from sway and rocking modes during seismic excitation. The critical acceleration for these modes were 0.2 g and 0.3 g, respectively (Section 3.5.3.9.3) for cases without a cabling system.
For these preliminary evaluations, the number of cables and diameter of cable were chosen in such a way that the performance goals and criteria stated in the previous section are met. Analytical methods were used to evaluate the sway mode; and numerical methods were used to evaluate rocking and uplift modes.

3.5.3.10.2.1 Sway mode

The evaluation of the sway mode with cabling focused on sizing the diameter of the cabling so that the restrained EPS blocks would not undergo excessive cyclic strain. The recommended allowable total axial strain of the system should not exceed 2 percent (Section 2.7); hence accounting for about 1 percent axial strain under dead and truck loads, the additional axial strain from cyclic loading should not exceed 1 axial percent.

However, cyclic strain was monitored in the numerical model for the sway mode (Section 3.5.3.9.3.3); hence the allowable strain should be defined in terms of shear strain, instead of axial strain. Therefore, the allowable shear strain ($\gamma_{allowable}$) in the EPS blocks was correspondingly estimated from elastic theory using Equation 3.68. For EPS 29, Possion's ratio is about 0.19; hence the corresponding allowable cyclic shear strain is about 1.2 percent. Thus, it is recommended that the maximum shear strain in the EPS support system with a cabling system should not exceed this value during seismic excitation in order to maintain the EPS blocks in the quasi-elastic state and not introduce the potential for excessive cyclic and post-cyclic deformation.

$$\Upsilon_{allowable} = \epsilon_{allowable}(1+\nu) \qquad (3.68)$$

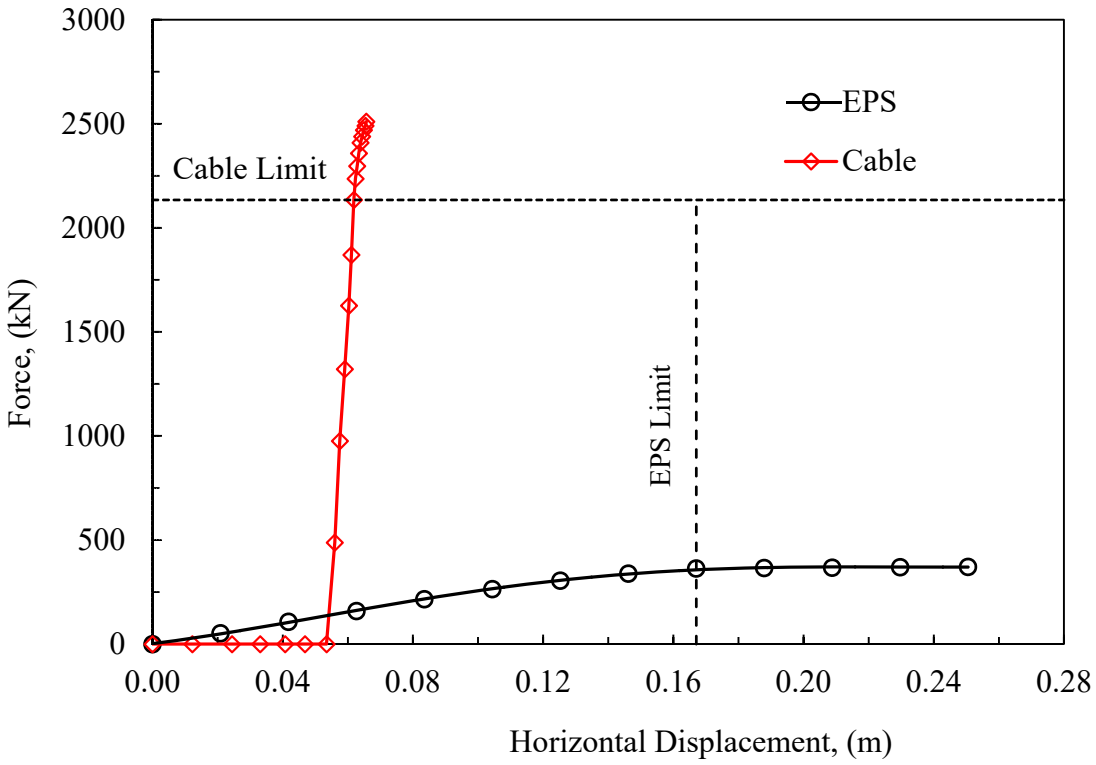

Figure 3-57. Force versus displacement relationship of EPS and cable

The force versus displacement relationships for the cable and EPS were determined from the properties of the respective materials. Because of its high stiffness or modulus, the tensile resistance in the cable is mobilized rapidly when compared with the shear resistance of the EPS blocks (Figure 3.57). The shear force and horizontal displacement relation for EPS placed in simple shear was calculated based on stress-strain relationships obtained from the uniaxial monotonic test results (Chapter 2) and application of elastic theory. The horizontal displacement was calculated as

the product of shear strain and height of the embankment. Similarly, the horizontal force was calculated as the product of shear stress and the length of the EPS embankment in the longitudinal direction. In case of the cable, the stress-strain relation of Grade 270 strand given in Nawy (2006) was used for the calculation of tensile force versus displacement. The tensile force along the cable was calculated as the product of stress and area of strand. The displacement (elongation) was calculated based on the force displacement relationship given in Eq. (3.69) where P is the axial tensile force in the cable, L is the length of cable, A is the cross-sectional area of cable and E is the Young's modulus of elasticity of Grade 270 strand.

$$\Delta = \frac{PL}{AE} \tag{3.69}$$

In terms of the demand on the EPS and cabling systems, the component of inertial force and its corresponding displacement in horizontal (i.e., sway) direction was calculated. The design horizontal force is simply the product of the total mass atop the EPS embankment (i.e., structural dead and live loads from the bridge and concrete foundations) times the level of excitation in terms of acceleration of gravity (g) in the horizontal direction. In order to size the cable, the number of strands and cross-sectional area of strand was varied in a trial-and-error method in order to achieve the desired resistance in the system within the allowable limits of the components. The cable limit is the maximum load that can sustain by the cable within linear range of stress-strain relationships. Similarly, the EPS limit was set as the acceptable shear strain for the EPS based on the findings summarized in Chapter 2.

It is important to note that some amount of shear deformation in the EPS embankment might be required in order for the steel cable to begin to provide tensile resistance during cyclic loading. This is due to the potential for slack to develop in the cabling as a result of pre-earthquake creep strain in the EPS embankment. Based on a 6-m height of embankment, the expected pre-earthquake creep deformation is about 0.06 m in 50 years, and the corresponding shear deformation required to mobilize the steel cable is about 0.053 m (Figure 3.57). Hence, during a seismic event, the EPS block will start to provide compressive and shear resistance from the initiation of the cyclic loading, and about 0.05 m of sway displacement is required to engage the cabling system.

The concept of strain compatibility was used to estimate the total force displacement behavior of the EPS embankment and cabling system. Strain compatibility requires that two different components undergo the same amount of strain and uses this requirement to estimate the individual rates of resistance developed by each component. These are added together to provide an estimate of the total force-displacement relation of the system, which is shown in Figure 3.58. The details of this calculation is given in Appendix G. The 1750 kN horizontal force shown in this figure corresponds to 1 g horizontal acceleration occurring at 0.06 m of horizontal sway displacement. The cable has been sized so that the displacement and the associated tensile strain remain below the "cable elastic limit." In addition, the sway (i.e., horizontal) displacement and is associated shear strain remain well below the allowable limit for the EPS blocks (Figure 3.58).

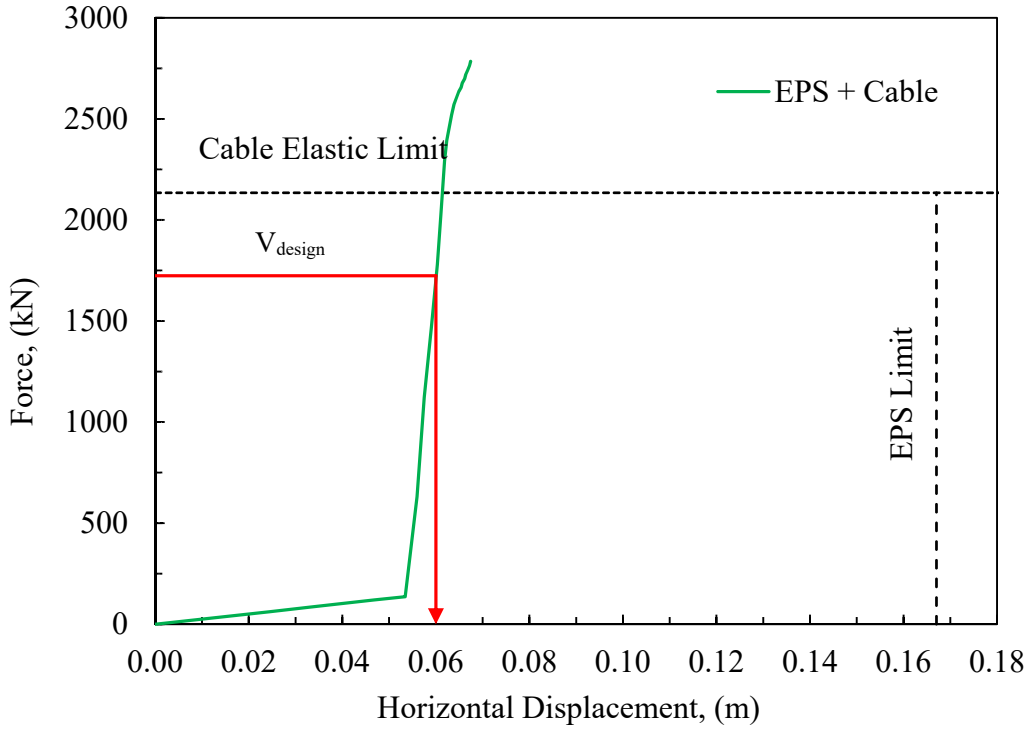

Figure 3-58. Force versus horizontal displacement relationship for combined EPS block and cable system.

Although grade 270 strand cable and EPS 29 was used for this evaluation, it is possible to use other cable grades and densities of EPS. The important concept is to select the combination of material properties that keep the materials within acceptable strain values for the design basis acceleration.

3.5.3.10.2.2 Rocking and Uplift

The potential for uplift at the basal edges corners of the foundation slab was also explored a different level of excitations using FLAC 3D. The relationship of horizontal acceleration (g) and vertical uplift (m) at the edges of the EPS embankment is shown in Figure 3.59. The modeling showed that uplift was about 0.11 m at an excitation level of 0.6 g. However, it is important to note that this modeling was done without the inclusion of a cabling system or embedment of the embankment.

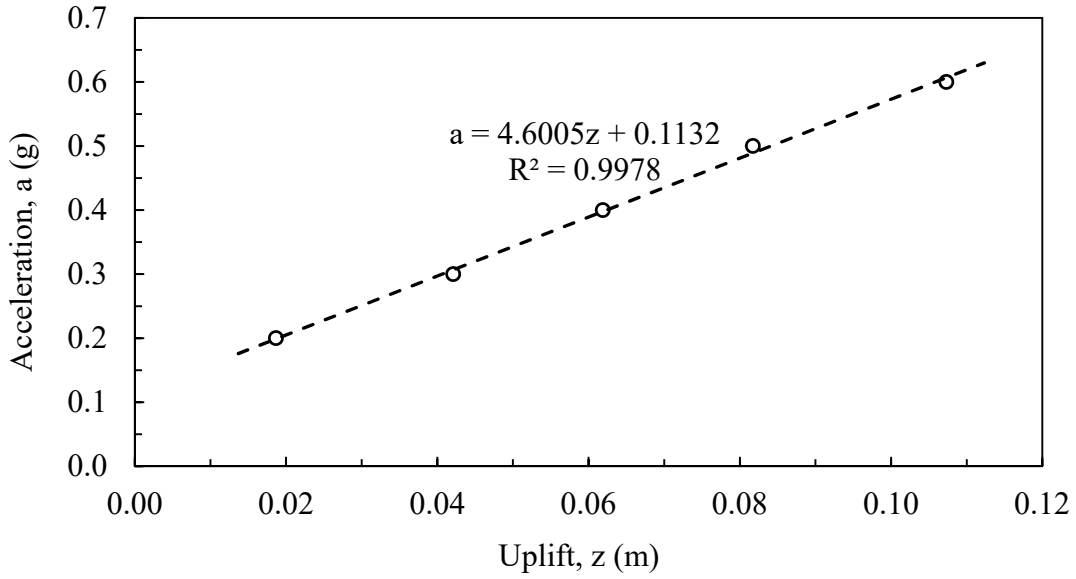

Figure 3-59 Relationship of horizontal acceleration and uplift of basal layer of EPS embankment for case without cabling

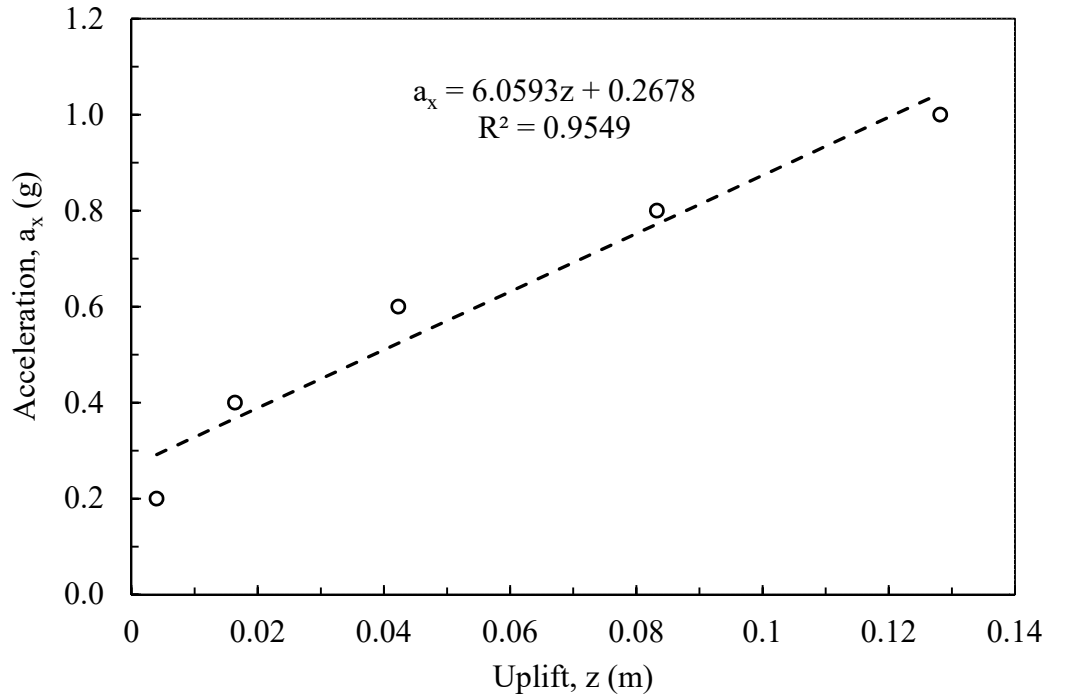

Figure 3-60. Relationship of horizontal acceleration and uplift of basal concrete foundation slab for case with cabling

If a cabling system is included in the constructed system, there is little possibility of significant uplift at the inter-layer interfaces of the EPS blocks or at the interfaces of the bridge foundation slab or the basal foundation slab. These were removed from the FLAC model. However, there remains a possibility of uplift or separation at the bottom of basal concrete foundation slab and the top of foundation soil interface. The potential amount of basal uplift at this interface was studied

by creating an interface at this location. This interface allowed for separation and slippage along the interface. The interface properties were calculated in the manner described in Section 3.5.3.9.2. At this interface, the foundation soil is much softer than the concrete slab. Hence, the properties of the soil were used to calculate the interface stiffness properties according to the recommendations of Itasca (2006) (Section 3.5.3.9.2). In addition, the effects of embedment of the basal slab were not considered in this model.

Based on the model and assumptions above, the uplift at the edges of the basal concrete slab was calculated at different levels of excitation (Figure 3.60). The estimated amount of uplift is approximately 0.13 m for 1.0 g of horizontal acceleration, which is probably an acceptable amount of uplift in terms of the overall performance of the system. The additional resistance to uplift resulting from this case (Figure 3.60) when compared with the non cabled case (Figure 3.59) is primarily due to the additional mass provided by the basal slab.

3.5.3.10.2.3 Recommendations for Cabling System

Therefore based on evaluations of sway, rocking and uplift, it appears that the use of a cable restraint is a viable counter-measure against deleterious effects to the bridge support system caused by severe earthquake shaking. It is clear that the use of cables placed in a diagonal pattern has the potential to significantly reduce any internal overstressing EPS blocks by limiting the amount of shear strain that develops during horizontal sway. Based on these evaluations, six strands of Grade 270 19-mm diameter cable are recommended for prismatic rectangular shaped bridge support systems experiencing significant seismic excitation (levels up to 1.0 g horizontal acceleration). In addition, the cable system evaluated consisted of cables placed externally to the EPS blocks (Figures 3.1 and 3.2). However, in its final construction configuration, it is recommended that these cables be protected by a fascia wall or other means. In addition, during construction, it is recommended that the cables be slightly tensioned once the dead load of the bridge has been applied to remove any slack in the cable created by the compression of the EPS during this loading. However, the amount of tensioning should be minor, so as not to provide significant additional load to the EPS blocks. In addition, these evaluations have shown that slack that develops in the cabling with time due to creep strain of the EPS embankment should not be a great concern. This was accounted for in the evaluations done for the force-displacement behavior of the system (Figure 3.58). In addition, the cabling requires anchorage to the concrete slabs forming the bridge foundation and basal foundation, respectively. The connection details of this anchorage system have not been explored in this study.

Lastly, even though the potential for significant uplift at inter-layer interface of EPS and at the basal foundation slab is eliminated by the cabling system, uplift at the foundation-soil interface may still occur during seismic rocking. However, the analysis summarized in Figure 3.60 suggests that the amount of uplift is relatively small (about 0.1 m) and is probably acceptable in terms of overall seismic performance of the support system. An exhaustive study of rocking and uplift for an EPS support system with cabling has not been included in this study due to the complexity of the numerical analyses required. Further work on this topic may be warranted, but in concept the proposed cabling system is a feasible mechanism to improve the overall seismic performance of the system. Also, inertial interaction between the bridge and the EPS support system has been accounted for in this study by including the mass of the bridge in the evaluations, herein; however kinematic interaction resulting from the potential for flexibility of the bridge system during seismic excitation has not been evaluated. This topic may also warrant additional analyses, especially in terms of detailing and designing the cable connections.

4 SUMMARY AND CONCLUSIONS

This report has investigated the use of EPS geofoam embankment to support bridge systems without the use of deep foundation systems or ground improvement. The viability of the system to support dead, live and earthquake loading was evaluated using laboratory, analytical and numerical methods for the cases of rectangular prismatic shaped and trapezoidal prismatic shaped embankments.

In terms of the recommended material properties and allowable stress levels for the EPS component of the bridge support system, it is recommended that the stress level associated with the applied gravitational dead load in the EPS blocks be limited to a value corresponding to 1 percent axial strain, as measured from a monotonic uniaxial load test. This recommendation is similar to that of Srirajan et al. (2001), but is different from that of NCHRP 529 in that the live loads are not considered in the recommended loading combination.

Regarding cyclic loading from extreme events, and based on post-cyclic loading creep tests of representative densities of EPS, it is further recommended that the applied dead, live and earthquake loads in the EPS block be limited to a combined stress level that does not exceed the compressive resistance associated with 2 percent axial strain, as measured in a monotonic uniaxial load test for the selected density of EPS. This recommendation is similar to that of the EPS White Book (2011) for the factored allowable stress associated with short term loading conditions which is taken to be 80 percent of the compressive resistance at 10 percent axial strain. This document recommends the use of the compressive resistance measured at 2 percent axial strain, which is approximately equivalent to 85 percent of the compressive resistance at 10 percent strain. These recommendations provide the basis of design and evaluation criteria in terms of the required material properties of the EPS.

Based on these allowable stress criteria, the potential size (i.e., length and width) of possible bridge structures was determined for one and two-lane concrete and steel structures, respectively. The potential length of the structures was sized for single and double lanes using the material properties associated with EPS 22 (kg/m^3) and EPS (29 kg/m^3), respectively. The length of the reinforced concrete bridge footing placed atop the EPS block system was varied from 2 m to 6 m, and the corresponding analyses suggest that a 47-m span length is possible for a double lane steel bridge supported on EPS 29. Similarly a 27-m span length is possible for a double lane concrete girder bridge supported on EPS 29. If longer span lengths are required than these evaluation cases, the modulus of the EPS could be increased to higher moduli associated with EPS 39 or EPS 45 in order to support the higher loads caused by the longer span lengths. However, for typical overpass structures, it appears that EPS 29 is sufficient in many cases to use as a bridge support system.

Additional numerical evaluations were done to assess the internal and external seismic stability in terms of inter-layer and basal sliding, horizontal sway and rocking modes. The critical acceleration (i.e., acceleration producing a factor of safety equal to 1.0) for inter-layer and basal sliding for rectangular prismatic and trapezoidal prismatic shaped embankments was found to be about 0.6 g for both cases. The modeling suggests that interlayer sliding does not initiate for acceleration values less than or equal to about 0.8 g; whereas basal sliding may occur for values exceeding 0.6 g. The inclusion of shear keys was included as a mechanism to increase the resistance to interlayer sliding. In addition, embedment of the basal EPS layer was evaluated as an additional means to inhibit basal sliding between the foundation soil and EPS block interface. These evaluations suggest that for horizontal excitation levels of 1.0 g, the required shear key coverage between two EPS layers is about 8 percent of the surface area of the interlayer sliding plane. In addition, the recommended

embedment depth is about 1.4 m to achieve sliding stability. However, this value is somewhat dependent upon site-specific soil conditions and compaction of backfill around the basal concrete slab; hence the required depth of embedment of an EPS support system needs to be evaluated on a case-by-case basis using representative foundation soil properties.

In terms of horizontal sway and rocking of the support system, these evaluations revealed that the peak cyclic shear stress started to exceed the allowable shear resistance of EPS 29 at horizontal excitation values of about 0.21 g. The most critical case was for excitation of rectangular prismatic shaped embankments excited in the transverse direction. However the critical acceleration could be increased by EPS blocks with higher moduli (e.g., EPS 35 or EPS 45). The critical horizontal acceleration for potential overstressing of the basal edges of the EPS embankment due to rocking was found to be about 0.19 g. Basal uplift of the EPS block was also initiated at horizontal acceleration levels of about 0.15 to 0.2 g for excitation in the transverse direction of rectangular prismatic shaped embankments.

To limit the potential for overstressing of the EPS blocks due to the horizontal sway and rocking modes, a cable restraint system was introduced and evaluated. These evaluations show that the inclusion of high-strength steel cables placed in a diagonal pattern connecting the bridge foundation to a basal concrete slab embedded in the foundation soil can significantly reduce the potential for internal overstressing of the EPS blocks. This restraint system enabled acceptable performance even for horizontal accelerations approaching 1 g. Based on these evaluations, six strands of Grade 270 cable having a diameter of 19-mm were recommended for prismatic rectangular shaped support systems of the configuration evaluated in this report.

However, even though the potential for significant uplift at inter-layer interfaces and at the basal foundation slab is eliminated by the cabling system, uplift at the foundation-soil interface may still occur during seismic rocking. However, the analysis herein suggests that the amount of uplift is relatively small (about 0.1 m) and is probably acceptable in terms of the overall seismic performance of the support system. Nonetheless, an exhaustive study of rocking and uplift for an EPS support system with cabling was included in this study.

Lastly, this study did not address the consequences of post-construction consolidation settlement in the foundation soils caused by the dead loads of the bridge support system. Such evaluations need to be performed on a site-specific basis to ensure that the anticipated amount of settlement is within acceptable limits. The use of a compensating or partially compensating foundation/embankment system can be used to reduce such settlement and increase sliding and rocking stability. In addition, the potential for kinematic interaction resulting from flexibility of the bridge system during seismic excitation was not evaluated by this study because the bridge structure was treated as a rigid mass. This topic and the design and detailing of the foundation and cable connections for the bridge support system warrant further study.

5 REFERENCES

Aaboe, R., and Frydenlund, T. E. (2011). "40 years of experience with the use of EPS geofoam blocks in road construction." *Proc., 4th Intl. Conf. on Geofoam Blocks in Construction Applications,* Lillestrom, Norway.

Aaboe, R. (1987). "13 Years of experience with expanded polystyrene as a lightweight fill material in road embankments." Norwegian Road Research Laboratory, Oslo, Norway, 21-27.

AASHTO (2012). AASHTO LRFD bridge design specifications, Washington DC 2001.

ASCE (2005). Seismic design criteria for structures, systems, and components in nuclear facilities, ASCE Standard 43-05, Reston, VA, USA.

ASTM D6817/D6817M "Standard Specification for Rigid Cellular Polystyrene Geofoam."

Amini, Z. A. (2014). "Dynamic characteristics and seismic stability of expanded polystyrene geofoam embankments." Ph.D. thesis, The University of Utah, Utah, USA.

ASTM D732 (2010). *Standard test method for shear strength of plastics by punch tool*, American society for testing and materials, West Conshohocken, PA, USA.

Athanasopoulos, G., Pelekis, P., and Xenaki, V. (1999). "Dynamic properties of EPS geofoam: an experimental investigation." *Geosynthetics International*, 6(3), 171-194.

Bartlett, S. F., Negussey, D., Kimble, M., and Sheeley, M (2000). "Use of geofoam as super-lightweight fill for I-15 reconstruction." *Proc., Transportation Research Board 79th Annual Meeting*, Transportation Research Board Washington, DC.

Bartlett, S. F., and Lawton, E. C (2008). "Evaluating the seismic stability and performance of freestanding geofoam embankment." *Proc., 6th National Seismic Conf. on Bridges and Highways*, Federal Highways Administration (FHWA) and Multidisciplinary Center for Earthquake Engineering Resarch (MCEER) Charleston, SC, 17.

Beinbrech, G., and Hillmann, R. (1997). "EPS in road construction current situation in Germany." *Geotextiles and Geomembranes*, 15(1), 39-57.

BenchmarkFoam (2009). "Physical properties of EPS." *Strength properties*, <http://benchmarkfoam.com/wpcontent/uploads/2009/09/physicalepsproperties_rev040510.pdf>. (November 15, 2014).

Brinch, H. (1953). *Earth pressure calculations*, Teknisk Forlag, Copenhagen.

Concrete-Properties (2014). "The engineering tool box." *Properties of normal strength Portland cement concrete*, <http://www.engineeringtoolbox.com/concrete-properties-d_1223.html>. (October 16, 2014).

Cowper, G. (1966). "The shear coefficient in Timoshenko's beam theory." *Journal of applied mechanics*, 33(2), 335-340.

Duškov, M. (1997). "Materials research on EPS20 and EPS15 under representative conditions in pavement structures." *Geotextiles and Geomembranes*, 15(1), 147-181.

EDO (1993). "EPS" EPS Devlopment Organization, 310 p. (in Japanese)

EPS White Book (2011). "EUMEPS Background Information on Standardization of EPS," Issued by EUMEPS in 2011, Version 31/03/11.

Elragi, A. F. (2000). "Selected engineering properties and application of EPS geofoam." Ph.D. thesis, State University of New York, Syracuse, USA.

Farnsworth, C., Bartlett, S. F., Negussey, D., and Stuedlein, A. (2008). "Rapid construction and settlement behavior of embankment systems on soft foundation soils." *Journal of geotechnical and geoenvironmental engineering*, 134(3), 289-301.

Geocomp (2006). "Triaxial cyclic user's manual."Boxborough, MA, USA, 71p.

Holtz, R. D., Kovacs, W. D., and Sheahan, T. C. (2010). *An introduction to geotechnical engineering*, Pearson, New Jersey, USA.

Horvath, J. S. (2004). "A tenchical note re calculating the fundamental period of an EPS-block-geofoam embankment." *Rpt. No. CGT-2004*, Manhattan College, School of Engineering, Bronx, New York, USA.

Horvath, J. S. (1995). *Geofoam geosynthetic*, Horvath Engr., P.C., Scarsdale, New Work, USA.

Horvath, J. (1994). "Expanded polystyrene (EPS) geofoam: an introduction to material behavior." *Geotextiles and Geomembranes*, 13(4), 263-280.

Housner, G. W. (1963). "The behavior of inverted pendulum structures during earthquakes." *Bulletin of the seismological society of America*, 53(2), 403-417.

Itasca (2005). "FLAC: Fast Lagrangian Analysis of Continua: structural elements, version 5." Minneapolis, MN.

Itasca (2006). "FLAC: Fast Lagrangian Analysis of Continua: structural elements, version 3.1." Minneapolis, MN.

Lingwall, B. N. (2011). "Development of an expanded polystyrene geofoam cover system for pipelines at fault crossings." Ph.D. Thesis, The University of Utah, Utah, USA.

MacGregor, J. G., and Wight, J. K. (2005). *Reinforced concrete design*, Pearson Prentice Hall, New Jersey.

Makdisi, F. I., and Seed, H. B. (1978). "Simplified procedure for estimating dam and embankment earthquake-induced deformations." *Journal of Geotechnical Engineering* 104(7), 849-867.

Maybehire (2012). "Quickbridge." *Specifications*, <http://www.mabeyhire.co.uk/temporary-bridging/quickbridge/>. (November 16, 2014).

McDonald, P., and Brown, P. (1993). "Ultra lightweight polystyrene for bridge approach fill." *Proc., 11th Southeast Asian Geotechnical Conference,* Singapore, 664-668.

Modjeski-Masters-Inc (2003). "Comprehensive design example for prestressed concrete girdger superstructure bridge with commentry."REPORT FHWA NHI -04-043, Pennsylvania, USA.

NCHRP 529 (2004). "Guideline and Recommended Standard for Geofoam Applicatinos in Highway Embankments," National Cooperative Highway Research Program (NCHRP), Transportation Research Board, Washington, D.C.

NCHRP Web Document No. 65*, "*Geofoam applications in the design and construction of highway embankments," Stark, T.D., Arellano, D, Horvath, J.S., Leshchinsky, D., NCHRP Project 24-11.

Newman, M. P., Bartlett, S., and Lawton, E. (2009). "Numerical modeling of geofoam embankments." *Journal of geotechnical and geoenvironmental engineering*, 136(2), 290-298.

Riad, H. L., and Horvath, J. S. (2004). "Analysis and design of EPS-geofoam embankments for seismic loading." *Proc., Geotechnical Engineering for Transportation Projects*, ASCE, Los Angeles, California, USA, 2028-2037.

Refsdal, G. (1985). "Plastic foam in road embankments: future trends for EPS use." Internal Report, Norwegian Road Research Laboratory, Oslo, Norway.

Seed, H. B., and Idriss, I. (1982). *Ground motions and soil liquefaction during earthquakes*, Earthquake Engineering Research Institute, Oakland, California, USA.

Sheeley, M., and Negussey, D. (2001). "An investigation of geofoam interface strength behavior." ASCE *Geotechnical Special Publication*, 292-303.

Snow, C. L., and Nickerson, C. R. (2004). "Case Study of EPS Geofoam Lightweight Fill for Settlement Control at Bridge Approach Embankment." *Proc., Geotechnical Engineer*

Srirajan, S., Negussey, D., and Anasthas, N. (2001). "Creep Behavior of EPS Geofoam," Proceedings of EPS 2001, 3rd International Conference, Dec. 10th-12, 2001, Salt Lake City, Utah, 12 p.

Stark, T., Arellano, D., Horvath, J., and Leshchinsky, D. (2004). "Guideline and recommended standard for geofoam applications in highway embankments."NCHRP Report 529, Transportation Research Board, Washington, D.C.

Stark, T., Arellano, D., Horvath, J., and Leshchinsky, D. (2000). "Guidelines for geofoam applications in embankment projects." *by National Cooperative Highway Research Program, Project*(24-11).

Stuedlein, A. W., and Negussey, D. (2013). "Use of EPS geofoam for support of a bridge." *Sound Geotechnical Research to Practice: Honoring Robert D. Holtz, Geotechnical Special Publication*(230), 334-345.

Tefera, T. H., Aaboe, R., Bruum, H., and Aunaas, K. (2011). "FEM simulation of full scale and laboratory model tests of EPS." The Norwegian Public Roads Administration, Norway.

Timoshenko, S., and Gere, J. M. (1972). *Mechanics of materials*, Van Nostrand Reinhold Co., New York, USA.

Trandafir, A. C., Bartlett, S. F., and Lingwall, B. N. (2010). "Behavior of EPS geofoam in stress-controlled cyclic uniaxial tests." *Geotextiles and Geomembranes*, 28(6), 514-524.

Tsukamoto, H. (2011). "History of R&D and design code for EDO-EPS method in Japan."Oslo, Norway

Zou, Y., Leo, C., and Small, J. (2000). "Behaviour of EPS geofoam as flexible pavement subgrade material in model tests." *Geosynthetics International*, 7(1), 1-22.

APPENDIX A - SIZING OF BRIDGE AND SUPPORT SYSTEM

Steel Bridge

Selection of Type of Steel Bridge

Acrow Bridge

From the personal communication with Acrow bridges regional office in Colorado (Needham, Randy), the maximum dead load including all elements of bridge for single lane road with one sided sidewalk is 5.25 m.

Width of sidewalk,

$B_{sidewalk} := 1.5;$ = 1.50 m

$B_{single-lane} := 3.75;$ = 3.75 m

$B_{total-single} := B_{sidewalk} + B_{single-lane};$ = 5.25 m

$DL := 1.04;$ = 1.04 tons/ft

Dead load in terms of SI unit is,

$DL_{Acrow} := \frac{1.04 \cdot 2 \cdot 1000}{68.52177};$ = 30.35532 kN/m

Mabey Bridge

The Mabey bridge website provides the information on quick bridges and its dimensions. From the information, the longest length of flat top type bridges was considered for the calculation.

Modular width,

$B_m := 1.725;$ = 1.725 m

Unit weight excluding parapet,

$M_{without\ parapet} := 14250;$ = 14250.0 kg

Parapet and curb weight (one side),

$M_{parapet-kerb(one\ side)} := 1960;$ = 1960.0 kg

Parapet and kerb weight on both sides,

$M_{parapet-kerb(one\ side)} := 2 \cdot M_{parapet-kerb(one\ side)};$ = 3920.0 kg

Total weight for single unit,

$M_{total} := M_{without\ parapet} + M_{parapet-kerb(one\ side)};$ =18170.0 kg

$DL_{Mabey} := M_{total} \cdot \frac{9.81}{1000} \cdot \frac{1}{B_m} \cdot B_{total-single} \cdot \frac{1}{20};$ = 27.125 kN/m

From the calculation of dead load of two bridges, it was found that weight per linear meter of Acrow bridges are slightly higher. So, weight per linear meter of Acrow bridge is considered for sizing of steel bridge.

$DL_{bridge} := \max(DL_{Acrow}, DL_{Mabey});$ = 30.35 kN/m

Load Calculation

Calculation of Dead Load

Width of pavement for double lane,

$B_{pavement} := 7.5;$ = 7.50 m

Width of bridge,

$B_{bridge} := B_{pavement} + B_{sidewalk};$ = 9.00 m

$DL_{bridge-double\ lane} := DL_{bridge} \cdot \frac{B_{bridge}}{B_{total-single}};$ = 52.038 kN/m

Footing dimensions are,

$B_{footing} := 9;$ = 9.00 m

$L_{footing} := 4;$ = 4.00 m

$\Upsilon_{concrete} := 23.56;$ = 23.56 kN/m^3

$h_{concrete} := 0.50;$ = 0.50 m

Dead load of footing,

$DL_{footing} := \Upsilon_{concrete} \cdot h_{concrete} \cdot B_{footing} \cdot L_{footing};$ = 424.08 kN

Total dead load from footing on both sides of abutment,

$DL_{footing-total} := 2 \cdot DL_{footing};$ = 848.16 kN

Calculation of Allowable Load

The compressive strength based on ASTM D6817 at 1 percent strain,

$\sigma_c := 75;$ = 75.00 kPa

Axial strain,

$\varepsilon_a := 0.01;$ = 0.01

$A_{footing} := L_{footing} \cdot B_{footing};$ = 36.00 m

Allowable load,

$Q := \sigma_c \cdot A_{footing};$ = 2700.00 kN

Maximum load that can support by abutment on both sides of bridge.

$Q_{allowable} := 2 \cdot Q;$ = 5400.00 kN

Calculation of Live Load

Live load of the truck was calculated from the loading configuration given in AASHTO 2012.The spacing between rear axle to driver axle and front vehicle to back vehicle is 14 ft and 5 ft respectively.

Length of loading,

$L_{loading} := \frac{(14 + 14 + 5)}{3.281};$ = 10.06 m

Point load,

$W_{point} := (32 + 32 + 8) \cdot 4.4482;$ = 320.27 kN

Load per meter run,

$LL := \frac{W_{point}}{L_{loading}} \cdot 2;$ = 63.68 kN/m

Calculation of Length of Bridge

Length of bridge is obtained from trial and error method.

$L_{bridge} := 31.6;$ = 31.60 m

Applied total load is,

$Q_{applied} := DL_{bridge-double\ lane} \cdot L_{bridge} + DL_{footing-total} + LL \cdot L_{bridge};$ = 4505.01 kN

Factor of safety,

$FS := \frac{Q_{allowable}}{Q_{applied}};$ = 1.20

Length of bridge for design,

$L_{bridge-design} := 31.0;$ = 31.0 m

Concrete Bridge

Width of pavement for double lane,

$B_{pavement} := 7.5;$ = 7.50 m $B_{sidewalk} := 1.5;$ = 1.50 m

Width of bridge,

$B_{bridge} := B_{pavement} + B_{sidewalk};$ = 9.00 m

Calculation of Dead Load

The calculation was made based on the comprehensive design example of concrete girder super structure bridge by Modjeski and Masters Inc. (2003),

Unit weight of concrete,

$\Upsilon_{concrete} := \frac{150}{6.366};$ = 23.56 kN/m

Design of Deck

Thickness,

$t := \frac{8}{12 \cdot 3.281};$ = 0.20 m

Deck weight per meter,

$W_{deck} := B_{pavement} \cdot \Upsilon_{concrete} \cdot t;$ = 35.91 kN/m

Design of Girder

Longitudinal girder,

Cross-sectional area of girder,

$A_{long-girder} := \frac{1085}{(12 \cdot 3.281)^2};$ = 0.70 m^2

Girder spacing,

$S_{long} := \frac{10}{3.281};$ = 3.05 m

Number of girders,

$N_{long} := 3;$ = 3

Girder weight per meter,

$W_{long-girder} := \Upsilon_{concrete} \cdot A_{long-girder} \cdot N_{long};$ = 49.48 kN/m

Cross Girder,

Cross-sectional area of girder,

$A_{cross-girder} := \frac{1085}{(12 \cdot 3.281)^2};$ = 0.70 m^2 $S_{cross} := \frac{25}{3.281};$ = 7.62 m

Number of girders,

$N_{cross} := 3;$ = 3

Girder weight per meter per width,

$W_{cross-girder} := \Upsilon_{concrete} \cdot A_{cross-girder} \cdot N_{cross};$ = 49.48 kN/m

Design of Parapet Wall

Cross-sectional area of parapet,

$A_{cross-parapet} := \frac{4.33}{3.281^2};$ = 0.402 m^2

Parapet weight per meter,

$W_{parapet} := \Upsilon_{concrete} \cdot A_{cross-parapet};$ = 9.48 kN/m

Number of parapets,

$N_{parapets} := 2;$ = 2

Total weight of parapets,

$W_{total-parapets} := N_{parapets} \cdot W_{parapet};$ = 18.95 kN/m

Design of Wearing Surface

Weight per meter square,

$W_{per-m2-wearing} := 0.03 \cdot 47.8802;$

$W_{per-meter-wearing} := W_{per-m2-wearing} \cdot B_{pavement};$ = 10.77 kN/m

Dead load per meter of bridge,

$DL_{per-meter} := W_{deck} + W_{long-girder} + W_{total-parapets} + W_{per-meter-wearing};$ = 115.11 kN/m

Footing dimensions,

$B_{footing} := 9;$ = 9.00 m

$L_{footing} := 4;$ = 4.00 m

$h_{concrete} := 0.50;$ = 0.50 m

Dead load from footing,

$DL_{footing} := \Upsilon_{concrete} \cdot h_{concrete} \cdot B_{footing} \cdot L_{footing};$ = 424.13 kN

Total dead load from footing on both sides of abutment,

$DL_{footing-total} := 2 \cdot DL_{footing};$ = 848.26 kN

Calculation of Allowable Load

Compressive strength based on ASTM D6817 at 1 percent strain is,

$\sigma_c := 75;$ = 75.00 kPa

Axial strain,

$\varepsilon_a := 0.01;$ = 0.01 $A_{footing} := L_{footing} \cdot B_{footing};$ = 36.00 m

Allowable load,

$Q := \sigma_c \cdot A_{footing};$ = 2700.00 kN

Maximum load that can be supported by abutment on both sides of bridge,

$Q_{allowable} := 2 \cdot Q;$ = 5400.00 kN

Calculation of Live Load

Live load from the truck,

According to AASHTO 2012, the spacing between rear axle to driver axle and front vehicle to back vehicle is 14 ft and 5 ft respectively.

Length of loading,

$L_{loading} := \frac{(14 + 14 + 5)}{3.281};$ = 10.06 m

Point load,

$W_{point} := (32 + 32 + 8) \cdot 4.4482;$ = 320.27 kN

Load per meter run,

$LL := \frac{W_{point}}{L_{loading}} \cdot 2;$ = 63.68 kN/m

Length of bridge was obtained from trial and error method.

$L_{bridge} := 17.9;$ = 17.90 m

Calculation of Length of Bridge

Applied total load,

$Q_{applied} := DL_{per-meter} \cdot L_{bridge} + DL_{footing-total} + LL \cdot L_{bridge} + W_{cross-girder} \cdot B_{bridge};$ = 4494.03 kN/m

Factor of safety,

$FS := \frac{Q_{allowable}}{Q_{applied}};$ = 1.20

Length of bridge for design,

$L_{bridge-design} := 18.0;$ = 18.0 m

APPENDIX B - FUNDAMENTAL PERIOD CALCULATIONS

Rectangular Prism

Density of EPS,

$\rho := 34.02;$ = 34.02 kg/m^3

Height of embankment,

$H := 6;$ = 6 m

Width of embankment,

$B := 9;$ = 9.00 m

Length of embankment,

$L := 4;$ = 4 m

Young's modulus of elasticity,

$E_c := 12547;$ = 12547 kPa

Poisson's ratio from Horvath (1995),

$\nu := 0.0056 \cdot \rho + 0.0024;$ = 0.192912

Shear modulus,

$$G := \frac{E_c}{2 \cdot (1 + \nu)};$$ = 5259 Pa

$g := 9.81;$ = 9.81 m/sec^2

Dead load from bridge,

$DL_{bridge} := 806.58;$ = 806.58 kN

Live load is taken as half of the live load from truck,

$LL_{truck} := 987.13;$ = 987.13 kN

Dead load from foundation,

$DL_{foundation} := 424.08;$ = 424.08 kN

Total load,

$$W := \left(DL_{bridge} + 0.5 \cdot LL_{truck} + DL_{foundation}\right);$$ = 1724.22 kN

Vertical effective stress at top of foundation,

$$\sigma_{v(prime)} := \frac{W}{L \cdot B};$$ = 47.89513889

Method I

Excitation along longitudinal-direction,

$$T_0 := \text{evalf}\left(2 \cdot \pi \cdot \left(\frac{\sigma_{v(prime)} \cdot H}{E_c \cdot g}\left(4 \cdot \left(\frac{H}{L}\right)^2 + \left(\frac{12 + 11 \cdot \nu}{5}\right)\right)\right)^{0.5}\right);$$ = 1.0440 sec

Excitation along transverse-direction,

$$T_0 := \text{evalf}\left(2 \cdot \pi \cdot \left(\frac{\sigma_{v(prime)} \cdot H}{E_c \cdot g}\left(4 \cdot \left(\frac{H}{B}\right)^2 + \left(\frac{12 + 11 \cdot \nu}{5}\right)\right)\right)^{0.5}\right);$$ = 0.6513 sec

Method II

Excitation along longitudinal-direction,

$$T_0 := \text{evalf}\left(2 \cdot \pi \cdot \left(\frac{\sigma_{v(prime)} \cdot H}{E_c \cdot g}\left(4 \cdot \left(\frac{H}{L}\right)^2 + 1 + \left(\frac{12 + 12 \cdot \nu}{5}\right)\right)\right)^{0.5}\right);$$ = 1.0888 sec

Excitation along transverse-direction,

$$T_0 := \text{evalf}\left(2\cdot\pi\cdot\left(\frac{\sigma_{v(prime)}\cdot H}{E_c\cdot g}\left(4\cdot\left(\frac{H}{B}\right)^2+1+\left(\frac{12+12\cdot\nu}{5}\right)\right)\right)^{0.5}\right); \quad = 0.7210 \text{ sec}$$

Analytical Method

Excitation along vertical-direction,

$$T_0 := \text{evalf}\left(2\cdot\pi\cdot\left(\frac{\sigma_{v(prime)}\cdot H}{E_c\cdot g}\right)^{0.5}\right); \quad = 0.3036 \text{ sec}$$

Trapezoidal Prism

Density of EPS,

$\rho := 34.02;$ = 34.02 kg/m^3

Height of embankment,

$H := 6;$ = 6 m

Width of embankment,

$B := 9;$ = 9.00 m

Length of embankment at top,

$L_{top} := 4;$ = 4 m

Slope of an embankment is 2H: 1V.

Length of embankment at bottom,

$L_{bottom} := L_{top} + 2\cdot 2\cdot H;$ = 28.00 m

Volume of trapezoidal section,

$$V_{trapezoidal-section} := B\cdot\frac{L_{top}+L_{bottom}}{2}\cdot H; \quad = 864.00 \text{ m^3}$$

According to Horvath (1995),

The equivalent length of prismatic section,

$$L := \frac{V_{trapezoidal-section}}{B\cdot H}; \quad = 16.00 \text{ m}$$

Young's modulus of elasticity,

$E_c := 12547;$ = 12547 Kpa

Poisson's ratio from Horvath (1995),

$\nu := 0.0056\cdot\rho + 0.0024;$ = 0.192912

Shear modulus,

$$G := \frac{E_c}{2\cdot(1+\nu)}; \quad = 5259 \text{ Pa}$$

$g := 9.81;$ = 9.81 m/sec^2

Dead load from bridge,

$DL_{bridge} := 806.58;$ = 806.58 kN

Live load is taken as half of the live load from truck,

$LL_{truck} := 987.13;$ = 987.13 kN

Dead load from foundation,

$DL_{foundation} := 424.08;$ = 424.08 kN

Total load,

$W := (DL_{bridge} + 0.5\cdot LL_{truck} + DL_{foundation});$ = 1724.22 kN

Vertical effective stress at top of foundation,

$$\sigma_{v(prime)} := \frac{W}{L \cdot B}; \quad = 11.97378472$$

Method I

Excitation along longitudinal-direction,

$$T_0 := evalf\left(2 \cdot \pi \cdot \left(\frac{\sigma_{v(prime)} \cdot H}{E_c \cdot g}\left(4 \cdot \left(\frac{H}{L}\right)^2 + \left(\frac{12 + 11 \cdot \nu}{5}\right)\right)\right)^{0.5}\right); \quad = 0.2794 \text{ sec}$$

Excitation along transverse-direction,

$$T_0 := evalf\left(2 \cdot \pi \cdot \left(\frac{\sigma_{v(prime)} \cdot H}{E_c \cdot g}\left(4 \cdot \left(\frac{H}{B}\right)^2 + \left(\frac{12 + 11 \cdot \nu}{5}\right)\right)\right)^{0.5}\right); \quad = 0.3256 \text{ sec}$$

Method II

Excitation along longitudinal-direction,

$$T_0 := evalf\left(2 \cdot \pi \cdot \left(\frac{\sigma_{v(prime)} \cdot H}{E_c \cdot g}\left(4 \cdot \left(\frac{H}{L}\right)^2 + 1 + \left(\frac{12 + 12 \cdot \nu}{5}\right)\right)\right)^{0.5}\right); \quad = 0.3193 \text{ sec}$$

Excitation along transverse-direction,

$$T_0 := evalf\left(2 \cdot \pi \cdot \left(\frac{\sigma_{v(prime)} \cdot H}{E_c \cdot g}\left(4 \cdot \left(\frac{H}{B}\right)^2 + 1 + \left(\frac{12 + 12 \cdot \nu}{5}\right)\right)\right)^{0.5}\right); \quad = 0.3605 \text{ sec}$$

Analytical Method

Excitation along vertical-direction,

$$T_0 := evalf\left(2 \cdot \pi \cdot \left(\frac{\sigma_{v(prime)} \cdot H}{E_c \cdot g}\right)^{0.5}\right); \quad = 0.1518 \text{ sec}$$

APPENDIX C - MODEL PARAMETERS

Foundation Material

$t1 := 0.50;$ = 0.50 m

$w := 9;$ = 9.00 m

$l1 := 4;$ = 4.00 m

$A := w \cdot l1;$ = 36.00 m^2

Assumptions,

$f_{prime(c)} := 5000;$ = 5000.00 psi

$\rho := 2400;$ = 2400.00 kg/m^3

From Reinforced Concrete Mechanics and Design Book (James G. MacGregor and James K. Wight), Poisson's ratio is in the range of 0.15 to 0.20.

$\nu := 0.18;$ = 0.18

$\Upsilon := 150;$ = 150.00 pcf

$W := \Upsilon;$ = 150.00 pcf

$Ec := 33 \cdot \left(W^{1.5}\right) \cdot \left(f_{prime(c)}\right)^{0.5} \cdot 6.89475729 \cdot 1e3;$ = $2.955662309\,10^{10}$ Pa

$G := \frac{Ec}{2 \cdot (1 + \nu)};$ = $12.52399283 \times 10^{09}$ Pa

$K := \frac{Ec}{3 \cdot (1 - 2 \cdot \nu)};$ = $15.3940745 \times 10^{09}$ Pa

Density of Foundation Material

From AASHTO 2012,

For extreme event, the live load factor is 0.5.

$DL_{foundation} := 23.56 \cdot t1 \cdot w \cdot l1;$ = 424.0800 kN

$Volume := t1 \cdot w \cdot l1;$ = 18.00 m^3

$Mass := \frac{\left(DL1 + 0.5 \cdot LL + DL_{foundation}\right)}{9.81} \cdot 1000;$ = $1.757619776\,10^{5}$ **kg**

$\rho := \frac{Mass}{Volume};$ = 9764.554311 **kg/m^3**

EPS Embankment

$h := 6.0;$ = 6.00 m

$w := 9;$ = 9.00 m

$l := 4;$ = 4.00 m

$Ec := 12547 \cdot 1e3;$ = 12.5470000×10^{6} **Pa**

$\rho := 34.02;$ = 34.02 kg/m^3

$\nu := 0.193;$ = 0.193

$G := \frac{Ec}{2 \cdot (1 + \nu)};$ = 5.2585918×10^{06} **Pa**

$K := \frac{Ec}{3 \cdot (1 - 2 \cdot \nu)};$ = 6.8116178×10^{06} **Pa**

Load from Bridge,

$DL1 := 806.58;$ = 806.58 kN

$LL := 987.13;$ = 987.13 kN

Base Soil

$E := 2e7;$ = 20.0000000×10^{6} **Pa**

$\rho := 1900;$ = 1900.00 kg/m^3

$\nu := 0.4;$ $= 0.4$

$G_{soil} := \frac{E}{2\cdot(1+\nu)};$ $= 7.1428571 \times 10^{06}$ **Pa**

$K_{soil} := \frac{E}{3\cdot(1-2\cdot\nu)};$ $= 3.3333333 \times 10^{07}$ **Pa**

Stiffness at Interface

From FLAC 3D manual the stiffness at interface is,

$$k_n := \left(\frac{K_{geofoam} + \frac{4}{3}\cdot G_{geofoam}}{\Delta z} \right);$$

Where, K and G are the bulk and shear moduli respectively. k_n and k_s are the normal and shear stiffness which are equal and Δz_{min} is the smallest width of an adjoining zone in the normal direction.

$\Delta z := 0.5;$ $= 0.5$

$$k_n := \left(\frac{K_{geofoam} + \frac{4}{3}\cdot G_{geofoam}}{\Delta z} \right);$$ $= 2.764614704\,10^{7}$ Pa

$k_s := k_n;$ $= 2.764614704\,10^{7}$ Pa

According to Amini (2014),

$k_{n1} := 50\cdot k_n;$ $= 1.382307352\,10^{9}$ Pa

$k_{s1} := 50\cdot k_s;$ $= 1.382307352\,10^{9}$ Pa

APPENDIX D - FLAC FUNDAMENTAL PERIOD CALCULATION

Fundamental period
Free Vibration

The FLAC code for the calculation of fundamental period under free vibration for 4 m long and double lane wide rectangular prism for the excitation along longitudinal-direction is given below.

```
;  Fundamental Time Period Calculation
;   Excitation along –longitudinal-direction
;  Free standing embankment with foundation for bridge at top
;  Length is equal to length of footing
;  Double lane with width of 9 m
new
;
;set mechanical ratio 1e-3
;
config dyn
set large
;----------GENERATE THE MODEL----------------------------
;Generate the EPS embankment below foundation
gen zone brick p0(0,0,0) p1(4,0,0) p2(0,9,0) &
p3(0,0,6)&
                    size 8,18,12 group E1
;
;Generate the foundation
gen zone brick p0(0,0,6) p1(4,0,6) p2(0,9,6) &
p3(0,0,6.5) &
                    size 8,18,1 group F1
;
;---------Assign material properties-----------------
model elas range group E1
prop bulk 6.8116e6 shear 5.2586e6 range group E1
;
model elas range group F1
prop bulk 15.3941e9 shear 12.524e9 range group F1
;
ini dens 34.02 range group E1
;
ini dens 9764.55 range group F1
;
;-------COLOR OF THE GROUP------------
group 1 Red range group E1
group 2 blue range group F1
;
;---BOUNDARY CONDITIONS FOR DYNAMIC CASE------------
fix y z range z -0.1,0.1
;----------SET DAMPING--------------------
;set dyn damp rayleigh 0.02 2
;
;------ Sin, Cos WAVE AS INPUT MOTION------------------
def setup
 omega=2*pi*freq
 period=1/freq
end
```

```
 set freq=1.8
setup
;Free Vibration(Pulse Loading)
def wave
if dytime>period
 wave=0
else
 wave=amp*sin(omega*dytime)
  endif
end
set amp=0.5
;
;Forced Vibration
;wave=amp*cos(2*pi/period*dytime)
;end
;
;---------FORCING FUNCTION--------------
apply xvel=1 hist wave range z -0.1,0.1
;apply yvel=1 hist wave range z -0.1,0.1
;apply zvel=1 hist wave range z -0.1,0.1
;
;--------HISTORIES-----------------------
his id 2 gp xdisp 0,0,0
his id 3 gp xdisp 0,0,6.5
his id 4 gp xvel 0,0,0
his id 5 gp xvel 0,0,6.5
his id 6 gp xacc 0,0,0
his id 7 gp xacc 0,0,6.5
;his id 8 gp ydisp 0,0,0
;his id 9 gp ydisp 0,0,6.5
;his id 10 gp yvel 0,0,0
;his id 11 gp yvel 0,0,6.5
;his id 12 gp yacc 0,0,0
;his id 13 gp yacc 0,0,6.5
his id 14 dytime
his id 15 wave
;
;-------------SOLVE FOR DYNAMIC----------
solve age 10
;
save fund1.sav
;
rest fund1
;
plot set title text
X displacement at top of embankment for 4 m length of footing
plot hist 3 vs 14
plot show
;-------------HISTORY OUTPUT IN TEXT FILE-----------
his write 3 vs 14 file Xforce.his
```

APPENDIX E - SLIDING MODE OF EPS EMBANKMENT

Rectangular Prism
Critical Acceleration

Bridge load,

$DL_{bridge} := 806.58;$ = 806.58 kN

$LL_{bridge} := 987.13;$ = 987.13 kN

Foundation load,

$DL_{foundation} := 424.08;$ = 424.08 kN

Geofoam embankment geometry,

$B := 9;$ = 9.00 m

$H := 6;$ = 6.00 m

$L := 4;$ = 4.00 m

Assumptions:

Soil below the embankment is sand. The vertical acceleration is negligible. The accelerations along longitudinal and transverse directions of the bridge are same. The spectral and peak ground acceleration is same. The block height is assumed to be 1m.

$g := 9.81;$ = 9.81 m/sec^2

Calculations:

The calculation of basal layer at zero interface is shown in Table E.1.

$$\sigma_{v0} := \frac{DL_{bridge} + 0.5 \cdot LL_{bridge} + DL_{foundation}}{(L \cdot B)};$$ = 47.8951 kPa

From the relation given by Sheeley and Negussey (2000), friction factor for geofoam-geofoam interface is:

$\tan\delta$ = 0.81

Table E.1. Calculation of critical acceleration for rectangular prism

Interface ----------	Horizontal acceleration (g)	Mass/unit area (kg/m2)	Inertial force (N/m2)	Frictional resisting force (W/K) (N/m2)	Frictional resisting force (WO/K) (N/m2)	Shear key coverage (%)	Cohesive resisting force (N/m2)	FS sliding (without key) ----------	FS sliding (with key) ----------
6	0.599	5020	29519	39886	39886	0	0	1.35	1.35
5	0.599	5020	29519	39886	39886	0	0	1.35	1.35
4	0.599	5020	29519	39886	39886	0	0	1.35	1.35
3	0.599	5020	29519	39886	39886	0	0	1.35	1.35
2	0.599	5020	29519	39886	39886	0	0	1.35	1.35
1	0.599	5020	29519	39886	39886	0	0	1.35	1.35
0	0.599	5020	29519	29545	29545	0	0	1.00	1.00

The relation given by Bartlett et al. (2000), the friction factor for geofoam-soil interface is:

$\tan\delta = 0.6$

Geofoam shear strength from Benchmark Foam (2009) is:

$\tau := \frac{33 \cdot 144 \cdot 95}{2000};$ $= 225.7200$ kPa

The critical acceleration was obtained from the goal seek in spreadsheet. The calculation for 6 layers is shown in Table E.1.

$a_{critical} := 0.5995;$ $= 0.5995$ g

Sample calculation for basal layer,

Mass per unit area,

$m := \frac{\sigma_{v0} \cdot 1000}{9.81};$ $= 4882.277$ kg/m^2

Inertial force,

$F_{inertial} := m \cdot a_{critical} \cdot g;$ $= 28713.136$ N/m^2

Frictional resisting force,

$F_{resisting} := \sigma_{v0} \cdot 0.6 \cdot 1000;$ $= 28737.083$ N/m^2

Factor of safety against sliding,

$FS_{sliding} := \frac{F_{resisting}}{F_{inertial}};$ $= 1.00$

Shear Key Coverage

Bridge load,

$DL_{bridge} := 806.58;$ $= 806.58$ kN

$LL_{bridge} := 987.13;$ $= 987.13$ kN

Foundation load,

$DL_{foundation} := 424.08;$ $= 424.08$ kN

Ground soil properties,

$\Upsilon_{soil} := \frac{1900 \cdot 9.81}{1000};$ $= 18.64$ kN/m^2

$\phi_{soil} := \text{evalf}\left(\frac{\pi}{180} \cdot 35\right);$ $= 0.6108652381$

$\delta_{soil} := \text{evalf}\left(\frac{\pi}{180} \cdot 31\right);$ $= 0.5410520681$

$c := 0;$ $= 0$

Geofoam embankment geometry,

$B := 9;$ $= 9.00$ m

$H := 6;$ $= 6.00$ m

$L := 4;$ $= 4.00$ m

Assumptions:

Soil below the embankment is sand. The vertical acceleration is negligible. The acceleration along longitudinal and transverse directions of the bridge are same. The spectral and peak ground acceleration is same. The block height is assumed to be 1m.

$g := 9.81;$ $= 9.81$ m/sec^2

Calculations:

The calculation for the top layer is shown in Table E.2.

$\sigma_{v0} := \frac{DL_{bridge} + 0.5 \cdot LL_{bridge} + DL_{foundation}}{(L \cdot B)};$ $= 47.8951$ kPa

From the relation given by Sheeley and Negussey (2000), the friction factor for geofoam-geofoam interface is: $\tan\delta = 0.81$

Table E.2. Calculation of shear key coverage for rectangular prism

Interface	Horizontal acceleration (g)	Mass/unit area (kg/m^2)	Inertial force (N/m^2)	Frictional resisting force (W/K) (N/m^2)	Frictional resisting force (WO/K) (N/m^2)	Shear key coverage (%)	Cohesive resisting force (N/m^2)	FS sliding (without key)	FS sliding (with key)
6	1.000	5020	49242	36695	39886	8	18058	0.81	1.11
5	1.000	5020	49242	36695	39886	8	18058	0.81	1.11
4	1.000	5020	49242	36695	39886	8	18058	0.81	1.11
3	1.000	5020	49242	36695	39886	8	18058	0.81	1.11
2	1.000	5020	49242	36695	39886	8	18058	0.81	1.11
1	1.000	5020	49242	36695	39886	8	18058	0.81	1.11
0	1.000	5020	49242	29545	29545	0	0	0.60	0.60

The friction factor for geofoam-soil according to Bartlett et al. (2000) is:

$\tan\delta = 0.6$

Geofoam shear strength from Benchmark Foam (2009),

$\tau := \frac{33 \cdot 144 \cdot 95}{2000};$ = 225.7200 kPa

For the acceleration of 1 g,

$a_x := 1;$ = 1 g

$a_y := 1;$ = 1 g

$a_z := 0;$ = 0

Mass per unit area,

$m := \frac{\sigma_{v0} \cdot 1000}{9.81};$ = 4882.277 kg/m^2

Inertial force,

$F_i := m \cdot a_x \cdot g;$ = 47895.139 N/m^2

Frictional resisting force,

$F_r := \sigma_{v0} \cdot 0.81 \cdot 1000;$ = 38795.062 N/m^2

Factor of safety against sliding,

$FS_{sliding} := \frac{F_r}{F_i};$ = 0.81

The factor of safety against sliding is 0.81. Following is the calculation for first layer. Similar calculations were made for other layers. The factor of safety should be in the range of 1.1 to 1.2 to make the structure safe against sliding. The shear key coverage was assumed to increase the factor of safety.

Shear key coverage = 8 percent

$S_c := \frac{8}{100};$ = 0.08

Frictional resisting force,

$F_r := \sigma_{v0} \cdot 0.81 \cdot 1000 \cdot (1 - S_c);$ = 35691.46 N/m^2

Cohesive resisting force,

$C_r := \tau \cdot 1000 \cdot S_c;$ = 18057.60 N/m^2

Factor of safety against sliding,

$FS_{sliding} := \frac{F_r + C_r}{F_i};$ = 1.12

Embedment Depth for Excitation along Longitudinal-direction

Bridge load,

$DL_{bridge} := 806.58;$ = 806.58 kN

$LL_{bridge} := 987.13;$ = 987.13 kN

Foundation load,

$DL_{foundation} := 424.08;$ = 424.08 kN

Ground soil properties,

$\Upsilon_{soil} := \frac{1900 \cdot 9.81}{1000};$ = 18.64 kN/m^2

$\phi_{soil} := \text{evalf}\left(\frac{\pi}{180} \cdot 35\right);$ = 0.6108652381

$\delta_{soil} := \text{evalf}\left(\frac{\pi}{180}\cdot 31\right);$ $= 0.5410520681$

$c := 0;$ $= 0$

Geofoam embankment geometry,

$B := 9;$ $= 9.00$ m

$H := 6;$ $= 6.00$ m

$L := 4;$ $= 4.00$ m

Assumptions:

Soil below the embankment is sand. The vertical acceleration is negligible. The accelerations along longitudinal and transverse directions of the bridge are same. The spectral and peak ground acceleration is same. The block height is assumed to be 1m.

$g := 9.81;$ $= 9.81$ m/sec^2

Calculations:

For the acceleration of 1 g,

$a_x := 1;$ $= 1$ g

$a_y := 1;$ $= 1$ g

$a_z := 0;$ $= 0$

The basal layer sliding requires embedment to stop sliding. The calculation of active earth pressure for seismic case is same as static. Coulomb's equation was used.

$\beta := \text{evalf}\left(\frac{\pi}{180}\cdot 0\right);$ $= 0.0000$

The backfill slope angle,

$i := 0;$ $= 0$

$$K_A := \text{evalf}\left(\left(\cos^2\left(\phi_{soil}-\beta\right)\right) \Big/ \left(\cos^2(\beta)\cdot\cos\left(\delta_{soil}+\beta\right)\cdot\left(1 + \sqrt{\frac{\sin\left(\delta_{soil}+\phi_{soil}\right)\cdot\sin\left(\phi_{soil}-i\right)}{\cos\left(\delta_{soil}+\beta\right)\cdot\cos(i-\beta)}}\right)^2\right)\right);$$ $= 0.2465569320$

$D1 := 1.4;$ $= 1.40$ m

$P_A := 0.5\cdot K_A\cdot \Upsilon_{soil}\cdot D1^2\cdot B;$ $= 40.5330$ kN

$P_{AE} := P_A;$ $= 40.5330$ kN

$P_{AEH} := P_{AE}\cdot\cos\left(\delta_{soil}\right);$ $= 34.7435$ kN

$P_{AEV} := P_{AE}\cdot\sin\left(\delta_{soil}\right);$ $= 20.8760$ kN

$\Delta P_{AE} := P_{AE} - P_A;$ $= 0.0000$ kN

For the embedment less than 5 ft, the seismic passive earth pressure can be estimated using the static methods. The reduction factor (*R*) is from AASHTO (2012),

$R := 0.836;$ $= 0.836$ for $\phi_{soil} = 35^0$, and $\delta/\phi_{soil} = 0.886$

From Fig.3.11.5.4-1 in AASHTO (2012),

For $\theta = 90^0$ and $\phi_{soil} = 35^0$,

$k_p := 10.1;$ $= 10.1$

Since the reduction factor is 0.836,

$K_P := R\cdot k_p;$ $= 8.4436$

$P_{PE} := 0.5 \cdot K_P \cdot \Upsilon_{soil} \cdot D1^2 \cdot B;$ = 1388.0939 kN

$P_{PEH} := P_{PE} \cdot \cos(\delta_{soil});$ = 1189.8287 kN

$P_{PEV} := P_{PE} \cdot \sin(\delta_{soil});$ = 714.9212 kN

$W := DL_{bridge} + 0.5 \cdot LL_{bridge} + DL_{foundation};$ = 1724.22 kN

$m := \frac{W \cdot 1000}{g};$ = 175761.9776 kg

Inertial force,

$F_i := \frac{m \cdot a_x \cdot g}{1000};$ = 1724.2250 kN

$R1 := P_{AEV} + W + P_{PEV};$ = 2460.0222 kN

$F_r := R1 \cdot \tan(\phi_{soil});$ = 1722.5261 kN

Factor of safety against sliding

$F_{Resisting} := F_r + P_{PEH};$ = 2912.3548 kN

$F_{Driving} := F_i + P_{AEH};$ =1758.9685 kN

$FS_{sliding} := \frac{F_{Resisting}}{F_{Driving}};$ = 1.655717399

Embedment Depth for Excitation along Transverse-direction

Bridge load,

$DL_{bridge} := 806.58;$ = 806.58 kN

$LL_{bridge} := 987.13;$ = 987.13 kN

Foundation load,

$DL_{foundation} := 424.08;$ = 424.08 kN

Ground soil properties,

$\Upsilon_{soil} := \frac{1900 \cdot 9.81}{1000};$ = 18.64 kN/m^2

$\phi_{soil} := evalf\left(\frac{\pi}{180} \cdot 35\right);$ = 0.6108652381

$\delta_{soil} := evalf\left(\frac{\pi}{180} \cdot 31\right);$ = 0.5410520681

$c := 0;$ = 0

Geofoam embankment geometry,

$B := 9;$ = 9.00 m

$H := 6;$ = 6.00 m

$L := 4;$ = 4.00 m

Assumptions:

Soil below the embankment is sand. The vertical acceleration is negligible. The acceleration along longitudinal and transverse direction of the bridge are same. The spectral and peak ground acceleration is same. The block height is assumed to be 1m.

$g := 9.81;$ = 9.81 m/sec^2

Calculations:

For the acceleration of 1 g,

$a_x := 1;$ = 1 g

$a_y := 1;$ = 1 g

$a_z := 0;$ $= 0$

The basal layer sliding requires embedment to stop sliding. The calculation of active earth pressure for dynamic is same as static. The Coulomb's equation was used.

$\beta := \text{evalf}\left(\frac{\pi}{180}\cdot 0\right);$ $= 0.0000$

The backfill slope angle,

$i := 0;$ $= 0$

$$K_A := \text{evalf}\left(\left(\cos^2\left(\phi_{soil}-\beta\right)\right) \Big/ \left(\cos^2(\beta)\cdot\cos\left(\delta_{soil}+\beta\right)\cdot\left(1 + \sqrt{\frac{\sin\left(\delta_{soil}+\phi_{soil}\right)\cdot\sin\left(\phi_{soil}-i\right)}{\cos\left(\delta_{soil}+\beta\right)\cdot\cos(i-\beta)}}\right)^2\right)\right);$$ $= 0.2465569320$

$D1 := 1.4;$ $= 1.40\ \text{m}$

$P_A := 0.5\cdot K_A\cdot \Upsilon_{soil}\cdot D1^2\cdot L;$ $= 18.0146\ \text{kN}$

$P_{AE} := P_A;$ $= 18.0146\ \text{kN}$

$P_{AEH} := P_{AE}\cdot\cos\left(\delta_{soil}\right);$ $= 15.4416\ \text{kN}$

$P_{AEV} := P_{AE}\cdot\sin\left(\delta_{soil}\right);$ $= 9.2782\ \text{kN}$

$\Delta P_{AE} := P_{AE} - P_A;$ $= 0.0000\ \text{kN}$

For the embedment less than 5 ft, the seismic passive earth pressure can be estimated using the static methods. The reduction factor (R) according to AASHTO (2012) is,

$R := 0.836;$ $= 0.836$ for $\phi_{soil} = 35^0$, and $\delta/\phi_{soil} = 0.886$

From Fig.3.11.5.4-1 in AASHTO (2012),

For $\theta = 90^0$ and $\phi_{soil} = 35^0$,

$k_p := 10.1;$ $= 10.1$

Since the reduction factor is 0.836,

$K_P := R\cdot k_p;$ $= 8.4436$

$P_{PE} := 0.5\cdot K_P\cdot \Upsilon_{soil}\cdot D1^2\cdot L;$ $= 616.9306\ \text{kN}$

$P_{PEH} := P_{PE}\cdot\cos\left(\delta_{soil}\right);$ $= 528.8127\ \text{kN}$

$P_{PEV} := P_{PE}\cdot\sin\left(\delta_{soil}\right);$ $= 317.7428\ \text{kN}$

$W := DL_{bridge} + 0.5\cdot LL_{bridge} + DL_{foundation};$ $= 1724.22\ \text{kN}$

$m := \frac{W\cdot 1000}{g};$ $= 175761.9776\ \text{kg}$

Inertial force,

$F_i := \frac{m\cdot a_x\cdot g}{1000};$ $= 1724.2250\ \text{kN}$

$R1 := P_{AEV} + W + P_{PEV};$ $= 2051.2460\ \text{kN}$

$F_r := R1\cdot\tan\left(\phi_{soil}\right);$ $= 1436.2979\ \text{kN}$

Factor of safety against sliding

$F_{Resisting} := F_r + P_{PEH};$ $= 1965.1107\ \text{kN}$

$F_{Driving} := F_i + P_{AEH};$ $= 1739.6666\ \text{kN}$

$FS_{sliding} := \frac{F_{Resisting}}{F_{Driving}};$ = 1.129590401

Trapezoidal Prism
Critical Acceleration

Bridge load,

$DL_{bridge} := 806.58;$ = 806.58 kN

$LL_{bridge} := 987.13;$ = 987.13 kN

Foundation load,

$DL_{foundation} := 424.08;$ = 424.08 kN

Geofoam embankment geometry,

$B := 9;$ = 9.00 m

$H := 6;$ = 6.00 m

$L_{top} := 4;$ = 4.00 m

$\Delta z := 1;$ = 1.00 m

Stress distribution slope is 2V:1H.

Assumptions:

Soil below the embankment is sand. The vertical acceleration is negligible. The acceleration along longitudinal and transverse direction of the bridge are same. The spectral and peak ground acceleration is same. The block height is assumed to be 1m.

$g := 9.81;$ = 9.81 m/sec^2

Calculations:

The calculation was made at the basal layer which is at zero interface shown in Table E.3.

$\sigma_{v0} := \frac{DL_{bridge} + 0.5 \cdot LL_{bridge} + DL_{foundation}}{(L_{top} \cdot B)};$ = 47.8951 kPa

From the relation given by Sheeley and Negussey (2000),

The friction factor for geofoam-soil interface is,

$\tan\delta$ = 0.81

The friction factor for geofoam-soil interface according to Bartlett et al. (2000) is,

$\tan\delta$ = 0.6

Geofoam shear strength from Benchmark Foam (2009) is,

$\tau := \frac{33 \cdot 144 \cdot 95}{2000};$ = 225.7200 kPa

The critical acceleration at the basal layer was calculated by using goal seek in spreadsheet.

$a_{critical} := 0.60055;$ = 0.60055 g

Sample calculation for first and basal layers,

First layer,

$\sigma_{v0(1)} := \sigma_{v0};$ = 47.8951 kPa

Mass per unit area,

Table E.3. Calculation of critical acceleration for trapezoidal prism

Interface	Horizontal acceleration *(g)*	Normal stress *(kPa)*	Mass/unit area *(kg/m^2)*	Inertial force *(N/m^2)*	Frictional resisting force (W/K) *(N/m^2)*	Frictional resisting force (WO/K) *(N/m^2)*	Shear key coverage *(%)*	Cohesive resisting force *(N/m^2)*	FS sliding (without key)	FS sliding (with key)
6	0.601	47.90	4882	28763	38795	38795	0	0	1.35	1.35
5	0.601	38.32	3906	23011	31036	31036	0	0	1.35	1.35
4	0.601	31.93	3255	19176	25863	25863	0	0	1.35	1.35
3	0.601	27.37	2790	16436	22169	22169	0	0	1.35	1.35
2	0.601	23.95	2441	14382	19398	19398	0	0	1.35	1.35
1	0.601	21.29	2170	12784	17242	17242	0	0	1.35	1.35
0	0.601	19.16	1953	11505	11495	11495	0	0	1.00	1.00

$m := \frac{\sigma_{v0(1)} \cdot 1000}{9.81};$ = 4882.277 kg/m^2

Inertial force,

$F_{inertial} := m \cdot a_{critical} \cdot g;$ = 28763.426 N/m^2

Frictional resisting force,

$F_{resisting} := \sigma_{v0(1)} \cdot 0.81 \cdot 1000;$ = 38795.062 N/m^2

Factor of safety against sliding,

$FS_{sliding} := \frac{F_{resisting}}{F_{inertial}};$ = 1.35

Critical acceleration = 0.600 g

For the basal layer,

$\sigma_{v0(0)} := \sigma_{v0} \cdot \left(\frac{L_{top} \cdot B}{\left(L_{top} + 6 \cdot \Delta z\right) \cdot B} \right);$ = 19.158 kPa

Mass per unit area,

$m := \frac{\sigma_{v0(0)} \cdot 1000}{9.81};$ = 1952.911 kg/m^2

Inertial force,

$F_{inertial} := m \cdot a_{critical} \cdot g;$ = 11505.370 N/m^2

Frictional resisting force,

$F_{resisting} := \sigma_{v0(0)} \cdot 0.6 \cdot 1000;$ = 11494.833 N/m^2

Factor of safety against sliding

$FS_{sliding} := \frac{F_{resisting}}{F_{inertial}};$ = 1.00

Shear Key Coverage

Bridge load,

$DL_{bridge} := 806.58;$ = 806.58 kN

$LL_{bridge} := 987.13;$ = 987.13 kN

Foundation load,

$DL_{foundation} := 424.08;$ = 424.08 kN

Geofoam embankment geometry

$B := 9;$ = 9.00 m

$H := 6;$ = 6.00 m

$L_{top} := 4;$ = 4.00 m

$\Delta z := 1;$ = 1.00 m

Stress distribution slope is 2V:1H.

$L_{bottom(stress)} := L_{top} + 0.5 \cdot H;$ = 7.00 m

Ground soil properties,

$\Upsilon_{soil} := \frac{1900 \cdot 9.81}{1000};$ = 18.64 kN/m^2

$\phi_{soil} := \text{evalf}\left(\frac{\pi}{180} \cdot 35 \right);$ = 0.6108652381

$\delta_{soil} := \text{evalf}\left(\frac{\pi}{180} \cdot 31 \right);$ = 0.5410520681

$\beta := 0;$ = 0

$c := 0;$ $= 0$

Assumptions:

Soil below the embankment is sand. The vertical acceleration is negligible. The acceleration along longitudinal and transverse directions of the bridge are same. The spectral and peak ground acceleration is same. The block height is assumed to be 1m.

$g := 9.81;$ $= 9.81$ m/sec^2

Calculations:

The detailed calculation is shown in Table F.4. The calculation of first layer is given below.

$$\sigma_{v0} := \frac{DL_{bridge} + 0.5 \cdot LL_{bridge} + DL_{foundation}}{(L_{top} \cdot B)}; \quad = 47.8951 \text{ kPa}$$

From the relation given by Sheeley and Negussey (2000), the friction factor for geofoam-geofoam interface is:

$\tan\delta = 0.81$

The friction factor for geofoam-soil interface according to Bartlett et al. (2000) is:

$\tan\delta = 0.6$

Geofoam shear strength from Benchmark Foam (2009) is,

$$\tau := \frac{33 \cdot 144 \cdot 95}{2000}; \quad = 225.7200 \text{ kPa}$$

From the spread sheet below,

For the acceleration of 1 g,

$a_x := 1;$ $= 1$ g

$a_y := 1;$ $= 1$ g

$a_z := 0;$ $= 0$

Sample calculation for fifth layer that is second from top,

$n := 2;$ $= 2$

Table E.4. Calculation of shear key coverage for trapezoidal prism

Interface	Horizontal acceleration (g)	Normal stress (kPa)	Mass/unit area (kg/m^2)	Inertial force (N/m^2)	Frictional resisting force (W/K) (N/m^2)	Frictional resisting force (WO/K) (N/m^2)	Shear key coverage (%)	Cohesive resisting force (N/m^2)	FS sliding (without key)	FS sliding (with key)
6	1.000	47.90	4882	47895	35691	38795	8	18058	0.81	1.12
5	1.000	38.32	3906	38316	29174	31036	6	13543	0.81	1.11
4	1.000	31.93	3255	31930	24570	25863	5	11286	0.81	1.12
3	1.000	27.37	2790	27369	21282	22169	4	9029	0.81	1.11
2	1.000	23.95	2441	23948	18622	19398	4	9029	0.81	1.15
1	1.000	21.29	2170	21287	16725	17242	3	6772	0.81	1.10
0	1.000	19.16	1953	19158	11495	11495	0	0	0.60	0.60

$\sigma_{v0(0)} := \sigma_{v0} \cdot \left(\frac{L_{top} \cdot B}{\left(L_{top} + (n-1) \cdot \Delta z\right) \cdot B} \right);$ = 38.316 kPa

Mass per unit area,

$m := \frac{\sigma_{v0(0)} \cdot 1000}{9.81};$ = 3905.822 kg/m^2

Inertial force,

$F_i := m \cdot a_x \cdot g;$ = 38316.111 N/m^2

Frictional resisting force,

$F_r := \sigma_{v0(0)} \cdot 0.81 \cdot 1000;$ = 31036.050 N/m^2

Factor of safety against sliding,

$FS_{sliding} := \frac{F_r}{F_i};$ = 0.81

Using the shear key coverage of 6 percent,

$S_c := \frac{6}{100};$ = 0.06

Frictional resisting force,

$F_r := \sigma_{v0(0)} \cdot 0.81 \cdot 1000 \cdot \left(1 - S_c\right);$ = 29173.89 N/m^2

Cohesive resisting force,

$C_r := \tau \cdot 1000 \cdot S_c;$ = 13543.20 N/m^2

Factor of safety against sliding,

$FS_{sliding} := \frac{F_r + C_r}{F_i};$ = 1.11

Embedment Depth for Excitation along Longitudinal-direction

Bridge load,

$DL_{bridge} := 806.58;$ = 806.58 kN

$LL_{bridge} := 987.13;$ = 987.13 kN

Foundation load,

$DL_{foundation} := 424.08;$ = 424.08 kN

Geofoam embankment geometry,

$B := 9;$ = 9.00 m

$H := 6;$ = 6.00 m

$L_{top} := 4;$ = 4.00 m

$\Delta z := 1;$ = 1.00 m

Stress distribution slope is 2V:1H.

$L_{bottom(stress)} := L_{top} + 0.5 \cdot H;$ = 7.00 m

Ground soil properties,

$\Upsilon_{soil} := \frac{1900 \cdot 9.81}{1000};$ = 18.64 kN/m^2

$\phi_{soil} := \text{evalf}\left(\frac{\pi}{180} \cdot 35 \right);$ = 0.6108652381

$\delta_{soil} := \text{evalf}\left(\frac{\pi}{180} \cdot 31 \right);$ = 0.5410520681

$\beta := 0;$ = 0

$c := 0;$ $= 0$

Assumptions:

Soil below the embankment is sand. The vertical acceleration is negligible. The acceleration along the longitudinal and transverse directions of the bridge are same. The spectral and peak ground acceleration is same. The block height is assumed to be 1m.

$g := 9.81;$ $= 9.81$ m/sec^2

Calculations:

$\sigma_{v0} := \frac{DL_{bridge} + 0.5 \cdot LL_{bridge} + DL_{foundation}}{(L_{top} \cdot B)};$ $= 47.8951$ kPa

$a_x := 1;$ $= 1$ g

$a_y := 1;$ $= 1$ g

$a_z := 0;$ $= 0$

Depth of embedment,

$D1 := 1.0;$ $= 1.00$ m

Exterior slope is 1V:2H.

$L_{top(EP)} := L_{top} + H \cdot 2 \cdot 2;$ $= 28.00$ m

$L_{bottom(EP)} := L_{top} + H \cdot 2 \cdot 2;$ $= 28.00$ m

$L_{bottom} := L_{top} + 2 \cdot 2 \cdot (H + D1);$ $= 32.00$ m

$\beta := -evalf\left(\arctan\left(\frac{L_{bottom} - L_{top}}{2 \cdot (H + D1)}\right)\right);$ $= -1.1071$

$i := 0;$ $= 0$

$= 0.02686566866$

$$K_A := evalf\left(\left(\cos^2(\phi_{soil} - \beta)\right) \Big/ \left(\cos^2(\beta) \cdot \cos(\delta_{soil} + \beta) \cdot \left(1 + \sqrt{\frac{\sin(\delta_{soil} + \phi_{soil}) \cdot \sin(\phi_{soil} - i)}{\cos(\delta_{soil} + \beta) \cdot \cos(i - \beta)}}\right)^2\right)\right);$$

$P_A := 0.5 \cdot K_A \cdot \gamma_{soil} \cdot D1^2 \cdot B;$ $= 2.2534$ kN

$P_{AE} := P_A;$ $= 2.2534$ kN

$P_{AEH} := P_{AE} \cdot \cos(-\beta - \delta_{soil});$ $= 1.9018$ kN

$P_{AEV} := P_{AE} \cdot \sin(-\beta - \delta_{soil});$ $= 1.2086$ kN

$\Delta P_{AE} := P_{AE} - P_A;$ $= 0.0000$ kN

For the embedment less than 5 ft, the seismic passive earth pressure can be estimated using the static methods. The reduction factor (R) is,

$R := 0.836;$ $= 0.836$ for $\phi_{soil} = 35^0$, and $\delta/\phi_{soil} = 0.886$

From Fig.3.11.5.4-1 in AASHTO (2012),

$\theta := evalf\left(\left(\frac{\pi}{2} - \beta\right) \cdot \frac{180}{\pi}\right);$ $= 153.4349488$

For $\theta = 153^0$ and $\phi_{soil} = 35^0$,

$k_p := 14;$ $= 14$

Since the reduction factor is 0.836,

$K_P := R \cdot k_p;$ $= 11.704$

$P_{PE} := 0.5 \cdot K_P \cdot \Upsilon_{soil} \cdot D1^2 \cdot B;$ = 981.6788 kN

$P_{PEH} := P_{PE} \cdot \cos\left(-\beta - \delta_{soil}\right);$ = 828.5379 kN

$P_{PEV} := P_{PE} \cdot \sin\left(-\beta - \delta_{soil}\right);$ = 526.5153 kN

$n := 8;$ = 8

$\sigma_{v0(0)} := \sigma_{v0} \cdot \left(\frac{L_{top} \cdot B}{\left(L_{top} + (n-1) \cdot \Delta z\right) \cdot B} \right);$ = 17.416 kPa

$W := \sigma_{v0(0)} \cdot \left(L_{top} + H + D1\right) \cdot B;$ = 1724.225000

$m := \frac{W \cdot 1000}{g};$ = 175761.9776 kg

Inertial force,

$F_i := \frac{m \cdot a_x \cdot g}{1000};$ = 1724.2250 kN

$R1 := P_{AEV} + W + P_{PEV};$ = 2251.9489 kN

$F_r := R1 \cdot \tan\left(\phi_{soil}\right);$ = 1576.8316 kN

Factor of safety against sliding

$F_{Resisting} := F_r + P_{PEH};$ = 2405.3694 kN

$F_{Driving} := F_i + P_{AEH};$ = 1726.1268 kN

$FS_{sliding} := \frac{F_{Resisting}}{F_{Driving}};$ = 1.393506773

Embedment Depth for Excitation along Transverse-direction

Bridge load,

$DL_{bridge} := 806.58;$ = 806.58 kN

$LL_{bridge} := 987.13;$ = 987.13 kN

Foundation load,

$DL_{foundation} := 424.08;$ = 424.08 kN

Geofoam embankment geometry,

$B := 9;$ = 9.00 m

$H := 6;$ = 6.00 m

$L_{top} := 4;$ = 4.00 m

$\Delta z := 1;$ = 1.00 m

Stress distribution slope is 2V:1H.

$L_{bottom(stress)} := L_{top} + 0.5 \cdot H;$ = 7.00 m

Ground soil properties,

$\Upsilon_{soil} := \frac{1900 \cdot 9.81}{1000};$ = 18.64 kN/m^2

$\phi_{soil} := \text{evalf}\left(\frac{\pi}{180} \cdot 35 \right);$ = 0.6108652381

$\delta_{soil} := \text{evalf}\left(\frac{\pi}{180} \cdot 31 \right);$ = 0.5410520681

$\beta := 0;$ = 0

$c := 0;$ = 0

Assumptions:

Soil below the embankment is sand. The vertical acceleration is negligible. The acceleration along longitudinal and transverse direction of the bridge are same. The spectral and peak ground acceleration is same. The block height is assumed to be 1m.

$g := 9.81;$ = 9.81 m/sec^2

Calculations:

$\sigma_{v0} := \frac{DL_{bridge} + 0.5 \cdot LL_{bridge} + DL_{foundation}}{(L_{top} \cdot B)};$ = 47.8951 kPa

$a_x := 1;$ = 1 g

$a_y := 1;$ = 1 g

$a_z := 0;$ = 0

Depth of embedment,

$D1 := 1.0;$ = 1.00 m

Exterior slope is 1V:2H.

$L_{top(EP)} := L_{top} + H \cdot 2 \cdot 2;$ = 28.00 m

$L_{bottom(EP)} := L_{top} + H \cdot 2 \cdot 2;$ = 28.00 m

$L_{bottom} := L_{top} + 2 \cdot 2 \cdot (H + D1);$ = 32.00 m

$\beta := -evalf\left(\arctan\left(\frac{L_{bottom} - L_{top}}{2 \cdot (H + D1)}\right)\right);$ = -1.1071

$i := 0;$ = 0

= 0.02686566866

$$K_A := evalf\left(\left(\cos^2(\phi_{soil} - \beta)\right) \Big/ \left(\cos^2(\beta) \cdot \cos(\delta_{soil} + \beta) \cdot \left(1 + \sqrt{\frac{\sin(\delta_{soil} + \phi_{soil}) \cdot \sin(\phi_{soil} - i)}{\cos(\delta_{soil} + \beta) \cdot \cos(i - \beta)}}\right)^2\right)\right);$$

$P_A := 0.5 \cdot K_A \cdot \Upsilon_{soil} \cdot D1^2 \cdot \left(\frac{(L_{bottom(EP)} + L_{bottom})}{2}\right);$ = 7.5112 kN

$P_{AE} := P_A;$ = 7.5112 kN

$P_{AEH} := P_{AE} \cdot \cos(-\beta - \delta_{soil});$ = 6.3395 kN

$P_{AEV} := P_{AE} \cdot \sin(-\beta - \delta_{soil});$ = 4.0286 kN

$\Delta P_{AE} := P_{AE} - P_A;$ = 0.0000 kN

For the embedment less than 5 ft, the seismic passive earth pressure can be estimated using the static methods. The reduction factor (R) is,

$R := 0.836;$ = 0.836 for ϕ_{soil} = 35⁰, and δ/ϕ_{soil} =0.886

From Fig.3.11.5.4-1 in AASHTO (2012),

$\theta := evalf\left(\left(\frac{\pi}{2} - \beta\right) \cdot \frac{180}{\pi}\right);$ = 153.4349488

For θ = 153⁰ and ϕ_{soil} = 35⁰,

$k_p := 14;$ = 14

Since the reduction factor is 0.836.

$K_P := R \cdot k_p;$ = 11.704

$P_{PE} := 0.5 \cdot K_P \cdot \Upsilon_{soil} \cdot D1^2 \cdot \left(\frac{\left(L_{bottom(EP)} + L_{bottom}\right)}{2} \right);$ = 3272.2628 kN

$P_{PEH} := P_{PE} \cdot \cos\left(-\beta - \delta_{soil}\right);$ = 2761.7929 kN

$P_{PEV} := P_{PE} \cdot \sin\left(-\beta - \delta_{soil}\right);$ = 1755.0510 kN

$n := 8;$ = 8

$\sigma_{v0(0)} := \sigma_{v0} \cdot \left(\frac{L_{top} \cdot B}{\left(L_{top} + (n-1) \cdot \Delta z\right) \cdot B} \right);$ = 17.416 kPa

$W := \sigma_{v0(0)} \cdot \left(L_{top} + H + D1\right) \cdot B;$ = 1724.225000

$m := \frac{W \cdot 1000}{g};$ = 175761.9776 kg

Inertial force,

$F_i := \frac{m \cdot a_x \cdot g}{1000};$ = 1724.2250 kN

$R1 := P_{AEV} + W + P_{PEV};$ = 3483.3046 kN

$F_r := R1 \cdot \tan\left(\phi_{soil}\right);$ = 2439.0362 kN

Factor of safety against sliding

$F_{Resisting} := F_r + P_{PEH};$ = 5200.8290 kN

$F_{Driving} := F_i + P_{AEH};$ = 1730.5645 kN

APPENDIX F – SIZING OF RESTRAINT CABLES

Sway Mode
Excitation along longitudinal-direction for 1 g

Geofoam embankment geometry,

$B := 9;\ = 9.00\ \text{m}$

$H := 7;\ = 7.00\ \text{m}$

$L1 := 4;\ = 4.00\ \text{m}$

Allowable axial strain due to the combined dead and cyclic load is,

$\varepsilon_{allowable} := 2;\ = 2\ \%$

$\nu := 0.193;\ = 0.193$

The sway mode with placement of cables is shown in Figure G.1.

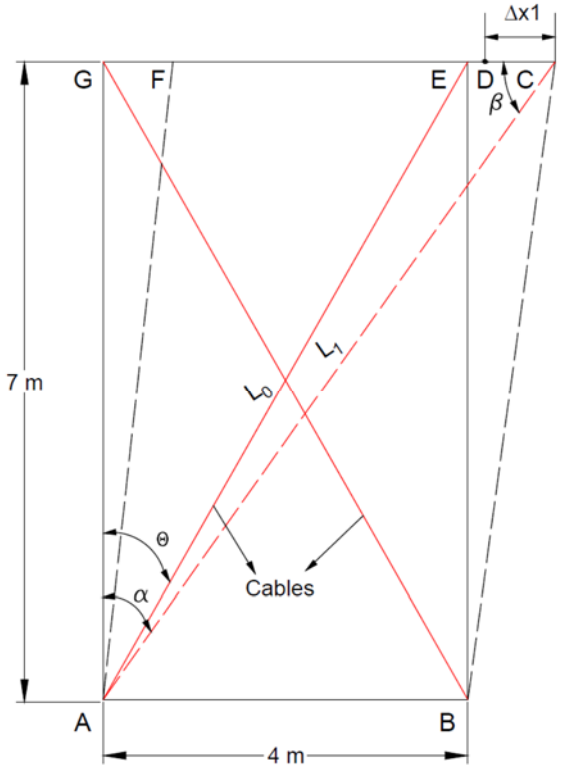

Figure F.1 Sway mode with placement of cables

During elastic limit,

$\Upsilon_{allowable} := \varepsilon_{allowable} \cdot (1 + \nu);\ = 2.386\ \%$

In Figure F.1, AE and BG are two cables. D is the position after which the cable started to take load. Δx1 is the displacement of the system after cable started to take load. EC is the total displacement of system.

From Figure F.1,

$\text{Tangent}_{theta} := \frac{L}{H};\ = \frac{4}{7}$

$\theta := \text{evalf}\left(\left(\arctan\left(\text{Tangent}_{theta}\right)\right) \cdot \frac{180}{\pi} \right);\ = 29.74488129$

Table F.1 and F.2 shows the calculation of force and displacement of both EPS and cable respectively. In table F.1, strain (ε) and stress (σ) was taken from the stress-strain relationship of EPS 29 obtained from monotonic uniaxial test.

Table F.1. Calculation of force and displacement of EPS

ϵ (%)	Υ (%)	Δx (m)	σ (kPa)	τ (kPa)	V_{EPS} (kN)
0.00	0.000	0.000	0.00	0.00	0.00
0.25	0.298	0.021	25.93	12.97	51.86
0.50	0.597	0.042	53.53	26.77	107.06
0.75	0.895	0.063	79.45	39.73	158.9
1.00	1.193	0.084	107.78	53.89	215.56
1.25	1.491	0.104	131.93	65.97	263.86
1.50	1.790	0.125	152.28	76.14	304.56
1.75	2.088	0.146	169.29	84.65	338.58
2.00	2.386	0.167	181.68	90.84	363.36
2.25	2.684	0.188	182.68	91.34	365.36
2.50	2.983	0.209	183.68	91.84	367.36
2.75	3.281	0.230	184.68	92.34	369.36
3.00	3.579	0.251	185.68	92.84	371.36

Table F.2. Calculation of force and displacement of cable

ϵ (%)	σ (kPa)	P (kN)	Pcosθ (kN)	Δx (m)	$\Delta x\cos\theta$ (m)	V_{cable} (kN)
0.00	0	0.00	0.00	0.000	0.0000	----------
0.10	330960	93.66	81.32	0.014	0.0122	----------
0.20	661920	187.32	162.64	0.028	0.0244	----------
0.30	896350	253.67	220.24	0.038	0.0331	----------
0.40	1103200	312.21	271.07	0.047	0.0407	----------
0.50	1268680	359.04	311.73	0.054	0.0468	----------
0.60	1447950	409.77	355.78	0.062	0.0534	0
0.70	1516900	429.28	372.72	0.064	0.0560	488
0.80	1558270	440.99	382.89	0.066	0.0575	976
0.90	1599640	452.70	393.05	0.068	0.0590	1321
1.00	1634115	462.45	401.52	0.069	0.0603	1626
1.10	1654800	468.31	406.61	0.070	0.0611	1870
1.20	1675485	474.16	411.69	0.071	0.0618	2135
1.30	1689275	478.06	415.08	0.072	0.0624	2236
1.40	1703065	481.97	418.46	0.072	0.0629	2297
1.50	1716855	485.87	421.85	0.073	0.0634	2358
1.60	1730645	489.77	425.24	0.074	0.0639	2409
1.70	1744435	493.68	428.63	0.074	0.0644	2440
1.80	1758225	497.58	432.02	0.075	0.0649	2470

1.90	1772015	501.48	435.41	0.075	0.0654	2490
2.00	1778910	503.43	437.10	0.076	0.0657	2511
2.10	1792700	507.33	440.49	0.076	0.0662	2531
2.20	1799595	509.29	442.18	0.077	0.0664	2551
2.30	1809938	512.21	444.72	0.077	0.0668	2572
2.40	1820280	515.14	447.27	0.077	0.0672	2592
2.50	1827175	517.09	448.96	0.078	0.0674	2612

In the Table F.1, *γ, Δx, τ* and V are the shear strain, horizontal displacement, shear stress and horizontal force. The calculation of force and displacement for strain level of 0.25 % is shown below.

$\varepsilon := 0.25;$ $= 0.25$ %

$\Upsilon := \varepsilon \cdot (1 + \nu);$ $= 0.29825$ %

$\Delta x := \frac{\Upsilon \cdot H}{100};$ $= 0.021$

$\sigma := 25.93;$ $= 25.93$ kPa

$\tau := \frac{\sigma}{2};$ $= 12.96$ kPa

$V := \tau \cdot L;$ $= 51.86$ kN

In Table F.2, *ε* and *σ* are taken from the stress-strain relationship of the strand of Grade 270 based on Nawy (2006).

The design force for the acceleration of 1 g along longitudinal direction is shown below.

$a := 1;$ $= 1$ g

Weight at top of embankment,

$W := 1724;$ $= 1724$ kN

$V_{design} := W \cdot a;$ $= 1724$ kN

The length of strand was obtained from Figure F.1.

$L_{strand} := evalf\left(\frac{L}{\sin\left(\theta \cdot \frac{\pi}{180} \right)} \right);$ $= 8.062257748$ m

Area of strand and number of strands were varied to get the design value within the limit of force and strain in cable and EPS. The calculation of force and displacement for strain level of 0.1 % is given below.

Area of strand for 19 mm diameter,

$A_{strand} := evalf\left(\frac{283}{1000^2} \right);$ $= 0.000283$ m^2

Numbers of strand,

$n := 6;$ $= 6$

$\varepsilon 1 := 0.1;$ $= 0.1$ %

$\sigma 1 := 330960;$ $= 330960$ kPa

Axial force,

$P1 := \sigma 1 \cdot A_{strand};$ $= 93.6617$ kN

Horizontal component force,

$P_{Horizontal} := evalf\left(P1 \cdot \cos\left(\theta \cdot \frac{\pi}{180} \right) \right);$ $= 81.3211$ kN

Young's modulus of elasticity,

$$E_{strand} := \frac{27500000}{100000} \cdot 689.5 \cdot 1000; \quad = 1.896125000\,10^{8} \text{ kPa}$$

Displacement (elongation),

$$\Delta x1 := \frac{P1 \cdot L_{strand}}{A_{strand} \cdot E_{strand}}; \quad = 0.0141 \text{ m}$$

Horizontal component of displacement,

$$\Delta x1_{Horizontal} := evalf\left(\Delta x1 \cdot \cos\left(\theta \cdot \frac{\pi}{180}\right)\right); \quad = 0.01222 \text{ m}$$

Since the cable was engaged at strain level of 0.6 %. The force in the cable was set zero up to this position. The combined plot of EPS and cable was made from the force and displacement relationship. The calculation of force and displacement for combined EPS and cable is shown in Table F.3. The limiting value of force in the cable was based on the stress value in the linear range of stress-strain relationship.

The design value was found to be within the limiting values of force and strain for both cable and EPS. The resisting forces on EPS and cable for the excitation level of 1 g were 157 kN and 2135 kN. The resisting force was found to be higher than the design load.

Number of strands = 6

Diameter of strand = 19 mm

Table F.3. Calculation of force and displacement for combined EPS and cable

Δx (m)	V_{EPS} (kN)	V_{cable} (kN)	V (kN)
0.0000	0.00	----------	0.00
0.0122	30.35	----------	30.35
0.0244	61.26	----------	61.26
0.0331	84.14	----------	84.14
0.0407	104.33	----------	104.33
0.0468	119.66	----------	119.66
0.0534	136.09	0.00	136.09
0.0560	142.41	487.93	630.34
0.0575	146.20	975.85	1122.05
0.0590	149.99	1321.47	1471.46
0.0603	153.15	1626.42	1779.57
0.0611	155.05	1870.39	2025.43
0.0618	156.94	2134.68	2291.62
0.0624	158.21	2236.33	2394.54
0.0629	159.53	2297.32	2456.85
0.0634	160.91	2358.31	2519.22
0.0639	162.29	2409.14	2571.43
0.0644	163.67	2439.63	2603.30
0.0649	165.05	2470.13	2635.18

0.0654	166.43	2490.46	2656.89
0.0657	167.12	2510.79	2677.91
0.0662	168.50	2531.12	2699.62
0.0664	169.20	2551.45	2720.65
0.0668	170.23	2571.78	2742.01
0.0672	171.27	2592.11	2763.38
0.0674	171.96	2612.44	2784.40